

Die approbierte Originalversion dieser Dissertation ist an der Hauptbibliothek der Technischen Universität Wien aufgestellt (<http://www.ub.tuwien.ac.at>).

The approved original version of this thesis is available at the main library of the Vienna University of Technology (<http://www.ub.tuwien.ac.at/englweb/>).

D O C U M E N T O R A L T H E S I S

**DEVELOPMENT AND APPLICATION OF A  
COMPUTATIONAL FLUID DYNAMICS CODE  
TO PREDICT THE THERMAL IMPACT ON  
UNDERGROUND STRUCTURES IN CASE OF FIRE**

submitted in satisfaction of the requirements for the degree of  
Doctor of Science in Civil Engineering  
of the Vienna University of Technology, Faculty of Civil Engineering

---

D I S S E R T A T I O N

**ENTWICKLUNG UND ANWENDUNG EINES  
STRÖMUNGSSIMULATIONSPROGRAMMES ZUR  
VORHERSAGE DER THERMISCHEN EINWIRKUNG  
AUF HOHLRAUMBAUTEN UNTER BRANDLAST**

ausgeführt zum Zweck der Erlangung des akademischen Grades eines  
Doktors der technischen Wissenschaften  
eingereicht an der Technischen Universität Wien Fakultät für Bauingenieurwesen

von

Dipl.-Ing. Aram Amouzandeh

Matrikelnummer: 00 25 882

Draschestraße 26/13, 1230 Wien, Österreich

Gutachter: Univ.-Prof. Dipl.-Ing. Dr. techn. Roman Lackner  
Material-Technologie Innsbruck  
Universität Innsbruck  
Technikerstraße 13, 6020 Innsbruck, Österreich

Gutachter: Ao.Univ.-Prof. Dipl.-Ing. Dr. techn. Reinhard Willinger  
Institut für Energietechnik und Thermodynamik  
Technische Universität Wien  
Getreidemarkt 9/302, 1060 Wien, Österreich

Wien, im Juni 2012

.....

# Danksagung

An erster Stelle möchte ich meiner Familie danken, die mir in jeder Phase meines Studiums Rückhalt geboten hat.

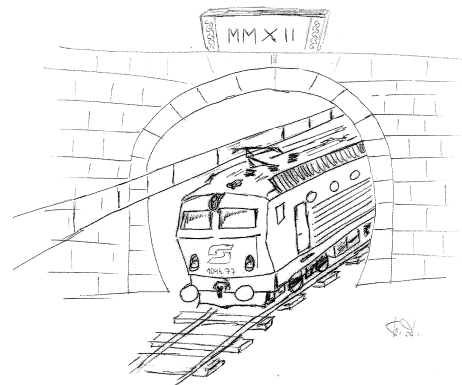
Herzlichst verbunden bin ich meinen Kollegen des Instituts für Mechanik der Werkstoffe und Strukturen der Technischen Universität Wien, vor allem für die Schaffung eines optimalen Arbeitsklimas während meines Doktoratsstudiums.

An dieser Stelle seien auch die Kollegen des monatlich statt findenden "OpenFOAM-Stammtisch" an der Technischen Universität Wien erwähnt, die mir stets wertvolle Anregungen bei Fragestellungen zur numerischen Strömungssimulation gegeben haben.

Weiters soll hier die großartige technische Betreuung durch das Team des "Vienna Scientific Cluster (VSC)" bei der Durchführungen numerischer Simulationen auf dem VSC genannt werden.

Die finanzielle Unterstützung durch das Bundesministerium für Verkehr, Innovation und Technologie im Rahmen der KIRAS-Projekte (Österreichisches Förderungsprogramm für Sicherheitsforschung) 813794 und 824781 "Sicherheit von Hohlraumbauten unter Feuerlast – Entwicklung eines Struktursimulationstools" sei ebenfalls dankend erwähnt.

Für ihr großes Interesse an Forschung und Entwicklung möchte ich den Partnern der KIRAS-Projekte danken: Materialtechnologie Innsbruck (MTI) der Universität Innsbruck, Institut für konstruktiven Ingenieurbau der Universität für Bodenkultur Wien, Schimetta Consult ZT GmbH, Ingenieurbüro Dr. Lindlbauer, ZT Reismann, ÖBB-Infrastruktur Bau Aktiengesellschaft, ASFINAG Autobahnen- und Schnellstraßen-Finanzierungs-Aktiengesellschaft, Wiener Linien GmbH & Co KG, ARGE Bautech, Forschungsinstitut der Vereinigung der österreichischen Zementindustrie.



## **Kurzfassung**

Die Brandbelastung während eines Feuers in Hohlraumbauten verursacht erheblichen Schaden an der Tragstruktur und beeinträchtigt dadurch die Gebrauchstauglichkeit und Tragsicherheit der Struktur. Im Falle eines Tunnelbrandes kommt es vor allem durch die thermische Einwirkung auf die Tragkonstruktionen aus Beton und Stahl zum Abplatzen oberflächennaher Schichten der Betoninnenschale. Zur Bestimmung der Sicherheit sich in Planung befindlicher Infrastruktur im Katastrophenfall Brand und im Zuge der Sanierung ist es notwendig, den möglichen Wärmeeintrag von der Brandquelle in die Struktur abzuschätzen. Unterstützt durch den konstanten Anstieg der Rechnerleistung vergangener Jahre, stellt die numerische Strömungssimulation eine vielversprechende Methode dar. In dieser Arbeit wird ein Strömungssimulationsprogramm entwickelt, welches die Vorhersage der thermischen Belastung der Tragstruktur im Brandfall ermöglichen soll und es im weiteren erlaubt, standardisierte Temperatur-Zeit Kurven durch die ermittelten Temperaturverläufe zu ersetzen. Ein solches Programm muss die Physik einer turbulenten, auftriebsgesteuerten Strömung abbilden und den Wärmetransport zufolge Wärmeleitung, Konvektion und Strahlung beinhalten. Zu diesem Zweck werden entsprechende Modelle mit Hilfe ausgesuchter Referenzbeispiele getestet, um sie dann in ein Simulationsprogramm zu integrieren. Die Leistungsfähigkeit des entwickelten Programmes wird im weiteren durch die Analyse von Brandexperimenten bestimmt bevor Brandszenarien in Tunnel mit unterschiedlichen Querschnitten realer Abmessungen und unter verschiedenen Ventilationsbedingungen simuliert werden.

## Abstract

Fire hazards in underground infrastructures can seriously endanger the integrity of the load-carrying structure. Especially in case of tunnel fires, the temperature loading causes significant thermal degradation of concrete and spalling of near-surface concrete layers is likely to take place. In order to avoid or minimise the destructive effects of fires in enclosures, a quantitative assessment of the thermal intake to the structure during such incidents is inevitable. Thanks to increasing computational performance, simulations of fire scenarios by means of *Computational Fluid Dynamics* represent a promising method nowadays. The aim of the underlying work is to develop a fire code to numerically determine the thermal impact of fires on the load-carrying structure. The so-obtained temperature development of both the fluid and the adjacent solid walls of the structure should then replace commonly used temperature-time curves. In the simulation of fires, the analysis tool has to reproduce turbulent buoyancy-driven flows induced by the combustion process, accounting for conductive, convective, and radiative heat transfer. To meet these demands, suitable sub models are introduced after assessing their performance by means of selected benchmark tests. All sub models are combined into a single code which is then applied to the re-analysis of real-scale fire experiments before the fire code is finally used to simulate fire scenarios in tunnels of real dimensions with different types of cross-sections, blockages and fire loads.

# Contents

<b>1</b>	<b>Introduction</b>	<b>1</b>
1.1	Motivation . . . . .	1
1.2	Outline . . . . .	2
<b>2</b>	<b>Natural fires</b>	<b>4</b>
2.1	Physics of fire . . . . .	4
2.1.1	Fire plumes . . . . .	6
2.2	Fire development in enclosures . . . . .	9
2.2.1	The growth stage . . . . .	9
2.2.2	The fully developed fire . . . . .	10
2.2.3	Backdraught . . . . .	11
2.2.4	Back-layering . . . . .	11
<b>3</b>	<b>Design fire scenarios</b>	<b>12</b>
3.1	Methods of estimating the Heat Release Rate (HRR) . . . . .	13
3.2	Design fires for tunnels . . . . .	14
3.2.1	Road tunnels . . . . .	14
3.2.2	Railway tunnels . . . . .	16
3.2.3	Metropolitan tunnels . . . . .	16
3.3	Mathematical description of design fires for tunnels . . . . .	19
3.3.1	Linear approximation . . . . .	19
3.3.2	Nonlinear approximation . . . . .	19
3.3.3	Exponential approximation . . . . .	20

---

<b>4</b>	<b>Computational Fluid Dynamics</b>	<b>24</b>
4.1	Governing equations for fires . . . . .	24
4.2	Numerical modelling of fires in enclosures . . . . .	27
4.2.1	Zone Models . . . . .	27
4.2.2	Field Models or Computational Fluid Dynamics (CFD) . . . . .	28
4.2.2.1	Finite Volume Method (FVM) . . . . .	28
4.3	Length and time scales within fires and consequences for CFD . . . . .	31
4.4	Possibilities and limitations of CFD . . . . .	32
<b>5</b>	<b>Development of a fire code</b>	<b>33</b>
5.1	Existing fire codes . . . . .	33
5.2	Development of the fire code in OpenFOAM . . . . .	35
5.2.1	Turbulence model . . . . .	36
5.2.1.1	RANS turbulence modelling . . . . .	38
5.2.2	The conjugate heat transfer . . . . .	42
5.2.2.1	Forced convection at a flat heated plate . . . . .	44
5.2.3	Buoyancy modifications of the standard $k$ - $\varepsilon$ model . . . . .	46
5.2.3.1	Application of buoyancy-modified $k$ - $\varepsilon$ models on a round turbulent buoyant plume . . . . .	49
5.2.4	Radiative heat transfer . . . . .	55
5.2.4.1	The P1-approximation and the Finite Volume Discrete Or- dinate Method . . . . .	56
5.2.4.2	Benchmark test 1: grey medium between two parallel (in- finitely long) walls . . . . .	58
5.2.4.3	Benchmark test 2: grey gas in a 2D rectangular enclosure	59
5.2.4.4	Conjugate heat transfer considering radiation . . . . .	62
5.2.5	Combustion model . . . . .	64
5.2.5.1	Thermo-physical properties of the fluid mixture . . . . .	68
5.2.5.2	Radiation properties of the fluid mixture . . . . .	69
5.2.5.3	Application of the combustion model to a buoyant diffu- sion flame . . . . .	70

<b>6</b>	<b>Application of the fire code on realistic geometries</b>	<b>77</b>
6.1	The Cardington compartment-fire test . . . . .	78
6.1.1	Results and discussion . . . . .	83
6.1.2	Conclusions . . . . .	87
6.2	The Buxton tunnel-fire test . . . . .	91
6.2.1	Results and discussion . . . . .	95
6.2.2	Conclusions . . . . .	103
6.3	Real-scale tunnel configurations . . . . .	106
6.3.1	Results and discussion . . . . .	110
6.3.1.1	Ventilation velocity 0.5 m/s . . . . .	110
6.3.1.2	Ventilation velocity 3 m/s . . . . .	118
6.3.2	Conclusions . . . . .	124
<b>7</b>	<b>Concluding remarks</b>	<b>127</b>
7.1	Conclusions . . . . .	127
7.2	Engineering model . . . . .	129
7.2.1	Heat transfer . . . . .	130
7.2.2	Longitudinal and cross-sectional distribution of the thermal load .	132
7.3	Outlook . . . . .	135
	<b>Bibliography</b>	<b>137</b>
<b>A</b>	<b>Parameters to describe the temperature dependency of fluid properties</b>	<b>145</b>
A.1	JANAF-coefficients . . . . .	145
A.1.1	Methane (CH <sub>4</sub> ) . . . . .	145
A.1.2	Air . . . . .	146
A.2	Constants for Sutherland's formula of dynamic viscosity . . . . .	147
A.3	Coefficients of weighting functions for the mean absorption coefficient . .	147
<b>B</b>	<b>Discretisation schemes and solver settings for real-scale simulations</b>	<b>148</b>
B.1	Discretisation schemes ( <i>fvSchemes</i> ) . . . . .	148
B.1.1	Fluid regions . . . . .	148
B.1.2	Solid regions . . . . .	149

B.2	Solver settings ( <i>fvSolution</i> ) . . . . .	150
B.2.1	Fluid regions . . . . .	150
B.2.2	Solid regions . . . . .	152
<b>C</b>	<b>Simulation results: Cardington</b>	<b>153</b>
C.1	Contour plots of temperature at $z = 1.53$ m . . . . .	153
<b>D</b>	<b>Simulation results: Buxton</b>	<b>156</b>
D.1	Contour plots of temperature at $z = 0$ m (reactive) . . . . .	157
D.2	Contour plots of temperature at $z = 0$ m (non-reactive) . . . . .	158
<b>E</b>	<b>Simulation results: real-scale tunnels</b>	<b>159</b>
E.1	Contour plots of temperature for a ventilation velocity of 0.5 m/s . . . . .	160
E.1.1	Rectangular cross-section ( $z = -2.3$ m) . . . . .	160
E.1.2	Arced cross-section ( $z = -2.3$ m) . . . . .	162
E.1.3	Rectangular cross-section ( $z = 0$ m) . . . . .	164
E.1.4	Arced cross-section ( $z = 0$ m) . . . . .	166
E.1.5	Arced and rectangular cross-section ( $x = 50$ and $100$ m) . . . . .	168
E.2	Vertical temperature profiles for a ventilation velocity of 0.5 m/s . . . . .	169
E.3	Temperature profiles inside tunnel lining for a ventilation velocity of 0.5 m/s	170
E.4	Contour plots of velocity magnitude for a ventilation velocity of 0.5 m/s .	171
E.5	Vertical profiles of horizontal velocity for a ventilation velocity of 0.5 m/s	172
E.6	Contour plots of temperature for a ventilation velocity of 3 m/s . . . . .	173
E.6.1	Rectangular cross-section ( $z = -2.3$ m) . . . . .	173
E.6.2	Arced cross-section ( $z = -2.3$ m) . . . . .	175
E.6.3	Arced and rectangular cross-section ( $x = 50$ and $100$ m) . . . . .	177
E.7	Vertical temperature profiles for a ventilation velocity of 3 m/s . . . . .	178
E.8	Temperature profiles inside tunnel lining for a ventilation velocity of 3 m/s	179
E.9	Contour plots of velocity magnitude for a ventilation velocity of 3 m/s . .	180
E.9.1	Arced and rectangular cross-section ( $x = 50$ and $100$ m) . . . . .	181



## List of symbols

$a$	thermal diffusivity ( $\text{m}^2/\text{s}$ ) <i>or</i> coefficient in the discretisation equation (*) <i>or</i> absorption coefficient ( $1/\text{m}$ )
$A$	pre-exponential factor ( $1/\text{s}$ )
$A_s$	constant for Sutherland's formula ( $\text{kg}/(\text{msK}^{1/2})$ )
$[A]$	coefficient matrix (*)
$b$	source term in the discretisation equation (*)
$b_{ni}$	polynomial coefficients of function $f_i$ (1)
$\mathbf{b}$	vector of source terms (*)
$B_0$	buoyancy added at the plume source ( $\text{m}^4/\text{s}^3$ )
$c_p$	specific heat capacity at constant pressure ( $\text{J}/\text{kg}/\text{K}$ )
$c_v$	specific heat capacity at constant volume ( $\text{J}/\text{kg}/\text{K}$ )
$C$	constant for McCaffrey's correlations in a buoyant diffusion flame (1)
$C_1, C_2, C_3$	dimensionless constants in the $\varepsilon$ -equation (1)
$C_\mu$	dimensionless constant in the definition of $\mu_t$ (1)
$Co$	Courant number (1)
$d$	depth (m)
$d_h$	hydraulic diameter (m)
$d_{ni}$	coefficients from JANAF-tables of thermodynamics for $c_p(T)$ (1)
$D$	characteristic dimension of a fire (m)
$D^*$	characteristic plume diameter (m)
$\mathcal{D}$	mass diffusivity ( $\text{m}^2/\text{s}$ )
$E$	energy or calorific value (J) <i>or</i> dimensionless constant of the logarithmic law of the wall (1)
$E_a$	activation energy ( $\text{J}/\text{mol}$ )
$f_i$	weighting function describing the temperature dependency of the absorption coefficient (1)
$Fr$	Froude number (1)
$\mathbf{g}$	gravitational acceleration vector ( $\text{m}/\text{s}^2$ )
$G$	production of turbulence due to buoyancy ( $\text{W}/\text{m}^3$ ) <i>or</i> incident radiative heat flux ( $\text{W}/\text{m}^2$ )
$h$	total specific enthalpy ( $\text{J}/\text{kg}$ ) <i>or</i>
$h_s$	specific sensible enthalpy ( $\text{J}/\text{kg}$ )
$h_0$	height of the neutral plane of velocity at an opening (m)
$H$	total height of an opening (m)
$\Delta h_C$	heat of combustion ( $\text{J}/\text{kg}$ )
$\Delta H_f^\circ$	heat of formation ( $\text{J}/\text{kg}$ )

---

$I$	radiative intensity (W/m <sup>2</sup> )
$I_b$	black-body intensity (W/m <sup>2</sup> )
$k$	parameter of an exponential HRR-time curve (1/s) <i>or</i> specific turbulent kinetic energy (m <sup>2</sup> /s <sup>2</sup> )
$K$	constant for McCaffrey's correlations in a buoyant diffusion flame (*)
$l_m$	turbulent mixing length (m)
$\ell$	integral length-scale (m)
$L$	characteristic length-scale (m)
$L_M$	Morton length-scale (m)
$Le$	Lewis number (1)
$m$	mass (kg) <i>or</i> exponent in McCaffrey's correlations in a buoyant diffusion flame (1)
$\dot{m}$	mass loss rate of fuel (kg/s)
$M_i$	number of moles of species $i$ (mol)
$M_0$	momentum added at the plume source (m <sup>4</sup> /s <sup>2</sup> )
$n$	parameter of an exponential HRR-time curve (1)
$\mathbf{n}$	surface normal vector (1)
$N$	number of species (1)
$Nu$	Nusselt number (1)
$p$	pressure (Pa)
$p_{rgh}$	background pressure (Pa)
$P$	production of turbulence due to velocity gradients (W/m <sup>3</sup> )
$P_J$	Jayatilke's P-function (1)
$Pr$	Prandtl number (1)
$q$	specific diffusive heat flux (W/m <sup>2</sup> )
$q_C$	combustion-heat source (W/m <sup>3</sup> )
$q_w$	specific wall-heat flux (W/m <sup>2</sup> )
$q_{Rw}$	specific radiative wall-heat flux (W/m <sup>2</sup> )
$\mathbf{q}_R$	vector of specific radiative heat flux (W/m <sup>2</sup> )
$\dot{Q}$	heat-release rate (W)
$\dot{Q}^*$	dimensionless heat-release rate (1)
$r$	reaction rate (1/s) <i>or</i> parameter of an exponential HRR-time curve (1) <i>or</i> aspect ratio (1)
$R$	individual gas constant (J/kg/K) <i>or</i> rate of formation (kg/m <sup>3</sup> /s)
$\mathcal{R}$	universal gas constant (8.314 J/mol/K)
$Re$	Reynolds number (1)
$s$	stoichiometric air/fuel mass ratio (1)
$\mathbf{s}$	direction vector (1)
$S$	surface (m <sup>2</sup> )

$S_Q$	volumetric heat source (W/m <sup>3</sup> )
$S_T$	volumetric heat source in the heat-conduction equation (W/m <sup>3</sup> )
$S_\phi$	source term in the transport equation of variable $\phi$ (*)
$\mathbf{S}$	surface vector (m <sup>2</sup> )
$t$	time (s)
$t_{max}$	time to maximum heat-release rate (s)
$\Delta t$	time interval (s)
$T$	temperature (K, °C)
$T_s$	reference temperature for Sutherland's formula (K)
$Tu$	turbulent intensity (1)
$u, v, w$ ( $u_i$ )	velocity components (m/s)
$u_\tau$	shear velocity (m/s)
$\mathbf{u}$	velocity vector (m/s)
$U$	velocity at fire source (m/s) <i>or</i> characteristic velocity (m/s)
$\bar{U}_c$	mean velocity magnitude at the boundary of the laminar sublayer of the thermal boundary layer (m/s)
$\bar{U}_P$	mean velocity magnitude at the grid point next to the wall (m/s)
$V$	volume (m <sup>3</sup> )
$W$	molar mass (kg/mol)
$x, y, z$ ( $x_i$ )	coordinates (m)
$\mathbf{x}$	position vector (m)
$\delta x$	distance between two nodal points (m)
$\Delta x$	$x$ -dimension of a control volume (m)
$y$	wall distance (m)
$y^+$	dimensionless wall distance (1)
$Y$	mass fraction (1)
$Z$	mixture fraction (1)

*Greek symbols*

$\alpha$	growth or decay coefficient of a HRR-time curve (1/s, W/s, W/s <sup>2</sup> ) enthalpy diffusivity (kg/m/s)
$\alpha_c$	convective heat-transfer coefficient (W/m <sup>2</sup> /K)
$\delta_{ij}$	Kronecker delta (1)
$\varepsilon$	specific turbulent dissipation rate (m <sup>2</sup> /s <sup>3</sup> )
$\epsilon$	surface emissivity (1)
$\phi$	field variable (*)
$\boldsymbol{\phi}$	vector of $\phi$ s of all control volumes (*)
$\Phi_f$	face flux (kg/s)
$\Phi_b$	dimensionless temperature (1)

$\gamma^*$	mass fraction of fine structure (1)
$\Gamma_\phi$	diffusion coefficient of variable $\phi$ (kg/m/s)
$\eta$	Kolmogorov length-scale (m)
$\kappa$	wave number (1/m) <i>or</i> von Karman constant (1)
$\lambda$	thermal conductivity (W/m/K) <i>or</i> Taylor length-scale (m)
$\mu$	dynamic viscosity (Pa s)
$\mu_t$	eddy or turbulent viscosity (Pa s)
$\nu$	kinematic viscosity (m <sup>2</sup> /s)
$\Psi_b$	dimensionless heat flux (1)
$\rho$	density (kg/m <sup>3</sup> )
$\sigma_\varepsilon, \sigma_k$	dimensionless constants in $k$ - $\varepsilon$ equations (1)
$\sigma_{SB}$	Stefan-Boltzmann constant ( $5.67 \cdot 10^{-8}$ W/m <sup>2</sup> /K <sup>4</sup> )
$\sigma_t$	turbulent Prandtl number (1)
$\tau_{ij}$	viscous stresses (Pa)
$\tau_w$	wall shear stress (Pa)
$\Omega$	solid angle (1, sr)
$\chi$	combustion efficiency (1) <i>or</i> reaction fraction of fine structures (1)

*Subscripts*

$\infty$	ambient conditions
$b$	boundary
$\beta_d$	ratio of integrated energy to the time $t_d$ and the calorific value
$d$	decay
$e$	exponential <i>or</i> face of a control volume at the east side of point $P$
$E$	nodal point at the east side of $P$
$f$	face <i>or</i> fluid
$fu$	fuel
$g$	growth
$i$	species index, index
$i, j, k$	coordinate index
$in$	inlet <i>or</i> inert
$l$	linear
$lam$	laminar
$n$	index

---

<i>o</i>	oxidiser
<i>out</i>	outlet
<i>p</i>	plate
<i>pr</i>	product
<i>P</i>	nodal point of a control volume
<i>q</i>	quadratic
<i>rad</i>	radiation
<i>ref</i>	reference
<i>s</i>	solid
<i>st</i>	stoichiometric conditions
<i>t</i>	turbulent
<i>tot</i>	total
<i>w</i>	face of a control volume at the west side of point <i>P</i> or wall
<i>W</i>	nodal point at the west side of <i>P</i>

*Superscripts*

$\bar{\bullet}$	Reynolds-averaged quantity or mean quantity
$\bullet'$	fluctuation

*Abbreviations*

BC	Boundary Condition
CDS	Central Differencing Scheme
CFD	Computational Fluid Dynamics
CV	Control Volume
DNS	Direct Numerical Simulation
EDM	Eddy Dissipation Model
fvDOM	Finite Volume Discrete Ordinate Method
FDS	Fire Dynamics Simulator
GGDH	Generalised Gradient Diffusion Hypothesis
HRR	Heat Release Rate
LES	Large Eddy Simulation
ÖBB	Österreichische Bundesbahnen
RANS	Reynolds Averaged Navier-Stokes
RTE	Radiative Transfer Equation
SGDH	Simple Gradient Diffusion Hypothesis
UDS	Upwind Differencing Scheme
UIC	Union International des Chemins de Fer

# Chapter 1

---

## Introduction

### 1.1 Motivation

In recent years, fire accidents in enclosures such as tunnels or compartments, caused numerous casualties as well as an immense economic loss, making a thorough investigation of such incidents necessary. The aim of the underlying thesis is to develop, study and apply a tool which allows us to estimate the thermal impact on the load-carrying structure in the case of fires in enclosures with the focus on tunnel fires. The emphasis lays on predicting the temporal evolution of the absorbed heat energy by the solid walls leading to a temperature rise at the surface and inside the solid which varies in time. The tool should consider the geometrical configuration of the investigated structure as well as different fire scenarios and objects involved in the fire accident. The predictions allow a replacement of commonly used temperature-time curves (e.g. Eurocode [2]), providing more realistic information on the transient development of the effect of fires as the individual circumstances of the studied configuration are taken into account. The obtained information on surface temperatures and absorbed thermal energy by the structure serves as boundary condition for the more detailed computation of the temperature development inside the solid. In case of concrete, temperature distributions can be calculated by considering the coupling of thermo-hydro-chemical transport processes in order to assess the risk of spalling, and thus the structural safety [97].

Theoretical considerations, where the conservation of mass, energy and momentum is applied on the domain of interest, can only provide a rough estimate on the fire development in an enclosure as the equations represent an average over the whole domain. Obviously, the division of the domain in several sub domains on which the balance equations are applied increases the accuracy of the solution, while the computational effort rises and

is accomplished with the help of computer programs. This approach is followed in the so-called "Zone Models" [49]. A further step towards more precise predictions is to increase the discretisation of the continuous domain to several thousands of sub domains or cells as it is done in "Field Modelling" or "Computational Fluid Dynamics (CFD)". Both approaches are described in more detail in the course of the thesis (see Chapter 4), advantages and disadvantages are worked out which finally lead to the application of CFD as the tool for estimating the thermal load on structures in the case of fires. The approach followed for fire simulations applying CFD is depicted in Fig. 1.1: beginning with the evolution of the fire's *Heat Release Rate (HRR)* which represents the severity of the fire scenario, the CFD analysis allows to assess the evolution of the surface temperature of the structure at risk.

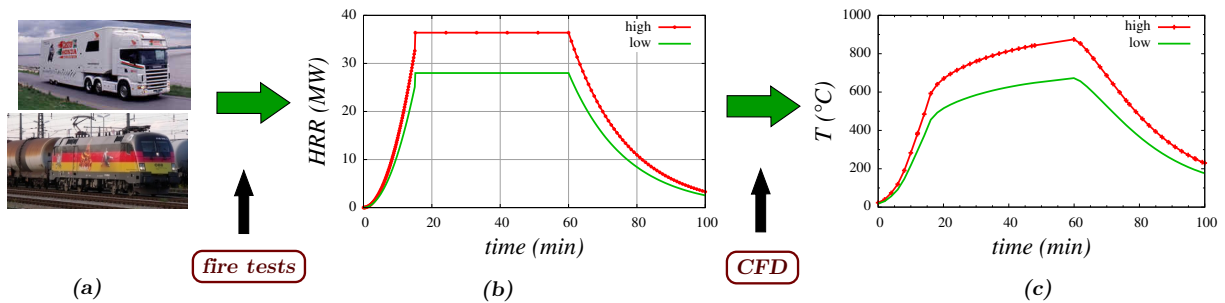


Figure 1.1: Application of CFD for the simulation of fires in enclosures: (a) type of fire load, (b) evolution of HRR, and (c) evolution of surface temperature

It should be kept in mind that the use of CFD for fire simulation has to be handled with care, as fire events represent a complex interaction of different mechanisms, i.e. pyrolysis, combustion, turbulence, convective and radiative heat transfer, ignition and flame spread, smoke and soot generation, etc. (see Chapter 2). Obviously, not all these processes can be reproduced in detail by the fire code and therefore simplifications and modelling of some features of a fire are needed. In that regard, CFD gives an estimate on the flow behaviour during a fire event. It is a valuable tool for sensitivity analysis with respect to different flow parameters reducing experimental effort. CFD makes all physical variables at all points in space and time of the resolved scales accessible and allows direct insight into transport dynamics. In combination with experimental investigations, CFD represents a powerful tool for efficient research in the field of fires in enclosures.

## 1.2 Outline

In the first part of this work, the physics of fire and the coupling of involved mechanisms such as chemical reactions, turbulence, radiation, etc. are worked out briefly, followed by an analysis of fire behaviour in enclosures. In the second part, a review of literature on different design fires, i.e. HRR-time curves describing specific fire scenarios, is summarised.

It includes HRR-time curves for passenger cars, buses, heavy good vehicles, main-line trains and metro trains representing the main input parameter for the CFD-simulation (see Fig. 1.1). In the third part, the mathematical model describing a fire is introduced and two approaches to solve the governing equations, i.e. zone and field modelling, are elaborated. Possibilities and limitations of both approaches are presented, finally leading to the choice of field modelling for the simulation of fire events. The third part defines the main requirements of the simulation tool and summarises a literature review on available fire codes in order to conclude on which CFD-code shall be used. The investigation of different sub models of the chosen code aiming to describe physical phenomena of interest by means of selected benchmark tests is then given. The fourth part concentrates on the application of the developed fire code. In order to assess its performance, two real-scale fire tests are re-analysed where additionally two ways of describing the fire source, i.e. the non-reactive and reactive approach, are investigated. In the fifth part, the code is finally used to simulate fire events in a rectangular and an arced tunnel cross-section at real dimensions under two different ventilation conditions. The results of fluid and wall temperatures at different locations in the tunnels of different cross-sections with varying ventilation conditions are studied and compared with recommendations found in respective standards.



# Chapter 2

---

## Natural fires

In order to be able to model a fire, first its different mechanism need to be investigated and understood. In the following, the term fire is used to describe an unwanted fire event, i.e. a fire accident. In the later part of the chapter, the behaviour of fires in enclosures is analysed.

### 2.1 Physics of fire

Fire as a process involves multiple chemical reactions between combustible species (*fuel*) and oxygen from the air (*oxidiser*) releasing thermal energy and combustion products. The visible part of the fire is the flame which consists of light emitting hot gases. Two classes of flames are distinguished, i.e. premixed and non-premixed (diffusion) flames. For the first type, fuel and oxidiser are mixed at a molecular level prior to ignition which commences the combustion process (see Fig 2.1 (*left*), e.g. spark-ignition engine), whereas for the second type, fuel and oxidiser mix (at a molecular level) simultaneously with the combustion. The mixing, and thus the burning rate, is governed by molecular diffusion of fuel and oxidiser (see Fig 2.1 (*right*), e.g. candle-light). Even though both types of flames can co-exist in some cases, diffusion flames are of major importance in fire events, and hence discussed further.

There exists a variety of fuels which range from the simplest gaseous hydrocarbons (e.g. methane) to solids of complex chemical composition (e.g. polyethylene). Under appropriate conditions, all types of fuel burn by reacting with oxygen present in the air. As the flame is a gas phase phenomena, liquid and solid fuels need to be converted into gaseous form. In case of a burning liquid, the heat released by the flame causes the liquid to

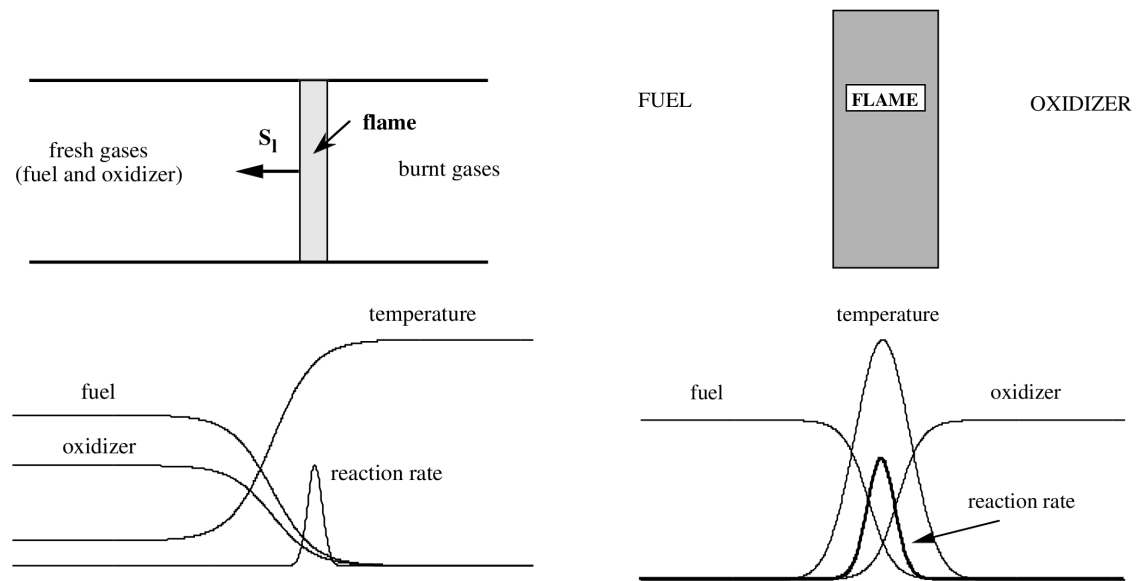


Figure 2.1: Structure of a premixed (*left*) and a diffusion flame (*right*) [88]

boil at the surface and vapour enters the flame and reacts. Solid materials exposed to a fire first undergo a thermal decomposition or pyrolysis producing pyrolysis gases, which volatilize from the surface and enter the combustion process. To start a fire, the gaseous fuel must mix with a sufficient amount of oxygen and the mixture needs to be exposed to a heat source allowing to sustain the chemical reaction. The dependency is commonly shown in a *fire triangle*: only if all of the three components, i.e. fuel, oxygen and heat, are present, combustion is possible (see Fig. 2.2 (*left*)). During the combustion process the interaction of chemical reactions, fluid dynamics and heat energy is observed (see Fig. 2.2 (*right*)). Higher temperatures allow to accelerate the chemical reaction, which in turn increases the rate of heat release. Heating up combustion gases causes density gradients leading to buoyancy and additional turbulence production, enhancing the mixing of fuel and oxidiser, and thus allows a more efficient chemical reaction.

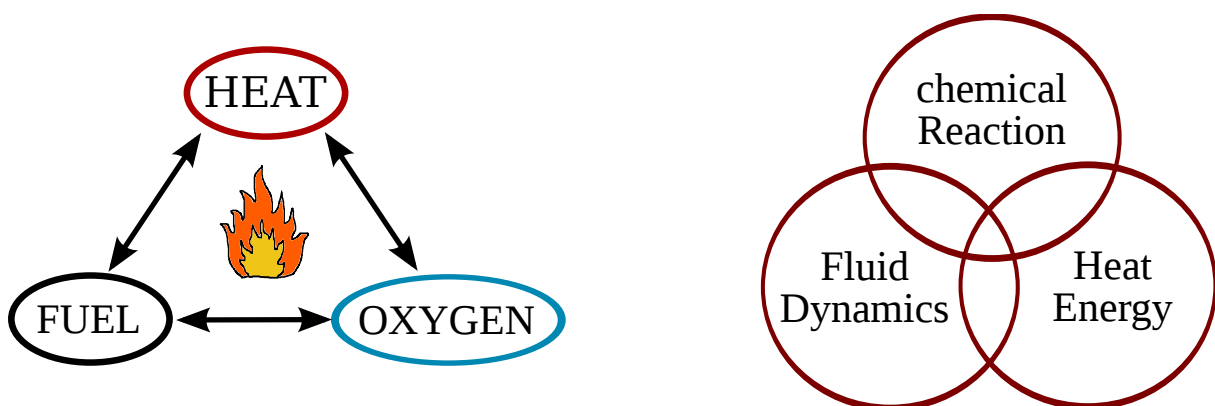


Figure 2.2: Fire triangle (*left*) and the interaction of different phenomena in a fire (*right*)

### 2.1.1 Fire plumes

Within the underlying study of natural fires, the case of flames fed by condensed fuels from liquids or solids are of main interest. The flames are characterised by low momentum of the volatiles at the source and are dominated by buoyancy. The relative importance of momentum and buoyancy is expressed by the *Froude* number,  $Fr$ , a dimensionless parameter defined as [26]

$$Fr = \frac{U^2}{gD}, \quad (2.1)$$

where  $U$  denotes the velocity of the gases at the source and  $D$  a characteristic dimension, normally taken as the fire-source diameter. Jet flames exhibit a high value of  $Fr$ , whereas natural fires or *buoyant flames* have low  $Fr$  due to low momentum of fuel gases at the fire source. Another important parameter is the HRR of the fire,  $\dot{Q}$ , which specifies the effective amount of heat energy released per unit of time by the combustion process and is written [26]

$$\dot{Q} = \chi \dot{m} \Delta h_C. \quad (2.2)$$

The factor  $\chi$  is the combustion efficiency taking incomplete combustion into account,  $\dot{m}$  the fuel mass flux and  $\Delta h_C$  the heat of combustion for a specific fuel. Dimensional considerations lead to a dimensionless heat-release rate,  $\dot{Q}^*$ , which can be interpreted as the square root of  $Fr$  expressed by  $\dot{Q}$ , reading [37]

$$\dot{Q}^* = \frac{\dot{Q}}{\rho_\infty c_p T_\infty \sqrt{g} D^{\frac{5}{2}}}, \quad (2.3)$$

where the subscript "∞" specifies ambient conditions. While jet flames correspond to values of  $\dot{Q}^* \sim 10^6$ , natural fires show values of  $\dot{Q}^*$  around six orders of magnitude lower [26].  $\dot{Q}^*$  is used to classify fire types as seen in Fig. 2.3. With an increasing fire diameter corresponding to decreasing  $\dot{Q}^*$ , a less ordered structure of the flames is observed. The continuous flames of laminar behaviour turn into increasingly turbulent discrete flames of reduced height compared to the diameter of the fire as shown by various experiments. Most of the knowledge available on turbulent diffusion flames comes from studies made on porous bed gas burners, allowing to correlate aspects of fire behaviour like flame height, plume velocity, temperature, etc. to  $\dot{Q}^*$  [37, 38, 59]. In [59], three distinct regions which can be identified in a fire plume are presented (see Fig. 2.4 (*left*)):

1. the *flame zone*: with a persistent flame and an accelerating flow of burning gases close to the burner outlet,
2. the *intermittent zone*: with intermittent flaming and a relative constant flow velocity, and

- 3. the *buoyant plume*: which is characterised by decreasing velocity and temperature with increasing distance from the burner surface.

The flow characteristics in the different zones of a fire plume are discussed in more detail in the course of modelling (see Chapter 4).

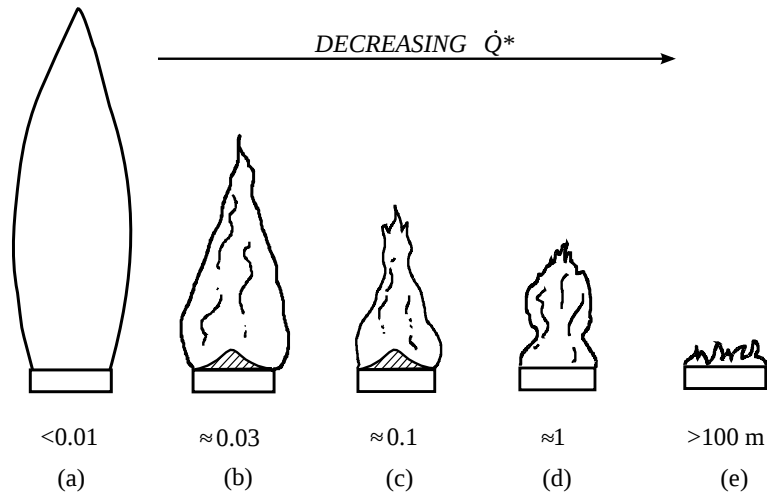


Figure 2.3: Classification of natural diffusion flames as *structured* (b and c, shaded areas show fuel-rich cores) and *unstructured* (a, d, and e) [26]

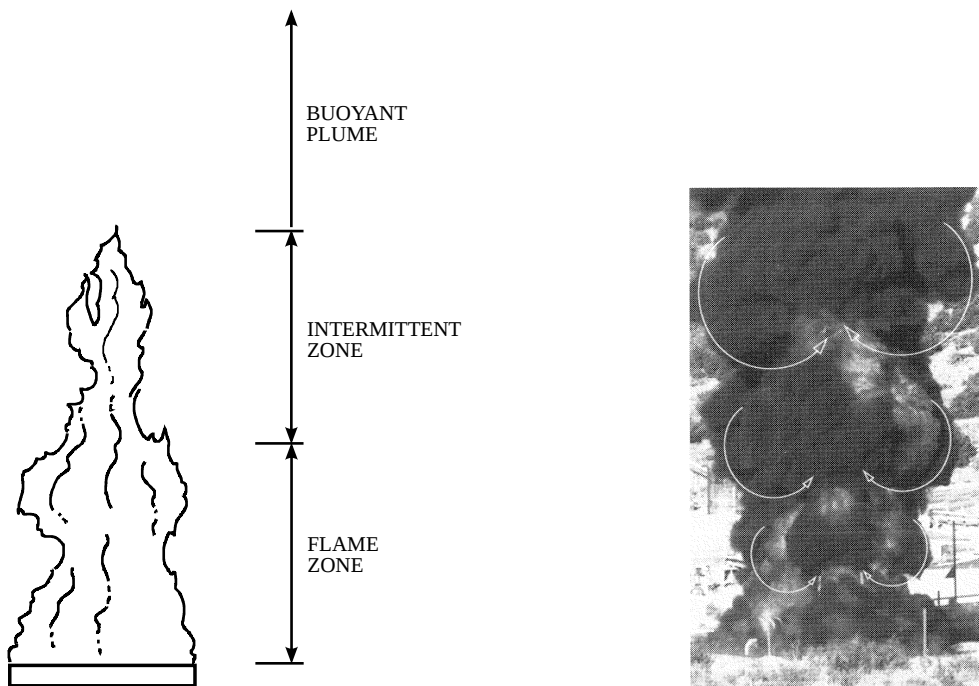


Figure 2.4: Different zones in a fire plume (*left*) [59] and vortex-like structure in a fire plume (*right*) [84]

It was already mentioned before that fire involves the coupling of different phenomena. Beginning with the pyrolysis of solid fuels or evaporation of liquid fuels by radiative and convective heat transfer, where the flammable gases enter the combustion process. The rate at which solid materials are decomposed by pyrolysis strongly depends on the incident heat flux from flames or a hot smoke layer, which controls ignition and flame spread. The large variety of products which are formed e.g. during the degradation of polymers whether oxygen is present or not, has an effect on the composition of the pyrolysis gases and directly influence the combustion process and its products [26]. Additionally, reaction rates of the chemical processes during combustion are a function of local temperature and the amount of oxygen present determined by entrainment of air and its mixing with fuel gas.

The influence of fluid dynamics on the combustion process is evident (air entrainment, turbulent mixing, heat transfer). On the other side, the released heat of the chemical reactions induces density gradients between hot combustion gases and surrounding fresh air. Exposed to the gravitational acceleration, they cause an upward moving flow due to buoyancy forces proportional to  $g(\rho_\infty - \rho)$ . Buoyancy causes a rotation of fluid elements where density gradients are present (vorticity generation) resulting in up-rising vortex-like structures in the fire plume (see Fig. 2.4 (*right*)). The structures pull air into the fire plume and significantly affect the rate of air entrainment [84]. Low  $\dot{Q}^*$  and additional turbulence production due to buoyancy let natural fires be a highly turbulent flow. Turbulence enhances the transport of momentum and scalars (e.g. temperature, species concentration, etc.) increasing mixing and convective heat transfer inside the fire plume as well as towards solid objects.

Another important mode of heat transfer encountered in fire events is the radiative heat transfer in a participating media, i.e. the combustion gases of varying composition. Thermal energy is transferred by radiation to objects in the near and far field causing ignition and flame spread, and can locally lead to quenching of the flame as a consequence of radiative cooling. Not only does the flame radiate thermal energy, but also soot particles whose emission is responsible for the luminosity of most diffusion flames (depending on the type of fuel). Soot, which represents the solid portion of a smoke layer, results from incomplete combustion on the fuel side of the reaction zone where it reaches high temperatures. Thus, soot is an important contributor to thermal radiation in fires [84].

In the scope of fires in enclosures, it has to be mentioned that solid boundaries can have an influence on the fire plume's behaviour. In the case of a flame burning against a wall, the rate of air entrainment may be reduced. In the same way, when the fire plume impinges on a ceiling and forms a ceiling jet, entrainment will be restricted. A reduction in entrained air increases the temperatures of the fire compared to the unbounded case due to less mixing with ambient air [26]. Hence, in both cases the presence of the boundary has an effect on the heat transfer to solid surfaces.

## 2.2 Fire development in enclosures

The development of a fire in an enclosure (e.g. compartment, tunnel) depends on many factors such as geometrical configuration of the enclosure, type of fuel and its location, lining material, ventilation condition, etc. Fire development can be described in terms of HRR vs. time plots (see Fig. 2.5), and in case of a compartment fire, it is divided in three stages [26]:

1. The growth or pre-flashover stage, in which the average compartment temperature is relatively low and the fire is localized in the vicinity of its origin.
2. The fully developed or post-flashover fire, during which all combustible items in the compartment are involved and flames appear to fill the entire volume.
3. The decay period, often identified as that stage of the fire after the average temperature has fallen to 80% of its peak value.

The term *flashover* is used to name the transition from the growth phase to the fully developed fire. In the following chapters, a summary of Stages 1 and 2 is given. A more detailed discussion can be found in [26].

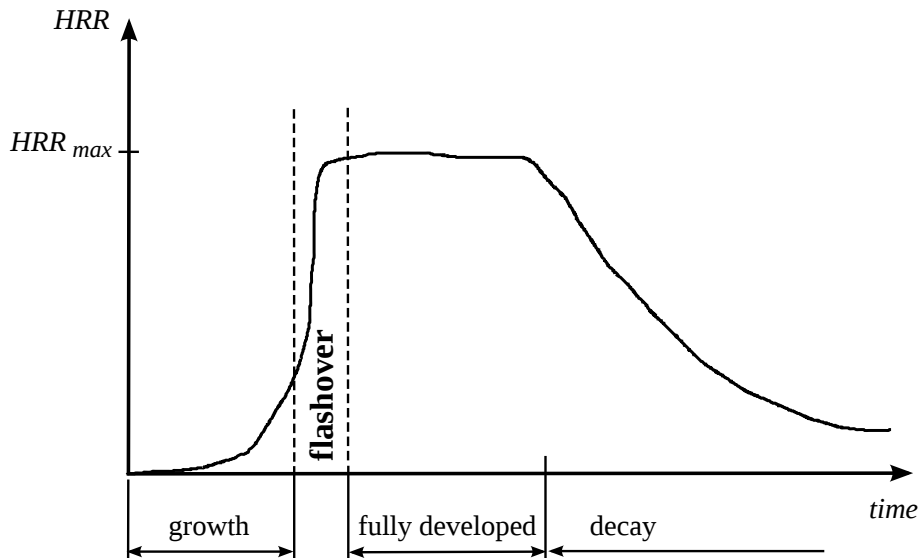


Figure 2.5: Three stages of a well-ventilated fire in an enclosure

### 2.2.1 The growth stage

After ignition, the fire is still small. It burns freely and the burning rate is only affected by the availability of fuel due to an air supply in excess, allowing complete combustion. If the

fire can grow through flame spread or ignition of combustible objects close to the initial fire, the confinement begins to influence the development. The fire forms a ceiling jet and flows along the ceiling till it reaches the walls and soon a smoke layer develops under the ceiling. The hot surfaces in the upper part of the enclosure and the growing layer of hot combustion gases and smoke re-radiate downwards, enhancing the burning rate of the existing fire and the rate of flame spread to contiguous items. At the moment the layer descends to any opening (door or window), hot combustion gases leave the enclosure and reduce the area of entering fresh air resulting in an increasing temperature of the upper layer. At the same time, the smoke layer continues to descend and envelopes the growing flame, leading to a situation where flashover is likely to begin.

In case the fire burns in a long corridor or a tunnel, the ceiling jet and the combustion gases spread horizontally resulting in a thinner smoke layer but exposes areas remote from the fire source to higher radiative heat flux.

The flashover is not a well-defined physical event but happens over a certain period of time whose duration depends on the circumstances explained above. Different conditions may define the flashover: ceiling temperatures of around 600 °C or a heat flux at floor level in the range of 20 W/m<sup>2</sup> [73]. In [26], the transition from a localized fire to the conflagration within the enclosure when all fuel surfaces are burning is the preferable definition marking the begin of a fully developed fire.

### 2.2.2 The fully developed fire

While time to flashover is important for evacuation of the enclosure, the conditions during flashover and the fully developed fire, when the thermal impact on the structure reaches its maximum (see Fig. 2.5), plays an important role when it comes to assessing the stability of the load carrying elements of the enclosure. In the stage of a fully developed fire, the exposed surfaces of all combustible items burn. This might not hold for the whole fire load in a tunnel fire (e.g. train tunnel) where it is distributed over a great length of the tunnel. The definition of a compartment fire is not strictly applicable to a tunnel and therefore the fully developed fire inside a tunnel is limited in most of the cases to a certain portion of the tunnel [35].

The fully developed fire can be of two regimes: (i) ventilation-controlled and (ii) fuel-controlled. In the first regime, the burning rate depends on the rate of air entering the enclosure. At the moment the rate of burning becomes independent of the ventilation rate but is mainly governed by the type of fuel and its surface area, the second regime is observed. In general, fuel-controlled fires are less severe when compared to ventilation-controlled fires as the excess air dilutes hot combustion gases resulting in lower temperatures. In tunnel fires, forced ventilation is used in order to control the smoke flow and to reduce the high thermal load concentration on the structure during a fire accident. The

additional ventilation may influencing the fire growth and the peak HRR as discussed later in Chapter 3.

In order to specify for design purpose the thermal loading of the structure during a fire, different histories for the gas temperature inside the enclosure have been developed and standardised, e.g. in the Eurocode [2]. In Fig. 2.6, standard temperature-time curves are depicted for tunnel fires characterised by different types of fire load. A parametric temperature-time curve for compartment fires is presented in [2].

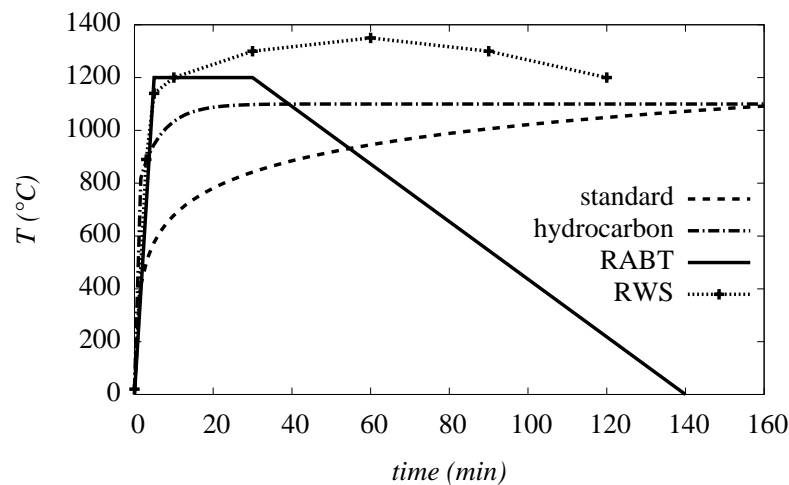


Figure 2.6: Temperature-time curves for tunnel fires: standard curve [2], hydrocarbon curve for hydrocarbon fuels [2], RABT-curve from German guidelines for road tunnels [31], and RWS-curve from Dutch guidelines (Rijkswaterstaat) for the fire of a fuel tanker [82]

### 2.2.3 Backdraught

In compartment fires, sometimes situations are observed where the fire consumes most of the oxygen during the growth stage and the rate of ventilation is insufficient to replenish it. The fire may self-extinguish or turns into a slowly burning flame. For the latter case, the conditions do not allow complete combustion and consequently unburnt and partially burnt fuel accumulate inside the enclosure of high temperature. At the moment where fresh air is allowed to enter the space, e.g. by opening a door or breaking a window, the accumulated gases rapidly burn producing the so-called *backdraught* [26].

### 2.2.4 Back-layering

*Back-layering* is referred to as the spread of smoke and hot combustion products against longitudinal ventilation during a fire in a tunnel due to buoyancy forces. The radiative power of the back-flowing hot gases has a significant influence on evacuation and fire fighting. The minimum ventilation velocity necessary to prevent *back-layering* is designated as critical velocity [83].



# Chapter 3

---

## Design fire scenarios

A fire scenario is characterised by the fire development as shown in Fig. 2.5, therefore determined by an evolution of the heat-release rate (HRR) over time. The HRR is considered as the most significant predictor of fire hazard [5]. Its peak value and duration is a measurement of the severity of a fire which depends on the fire load and the conditions within the enclosure. Thus, the HRR vs. time serves as a main input parameter not only to assess the thermal impact on the structure but also to plan fire-safety measures [35].

In most fire accidents solid fuels are involved which are of complex compositions consisting of different materials. It was discussed in Chapter 2 that solid fuels need to undergo a process of thermal decomposition, i.e. pyrolysis, in order to be transformed into gaseous fuels which are burnt and contribute to the heat release. The rate at which solid materials are pyrolysed and flammable gases are released, depend on many factors such as incident heat flux, oxygen concentration at the fuel surface, thermo-physical parameters and the kinetic parameters of the Arrhenius law,  $A$  and  $E_a$ . The Arrhenius law is a model used to describe the reaction rate during pyrolysis of a certain material, reading

$$r = A \cdot \exp\left(\frac{-E_a}{RT}\right), \quad (3.1)$$

and allows together with the heat of combustion of the pyrolysis gases to calculate the HRR. From the perspective of modelling, many uncertainties are related with the description of fire development beginning from the pyrolysis process as it is based on the knowledge of the detailed composition of the fire load. A possibility to bypass this problem is to directly prescribe the history of the HRR derived from real-scale experiments, which mimic fire scenarios within a specific geometry involving a particular fire load (e.g. car, train compartment, furniture, etc.). These so-called *design fires* can be considered as

an idealisation of a real fire including interaction with their environment, e.g. geometrical features, ventilation, etc., and may include, beside the three stages of fire development, subsequent fire spread. In [13], a number of fire experiments in tunnels were studied with respect to the influence of geometry on the HRR concluding that the HRR is higher in a narrow tunnel compared to a wide tunnel of the same height. It is also stated that forced ventilation may have a much stronger influence on the HRR than the geometry. In [56], a series of tunnel fire tests aiming to investigate the effect of forced ventilation on the HRR development was reviewed. Differences in the experimental set ups influencing the effect of ventilation on the HRR, i.e. tunnel geometry, well-ventilated and under-ventilated conditions or the size of the heat source, could be identified. In some of the tests an increase of the ventilation velocity led to an accelerated fire growth and an increase in the peak HRR but for a quantitative assessment more detailed experiments are necessary [56]. Consequently, it is of importance to consider both the geometry and the ventilation conditions when a design fire is estimated [13].

The approach of directly using HRR-time curves from *design fires* as main input parameter to assess the thermal action on the structure is applied in the underlying thesis (see Fig. 1.1). In the following chapters, methods of estimating the HRR are presented and a literature study on design fires for tunnels is summarised.

### 3.1 Methods of estimating the Heat Release Rate (HRR)

The most common methods used to estimate the HRR in a fire are through measuring (i) the mass loss rate of fuel,  $\dot{m}$ , and (ii) the rate of oxygen consumption in the course of the fire. In the first method, the mass loss rate is determined by a load cell or the flow rate of liquid fuel in pool fires in order to keep the liquid surface at a certain level. The HRR is then calculated with the expression presented in Eqn. (2.2). In the second method, the HRR is derived from the consumption rate of oxygen during the combustion known as *Oxygen Consumption Calorimetry*. While the heat of combustion of different materials greatly vary, the amount of heat released per unit mass of oxygen consumed is nearly constant with an average value of 13.1 MJ/kg [39]. As a result, the measurement of oxygen concentration by gas analysis of incoming and out-coming air in the enclosure during the fire allows to estimate the HRR. In [71], the equations relating rate of oxygen depletion to HRR is developed for open and closed systems. The application of the method to tunnel fires as well as related problems and uncertainties are worked out in [40]. Applied on tunnel fires, HRR-time curves are estimated by measuring the mass flow and the oxygen concentration in both the inflowing and exhausted gases.

## 3.2 Design fires for tunnels

In recent years many real-scale fire experiments were carried out involving vehicles of different types and calorific value such as passenger cars and *Heavy Goods Vehicle (HGV)* of different loads, locomotives, freight trains, train and metro compartments. The vehicles were burnt under the hood of an oxygen-consumption calorimetry, in car parks or abandoned tunnel sections. The results of the experiments like temperature-time and HRR-time curves, smoke production and smoke movement were presented and summarised in various publications [7, 21, 24, 35, 40, 41, 43, 55]. In this chapter, selected design fires for road, railway and metro tunnels are presented.

### 3.2.1 Road tunnels

In Appendix C of [24], standardised HRR-time curves for fire sources of passenger cars, loaded HGVs and fuel tankers are suggested. The HRR-time curves are categorised according to the peak HRR (4 - 200 MW) and the calorific value (6 - 960 GJ). The growth and decay phase are approximated by linear functions. Beside the total HRR, an estimate of the convective portion of the fire is also given. Furthermore, fires of multiple objects involved through fire spread from one to another vehicle are included. Fig. 3.1 shows design fires for a small passenger car and 3 small passenger cars which burn through fire spread. The HRR-time curves for a HGV carrying highly combustible load and for a fuel tanker loaded with 20 t of flammable liquid are depicted in Fig. 3.2. In both graphs (Figs. 3.1 and 3.2) the total and the convective HRRs are shown.

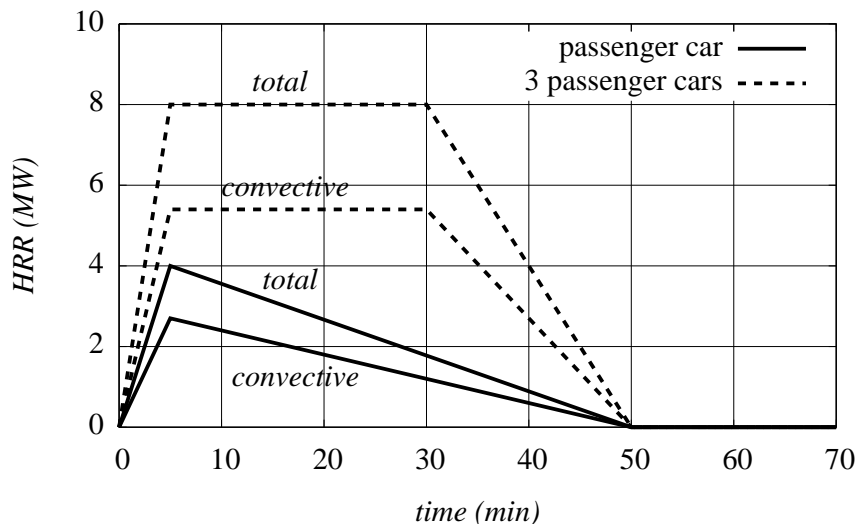


Figure 3.1: Design fires for fire loads of different calorific value showing the total and the convective HRR: small passenger car (6 GJ) and 3 small passenger cars involved through fire spread (18 GJ). Data reproduced from original reference [24]

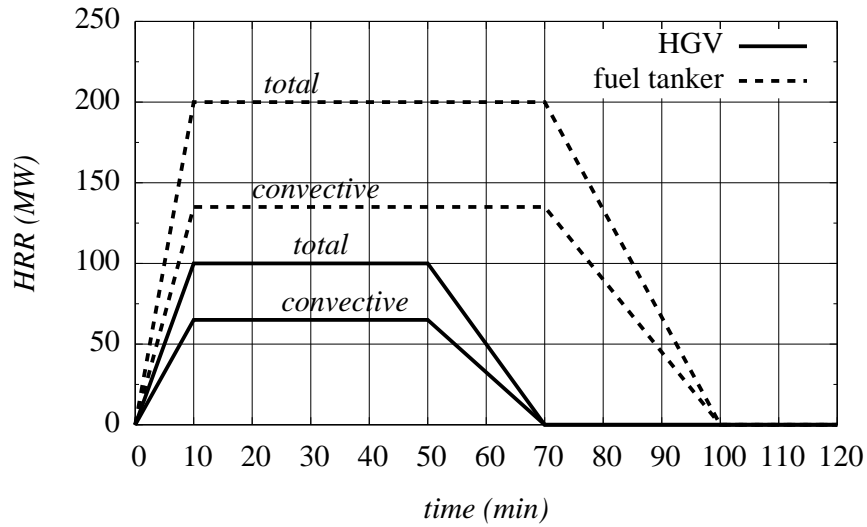


Figure 3.2: Design fires for fire loads of different calorific value showing the total and the convective HRR: HGV carrying highly combustible load (330 GJ) and fuel tanker loaded with 20 t of flammable liquid (960 GJ). Data reproduced from original reference [24]

<i>time</i> (min)	<i>HRR passenger car</i> (MW)		<i>HRR 3 passenger cars</i> (MW)	
	<i>total</i>	<i>convective</i>	<i>total</i>	<i>convective</i>
0	0.0	0.0	0.0	0.0
5	4.0	2.7	8.0	5.4
30	8.0	5.4	8.0	5.4

Table 3.1: HRR values at different time instants corresponding to Fig. 3.1 [24]

Fig. 3.3 shows the results of 4 large-scale fire tests with a mock-up of a HGV trailer in the Runehamar road tunnel [43]. In the test series initial ventilation velocities were in the range of 2.8-3.2 m/s. The mock-ups were loaded with mixed commodity of wood pallets and polyethylene pallets (test T1, 247 GJ), wood pallets and polyurethane mattresses (test T2, 135 GJ), furniture and fixtures with ten truck rubber tyres (test T3, 179 GJ), and paper cartons and polystyrene cups (test T4, 62 GJ). In all tests, the fire growth

<i>time</i> (min)	<i>HRR HGV</i> (MW)		<i>HRR fuel tanker</i> (MW)	
	<i>total</i>	<i>convective</i>	<i>total</i>	<i>convective</i>
0	0	0	0	0
10	100	65	200	135
50	100	65	200	135
70	200	135	200	135

Table 3.2: HRR values at different time instants corresponding to Fig. 3.2 [24]

could be reasonably described by a linear increase. For test T1, a maximum HRR of 202 MW was estimated which corresponds to a peak HRR proposed for fire scenarios involving flammable liquids (see e.g. Fig. 3.2).

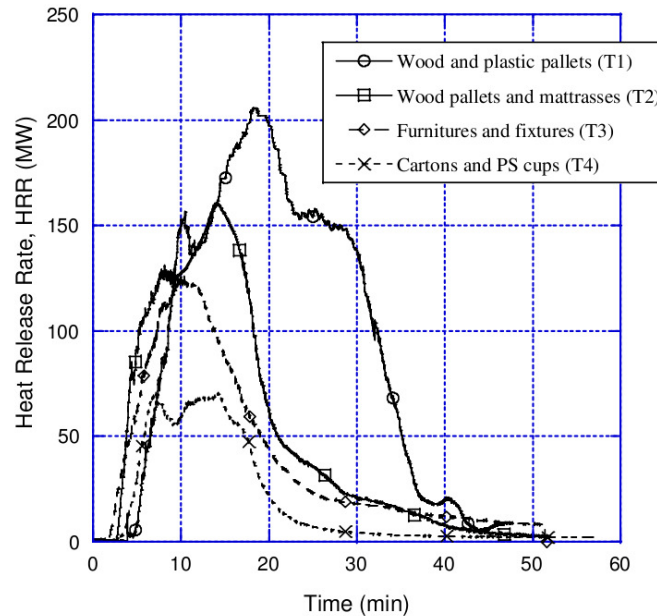


Figure 3.3: Measured HRR-time curves for 4 large-scale fire tests in the Runehamar road tunnel with fire loads of different calorific value: 247 GJ (T1), 135 GJ (T2), 179 GJ (T3) and 62 GJ (T4) [43]

### 3.2.2 Railway tunnels

The most comprehensive set of HRR-time curves for mainland railways are given by the German Railways (*Deutsche Bahn*) [3]. Fig. 3.4 depicts design fires for different locomotives, passenger carriages and freight waggons.

The history of the HRR in a tunnel fire test using a German passenger train (*Inter City*) as fire load was measured during the EUREKA project presented in [40] (see Fig. 3.5). The total heat content of the train was estimated with 77 GJ. Two peaks of approximately 12 MW and a fire duration greater than 120 minutes could be observed (compare with passenger carriage in Fig. 3.4).

### 3.2.3 Metropolitan tunnels

In the technical report of the European Thematic Network FIT – Fire in Tunnels [35], it is stated that the rolling stock of metropolitan railways differs widely due to age, vehicle dimensions and the used materials. As a consequence, it is very difficult to give unique

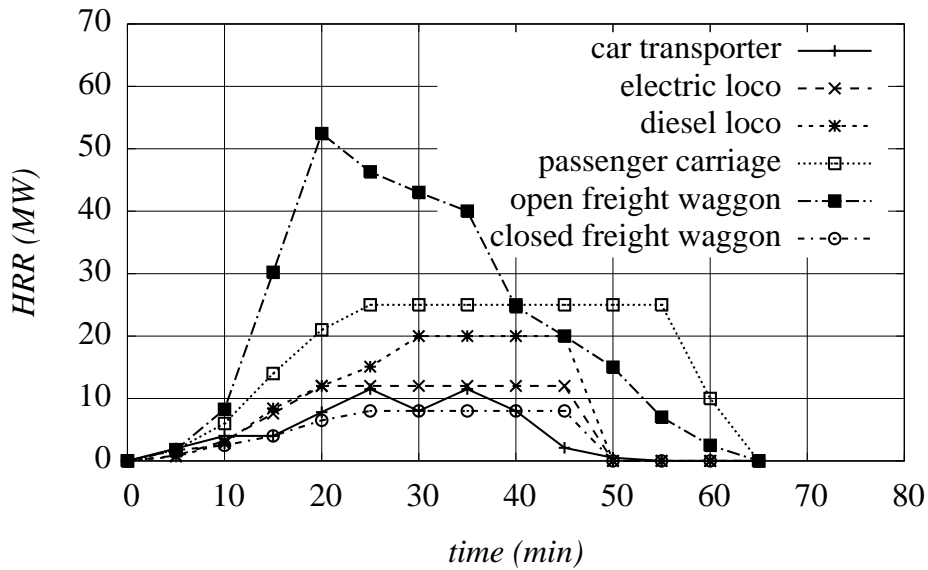


Figure 3.4: Design fire curves for railway tunnels: car transporter (24 GJ), electric locomotive (42 GJ), diesel locomotive (61 GJ), passenger carriage (64 GJ), open freight waggon with lorries (85 GJ, depending on freight carried) and closed freight waggon (141 GJ, depending on freight carried). Data reproduced from original reference [3]

<i>time</i> (min)	<i>car</i> <i>transporter</i>	<i>electric</i> <i>loco</i>	<i>diesel</i> <i>loco</i>	<i>passenger</i> <i>carriage</i>	<i>open freight</i> <i>waggon</i>	<i>closed freight</i> <i>waggon</i>
0	0.0	0.0	0.0	0.0	0.000	0.0
5	2.0	0.85	0.7	1.8	1.800	1.7
10	4.0	3.2	2.8	6.0	8.260	2.5
15	4.0	7.6	8.4	14.0	30.215	4.0
20	7.8	12.0	12.0	21.0	52.440	6.5
25	11.5	12.0	15.1	25.0	46.300	8.0
30	8.0	12.0	20.0	25.0	43.000	8.0
35	11.5	12.0	20.0	25.0	40.000	8.0
40	8.0	12.0	20.0	25.0	24.700	8.0
45	2.1	12.0	20.0	25.0	20.000	8.0
50	0.5	0.0	0.0	25.0	15.000	0.0
55	0.0	0.0	0.0	25.0	7.000	0.0
60	0.0	0.0	0.0	10.0	2.500	0.0
65	0.0	0.0	0.0	0.0	0.000	0.0

Table 3.3: HRR values in MW corresponding to Fig. 3.4 [3]

fire loads for underground railway carriages. However, data is available from a test series within the EUREKA project where a German subway coach with a calculated calorific

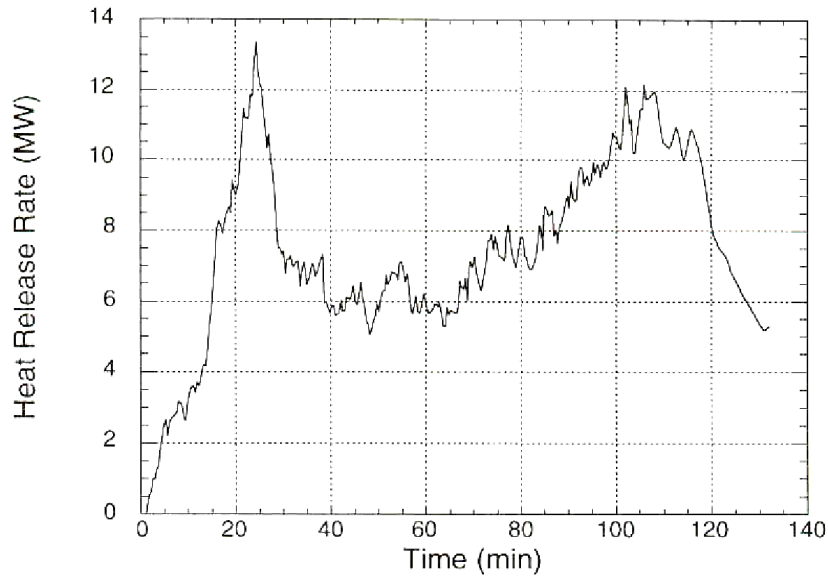


Figure 3.5: HRR-time curve of a German passenger train (*Inter City*) with an estimated heat content of 77 GJ [40]

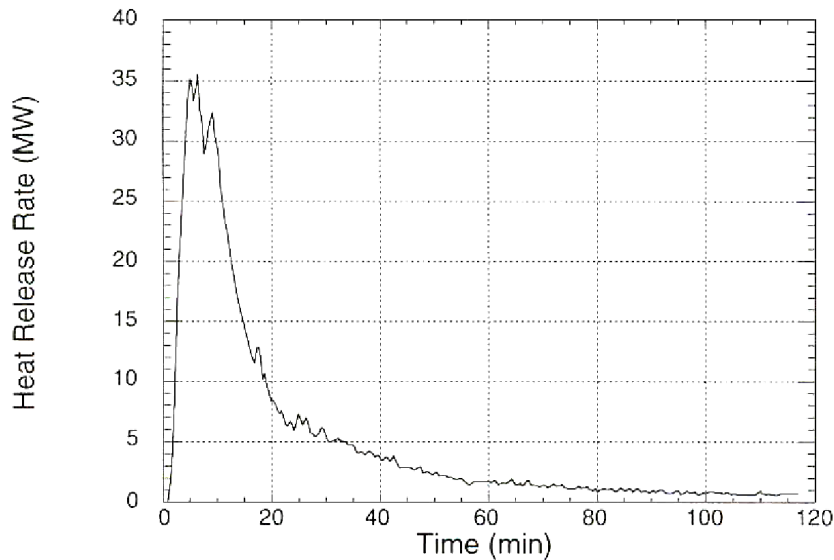


Figure 3.6: HRR-time curve of a German subway coach with an estimated heat content of 41.3 GJ [40]

value of 41.3 GJ was included. The HRR-time curve is depicted in Fig. 3.6 [40].

The calorific value for a whole tram set (*ULF*) operated by the Vienna Transport Authority (*Wiener Linien*) was estimated with 168.4 GJ [32]. In [32], a scenario for a fully developed fire is mentioned, where after 28 minutes a maximum HRR of 29 MW is reached, and, assuming a consumption of the whole tram set, a total fire duration of 125 minutes is given.

### 3.3 Mathematical description of design fires for tunnels

For design purpose it is often convenient to describe the HRR-time curve with mathematical expressions. From the shape of design fire curves presented in the previous chapter, it seems reasonable to approximate each of the three phases of a fire, i.e. growth, fully developed (nearly constant HRR) and decay phase (see Fig. 2.5), with a mathematical function such as a linear, quadratic or exponential function. The phases are defined through the intervals  $0 \leq t < t_{max}$ ,  $t_{max} \leq t < t_d$  and  $t_d \leq t < t_{tot}$ , respectively, where  $t_{max}$  stands for the moment the maximum HRR is reached,  $t_d$  for the beginning of the decay phase and  $t_{tot}$  for the total duration of the fire. HRR measurements of real-scale fire experiments allow to derive the total calorific value of the fire load,  $E_{tot}$ , and the resulting maximum HRR,  $\dot{Q}_{max}$ . Based on these two input parameters, different mathematical expressions were developed to describe the fire development and are presented in [41, 42] and summarised in the following sections.

#### 3.3.1 Linear approximation

In the same way as suggested by French guide lines [24], a linear approximation for all three stages of fire development is used (see Fig. 3.1 and 3.2). The growth and decay phases are thus described as

$$\dot{Q}(t) = \alpha_{g,l}t \quad \text{and} \quad \dot{Q}(t) = \dot{Q}_{max} - \alpha_{d,l}(t - t_d), \quad (3.2)$$

respectively, with  $\alpha_{g,l}$  and  $\alpha_{d,l}$  standing for the constant growth and decay rate, respectively, of  $\dot{Q}$ . In Tab. 3.4, characteristic fire tests are compiled to guide the choice of the necessary parameters for a tri-linear design curve. With the growth and decay rates the time instants  $t_{max}$  and  $t_d$  can be calculated, using

$$t_{max} = \frac{\dot{Q}_{max}}{\alpha_{g,l}} \quad \text{and} \quad t_d = \frac{E_{tot}}{\dot{Q}_{max}} + t_{max} - \frac{\alpha_{g,l}t_{max}^2}{2\dot{Q}_{max}} - \frac{\dot{Q}_{max}}{2\alpha_{d,l}}, \quad (3.3)$$

respectively.

#### 3.3.2 Nonlinear approximation

For the fire growth ending at  $t_{max}$ , a quadratic function and for the decay beginning at  $t_d$  an exponential function is used, reading

$$\dot{Q}(t) = \alpha_{g,q}t^2 \quad \text{and} \quad \dot{Q}(t) = \dot{Q}_{max}e^{-\alpha_{d,e}(t-t_d)}, \quad (3.4)$$



<i>Fire load</i>	<i>tunnel height (m)</i>	$E_{tot}$ (GJ)	$\dot{Q}_{max}$ (MW)	$t_{max}$ (min)	$t_d$ (min)	$t_{tot}$ (min)	$\alpha_{g,l}$ (kW/s)	$\alpha_{d,l}$ (kW/s)
2-3 cars	2.7	17	8	5	25	45	26.67	6.67
1 van	3.5	38	15	5	35	55	50.00	12.50
1 HGV	> 3.5	144	30	10	70	100	50.00	16.67
1 HGV	> 3.5	450	100	10	70	90	166.67	83.33
1 tanker	> 3.5	960	200	10	70	100	333.33	111.67

Table 3.4: Design parameters for tri-linear HRR-time curves [42]

respectively. Values for the quadratic and exponential coefficient,  $\alpha_{g,q}$  and  $\alpha_{d,e}$ , respectively, are given in Tab. 3.5. The time instants  $t_{max}$  and  $t_d$  can then be calculated using

$$t_{max} = \sqrt{\frac{\dot{Q}_{max}}{\alpha_{g,q}}} \quad \text{and} \quad t_d = \frac{\chi E_{tot}}{\dot{Q}_{max}} + \frac{2}{3}t_{max} - \frac{1}{\alpha_{d,e}}, \quad (3.5)$$

respectively. In case of  $t_d \leq t_{max}$ , the HRR-time curve does not show a constant period of  $\dot{Q}_{max}$  and a new value for the maximum HRR needs to be estimated, using

$$\dot{Q}_{max} \approx \chi \alpha_{d,e} E_{tot} \left( 1 - \frac{\alpha_{d,e}^{3/2}}{6} \sqrt{\frac{\chi E_{tot}}{\alpha_{g,q}}} \right)^2. \quad (3.6)$$

<i>Fire load</i>	$\dot{Q}_{max}$ (MW)	$\alpha_{g,q}$ (kW/s <sup>2</sup> )	$\alpha_{d,e}$ (1/s)
car	4	0.01	0.0010
bus	30	0.10	0.0007
train (steel body)	15	0.01	0.0010
subway car (aluminum construction)	35	0.30	0.0010

Table 3.5: Design parameters for quadratic HRR-time curves [42]

### 3.3.3 Exponential approximation

A single exponential expression can be used to describe a design fire characterising a fuel-controlled fire or a fire with a negligible period of constant maximum HRR, using

$$\dot{Q}(t) = \dot{Q}_{max} n r (1 - e^{-kt})^{n-1} e^{-kt}. \quad (3.7)$$

The parameter  $n$  has no physical meaning. In case information on  $t_{max}$  is available,  $n$  may be estimated as [42]

$$n \approx 0.74294e^{2.9\dot{Q}_{max}t_{max}/E_{tot}}. \quad (3.8)$$

Then the parameters  $r$  and  $k$  are determined, using

$$r = \left(1 - \frac{1}{n}\right)^{1-n} \quad \text{and} \quad k = r \frac{\dot{Q}_{max}}{E_{tot}}, \quad (3.9)$$

respectively. Due to the fact that the exponential decay has an infinite limit ( $t \rightarrow \infty$ ), it is not possible to derive a total duration of the fire,  $t_{tot}$ . Therefore, the parameter  $\beta_d$ , a value in the range of 0.95 to 1 [42] is introduced, representing the ratio of integrated energy to the time  $t_{tot}$  and the total calorific value,  $E_{t_{tot}}/E_{tot}$ . Together with  $n$  and  $k$ , the time instants  $t_{max}$  and  $t_{tot}$  can be calculated, using

$$t_{max} = \frac{\ln(n)}{k} \quad \text{and} \quad t_{tot} = \frac{1}{k} \ln \left( \frac{1}{1 - \beta_d^{1/n}} \right), \quad (3.10)$$

respectively. It was mentioned before that Eqn. (3.7) can not be used for a fire development exhibiting a longer period of constant maximum HRR. In [42], a function which is able to reproduce a constant plateau was developed by summing up two exponential functions (see Eqn. (3.7)), reading

$$\dot{Q}(t) = \dot{Q}_{max} \left[ n_1 r_1 (1 - e^{-k_1 t})^{n_1 - 1} e^{-k_1 t} + n_2 r_2 (1 - e^{-k_2 t})^{n_2 - 1} e^{-k_2 t} \right], \quad (3.11)$$

where the exponents  $k_1$  and  $k_2$  are calculated, using

$$k_1 = \frac{\dot{Q}_{max}}{E_{tot}} \left( r_1 + \frac{10}{7} r_2 \right) \quad \text{and} \quad k_2 = \frac{\dot{Q}_{max}}{E_{tot}} \left( \frac{7}{10} r_1 + r_2 \right). \quad (3.12)$$

In Tab. 3.6, a set of numerical combinations for the coefficients  $n_1, n_2, r_1$  and  $r_2$ , where Eqn. (3.11) generates a period of constant HRR is shown. A plot of three curves using three different combinations of coefficients corresponding to  $n_1 = 1.5, 5$  and  $10$  are depicted in Fig. 3.7. It shows, that the time at which the plateau of  $\dot{Q}_{max}$  is reached increases with increasing values of  $n_1$ . Figs. 3.8 and 3.9 show applications of Eqns. (3.7) and (3.11) to approximate experimentally-obtained HRR-time curves.

$n_1$	$n_2$	$r_1$	$r_2$
1.5	4.757	1.654	1.530
2	6.495	1.894	1.612
3	9.710	2.135	1.730
4	12.220	2.231	1.741
5	14.610	2.290	1.760
6	16.865	2.330	1.774
7	19.040	2.360	1.788
8	20.980	2.376	1.789
9	22.835	2.387	1.789
10	24.675	2.398	1.792

Table 3.6: Set of coefficients to be used in Eqns. (3.11) and (3.12) [42]

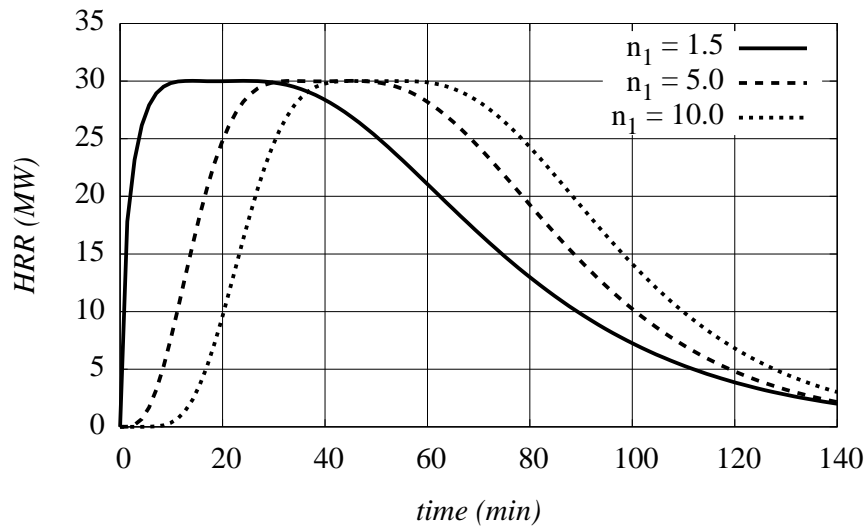


Figure 3.7: HRR-time curves using Eqn. (3.11) for different combinations of coefficients  $n_1, n_2, r_1$  and  $r_2$  from Tab. 3.6, and  $Q_{max} = 30$  MW and  $E_{tot} = 144$  GJ

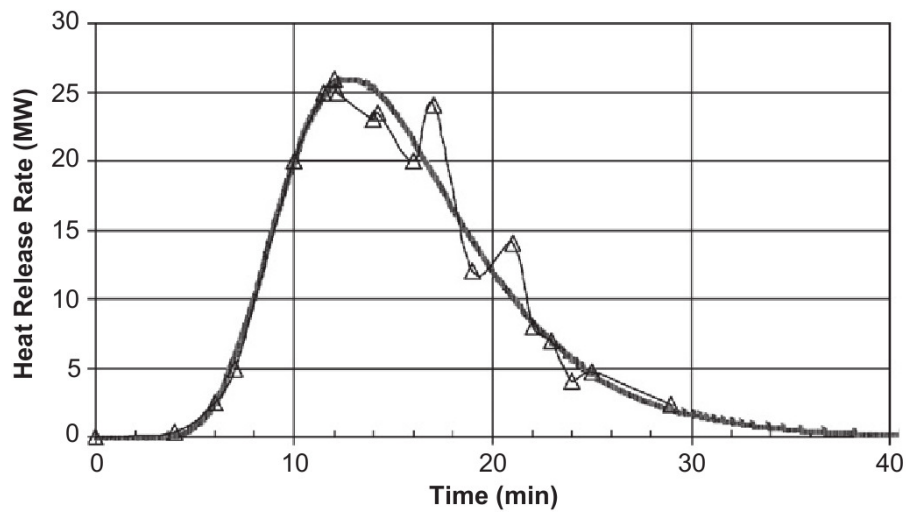


Figure 3.8: Measured HRR-time curve (*symbols*) which is approximated by Eqn. (3.7) with  $n = 16$  (*solid line*) [42]

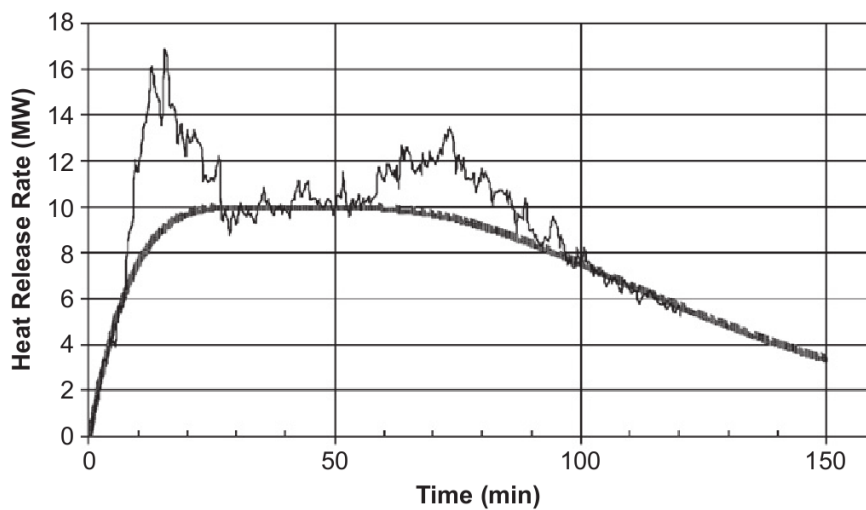


Figure 3.9: Measured HRR-time curve (*thin line*) which is approximated by Eqn. (3.11) using  $n_1 = 2$  (*thick line*) [42]

# Chapter 4

## Computational Fluid Dynamics

In this chapter, the equations governing the dynamics of a fire are presented, followed by a description of two numerical approaches to model a confined fire, i.e. *Zone Models* and *Field Models* or *Computational Fluid Dynamics (CFD)*. Advantages and disadvantages of both approaches are discussed in order to justify why CFD is used to predict the heat transfer from the fire source to the load carrying structure, where a more detailed introduction to CFD is given. Finally, implications for CFD are derived considering the different length and time scales encountered in fires.

### 4.1 Governing equations for fires

The mathematical model for the processes in a fire mainly consists of a set of differential equations. For the reactive flow of a weakly compressible fluid at low Mach number, the governing equations are the conservation of mass (or continuity equation, Eqn. (4.1)), momentum (or Navier-Stokes equations, Eqn. (4.2)), energy (Eqn. (4.3)) and species (Eqn. (4.4)) [65]:

$$\frac{\partial \rho}{\partial t} + \frac{\partial}{\partial x_i} (\rho u_i) = 0, \quad (4.1)$$

$$\frac{\partial}{\partial t} (\rho u_i) + \frac{\partial}{\partial x_j} (\rho u_j u_i) = -\frac{\partial p}{\partial x_i} + \frac{\partial \tau_{ij}}{\partial x_j} + \rho g_i, \quad (4.2)$$

$$\frac{\partial}{\partial t} (\rho h) + \frac{\partial}{\partial x_j} (\rho u_j h) = \frac{\partial q_j}{\partial x_j} + \tau_{ij} \frac{\partial u_i}{\partial x_j} + \frac{\partial p}{\partial t} + u_j \frac{\partial p}{\partial x_j} + S_Q, \quad (4.3)$$

$$\frac{\partial}{\partial t} (\rho Y_i) + \frac{\partial}{\partial x_j} (\rho u_j Y_i) = \frac{\partial}{\partial x_j} \left( \rho \mathcal{D}_i \frac{\partial Y_i}{\partial x_j} \right) + R_i. \quad (4.4)$$

For a Newtonian fluid the viscous stresses  $\tau_{ij}$  in the momentum equation read

$$\tau_{ij} = \mu \left( \frac{\partial u_i}{\partial x_j} + \frac{\partial u_j}{\partial x_i} \right) - \frac{2}{3} \mu \delta_{ij} \frac{\partial u_k}{\partial x_k}. \quad (4.5)$$

The total specific enthalpy of the fluid mixture,  $h$ , consisting of  $N$  species reads

$$h = \sum_{i=1}^N h_i Y_i, \quad (4.6)$$

where  $h_i$  stands for the total specific enthalpy of species  $i$ , and  $Y_i$  for the mass fraction of species  $i$ , reading

$$Y_i = \frac{m_i}{\sum_{i=1}^N m_i} \quad \text{where} \quad \sum_{i=1}^N Y_i = 1. \quad (4.7)$$

The diffusive heat flux  $q_j$  in the energy equation is defined by Fourier's law, reading [65]

$$q_j = \lambda \frac{\partial T}{\partial x_j} + \rho \sum_{i=1}^N h_i \left( \mathcal{D}_i \frac{\partial Y_i}{\partial x_j} \right), \quad (4.8)$$

where  $\lambda$  denotes the thermal conductivity of the fluid mixture and the second summand describes enthalpy transport due to species diffusion. It is common to neglect inter-diffusion processes between species assuming a unit Lewis number,  $Le = a/\mathcal{D}$  (with  $a$  as the thermal diffusivity and  $\mathcal{D}$  the mass diffusivity), allowing to omit the second summand in Eqn. (4.8) [95]. Applying the assumption of a weakly compressible fluid does not only allow to neglect the dissipation term  $\tau_{ij}(\partial u_i/\partial x_j)$  in Eqn. (4.3), but also to express  $q_j$  in Eqn. (4.8) by the enthalpy gradient, finally reading [96]

$$q_j = \frac{\lambda}{c_p} \frac{\partial h}{\partial x_j}, \quad (4.9)$$

where  $c_p$  stands for the specific heat capacity of the mixture.  $S_Q$  in Eqn. (4.3) is a heat-source term typically from radiation.

In the underlying work, the energy equation is used in the form of the specific sensible enthalpy  $h_s$ . Assuming a weakly compressible fluid, the total specific enthalpy of species  $i$  can be written [95]

$$h_i(T) = hs_i(T) + \Delta H_{f,i}^o = \int_{T_{ref}}^T c_{p,i} dT + \Delta H_{f,i}^o, \quad (4.10)$$

where  $\Delta H_{f,i}^o$  stands for the heat of formation of species  $i$ . Inserting Eqn. (4.10) into Eqn. (4.6) and using the resulting expression to substitute  $h$  in Eqn. (4.3), leads to the energy equation in terms of  $hs$ , reading

$$\frac{\partial}{\partial t} (\rho hs) + \frac{\partial}{\partial x_i} (\rho u_i hs) = \frac{\partial}{\partial x_i} \left( \frac{\lambda}{c_p} \frac{\partial hs}{\partial x_i} \right) + \frac{\partial p}{\partial t} + u_i \frac{\partial p}{\partial x_i} + q_C + S_Q, \quad (4.11)$$

with  $q_C$  representing the energy released by the combustion process (see Chapter 5.2.5). The kinetic energy is neglected due to the assumption of a weakly compressible fluid [95]. As a result, the specific sensible enthalpy of a fluid mixture is calculated, using

$$hs(T) = \int_{T_{ref}}^T c_p dT. \quad (4.12)$$

Eqns. (4.1) to (4.12) describe transport processes and attributes of a fluid. For the investigation of heat transfer to structural elements during a fire, also the transport of thermal energy within solids is of interest. In order to determine the temperature distribution inside solids, the equation of heat conduction needs to be solved, reading [72]

$$\frac{\partial}{\partial t} (\rho_s c_{ps} T_s) = \frac{\partial}{\partial x_i} \left( \lambda_s \frac{\partial T_s}{\partial x_i} \right) + S_T, \quad (4.13)$$

where the subscript  $s$  indicates properties of the solid.

From the presented transport equations it can be seen that Eqns. (4.1) to (4.4), Eqn. (4.11) and Eqn. (4.13) can be expressed in the form of a generic differential equation, reading [72]

$$\frac{\partial}{\partial t} (\rho \phi) + \frac{\partial}{\partial x_i} (\rho u_i \phi) = \frac{\partial}{\partial x_i} \left( \Gamma_\phi \frac{\partial \phi}{\partial x_i} \right) + S_\phi, \quad (4.14)$$

where  $\phi$  is the field variable,  $\Gamma_\phi$  the diffusion coefficient and  $S_\phi$  the source term. The four terms in the generic differential equation are identified as the unsteady term, convection term, the diffusion term and the source term. In order to solve Eqn. (4.14), respective *Boundary Conditions (BC)* need to be formulated. In general, there exist two types of BCs: (i) fixed-value or *Dirichlet* BC and (ii) fixed-gradient or *Neumann* BC. In the first case, the value of  $\phi$  on the boundary,  $\phi_b$ , is fixed to a value  $\bar{\phi}$ :  $\phi_b = \bar{\phi}$ . In the second case, the gradient of  $\phi$  normal to the boundary face is fixed to a value  $g_b$ :  $(\mathbf{n} \cdot \nabla \phi)_b = g_b$ .

## 4.2 Numerical modelling of fires in enclosures

In many cases the methods of classical mathematics are not capable of solving the set of governing equations presented in Chapter 4.1 to analyse problems of practical interest. Hence, numerical methods were developed in the recent decades and thanks to increasing computer power it has become possible to model multiple physical processes of many practical applications in engineering including the dynamics of fire. The approach of most numerical models is based on dividing the continuous domain of interest into discrete sub domains, on which the set of conservation equations is applied to. In the subsequent chapters, the two approaches, i.e. *Zone Models* and *Field Models* or CFD are presented.

### 4.2.1 Zone Models

Zone models are numerical models which are able to calculate the development of gas temperature over time in confined fires. Each enclosure is typically divided into two horizontal layers (zones), i.e. an upper hot layer and a lower cold layer, where the temperatures in each layer is assumed uniform (see Fig. 4.1). Ordinary differential equations for the conservation of mass and energy are integrated within each zone, allowing, together with the equation of state (e.g. ideal-gas law) to predict pressure, temperatures and layer height or likelihood of flashover [49]. In combination to the two-zone model, semi-empirical models are added in order to account for phenomena such as fire plume, air entrainment, radiative heat transfer, etc. [87].

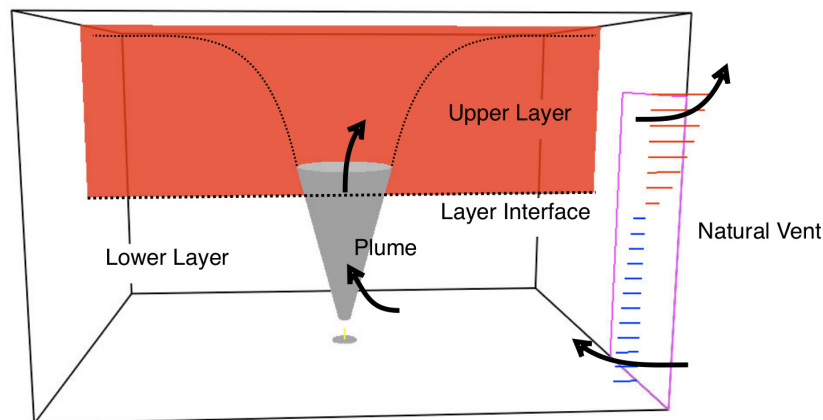


Figure 4.1: Domain discretisation of a two-zone model (arrows indicate the transport of mass and enthalpy) [50]

The basic assumptions of zone models, such as e.g. uniform temperatures in each zone, inherently limit their application. As far as global phenomena like quantity of smoke to be extracted or begin of flashover are of main interest, they may provide a reasonable approximation of reality. At the moment where local phenomena and detailed spatial



distributions of physical quantities need to be investigated, zone models do not lead to accurate predictions. Consequently, zone models are not appropriate for a detailed estimation of the heat transfer to the structure during a fire, and thus the use of field models becomes necessary.

## 4.2.2 Field Models or Computational Fluid Dynamics (CFD)

The approach of field models is based on the idea of dividing the computational domain into a finite number of elements typically in the order of thousands (see Fig. 4.2). The unknown values of field variables are sought at each location or grid point of the discrete elements in the computational domain. By applying the respective conservation equation to each of the element, the discretisation method generates a set of algebraic equations for the unknowns. An appropriate algorithm is applied in order to solve the system of algebraic equations on a computer to obtain the numerical values of the variable on each grid point. For transient problems the solution of the differential equations is not only calculated on discrete points in space but also at discrete instants of a considered time span. Obviously, the accuracy of the numerical solution produced with CFD depends on the quality of the used discretisation methods [29].

The merit of providing high resolutions of field variables in time and space makes CFD a suitable tool for the detailed analysis of heat transfer during fire events in underground structures. Therefore, CFD is used for the underlying analyses of tunnel fires. In the following, a short introduction into the discretisation method used in the present work, i.e. *Finite Volume Method (FVM)*, is given.

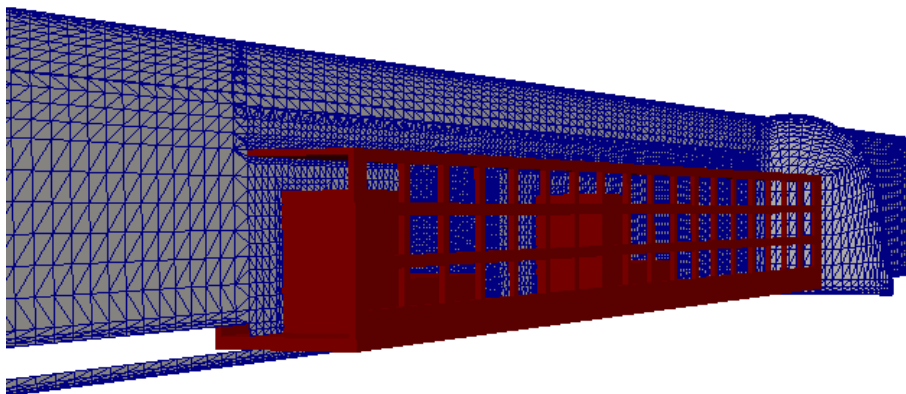


Figure 4.2: Domain discretisation in field modelling

### 4.2.2.1 Finite Volume Method (FVM)

The approach of FVM is illustrated by applying it to the generic differential equation (Eqn. (4.14)) for a one dimensional problem at steady state. For a more detailed description

of FVM and the way how transient terms are treated, the reader is referred to standard text books [29, 66, 72].

In FVM, the computational domain is subdivided into a finite number of contiguous *Control Volumes (CVs)*. The grid point  $P$  lays in the centre of the CV surrounded by the grid points  $W$  and  $E$  of neighbouring CVs (see Fig. 4.3). The FVM requires that the considered conservation equation is satisfied over the CV of volume  $V$  in the integral form, reading

$$\int_V \frac{\partial}{\partial x} (\rho u \phi) dV = \int_V \frac{\partial}{\partial x} \left( \Gamma_\phi \frac{\partial \phi}{\partial x} \right) dV + \int_V S_\phi dV. \quad (4.15)$$

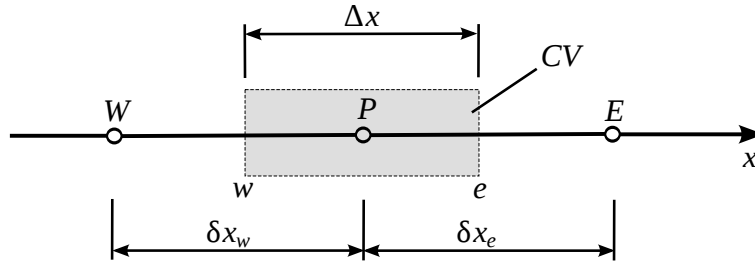


Figure 4.3: FVM grid for a 1D problem showing the CV and its boundary faces  $w$  and  $e$

For the following discussion the velocity field and the fluid properties  $\rho$  and  $\Gamma_\phi$  are assumed to be known at all locations. The spatial discretisation of Eqn. (4.15) is effectuated by applying the Gauss' theorem. Gauss' theorem transforms a volume integral over the volume  $V$  into a surface integral over the volume's surface  $\partial V$ , reading

$$\int_V \nabla \cdot (\rho \mathbf{u} \phi) dV = \int_{\partial V} (\rho \phi) \mathbf{u} \cdot d\mathbf{S}, \quad (4.16)$$

with  $d\mathbf{S}$  as the surface vector. Taking into account that the CV's surface consists of a series of flat surfaces and assuming a homogeneous distribution of all parameters over each surface, the surface integral can be approximated by a sum over all bounding surfaces  $f$  of the CV, reading

$$\int_{\partial V} (\rho \phi) \mathbf{u} \cdot d\mathbf{S} = \sum_f (\rho \phi)_f \mathbf{u}_f \cdot \mathbf{S}_f. \quad (4.17)$$

With Gauss' theorem, the spatial discretisation of Eqn. (4.15) finally reads

$$(\rho u \phi)_e - (\rho u \phi)_w = \left( \Gamma_\phi \frac{\partial \phi}{\partial x} \right)_e - \left( \Gamma_\phi \frac{\partial \phi}{\partial x} \right)_w + S_\phi \Delta x. \quad (4.18)$$

In order to determine the convective and diffusive face fluxes, they have to be expressed in terms of nodal values by interpolation. This is realised by means of *differencing schemes*. A description of most common differencing schemes and their order of accuracy can be found in [29, 72]. Here, the *Upwind Differencing Scheme (UDS)* for the convection terms is used, assuming that the value of  $\phi$  at an interface is equal to  $\phi$  at the grid point on the upwind side of the face. Hence,  $\phi_e = \phi_P$  if  $u_e > 0$  and  $\phi_e = \phi_E$  if  $u_e < 0$ . The value for  $\phi_w$  is calculated similarly. Linear interpolation, also known as *Central Differencing Scheme (CDS)*, is used for diffusion terms, finally allowing to rewrite Eqn. (4.18) in terms of nodal values, reading

$$(\rho u)_e \phi_P - (\rho u)_w \phi_W = \frac{\Gamma_{\phi e} (\phi_E - \phi_P)}{\delta x_e} - \frac{\Gamma_{\phi w} (\phi_P - \phi_W)}{\delta x_w} + S_\phi \Delta x, \quad (4.19)$$

where the fluid flow is assumed in positive  $x$ -direction. The discretisation equation Eqn. (4.19) is typically re-casted in a compact form, reading

$$a_P \phi_P = a_E \phi_E + a_W \phi_W + b, \quad (4.20)$$

where  $b$  is the source term. The coefficients  $a_P$ ,  $a_E$  and  $a_W$  contain a convective and diffusive contribution, where their form depends on the chosen differencing schemes. For every CV in the computational domain, an equation of the form of Eqn. (4.20) can be assembled. As the value of  $\phi_P$  depends on the values in the neighbouring cells, a system of algebraic equations is created, which in matrix form reads

$$[A]\boldsymbol{\phi} = \mathbf{b}, \quad (4.21)$$

where  $[A]$  is a matrix with coefficients  $a_P$  on the diagonal and the neighbouring coefficients  $a_E$  and  $a_W$  off the diagonal.  $\boldsymbol{\phi}$  denotes the vector of  $\phi$ s of all CVs, called the solution vector, and  $\mathbf{b}$  the vector of source terms. Together with the respective BCs, an equation of the form of Eqn. (4.21) is solved for each field variable of interest (e.g.,  $u$ ,  $v$ ,  $w$ ,  $T$ ,  $Y$ , etc.) in order to obtain the value of the variable on each grid point of the domain. For the solution of the system of equations, two classes of solution algorithms exist, i.e. direct and iterative methods. Direct methods produce the solution in a finite number of arithmetic operations, whereas iterative methods start from an initial guess and continue to improve the current approximation successively. The iterative process is stopped at a moment where a certain solution tolerance is reached. While direct methods are appropriate for small systems, iterative methods are more economical for large systems as encountered in most applications for CFD [45]. A detailed description of iterative solution methods for CFD can be found in [66].

The great advantage of the FVM is the exact satisfaction of the integral conservation of quantities (mass, momentum, energy, etc.) in any group of CVs and in the whole

computational domain. Consequently, even solutions obtained on a coarse grid exhibit exact integral balances [72].

### 4.3 Length and time scales within fires and consequences for CFD

A look at typical length and time scales of the physical mechanism involved in natural fires allow to work out implications for modelling of such events as presented in [84]. The smallest length scales in sooty fires are determined by the growth of soot particles from the molecular length-scales  $O(\text{nm})$ . The largest length scales depend on the application: in laboratory experiments fire sizes are in the range of  $O(\text{cm})$ - $O(\text{m})$ , in building fires  $O(\text{m})$ , and in forest fires  $O(\text{km})$ . The range from  $10^{-9}$  m to  $10^3$  m spans 12 orders of magnitude for the length scales of physics, relevant for natural fires. For the time scales, theoretically the smallest scale is determined by the transport of thermal radiation at the speed of light. For most engineering applications the speed of light is much larger compared to local time and length scales so that it may be neglected [62]. Furthermore, the interaction between radiation transport and momentum and scalar transport is defined by radiation properties of the participating media (e.g. absorption coefficient). Hence, the smallest relevant time scales are times of chemical kinetics (e.g. molecular transport, rearrangement of chemical bonds, etc.) within the combustion process,  $O(\text{ms})$ . The upper bound of the time scale again depends on the problem under consideration: fires in underground mines can burn for decades,  $O(10^8 \text{ s})$ , forest fires last days,  $O(10^5 \text{ s})$ , and tunnel and building fires last for hours,  $O(10^4 \text{ s})$ .

From the discussion above it can be seen that the different transport phenomena in a turbulent fire plume are present over a broad range of time and length scales. In general, all the ranges of the scales are important in the coupled processes of a fire but non of them are dominant over all the length or time scales. The relative importance of transport processes is often expressed by non-dimensional numbers. Examples are the advection to diffusion ratio which is the *Reynolds* number, both the *Froude* and the *Richardson* number represent the ratio of advective to buoyant time scale, or the *Damköhler* number describing the comparison of a given chemical time scale with an advective or diffusive time scale.

It is obvious that the resolution of the whole range of length and time scales increases the computational effort beyond current processor capacities. Thus, not all the length and time scales can be resolved by solving the discretised conservation equations. Consequently, the range of length scales must be divided into three parts by introducing two length-scale cut-offs, a smaller and a larger one. Above the larger cut-off the length scales are too large in order to be captured and are represented by the boundary conditions in a simulation. Similarly, length scales below the smallest cut-off are length scales that

have to be modelled and are represented as source or linear advection terms in the transport equations. Everything in between the boundary conditions and these source terms is described by the resolved range of length scales in which the discretised conservation equations are solved. The length scale cut-offs implicitly introduce cut-offs for time scales corresponding to time scales of transport processes at the length scale cut-offs. Within the splitting of the range of scales into the three parts, the modelled range is the largest. The common modelling approach seeks to identify a correlating variable in the resolved regime and ties the modelling process to the correlating variable. In turn the mean value produced in the modelling process is passed on to the resolved equations as a source or advection term. As a result for the numerical simulation of fires, the fluid transport at large scales is simulated and the higher spatial and temporal frequency physics must be modelled.

## 4.4 Possibilities and limitations of CFD

The most important advantage of CFD is its low cost and high speed compared to a corresponding experimental investigation. CFD simulations may save money and time specially when it comes to parameter studies. The numerical results of a CFD simulation give access to all the relevant variables (such as velocities, pressures, temperatures) in the whole domain of interest which is not possible in an experiment. CFD also allows to prescribe BCs which are realised only with great efforts in an experiment, e.g. ideally insulated surface, opaqueness of a fluid, etc. Additionally, it poses the ability to mimic ideal conditions (e.g. two-dimensionality, constant density, etc.) in order to isolate basic phenomena.

These advantages are based on the assumption that the governing equations are solved accurately, which is extremely difficult for most flows of engineering interest. Numerical results are always an approximation of reality as a result of errors introduced by each part in the course of determination. Beginning with the validity of the underlying mathematical model, i.e. the governing equations mostly containing idealisations (e.g. weakly-compressible fluid), whereas the experiment reproduces the whole physics. Approximations are made during the discretisation of the governing equations in time and space as demonstrated in Chapter 4.2.2.1. To solve the system of discretised equations (Eqn. (4.21)) iterative methods are used and have to run for a very long time to produce accurate solutions. In reality the iteration process is stopped at a certain level of accuracy due to lack of time resulting in further errors. As mentioned in Chapter 4.3, a numerical simulation cannot resolve all time and length scales of a problem making the introduction of models (e.g. for turbulence, combustion, etc.) necessary, which again, can only approximate reality. In order to assess the validity of these models one relies on experimental data. Consequently, the assumptions made and approximations used to produce numerical results with CFD have to be kept in mind while interpreting them.

# Chapter 5

---

## Development of a fire code

In the previous chapter it was concluded that CFD shall be used for the underlying analyses. A review of existing codes was conducted based on the study presented in [68], in order to identify if an existing computer model can be used or if the code-development can be based on an available code. After specifying the requirements of the code, a suitable computer model is chosen and the investigation of different sub models of the code are presented in this chapter.

### 5.1 Existing fire codes

The code has to reproduce a turbulent buoyancy-driven flow induced by the combustion process, accounting for conductive, convective and radiative heat transfer. To meet these demands, suitable sub models for turbulence and combustion must be included, as well as a method to describe the radiative heat transfer within the fluid region. As one of the focuses lays on the heat transfer to the tunnel structure, the treatment of the heat transfer at the fluid-solid interface, i.e. the conjugate heat transfer, is of great interest. In any case the source code should be open for the reasons of a better understanding of certain features and possible modifications of the code. Based on the formulated specifications, a comparison of selected codes is presented in Tab. 5.1, where only two codes are open-source, i.e. *Fire Dynamics Simulator (FDS)* [60] and *OpenFOAM* [70]. FDS is a code specialised on fire simulations including sub models such as pyrolysis or liquid sprays. On the other hand, *OpenFOAM* is a multi-purpose CFD package which has a large user base also contributing to its development. As a result, it represents a great flexibility in the choice of sub models like turbulence or radiation (see Tab. 5.1).

<b>Name</b>	<b>FDS</b>	<b>OpenFOAM</b>	<b>SOFIE</b>
<i>Availability</i>	freeware/open-source	freeware/open-source	research licence
<i>Contact</i>	www.fire.nist.gov/fds	www.open CFD.co.uk	p.a.rubini@hull.ac.uk
<i>Programming language</i>	FORTRAN/C	C++	FORTRAN/C
<i>Discretisation method</i>	finite difference method	finite volume method	finite volume method
<i>Mesh</i>	cartesian 3D	unstructured 3D	unstructured 3D
<i>Turbulence model</i>	LES	LES, RANS	RANS
<i>Combustion model</i>	mixture fraction	amongst others: mixture fraction	mixture fraction/eddy break-up model
<i>Radiation model</i>	discrete ordinate method	P1-approximation, discrete ordinate method	discrete transfer method
<i>Heat transfer to boundaries</i>	heat transfer coefficient $h = h(Pr, Re)$	heat transfer coefficient using wall functions	heat transfer coefficient using wall functions
<i>Conjugate heat transfer</i>	yes	yes	yes
<b>Name</b>	<b>Jasmine</b>	<b>Smartfire</b>	<b>Solvent</b>
<i>Availability</i>	academic licence	commercial licence	commercial licence
<i>Contact</i>	www.bre.co.uk/fire	www.fseg.gre.ac.uk	www.tunnelfire.com
<i>Programming language</i>	FORTRAN	C++	FORTRAN/C++
<i>Discretisation method</i>	finite volume method	n.s.	finite volume method
<i>Mesh</i>	structured 3D	unstructured 3D	n.s.
<i>Turbulence model</i>	RANS	RANS	RANS
<i>Combustion model</i>	mixture fraction/eddy break-up model	yes (not further specified)	non
<i>Radiation model</i>	six-flux, discrete transfer method	multi-ray method, six-flux method	six-flux method
<i>Heat transfer to boundaries</i>	heat transfer coefficient using wall functions	n.s.	heat transfer coefficient using wall functions
<i>Conjugate heat transfer</i>	yes	n.s.	yes

Table 5.1: Comparison of selected fire codes (n.s. = not specified)

Three main reasons led to the conclusion to use the OpenFOAM framework for the development of a code to simulate fires in underground structures:

- OpenFOAM applies the FVM for the discretisation of the governing equations where the integral conservation of each quantity is exactly satisfied independent on the spatial discretisation of the computational domain (see Chapter 4.2.2.1).
- Beside *Large Eddy Simulation (LES)*, the *Reynolds Averaged Navier-Stokes (RANS)* approach for modelling turbulence is also implemented in OpenFOAM. It allows a lower spatial resolution than the approach of LES, which in turn reduces computational efforts (see Chapter 5.2.1). This is important in regard to the big domains encountered in tunnel fires in the order of  $O(10000\text{s m}^3)$ .
- Over the recent years the number of users of OpenFOAM has risen rapidly. It can be seen from various events such as the OpenFOAM Workshop ([www.extend-project.de/openfoam-workshop](http://www.extend-project.de/openfoam-workshop)) or the Open Source CFD International Conferences connecting a large group of users. This brings the advantage of a strong exchange of experience with the software, which is also realised through an active online forum ([www.cfd-online.com/Forums/openfoam](http://www.cfd-online.com/Forums/openfoam)).

## 5.2 Development of the fire code in OpenFOAM

The code development in OpenFOAM was started with version 1.6.x and completed in version 1.7.1. The starting point is OpenFOAM's *chtMultiRegionFoam* solver. The solver couples conjugated heat transfer in a solid to a buoyancy-driven flow at low Mach number of a compressible Newtonian fluid. First, the governing equations of the fluid region (Eqns. (4.1) to (4.3)) are solved, followed by the calculation of the temperature field in the solid region (Eqn. (4.13)) before advancing to the next time step. To link the pressure and the velocity field in the fluid region, a special procedure is necessary as no explicit equation to calculate the pressure is available. The link is effectuated by the *Pressure Implicit with Splitting of Operators (PISO)* algorithm [44]. The PISO algorithm is based on the calculation of a pressure field that guarantees the conservation of mass. Hereby, a pressure equation is constructed by taking the divergence of the momentum equation (Eqn. (4.2)) in its discretised form Eqn. (4.20) and entering it into the continuity equation (Eqn. (4.1)). The PISO algorithm as it is implemented in the *chtMultiRegionFoam* solver can be summarised as follows:

1. Velocity predictor in the fluid region: guess a pressure field and solve the discretised momentum equation to compute an intermediate velocity field.
2. Compute the mass fluxes at the cell faces from the intermediate velocity field.



3. Solve the pressure equation with the computed mass fluxes.
4. Correct the mass fluxes at the cell faces based on the new pressure field.
5. Correct the velocity field on the basis of the corrected mass fluxes.
6. Repeat from 2 with the corrected velocity field for the prescribed number of PISO-corrector steps.

For the description of a buoyant flow, static pressure,  $p$ , is split into two parts, i.e. the background pressure,  $p_{rgh}$ , and the hydrostatic pressure,  $\rho gy$ , reading

$$p = p_{rgh} + \rho gy, \quad (5.1)$$

in the *chtMultiRegionFoam* solver, with  $y$  standing for the coordinate in the direction of the gravitational acceleration,  $g$ . Consequently, the pressure equation is constructed and solved for  $p_{rgh}$  and  $p$  is calculated from Eqn. (5.1). The velocity field which is calculated in Step 5 of the PISO algorithm, is recovered from the face fluxes of the finite-volume faces in order to create a "pseudo-staggered" finite volume numeric in OpenFOAM's co-located grid, i.e. same grids for velocity and pressure [69]. In FVM, staggered grids are used in order to avoid decoupling of the velocity and pressure field by calculation of velocity at CV faces and pressure at CV centers [72].

As mentioned before, both turbulence models LES and RANS are available in OpenFOAM. It will be pointed out in Chapter 5.2.1 why RANS is used for the underlying analysis. No models to describe radiative heat transfer<sup>1</sup> and combustion are included in *chtMultiRegionFoam*. Hence, beside the implementations of buoyancy-modified turbulence models, radiative heat transfer, conjugate heat transfer including radiation and a combustion model are introduced into the *chtMultiRegionFoam* solver and investigated by means of analytical solutions and experimental data. Finally, all features are combined into a single code.

### 5.2.1 Turbulence model

Most flows in engineering practice are turbulent, so are natural fires. Turbulence comes from the instability of the viscous flow at high Reynolds number, reading

$$Re = \frac{UL}{\nu}, \quad (5.2)$$

with  $U$  and  $L$  as a characteristic velocity and length scale, respectively, and  $\nu$  as the kinematic viscosity. The instabilities are a consequence of the interaction between the

---

<sup>1</sup>Prior to version 1.7.0 no radiation model was present in the *chtMultiRegionFoam* solver.

viscous and non-linear terms in the momentum equations (Eqn. (4.2)) [93]. It is difficult to give a definition of turbulence but main characteristics of turbulent flows shall be given below [29]:

- Turbulent flows are highly unsteady. This can be seen e.g. from velocity as a function of time at a point in the flow field (see Fig. 5.1).
- Turbulent flows are three-dimensional as the instantaneous fluctuates in the flow field happen in all three spatial directions.
- They are dominated by strong vorticity.
- The random movement due to turbulence enhances the mixing of conserved variables accomplished by diffusion, thus called *turbulent diffusion*.
- The process of turbulent mixing is dissipative where kinetic energy is irreversibly converted into heat.
- The turbulent fluctuations extend over a broad range of length and time scales.

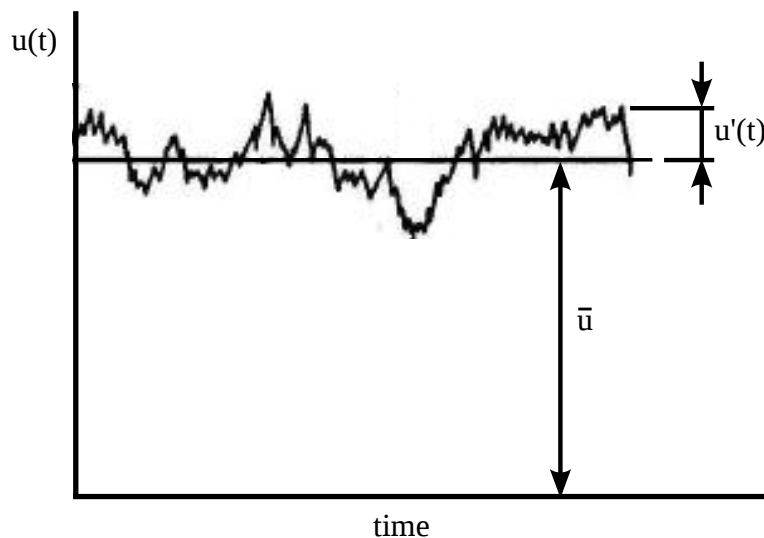


Figure 5.1: Velocity as a function of time at a point in a turbulent flow field

In regard to the last point, three length scales are referred to in turbulent flows (with associated time scales), i.e. the Kolmogorov length-scale,  $\eta$ , the Taylor length-scale,  $\lambda$ , and the integral length-scale,  $\ell$ . The large eddies, which have dimensions comparable to the dimensions in the mean flow, contain most of the energy obtained through shear and buoyancy production from the mean flow [93]. In the course of an energy cascade, the big eddies break down and transfer kinetic energy to the smaller eddies, where the energy is finally dissipated at the smallest eddies of Kolmogorov length-scale. Fig. 5.2 depicts the

spectrum of turbulent kinetic energy,  $E$ , plotted over the wave number,  $\kappa$  (proportional to the inverse of the eddy dimension), showing that the big eddies carry the energy which is then dissipated at smallest length scales.

When it comes to simulate turbulent flows, turbulence can be modelled in different ways including *Direct Numerical Simulation (DNS)*, LES and RANS. DNS resolves all involved length and time scales of the turbulent motion (thus, cannot be considered as a model) resulting in a considerably high computational time. In LES, the larger energy carrying eddies are resolved down to the inertial range and eddies of smaller length scales are modelled using a sub-grid model. The RANS approach statistically averages the instantaneous fluctuations of the flow field resulting in terms that must be modelled due to the non-linearity of the Navier-Stokes equations. Hence, all unsteadiness of turbulence is averaged out and only the smooth mean field needs to be resolved [29]. The situations in treating turbulence with DNS, LES and RANS is shown in Fig. 5.3. DNS is not appropriate for practical applications as a result of the high computational costs. LES describes turbulence in a more universal way than RANS but with the expense of higher computational costs stemming from the necessity of finer computational grids. This main drawback of LES results in the choice of using RANS for the underlying investigation, similar to most of the codes presented in Tab. 5.1.

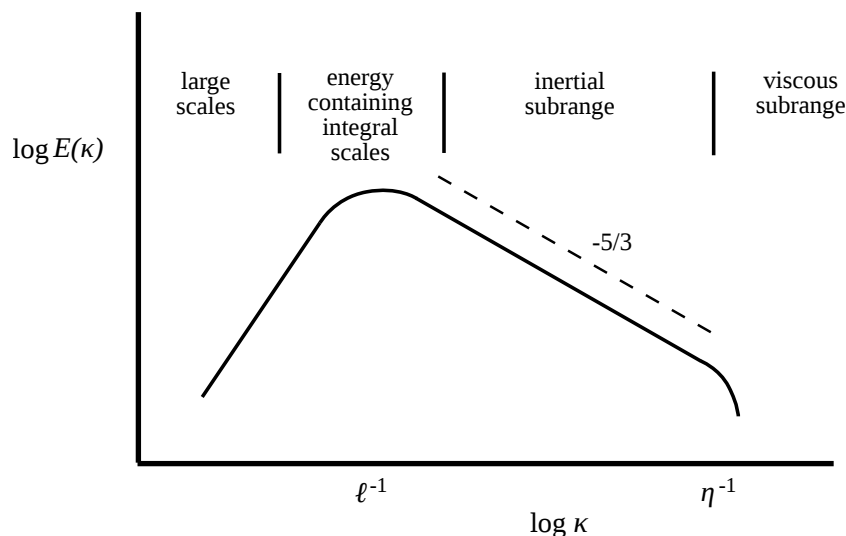


Figure 5.2: Turbulent kinetic energy spectrum,  $E$ , as a function of the wave number  $\kappa$  [65]

### 5.2.1.1 RANS turbulence modelling

As already mentioned before, RANS averages the temporal variation of flow parameters and is only interested in the time mean. Thus, every variable  $\phi$  is represented as the sum of a time-averaged value,  $\bar{\phi}$ , and a fluctuation about that value,  $\phi'$ , (see, e.g. Fig. 5.1) reading

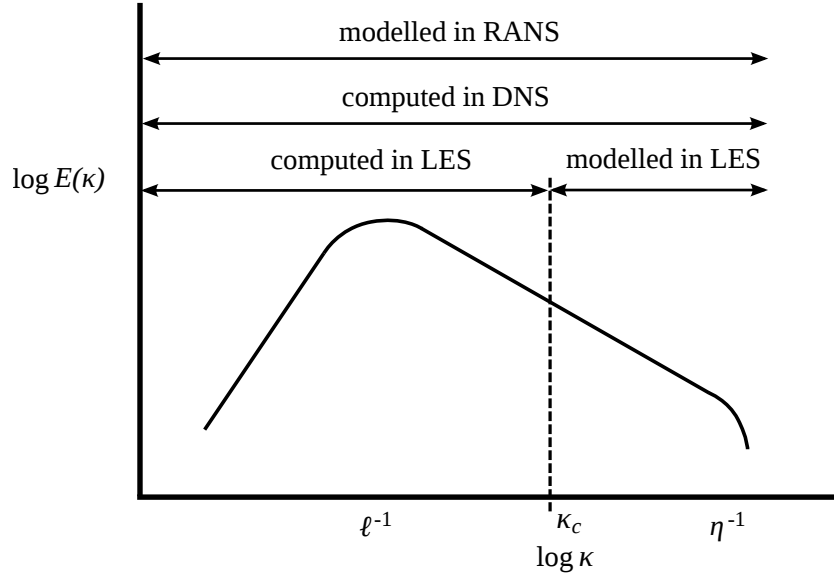


Figure 5.3: Resolved and modelled turbulent kinetic energy spectrum,  $E$ , for DNS, LES and RANS [65]

$$\phi(x_i, t) = \bar{\phi}(x_i, t) + \phi'(x_i, t), \quad (5.3)$$

where

$$\bar{\phi}(x_i, t) = \frac{1}{\Delta t} \int_t^{t+\Delta t} \phi(x_i, t) dt \quad \text{and} \quad \overline{\phi'}(x_i, t) = 0. \quad (5.4)$$

During averaging of the conservation equations (see Chapter 4.1) linear terms give the averaged term, whereas averaging non-linear terms (convection terms) produce a covariance  $\overline{\rho u_i' \phi'}$ . In the Navier-Stokes equations the covariance appears as  $\overline{\rho u_i' u_j'}$  and is called *Reynolds stresses* and for the other scalar variables they are called *turbulent scalar fluxes*. These terms are unknown and no additional equations are available to calculate them (*Turbulent Closure Problem*). As a result they need to be modelled in order to relate them with the mean-flow quantities. A common way is the Boussinesq eddy-viscosity assumption, where the Reynolds stresses are described as diffusion terms using an eddy or turbulent viscosity,  $\mu_t$ , reading [29]

$$-\overline{\rho u_i' u_j'} = \mu_t \left( \frac{\partial \bar{u}_i}{\partial x_j} + \frac{\partial \bar{u}_j}{\partial x_i} \right) - \frac{2}{3} \bar{\rho} k \delta_{ij}, \quad (5.5)$$

with  $k$  as the specific turbulent kinetic energy, determined using

$$k = \frac{1}{2} \overline{u_i' u_i'}. \quad (5.6)$$

The turbulent scalar fluxes are modelled through the eddy-diffusion model, reading [29]

$$-\overline{\rho u_j' \phi'} = \Gamma_{\phi t} \left( \frac{\partial \bar{\phi}}{\partial x_j} \right), \quad (5.7)$$

applying the *Simple Gradient Diffusion Hypothesis (SGDH)*, with  $\Gamma_{\phi t}$  as the turbulent diffusion coefficient for variable  $\phi$ . Finally, the governing equations for a non-reactive flow using RANS can be written, reading

$$\frac{\partial \bar{p}}{\partial t} + \frac{\partial}{\partial x_i} (\overline{\rho u_i}) = 0, \quad (5.8)$$

$$\frac{\partial}{\partial t} (\overline{\rho u_i}) + \frac{\partial}{\partial x_j} (\overline{\rho u_j u_i}) = -\frac{\partial \bar{p}}{\partial x_i} + \frac{\partial}{\partial x_j} (\overline{\tau_{ij}} - \overline{\rho u_i' u_j'}) + \bar{\rho} g_i \quad (5.9)$$

and

$$\frac{\partial}{\partial t} (\overline{\rho h}) + \frac{\partial}{\partial x_i} (\overline{\rho u_i h}) = \frac{\partial}{\partial x_i} \left[ \left( \frac{\lambda}{c_p} + \frac{\mu_t}{\sigma_t} \right) \frac{\partial \bar{h}}{\partial x_i} \right] + \frac{\partial \bar{p}}{\partial t} + \bar{u}_i \frac{\partial \bar{p}}{\partial x_i} + S_Q. \quad (5.10)$$

In case of a reactive flow, the energy equation in terms of  $hs$  and the species transport equations read

$$\frac{\partial}{\partial t} (\overline{\rho h s}) + \frac{\partial}{\partial x_i} (\overline{\rho u_i h s}) = \frac{\partial}{\partial x_i} \left[ \left( \frac{\lambda}{c_p} + \frac{\mu_t}{\sigma_t} \right) \frac{\partial \bar{h s}}{\partial x_i} \right] + \bar{u}_i \frac{\partial \bar{p}}{\partial x_i} + q_C + S_Q, \quad (5.11)$$

and

$$\frac{\partial}{\partial t} (\overline{\rho Y_i}) + \frac{\partial}{\partial x_j} (\overline{\rho u_j Y_i}) = \frac{\partial}{\partial x_j} \left[ \left( \bar{\rho} D_i + \frac{\mu_t}{\sigma_t} \right) \frac{\partial \bar{Y}_i}{\partial x_j} \right] + \bar{R}_i, \quad (5.12)$$

respectively, with  $Pr$  and  $\sigma_t$  standing for the Prandtl and turbulent Prandtl number, reading

$$Pr = \frac{\mu c_p}{\lambda} \quad \text{and} \quad \sigma_t = \frac{\mu_t c_p}{\lambda_t}, \quad (5.13)$$

respectively, and with the assumption of a unit Lewis number. The laminar and turbulent diffusion coefficients are summarised to an effective diffusion coefficient, like it is done for the viscosity and the enthalpy diffusivity, reading

$$\mu_{eff} = \mu + \mu_t \quad \text{and} \quad \alpha_{eff} = \alpha + \alpha_t = \frac{\lambda}{c_p} + \frac{\mu_t}{\sigma_t}, \quad (5.14)$$

respectively. In order to calculate  $\mu_t$ , the most common two-equation turbulence model, i.e. the standard  $k$ - $\varepsilon$  turbulence model [48, 52], is applied here, reading

$$\mu_t = \bar{\rho} C_\mu \frac{k^2}{\varepsilon}, \quad (5.15)$$

with the dimensionless constant  $C_\mu = 0.09$  and  $\varepsilon$  denoting the specific turbulent dissipation rate, defined as

$$\varepsilon = \nu \frac{\overline{\partial u'_i{}^2}}{\partial x_j}. \quad (5.16)$$

Consequently, two additional transport equations for  $k$  and  $\varepsilon$  need to be solved, reading

$$\frac{\partial}{\partial t} (\bar{\rho} k) + \frac{\partial}{\partial x_i} (\bar{\rho} \bar{u}_i k) = \frac{\partial}{\partial x_i} \left[ \left( \mu + \frac{\mu_t}{\sigma_k} \right) \frac{\partial k}{\partial x_i} \right] + P + \bar{\rho} \varepsilon, \quad (5.17)$$

and

$$\frac{\partial}{\partial t} (\bar{\rho} \varepsilon) + \frac{\partial}{\partial x_i} (\bar{\rho} \bar{u}_i \varepsilon) = \frac{\partial}{\partial x_i} \left[ \left( \mu + \frac{\mu_t}{\sigma_\varepsilon} \right) \frac{\partial \varepsilon}{\partial x_i} \right] + C_1 \frac{\varepsilon}{k} P - C_2 \bar{\rho} \frac{\varepsilon^2}{k}, \quad (5.18)$$

with the dimensionless model constants  $C_1 = 1.44$ ,  $C_2 = 1.92$ ,  $\sigma_k = 1$  and  $\sigma_\varepsilon = 1.3$  and  $P$  describing the production of turbulence due to velocity gradients, estimated using

$$P = \mu_t \left( \frac{\partial \bar{u}_i}{\partial x_j} + \frac{\partial \bar{u}_j}{\partial x_i} \right) \frac{\partial \bar{u}_i}{\partial x_j}. \quad (5.19)$$

BCs are needed for the model equations. To avoid resolving the viscous sublayer in the near-wall region, one relies on a logarithmic velocity profile in the turbulent boundary layer by using *wall functions*. In the approach of *wall functions*, the first grid point is put within the logarithmic region corresponding to a dimensionless wall distance,  $y^+ > 30$  [29], where  $y^+$  is defined as

$$y^+ = \frac{y \bar{\rho} u_\tau}{\mu}. \quad (5.20)$$

$y$  denotes the wall distance and  $u_\tau$  the shear velocity which is calculated from the wall shear stress  $\tau_w$ , reading

$$u_\tau = \sqrt{\frac{|\tau_w|}{\bar{\rho}}}. \quad (5.21)$$

The application of *wall functions* allows to derive an expressions for  $\varepsilon$  at the grid point  $P$  next to the wall from  $k$  at the same point,  $k_P$ , reading

$$\varepsilon_P = \frac{C_\mu^{3/4} k_P^{3/2}}{\kappa y}, \quad (5.22)$$

as well as an expression for  $P$  at the wall, whereas a zero-gradient BC is applied for  $k$  [29]. In OpenFOAM, the approach of modifying  $\mu_t$  at the wall in a way to guarantee the correct shear stress is followed:  $\mu_{tw}$  is set to zero for points within the laminar sublayer ( $y^+ < y_{lam}^+$ ) and is calculated for points outside the laminar sublayer, using

$$\mu_{tw} = \mu \left[ \frac{y^+}{\frac{1}{\kappa} \ln(Ey^+)} - 1 \right], \quad (5.23)$$

with the model constants  $\kappa = 0.41$  and  $E = 9.8$  and the subscript  $w$  indicating values at the wall. Finally,  $P$  at the wall can be calculated, using

$$P_w = \tau_w \frac{C_\mu^{1/4} k_w^{1/2}}{\kappa y} = (\mu_{tw} + \mu_w) \left( \frac{\partial \bar{u}}{\partial n} \right)_w \frac{C_\mu^{1/4} k_w^{1/2}}{\kappa y}. \quad (5.24)$$

It is well known that the standard  $k$ - $\varepsilon$  model strongly underestimates the effects of buoyancy on the turbulence production [86]. In order to overcome this problem, a so-called buoyancy augmentation of the standard  $k$ - $\varepsilon$  turbulence model is necessary (see Chapter 5.2.3).

## 5.2.2 The conjugate heat transfer

The heat transfer between the solid and the fluid region is not tested against experimental data as such experiments are rare. However, the implementation of the conjugate heat transfer in the *chtMultiRegionFoam* solver is compared with semi-empirical correlations for the forced convection at a flat heated plate. Strictly, the correlations are not applicable to conjugate heat transfer problems as they assume a constant surface temperature along the entire plate, but shall give information on which order of magnitude the predicted heat transfer lays compared to the correlations.

The situation in the computational grid at the solid-fluid interface, where two (finite) control volumes (one fluid and one solid volume) share the interface, is shown schematically in Fig. 5.4. At the interface, two main requirements must be fulfilled: (i) a common interface temperature in the fluid and the solid region, and (ii) the same magnitude of thermal energy transferred through the interface in both regions. The energy balance using the common wall temperature,  $T_w$ , can be written as

$$\frac{\lambda_f}{\delta x_f} (T_w - T_P) = \frac{\lambda_s}{\delta x_s} (T_E - T_w), \quad (5.25)$$

from which  $T_w$  can be expressed, reading

$$T_w = \frac{T_E (\lambda_s / \delta x_s) + T_P (\lambda_f / \delta x_f)}{(\lambda_s / \delta x_s) + (\lambda_f / \delta x_f)}. \quad (5.26)$$

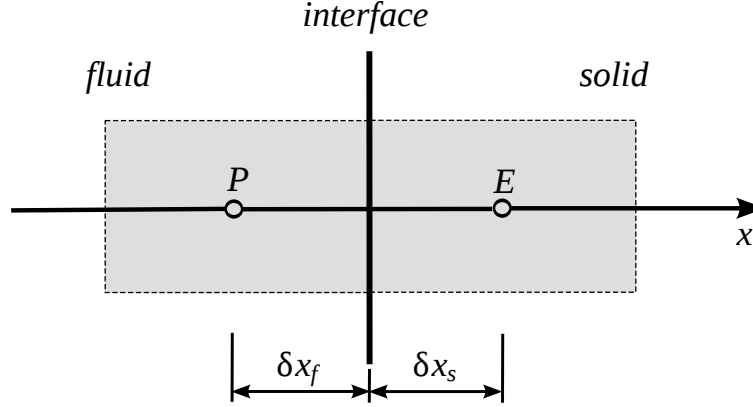


Figure 5.4: Grid configuration at the solid-fluid interface

Eqn. (5.26) is in accordance with the derivation of an interface conductivity as the harmonic mean value of  $\lambda_s$  and  $\lambda_f$  presented in [72]. The thermal conductivity of the fluid,  $\lambda_f$ , in the wall-adjacent CV is derived from the effective enthalpy diffusivity, reading

$$\lambda_f = c_p \alpha_{eff} = c_p \left( \alpha_t + \frac{\mu}{Pr} \right). \quad (5.27)$$

According to the Reynolds analogy of similarities of momentum and energy transfer in turbulent flows,  $\alpha_t$  is obtained using

$$\alpha_t = \frac{\mu_t}{\sigma_t}. \quad (5.28)$$

The value of the interface temperature from Eqn. (5.26) is used as BC for the energy equation at both the fluid and solid side (Eqns. (5.10) or (5.11) and Eqn. (4.13), respectively), realising the coupling of heat transfer in the two regions. In OpenFOAM 1.7.1<sup>2</sup>, Eqn. (5.28) is also used to determine the value at the wall,  $\alpha_{tw}$ , whereas the assumption of a constant turbulent Prandtl number is only acceptable in the inertial sublayer for  $y^+ > 100$  [11]. In order to account for the varying heat transfer over the boundary layer, similar to the velocity boundary layer wall functions for the temperature, i.e. interpolation functions in the region between the wall and the grid point adjacent to the wall, can be developed, allowing to calculate  $\alpha_{eff,w}$ . The thermal wall functions for a compressible flow, which is available for OpenFOAM 2.0.0 applying the P-function,  $P_J$ , from Jayatilleke [47] and compressibility effects (though compressibility effects are not important here) as presented in [89], is taken into the present code. For a near-wall point within the laminar

<sup>2</sup>No thermal *wall functions* are available for compressible flows prior to OpenFOAM 2.0.0



sublayer of the thermal boundary layer (corresponding to  $y^+ < y_{lam}^+$ )  $\alpha_{eff,w}$  is calculated, using

$$\alpha_{eff,w} = \mu \frac{y^+}{Pr y^+ + 0.5 Pr \bar{\rho}_w u_\tau \bar{U}_P^2 / q_w}, \quad (5.29)$$

and for a wall distances outside the laminar sublayer of the thermal boundary layer (corresponding to  $y^+ > y_{lam}^+$ )  $\alpha_{eff,w}$  is determined, using

$$\alpha_{eff,w} = \mu \frac{y^+}{\sigma_t \left[ \frac{1}{\kappa} \ln(E y^+) + P_J \right] + 0.5 \bar{\rho}_w u_\tau \left[ \sigma_t \bar{U}_P^2 + (Pr - \sigma_t) \bar{U}_c^2 \right] / q_w}, \quad (5.30)$$

where  $\bar{U}_P$  and  $\bar{U}_c$  are the magnitude of the mean velocities at the grid point next to the wall and the magnitude of the mean velocities at the border of the laminar sublayer of the thermal boundary layer ( $y^+ = y_{lam}^+$ ), respectively.  $q_w$  is the convective wall-heat flux taken from the last iteration step and  $P_J$  Jayatilke's P-function, reading [47]

$$P_J = 9.24 \left[ \left( \frac{Pr}{\sigma_t} \right)^{3/4} - 1 \right] \left[ 1 + 0.28 \exp \left( -0.007 \frac{Pr}{\sigma_t} \right) \right]. \quad (5.31)$$

The second summand in the denominator of Eqns. (5.29) and (5.30) consider compressibility effects as can be seen, e.g. from Eqn. (5.29), where omitting the term yields the laminar enthalpy diffusivity. Similar to the calculation of  $\tau_w$  (see Eqn. (5.24)), the new value of the convective wall-heat flux is then determined, using

$$q_w = \alpha_{eff,w} \left( \frac{\partial \bar{h}}{\partial n} \right)_w. \quad (5.32)$$

### 5.2.2.1 Forced convection at a flat heated plate

The 2D set-up consists of a heated plate with a length  $L = 1$  m and a thickness of 0.02 m. The bottom of the plate is kept to a constant temperature  $T_p = 323$  K (see Fig. 5.5). Air enters the domain with a constant inlet velocity  $u_{in} = 10$  m/s in  $x$ -direction and a temperature of 293 K, resulting in  $Re = 6 \cdot 10^5$ . The used thermo-physical parameters, evaluated at a temperature of 308 K, are  $\nu = 168 \cdot 10^{-7}$  m<sup>2</sup>/s,  $\lambda = 26.8 \cdot 10^{-3}$  W/m/K,  $Pr = 0.7$  and  $\sigma_t = 0.85$ .

For the simulations with the *chtMultiRegionFoam* solver, upstream of the plate an adiabatic floor with a *slip* BC is located in order to allow a smooth inflow. The standard  $k$ - $\varepsilon$  model is applied as no significant buoyancy effects are expected. The inlet values for  $k$  and  $\varepsilon$  are calculated with the expressions, reading

$$k_{in} = \frac{3}{2} u_{in}^2 T u_{in}^2 \quad (5.33)$$

and

$$\varepsilon_{in} = \frac{C_\mu^{\frac{3}{4}} k_{in}^{\frac{3}{2}}}{l_m}, \quad (5.34)$$

with a turbulent mixing length  $l_m$  calculated, using

$$l_m = \frac{L}{15}, \quad (5.35)$$

resulting in  $k_{in} = 0.375 \text{ m}^2/\text{s}^2$  and  $\varepsilon_{in} = 0.57 \text{ m}^2/\text{s}^3$ , where a turbulent intensity of  $Tu_{in} = 5\%$  is assumed. The remaining BCs are indicated in Fig. 5.5. Three different resolutions of the grid near the wall are investigated, resulting in  $y^+ = 20, 45, \text{ and } 85$ . For the discretisation schemes, the *Gamma* scheme [46] and *central-difference* are used for the convection terms and diffusion terms, respectively.

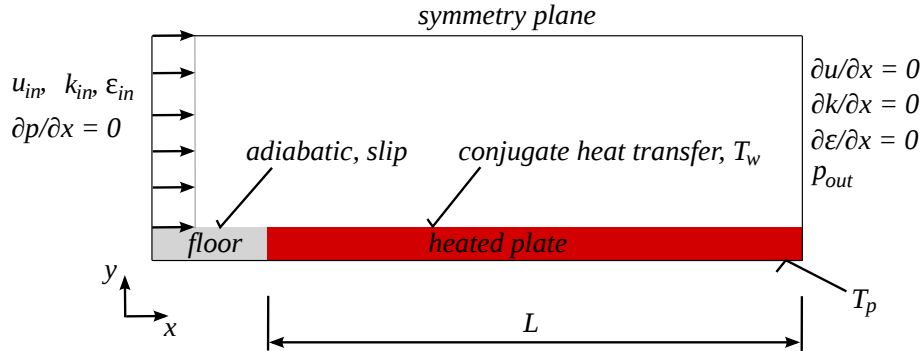


Figure 5.5: Set-up for the simulation of forced convection at a flat heated plate

Two cases are investigated: (i) a constant plate temperature without conjugate heat transfer ( $T_w = T_p$ ), and (ii) a constant temperature of the bottom of the plate,  $T_p$ , enabling conjugate heat transfer at the fluid-solid (plate) interface. The first case should allow for assessment of performance of the implemented wall functions for the temperature, whereas the second case should allow for estimation of the behaviour of the model for simulation of conjugate heat transfer. The numerically-obtained Nusselt number, reading

$$Nu = \frac{q_w L}{\lambda(T_p - T_\infty)}, \quad (5.36)$$

is compared with the semi-empirical correlation for the forced convection at a heated plate for  $Re > 5 \cdot 10^5$ , reading [33]

$$Nu = \frac{0.037Re^{0.8}Pr}{1 + 2.443Re^{-0.1}(Pr^{2/3} - 1)}. \quad (5.37)$$

For the analysed problem Eqn. (5.37) gives  $Nu = 1258$ . In Tab. 5.2 the numerical results are summarised comparing results for the cases of a constant value of  $\sigma_t = 0.85$  in the boundary layer (Eqn. (5.28)) and for the case of applying temperature wall-functions (Eqns. (5.29) and (5.30)). For the calculation of  $Nu$  the wall-heat flux averaged over the total length is used.

$y^+$	<i>constant <math>\sigma_t</math></i>		<i>wall functions</i>	
	$Nu$	error (%)	$Nu$	error (%)
20	1204	4	1215	3
45	1150	9	1190	5
$(T_w = T_p)$ 45	1188	6	1230	2
80	1091	13	1152	8

Table 5.2: Prediction of the Nusselt number applying a constant  $\sigma_t$  and temperature wall-functions compared with the correlation Eqn. (5.37) (for  $T_w = T_p$  a constant temperature over the thickness of the plate is prescribed)

Results for a constant temperature over the thickness of the plate obtained with the application of temperature wall-functions show best agreement with the correlation (Eqn. (5.37)). In this case, the deviation from Eqn. (5.37) of 2 % exhibits a satisfactory result. For the cases where conjugate heat transfer is activated, lower  $Nu$  are predicted than in the previous case due to convective cooling at the plate surface resulting in  $T_w < T_p$ , and thus in a lower  $q_w$  (see Fig. 5.6 for  $y^+ = 45$ ). Moreover, it can be seen that using temperature wall-functions lead to a lower variation of results with respect to  $y^+$  than assuming a constant  $\sigma_t$  in the boundary layer due to the consideration of the wall distance in the calculation of  $\alpha_{eff,w}$  in Eqns. (5.29) and (5.30). This fact brings the great advantage of a reasonable prediction of the heat transfer to walls with varying  $y^+$ , as encountered in a tunnel fire in consequence of changing flow and thermal conditions at different longitudinal positions in the tunnel.

### 5.2.3 Buoyancy modifications of the standard $k$ - $\varepsilon$ model

The driving force of a fire-induced fluid flow mainly comes from buoyancy effects stemming from large density gradients. In order to predict the spreading and propagation of hot combustion gases in case of a fire event accurately, the influence of buoyancy on turbulence production has to be taken into account. The fact that the standard  $k$ - $\varepsilon$  model underestimates these effects, a buoyancy augmentation is necessary. It is characterised by additional source terms in the transport equations for  $k$  and  $\varepsilon$ , yielding [67]

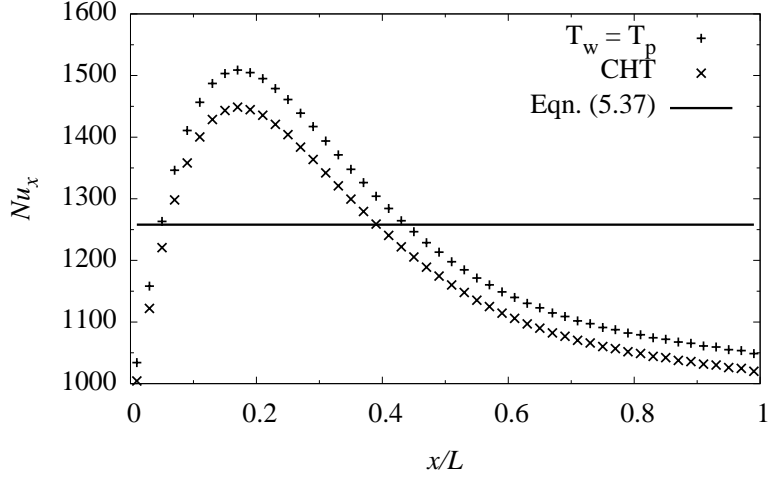


Figure 5.6: Distribution of the local Nusselt number,  $Nu_x$ , for a constant plate temperature ( $T_w = T_p$ ) and enabled conjugate heat transfer (CHT) for  $y^+ = 45$  and the use of temperature wall-functions compared with the averaged  $Nu$  (Eqn. (5.37))

$$\frac{\partial}{\partial t} (\bar{\rho}k) + \frac{\partial}{\partial x_i} (\bar{\rho}u_i k) = \frac{\partial}{\partial x_i} \left[ \left( \mu + \frac{\mu_t}{\sigma_k} \right) \frac{\partial k}{\partial x_i} \right] + P + G + \bar{\rho}\varepsilon, \quad (5.38)$$

and

$$\frac{\partial}{\partial t} (\bar{\rho}\varepsilon) + \frac{\partial}{\partial x_i} (\bar{\rho}u_i \varepsilon) = \frac{\partial}{\partial x_i} \left[ \left( \mu + \frac{\mu_t}{\sigma_\varepsilon} \right) \frac{\partial \varepsilon}{\partial x_i} \right] + C_1 \frac{\varepsilon}{k} P + C_1 \frac{\varepsilon}{k} (1 - C_3) G - C_2 \bar{\rho} \frac{\varepsilon^2}{k}, \quad (5.39)$$

including the turbulence production due to buoyancy,  $G$ . In the literature, buoyancy modifications are mainly based on two approaches of calculating the additional source terms: (i) the *Simple Gradient Diffusion Hypothesis (SGDH)* which only considers the density gradient aligned with the gravitational acceleration, and (ii) the *Generalised Gradient Diffusion Hypothesis (GGDH)* [22] which also includes lateral density gradients. The turbulence production due to buoyancy effects is defined as [86]

$$G = \frac{\overline{\rho' u_i'}}{\bar{\rho}} \left( \frac{\partial \bar{p}}{\partial x_i} + \rho_\infty g_i \right). \quad (5.40)$$

Since  $|\partial \bar{p} / \partial x_i| \ll \rho_\infty g_i$ , the pressure derivative can be neglected, whereas the term  $\overline{\rho' u_i'}$  requires modelling, which can be effectuated by either the SGDH or the GGDH approach, reading

$$(\overline{\rho' u_i'})_{SGDH} = -g_i \frac{\mu_t}{\sigma_t} \frac{1}{\bar{\rho}} \frac{\partial \bar{\rho}}{\partial x_i} \quad (5.41)$$

and

$$\overline{(\rho' u_i')}_{GGDH} = -\frac{3}{2} g_i \frac{\mu_t}{\sigma_t} \frac{1}{\bar{\rho} k} \left( \overline{u_i' u_j'} \frac{\partial \bar{\rho}}{\partial x_j} \right), \quad (5.42)$$

respectively, with no summation over  $i$ . It is suggested in [86] to replace the turbulent normal stress  $\overline{u_k' u_k'}$  in Eqn. (5.42) with  $k$  due to the poor prediction of turbulent normal stresses with  $k$ - $\varepsilon$  models. Inserting Eqns. (5.41) and (5.42) into Eqn. (5.40), respectively, finally yields

$$G_{SGDH} = -g_i \frac{\mu_t \rho_\infty}{\sigma_t \bar{\rho}^2} \frac{\partial \bar{\rho}}{\partial x_i} \quad (5.43)$$

and

$$G_{GGDH} = -\frac{3}{2} g_i \frac{\mu_t \rho_\infty}{\sigma_t \bar{\rho}^2 k} \left( \overline{u_i' u_j'} \frac{\partial \bar{\rho}}{\partial x_j} \right), \quad (5.44)$$

respectively. Within the underlying analyses, the following model constants are used:  $C_1 = 1.44$ ,  $C_2 = 1.92$ ,  $\sigma_k = 1$ ,  $\sigma_\varepsilon = 1.3$ , and  $\sigma_t = 0.85$  and  $C_3 = 0.8$  for the GGDH [86]. In [86],  $C_3 = 0.8$  is also used for the SGDH, whereas in [67] the source term for the turbulent dissipation rate is neglected for stable flow conditions ( $G_{SGDH} < 0$ ), where  $G_{SGDH}$  enters Eqn. (5.39) in the form of  $\max(G_{SGDH}, 0)$  with  $C_3 = 0$ . It is worth mentioning, that different modes of consideration of  $G$  in the  $\varepsilon$ -equation by different authors are reviewed in [86].

Numerous fire codes mentioned in [68] rely on the SGDH buoyancy-modification. In [64], SGDH is used to describe thermal plumes, reporting improved results compared to the standard  $k$ - $\varepsilon$  model in terms of plume-spreading rates whereas in [63], a horizontal non-isothermal jet in a room is simulated applying the SGDH and strong discrepancies between experimental and numerical results are observed. In [86, 92], different forms of buoyancy augmentation are studied in non-reactive flows, suggesting the GGDH for buoyant plumes. Other authors (e.g. [30]) report good results with the SGDH for fire simulations in terms of plume-spreading rates and temperature stratification compared to the standard model. On the other hand, only few investigations using the GGDH for fire simulations can be found. In [94], the GGDH approach is used to determine  $G$ , but also to calculate all turbulent scalar fluxes in the governing equations. The application of this model to a buoyant diffusion flame exhibited excellent agreement with experimental data. In order to work out the performance of the mentioned buoyancy modifications for non-reactive flows, Chapter 5.2.3.1 concentrates on the application of both approaches on a round turbulent buoyant plume. Later in Chapter 5.2.5.3, the SGDH and GGDH buoyancy augmentations in conjunction with a simple combustion model are used to describe a turbulent buoyant diffusion flame.

### 5.2.3.1 Application of buoyancy-modified $k$ - $\varepsilon$ models on a round turbulent buoyant plume

The numerical results obtained with *chtMultiRegionFoam* applying the standard as well as the SGDH and GGDH buoyancy-augmented  $k$ - $\varepsilon$  models are compared with the experimental findings presented in [80] for an isolated, round turbulent plume depicted in Fig. 5.7.

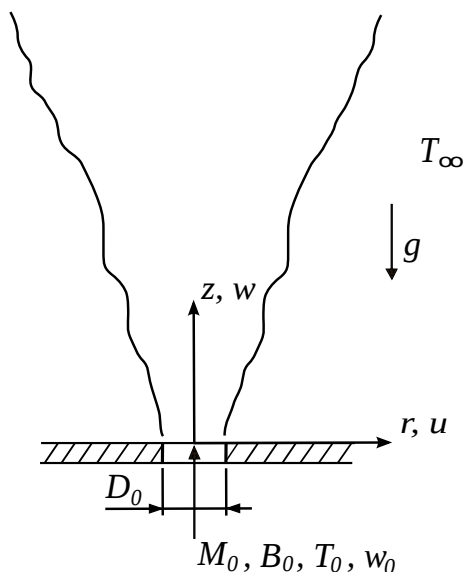


Figure 5.7: Set-up of the plume experiment ( $T_0 > T_\infty$ )

The considered experiments [91] are characterised by hot air ( $T_0 = 573$  K) entering a quiescent environment ( $T_\infty = 302$  K) at a velocity  $w_0 = 0.67$  m/s through a round opening with a diameter  $D_0 = 0.0635$  m. Velocity and temperature profiles were measured at various locations in the area of self-preserving conditions of the plume. In [80], it is reported that self-preserving conditions are reached at  $z/L_M > 5$ , where  $z$  denotes the vertical distance from the source and  $L_M$  the Morton length scale.  $L_M$  characterises the vertical distance from the source, where the momentum created by buoyancy forces surmounts the velocity momentum added at the source and the flow becomes buoyancy-dominated. The Morton length scale is defined as [25]

$$L_M = \frac{M_0^{3/4}}{B_0^{1/2}}, \quad (5.45)$$

with  $M_0$  and  $B_0$  standing for the momentum and the buoyancy, respectively, added at the source ( $z = 0$ ), obtained by

$$M_0 = 2\pi \int_0^{D_0/2} \bar{w}^2 r dr \quad (5.46)$$

and

$$B_0 = 2\pi \frac{g}{\rho_\infty} \int_0^{\frac{D_0}{2}} \bar{w}(\rho_\infty - \rho_0) r dr, \quad (5.47)$$

respectively. In the considered plume experiment  $B_0 = 0.01 \text{ m}^4/\text{s}^3$  and  $L_M = 0.0837 \text{ m}$ . Velocity and temperature profiles of self-preserving plumes are commonly described by Gaussian functions, where the pre-exponential factor and the exponent are determined by curve-fitting the experimental values. For the underlying experiments, this was done for vertical velocity and temperature profiles in the region of  $6.5 < z/L_M < 16$ , giving the following dimensionless correlations [80]:

$$\bar{w} B_0^{-1/3} z^{1/3} = 3.4 e^{-58\eta^2} \quad (5.48)$$

and

$$g\beta\Delta T B_0^{-2/3} z^{5/3} = 9.4 e^{-68\eta^2}. \quad (5.49)$$

In Eqns. (5.48) and (5.49),  $\eta = r/z$  represents the self-similarity variable and  $\Delta T$  denotes the excess temperature  $\bar{T} - T_\infty$ . A similar approach is used to gain correlations for the velocity fluctuations  $w'^2$  and  $u'^2$ , which, together with the assumption that the tangential and radial velocity fluctuations are equal, allow to estimate the specific turbulent kinetic energy  $k$ , reading

$$k = \frac{1}{2} (w'^2 + 2u'^2). \quad (5.50)$$

The best fit of the experiments gives the following non-dimensional expression:

$$k B_0^{-2/3} z^{2/3} = \frac{1}{2} \left[ \frac{(0.65 + 67.35\eta^2 - 227.26\eta^4)}{(1 + 30\eta^2)^4} + 2 \frac{(1.1 + 200\eta^2)}{(1 + 38\eta^2)^4} \right]. \quad (5.51)$$

The described experiments are analysed with the *chtMultiRegionFoam* solving the governing equations for a non-reactive flow (Eqns. (5.8) to (5.10)), where conjugated heat transfer is disabled. The ideal-gas law is used as equation of state and the constant thermo-physical parameters  $c_p = 1000 \text{ J/kg/K}$ ,  $\mu = 1.8 \cdot 10^{-5} \text{ Pa s}$  and  $Pr = 0.7$  are applied. The temperature is derived from the enthalpy using the simple expression  $T = h/c_p$ . For the CFD simulations the following numerical set-up is used:

- **Grid:** an axis-symmetric grid with a domain size of 3 m in axial and 1 m in radial direction is employed. Results are shown for the grid consisting of 10 uniform cells at the source and 70 cells expanding according to a geometric series with a common ratio of  $6^{1/69}$  in the remaining radial direction. In the axial direction, 200 cells are

equally distributed. In order to check for grid-independent results, a coarse and a fine grid are considered in addition, with 40 x 100 and 160 x 400 cells, respectively.

- **Boundary conditions:** at the open boundaries of the domain, *pressureNormalInletOutletVelocity* for velocity and a *fixedValue* of 101325 Pa for pressure  $p_{rgh}$  are prescribed at the side, *inletOutlet* with zero as *inletValue* for velocity and the *buoyantPressure* for  $p_{rgh}$  are considered at the top. Through the *pressureNormalInletOutletVelocity* BC, zero-gradient is applied for outflow, whereas for inflow the velocity is obtained from the flux in direction normal to the boundary face. The *inletOutlet* BC prescribes the *inletValue* for inflow at the boundary, whereas sets the BC to zero-gradient for an outflow. The *buoyantPressure* prescribes the pressure gradient normal to the boundary face, using

$$\frac{\partial p_{rgh}}{\partial n} = -\frac{\partial \rho}{\partial n} (\mathbf{g} \cdot \mathbf{x}_f), \quad (5.52)$$

with  $\mathbf{x}_f$  as the vector pointing to the respective boundary face. At the source, a fixed value of 0.67 m/s is prescribed for velocity and *buoyantPressure* for  $p_{rgh}$ . Values for  $k$  and  $\varepsilon$  at the source are determined with Eqns. (5.33) to (5.35), resulting in values of  $k_0 = 1.7 \cdot 10^{-5} \text{ m}^2/\text{s}^2$  and  $\varepsilon_0 = 2.7 \cdot 10^{-6} \text{ m}^2/\text{s}^3$ , assuming a turbulent intensity of  $Tu_0 = 0.5 \%$  [80] and using  $D_0$  instead of  $L$  for the calculation of the turbulent mixing length [61].  $k = 10^{-6} \text{ m}^2/\text{s}^2$  and  $\varepsilon = 10^{-9} \text{ m}^2/\text{s}^3$  are used for the ambient.

- **Initial conditions:** the ambient has a temperature of 293 K and is at rest.
- **Discretisation:** for the discretisation schemes, the *Gamma* scheme [46] and *central-difference* are used for the convection terms and diffusion terms, respectively.

To obtain a steady-state solution, a transient calculation is conducted until all flow parameters are constant.

It was found that both ways of adding  $G_{SGDH}$  to Eqn. (5.39) for the SGDH (according to [67] ( $C_3 = 0$ ) and [86] ( $C_3 = 0.8$ )) produced identical results. Hence, results with the SGDH approach are shown for the method proposed in [86]. For axial positions of  $z = 1.4, 1.9$  and  $2.4$  m, the radial profiles of mean vertical velocity and mean buoyancy in dimensionless form obtained with the SGDH buoyancy modification coincide with reasonable accuracy as depicted in Figs. 5.8 and 5.9. Hence, self-preserving conditions can be assumed and further results are shown at  $z = 1.4$  m only.

Figs. 5.10 and 5.11 compare numerical results for the radial profiles obtained with the different buoyancy-modifications to the correlations given in Eqns. (5.48) and (5.49). The GGDH buoyancy-augmented turbulence model predicts the plume widths and the peak values for the velocity and buoyancy profiles with higher accuracy compared to the standard turbulence model or the SGDH approach. Tab. 5.3 lists peak values and



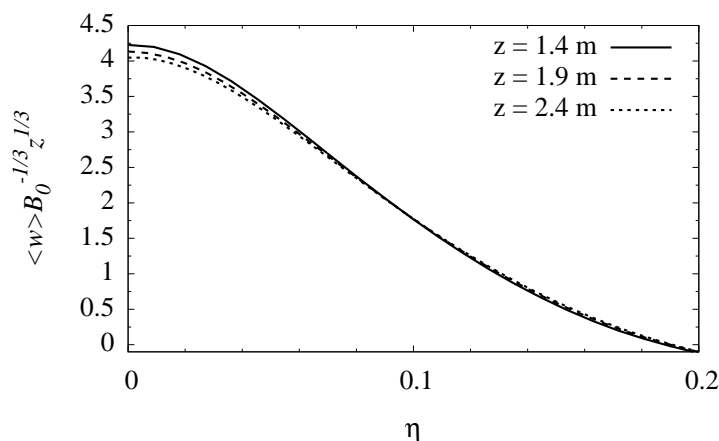


Figure 5.8: Non-dimensional vertical mean velocity profile at different axial positions obtained from the SGDH buoyancy modification ( $\langle w \rangle = \bar{w}$ )

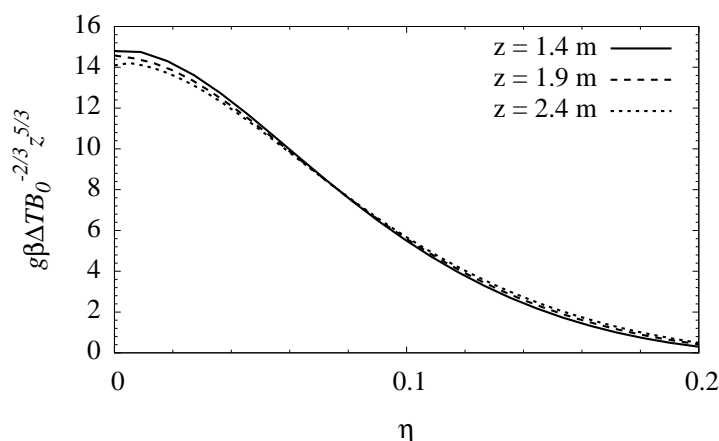


Figure 5.9: Non-dimensional mean buoyancy profile at different axial positions obtained from the SGDH buoyancy modification

half-widths (i.e the point  $\eta = r/z$  where half of the center-line value is reached) for both profiles, also illustrating the improved performance of the GGDH approach. Little difference in results is obtained with the standard and the SGDH model which was also concluded in [86, 92]. The radial distribution of relative and total production of  $k$  (Fig. 5.12) shows a lower total production for GGDH due to lower velocity gradients and a wider radial distribution (see also Fig. 5.10), but a higher importance of  $G$  than in the case of the SGDH model resulting in wider plume widths.

An interesting result is the prediction of the radial distribution for the specific turbulent kinetic energy,  $k$ , depicted in Fig. 5.13, as it is in contrast to the findings presented in [86], where the same plume experiments with the same buoyancy-modified  $k$ - $\varepsilon$  models were investigated. In [86], all the analysed models underpredict  $k$ , whereas the present study shows good agreement of the numerical results with the experimental data (see Fig. 5.13).

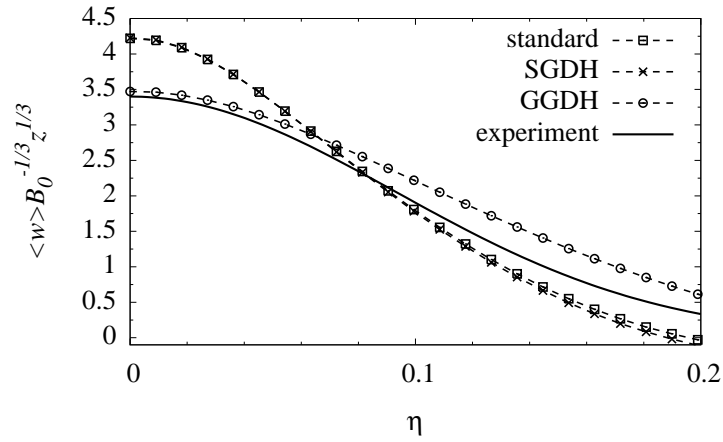
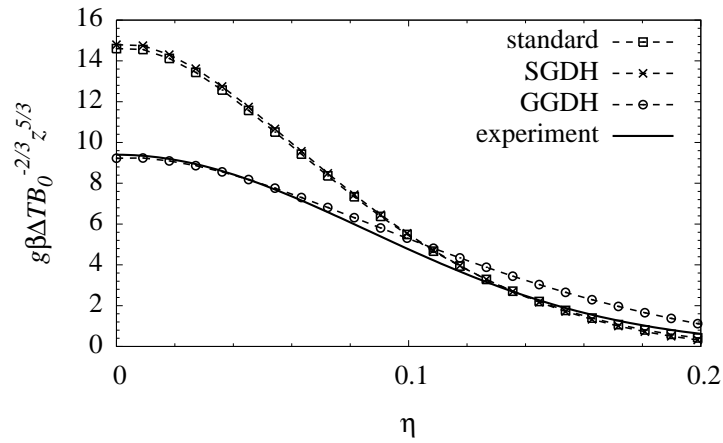
Figure 5.10: Non-dimensional radial profile of mean vertical velocity ( $\langle w \rangle = \bar{w}$ )

Figure 5.11: Non-dimensional radial profile of mean buoyancy

	$(\bar{w} B_0^{-1/3} z^{1/3})_c$	$\eta_{w/2}$	$(g\beta\Delta T B_0^{-2/3} z^{5/3})_c$	$\eta_{T/2}$
experiment	3.40	0.109	9.40	0.101
standard	4.22	0.089	14.61	0.082
SGDH	4.23	0.088	14.80	0.082
GGDH	3.47	0.126	9.23	0.112

Table 5.3: Peak values and half-widths of dimensionless mean vertical velocity and buoyancy profiles ( $\eta_{w/2}$  and  $\eta_{T/2}$ )

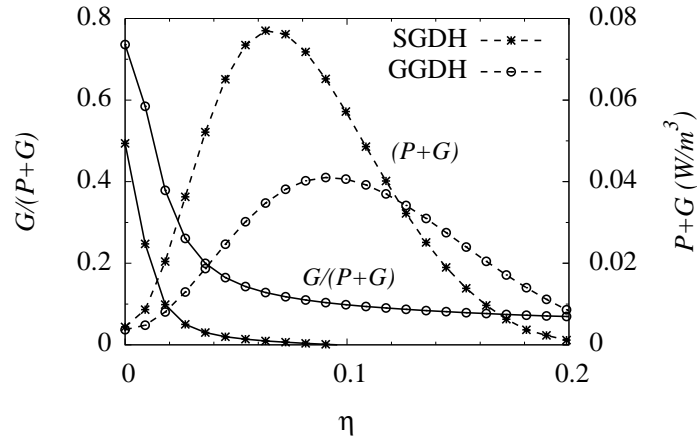


Figure 5.12: Radial distribution of relative (*solid lines*) and total (*dashed lines*) turbulence production

On the other hand, discrepancies are observed between the predicted turbulent normal stresses in vertical and radial directions,  $\overline{u'u'}$  and  $\overline{w'w'}$ , respectively (see Figs. 5.14 and 5.15). Like in [86], both normal turbulent stresses are of same magnitude, which is not seen in the experiments, and thus justifies the substitution of  $\overline{w'w'}$  with  $k$ . Furthermore, in the underlying investigation higher normal turbulent stresses than in [86] are predicted, leading to higher values of  $k$ . This is in consequence of higher turbulence production due to velocity gradients,  $P$ , in the present study, as in [86] lower absolute turbulence production (though no units are given) and higher relative turbulence production at the centre line than observed in the present simulations, are reported.

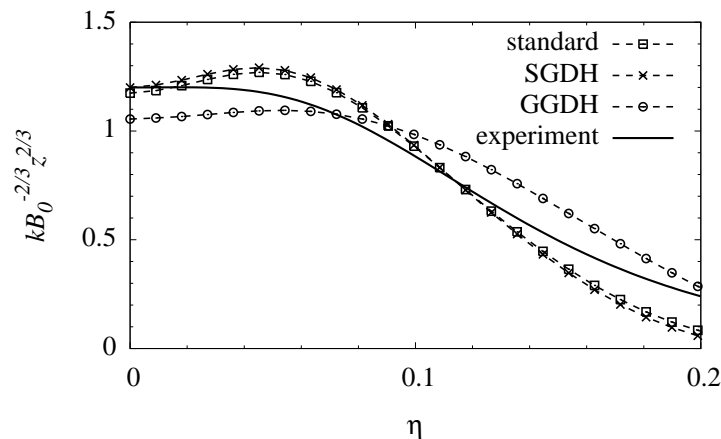


Figure 5.13: Non-dimensional radial profile of specific turbulent kinetic energy

From the presented results, the GGDH buoyancy modification shows promising behaviour for fire simulations. Its performance to predict the flow of a turbulent diffusion flame is discussed later (see Chapter 5.2.5.3).

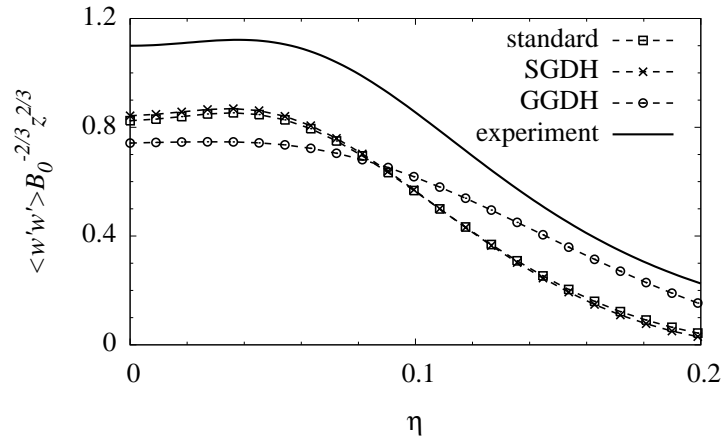


Figure 5.14: Non-dimensional profile of vertical turbulent normal stresses ( $\langle w'w' \rangle = \overline{w'w'}$ )

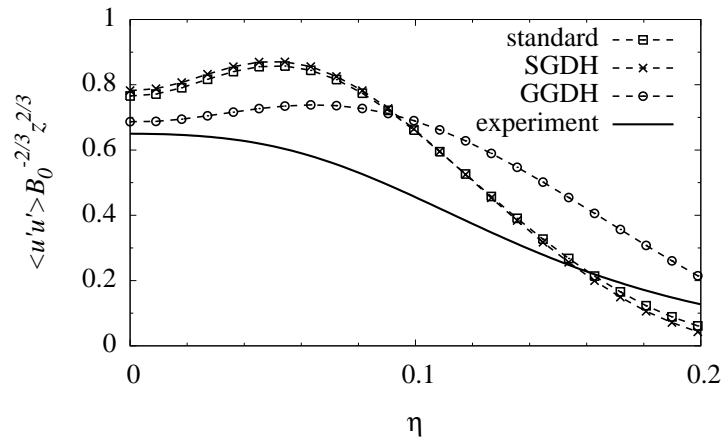


Figure 5.15: Non-dimensional profile of radial turbulent normal stresses ( $\langle u'u' \rangle = \overline{u'u'}$ )

## 5.2.4 Radiative heat transfer

Real-scale experiments and analyses of fires in tunnels revealed that radiation represents an important mode of heat transfer during fire accidents [35, 55]. The thermal energy is transferred through both convection and radiation with an increasing fraction of radiation at large temperatures, typically above 400 °C [26]. Thermal radiation involves heat transfer by electromagnetic waves, and is thus not bounded to a medium like a fluid in case of convection. Consequently, incident radiation from the far field can have a significant effect even if the local gas temperature is not high. As mentioned in Chapter 2.1, the radiation feedback, which pre-dominantly comes from the flame itself and the hot gases collected under the tunnel ceiling, is the main parameter governing ignition and flame spread.

From the explanations above it can be concluded that radiation must be taken into account

when investigating fires in underground structures and specially when it comes to predicting the heat transfer into the load-carrying structure. Hence, two procedures of treating thermal radiation within a participating medium currently available in OpenFOAM, i.e. the P1-approximation and the *Finite Volume Discrete Ordinate Method (fvDOM)* are analysed by means of two problems for which accurate solutions exist. The superior of the two treatments is then incorporated into the *chtMultiRegionFoam* solver, including the effect of radiation on the conjugate heat transfer.

#### 5.2.4.1 The P1-approximation and the Finite Volume Discrete Ordinate Method

For the following two benchmark analyses, the transfer of thermal radiation is considered in a participating medium neglecting scattering and the dependency of the radiation properties on the wave number (*grey gas*). Furthermore, the surfaces enclosing the medium consist of opaque, diffusely emitting and diffusely reflecting grey walls. The governing equation for the transport of radiative intensity,  $I(\mathbf{x}, \mathbf{s})$ , along the path  $\mathbf{s}$  within such a medium reads [62]

$$\mathbf{s} \cdot \nabla I(\mathbf{x}, \mathbf{s}) = a [I_b(\mathbf{x}) - I(\mathbf{x}, \mathbf{s})], \quad (5.53)$$

and is called the *Radiative Transfer Equation (RTE)*.  $a$  and  $I_b(\mathbf{x})$  denote the absorption coefficient and the black-body intensity, respectively. Eqn. (5.53) implicates radiative equilibrium as the emission coefficient of the medium is equal to the absorption coefficient. The net contribution of radiative energy into each volume element, as it appears as additional source term in the energy equation (Eqns. (5.10) or (5.11)), is expressed by the negative divergence of the specific radiative heat-flux vector, reading

$$-\nabla \cdot \mathbf{q}_R(\mathbf{x}) = a [G(\mathbf{x}) - 4\pi I_b(\mathbf{x})]. \quad (5.54)$$

The incident radiative energy,  $G(\mathbf{x})$ , is calculated by integrating  $I(\mathbf{x}, \mathbf{s})$  over all solid angles,  $\Omega$ , using

$$G(\mathbf{x}) = \int_{4\pi} I(\mathbf{x}, \mathbf{s}) d\Omega. \quad (5.55)$$

The approach of the P1-approximation belongs to the method of spherical harmonics. Within the method of spherical harmonics, the radiative intensity is expressed as a two-dimensional (in  $\mathbf{x}$  and  $\mathbf{s}$ ) generalised Fourier series using spherical harmonics in order to convert the RTE into simple partial differential equations. The approximation is introduced by truncating the Fourier series after a few terms to simplify the problem, where the P1-approximation represents the approximation of lowest order. Substituting the truncated Fourier series into the RTE, finally yields a transport equation for  $G(\mathbf{x})$ , reading [62]

$$\nabla \cdot \left[ \frac{1}{3a} \nabla G(\mathbf{x}) \right] = a [G(\mathbf{x}) - 4\pi I_b(\mathbf{x})]. \quad (5.56)$$

As BC, the *Marshak's* BC is applied, which reads

$$\frac{1}{3a} \mathbf{n} \cdot \nabla G(\mathbf{x}) = \frac{\epsilon}{2(2 - \epsilon)} [G(\mathbf{x}) - 4\pi I_{bw}], \quad (5.57)$$

where  $\epsilon$  stands for the surface emissivity. The radiative wall-heat flux,  $q_{Rw}$ , can then be derived, yielding

$$q_{Rw} = \frac{\epsilon}{2(2 - \epsilon)} [4\pi I_{bw} - G(\mathbf{x})]. \quad (5.58)$$

The fvDOM applies FVM to discretise the RTE [77], and thus fits well with FVM in CFD. Similar to the spatial discretisation, the solid angle domain of  $4\pi$  is divided into  $N$  discrete directions,  $\mathbf{s}_i$ , and the RTE is discretised and solved for each direction. The BC is developed from an energy balance of radiative energy, which reads for directions leaving the boundary face (corresponding to  $\mathbf{s}_i \cdot \mathbf{n} > 0$ ) [62]

$$I_w = \frac{\epsilon I_{bw} + (1 - \epsilon) \sum_{i,in} I_i |\mathbf{s}_i \cdot \mathbf{n}|}{\sum_{i,out} \mathbf{s}_i \cdot \mathbf{n}}, \quad (5.59)$$

and is set to a zero-gradient BC for directions entering the boundary face, corresponding to  $\mathbf{s}_i \cdot \mathbf{n} < 0$ . In Eqn. (5.59),  $I_i$  denotes the intensities leaving the adjacent CVs going into the CV aligned to the considered boundary face.  $I_w$  results from summation of radiative intensities over all directions at the wall. Hence, it corresponds to  $q_{Rw}$ .

A so-called *radiation model* is implemented into OpenFOAM's *chtMultiRegionFoam* solver as an additional sub model solving the RTE according to the method chosen, which is either P1 or fvDOM. Beside the calculation of  $G(\mathbf{x})$ ,  $I(\mathbf{x}, \mathbf{s}_i)$  and  $q_{Rw}$ , the negative divergence of the specific radiative heat-flux vector is determined using Eqn. (5.54) and added to the energy equation (Eqns. (5.10) or (5.11)). Thus, the RTE is solved before entering the energy equation. The user specifies the number of fluid iterations after which the RTE is calculated through the parameter *solverFreq*. For the case *solverFreq* = 1, the RTE is solved for each fluid iteration.

The two presented approaches to treat thermal radiation are investigated by simulating two benchmark problems: (i) two parallel, infinitely long black and diffuse walls with an emitting and absorbing grey medium in-between, and (ii) an emitting and absorbing grey medium in a 2D rectangular enclosure. Numerical results are compared with analytical solutions presented in [81] and [19], respectively. In the simulation of both benchmark tests, only radiative heat transfer is considered. Hence, the fluid contributes only via absorption and emission with a constant and homogeneous absorption/emission coefficient.

Therefore, conjugate heat transfer is disabled and convection is eliminated by setting the gravitational acceleration vector  $\mathbf{g} = (0 \ 0 \ 0)$  and by switching off the turbulence model. Conduction within the fluid is deactivated by setting the Prandtl number to infinity, finally yielding a zero enthalpy diffusivity.

#### 5.2.4.2 Benchmark test 1: grey medium between two parallel (infinitely long) walls

The set-up used for the analysed benchmark test is depicted in Fig. 5.16, showing two black diffuse walls of  $T_1$  and  $T_2$  (with  $T_1 < T_2$ ) at a distance  $D$ . The numerical simulations are performed in 1D applying a spatial discretisation of 40 cells for both radiation models. For the fvDOM, this results in a solid-angle discretisation of two discrete rays. At the two walls, a *fixedValue* temperature BC with  $T_1$  and  $T_2$  as well as Marshak's BC (*MarshakRadiationFixedT*, see Eqn. (5.57)) and (*greyDiffusiveRadiation*, see Eqn. (5.59)) for  $G$  in case of P1 and  $I$  in case of fvDOM, respectively, are prescribed together with unit emissivity. For the FVM discretisation of the respective equations, linear interpolation is used for  $G$  and a uniform distribution for  $I$  applying the upwind scheme.

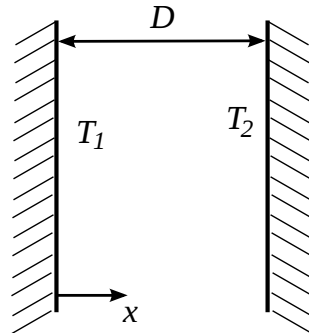


Figure 5.16: Configuration for the benchmark test of a grey medium between two parallel, infinitely long walls [81]

The analytical solution for this problem is taken from [81] and compared with the obtained numerical results. Temperature distributions are depicted in Fig. 5.17 in dimensionless form, using

$$\Phi_b = \frac{T(x)^4 - T_2^4}{T_1^4 - T_2^4}, \quad (5.60)$$

for various values of optical thickness,  $\kappa_D = a \cdot D$ . The solid lines correspond to the simulation whereas the symbols refer to the analytical solution. As expected, the temperature distribution is constant between the walls for the case of a non-participating medium corresponding to  $\kappa_D = 0$ , whereas an increasing temperature gradient is observed with growing  $\kappa_D$  due to higher absorption of radiative energy. Both models show good agreement with the analytical results. Slight deviations from the analytical solution can be

observed for optically thin media using the P1-approximation. This is well known for cases where collimated irradiation is present (see, e.g. [62]). The fvDOM predicts the temperature profiles more accurately. However, for the highest optical thickness  $\kappa_D = 10$ , it was necessary to solve the RTE after each flow iteration, corresponding to  $solverFreq = 1$ , instead of after each tenth in order to obtain accurate results.

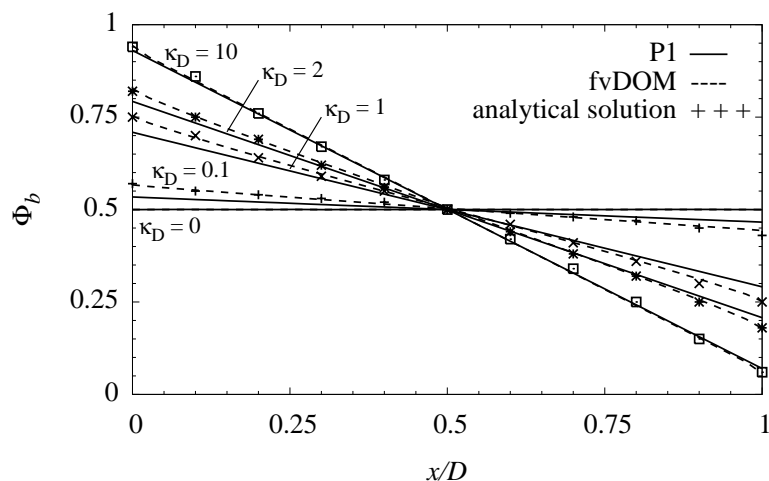


Figure 5.17: Distributions of dimensionless temperature (Eqn. (5.60)) using the P1-approximation and the fvDOM for different values of  $\kappa_D$

The wall-heat flux represents an important quantity when it comes to predicting the heat transfer from the fluid to the solid wall realistically. Hence, this quantity is shown in Fig. 5.18 in dimensionless form, using

$$\Psi_b = \frac{q_{Rw}}{\sigma_{SB}(T_1^4 - T_2^4)}, \quad (5.61)$$

for different values of optical thickness,  $\kappa_D$ , with  $\sigma_{SB} = 5.67 \cdot 10^{-8} \text{ W/m}^2/\text{K}^4$  as the Stefan-Boltzmann constant. It is obvious that the heat flux of the two side walls has to be equal at the state of radiative equilibrium. This is observed in the numerical results for both models. Again both models show good agreement with the analytical results as it is expected for the simple problem of two parallel walls. However, the P1-approximation slightly over-predicts the heat flux for lower optical thicknesses and shows improving accuracy with increasing  $\kappa_D$  as shown in Fig. 5.18.

### 5.2.4.3 Benchmark test 2: grey gas in a 2D rectangular enclosure

In the following, the benchmark test of a 2D rectangular medium exposed to diffuse radiation  $I_D = 1 \text{ W/m}^2$  at the top of the domain is studied (see Fig. 5.19). This problem was investigated in [19], where the integral equation for radiative transfer is solved numerically by removing the singularity, yielding accurate results. Similarly to the previous



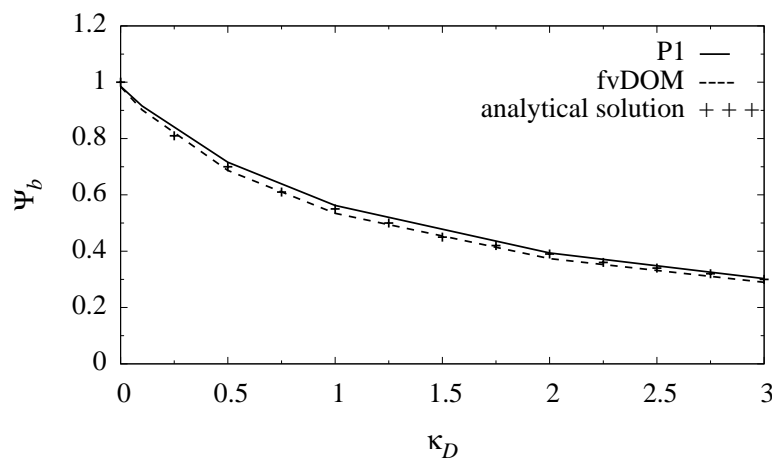


Figure 5.18: Dimensionless specific radiative wall-heat flux (Eqn. (5.61)) as a function of  $\kappa_D$  using the P1-approximation and the fvDOM

benchmark test, the absorbing and emitting medium is characterised by a constant and homogeneous absorption/emission coefficient. In [19], the solution is given for the case of black surfaces ( $\epsilon = 1$ ), where all walls are free of thermal load except for the top wall. In the simulations, wall temperatures equal to zero result in a division by zero, thus they are set to 1 K. For the wall at the top, a temperature of  $T_w = 86.28$  K is prescribed, derived from the Stefan-Boltzmann law, reading

$$T_w = \left( \frac{\pi I_D}{\sigma_{SB}} \right)^{1/4}, \quad (5.62)$$

in order to realise a fixed intensity  $I_D = 1$  W/m<sup>2</sup>. BCs for  $G$  are Marshak's BC (*MarshakRadiation*, see Eqn. (5.57)) and Eqn. (5.59) (*greyDiffusiveRadiation*) for  $I$ . The sensitivity analysis with respect to grid size suggests a constant grid size in all coordinate directions of 0.0125 m for both radiation models. A solid-angle discretisation and of 24 discrete rays is applied for the fvDOM-model. For the FVM discretisation of the respective equations, linear interpolation is used for  $G$  and upwind for  $I$ .

While in the example of two parallel walls the optical thickness was varied and the geometry kept constant, the optical thickness in vertical direction is kept constant in this benchmark test with  $\kappa_{z0} = a \cdot z_0 = 1$  and the aspect ratio  $r = 2y_0/z_0$  is varied in order to investigate the influence of changing geometries.

The vertical temperature distribution in non-dimensional form in the center of the enclosure ( $y = 0$ ), using

$$\Phi_b = \frac{\sigma_{SB} T(z)^4}{\pi I_D}, \quad (5.63)$$

is depicted in Fig. 5.20 for different aspect ratios,  $r$ . A small value for  $r$  results in a

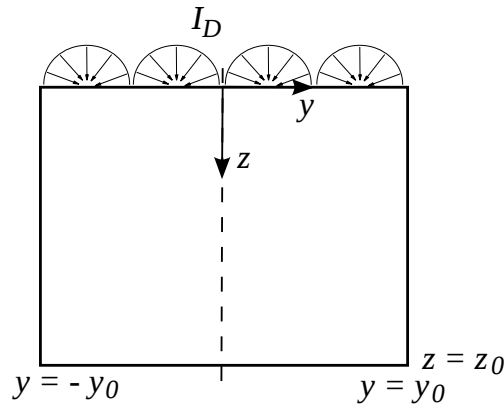


Figure 5.19: Geometry and coordinate system of rectangular medium exposed to diffuse radiation [19]

column-shaped enclosure whereas great aspect ratios correspond to a slab approaching the result of a 1D problem. As already observed in the previous example, results produced with the fvDOM are more accurate than those obtained with the P1-approximation. It is worth mentioning that the numerical results mainly deviate from the results given in [19] in the region close to the wall with prescribed radiation. These differences are greater with decreasing aspect ratio  $r$  as for great values of  $r$  the situation approaches the configuration of the previous benchmark test, where both radiation models yielded good agreement with the analytical solution.

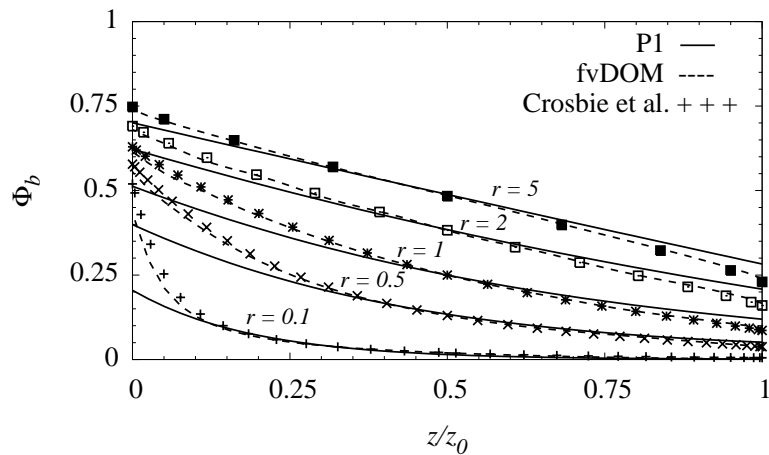


Figure 5.20: Distributions of dimensionless temperature (Eqn. (5.63)) in the center of the domain using the P1-approximation and the fvDOM for different values of  $r = 2y_0/z_0$

The non-dimensional specific heat fluxes along the side and bottom wall, using

$$\Psi_b = \frac{q_{Rw}}{\pi I_D}, \quad (5.64)$$

are plotted in Figs. 5.21 and 5.22 for different aspect ratios,  $r$ . The results obtained with the fvDOM show excellent agreement with [19] for profiles both along the side and bottom wall, where at the bottom wall small oscillations for  $r = 0.1, 0.5$  and  $1$  are observed. This can be attributed to the so-called *ray effect*, which is related to the solid-angle discretisation and is a well-known deficiency of the fvDOM (see, e.g. [78]). The P1-approximation has problems in predicting wall-heat fluxes accurately. The heat flux along the side wall is strongly over-estimated. For small aspect ratios like in the case of  $r = 0.1$ , better agreement with the solution presented in [19] is observed, where the influence of the top wall is small and the results are more accurate with increasing distance from the top. For the case where contributions from the top wall gain importance (e.g., for  $r = 5$ ), the P1-approximation fails to produce accurate results. On the other hand, profiles for the bottom-flux agree well with the results given in [19]. Hence, it can be concluded that for the analysed problem, the P1-approximation shows difficulties in predicting wall-heat fluxes in case of incident radiation from non-parallel walls with a local source. This is in agreement with explanations on the limitation of the P1-approximation found in [79].

In both benchmark tests, the fvDOM exhibits excellent agreement with the reference solutions for temperatures and wall-heat fluxes. Consequently, the fvDOM is chosen as sub model to be implemented to account for radiative heat transfer.

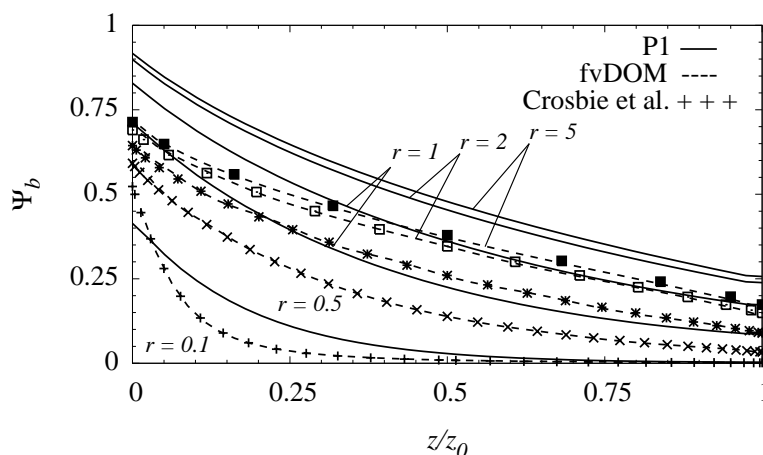


Figure 5.21: Dimensionless specific radiative heat flux (Eqn. (5.64)) at side wall using the P1-approximation and the fvDOM for different values of  $r = 2y_0/z_0$

#### 5.2.4.4 Conjugate heat transfer considering radiation

In the treatment of conjugate heat transfer presented in Chapter 5.2.2 the radiative wall-heat flux,  $q_{Rw}$ , is not taken into account. Usually,  $q_{Rw}$  needs to be added on the fluid side of Eqn. (5.25) (see Fig. 5.4) in order to consider radiative heat transfer at the solid-fluid interface, resulting in an expression for the common wall temperature, reading

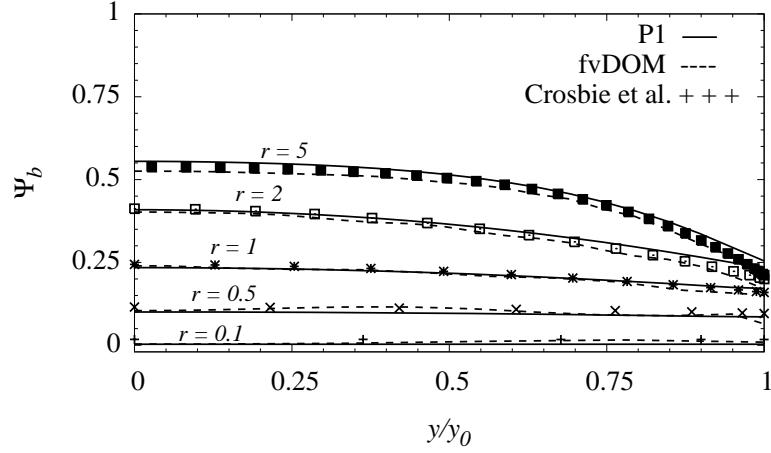


Figure 5.22: Dimensionless specific radiative heat flux (Eqn. (5.64)) at bottom wall using the P1-approximation and the fvDOM for different values of  $r = 2y_0/z_0$

$$T_w = \frac{T_E (\lambda_s/\delta x_s) + T_P (\lambda_f/\delta x_f) + q_{Rw}}{(\lambda_s/\delta x_s) + (\lambda_f/\delta x_f)}, \quad (5.65)$$

where  $q_{Rw} > 0$  and  $q_{Rw} < 0$  indicate an incoming and outgoing heat flux to the wall, respectively. Numerical experiments show that the implementation of Eqn. (5.65) into the standard OpenFOAM BC for conjugate heat transfer gives reasonable results for small temperatures. On the other hand, numerical instabilities are encountered with an increase of radiative heat fluxes reaching the wall, which leads to unrealistic temperature predictions. A numerically more stable behaviour is observed with the method proposed in [4, 54], where the radiative contribution is not used to calculate  $T_w$  but is added as source term to the energy equation at both the fluid and solid side (Eqns. (5.10) or (5.11) and (4.13), respectively) at control volumes adjacent to the solid-fluid interface. In the present case,  $T_w$  is determined using Eqn. (5.26) and the radiative heat source on the fluid side is taken into account via Eqn. (5.54). In the solid region, the volumetric heat source is then calculated using

$$S_T = \frac{q_{Rw} S_f}{\Delta V}, \quad (5.66)$$

with  $S_f$  and  $\Delta V$  as the surface area the control volume shares with the wall and the control volume's volume, respectively. In order to investigate the described method considering radiation in the conjugate heat transfer, the example of a heated plate discussed in Chapter 5.2.2.1 is re-analysed with the adaption of the model described above. A constant plate temperature of  $T_p = 700$  K is prescribed and a constant absorption coefficient of the fluid,  $a = 2 \text{ m}^{-1}$ , is considered. The distributions of interface temperatures for two different values of surface emissivity ( $\epsilon = 0.3$  and  $0.8$ ) are depicted in Fig. 5.23. The solid

lines correspond to results obtained with the presented method considering radiation in the conjugate heat transfer (curves indicated by  $T_w$ ). These curves are compared to temperatures calculated using Eqn. (5.65) during the simulation (curves indicated by  $T_{w,rad}$ ). As expected, higher interface temperatures are observed with a smaller emissivity due to reduced cooling in consequence of radiation. This effect is even stronger in case the radiative wall-heat flux is not taken into account in the treatment of conjugate heat transfer, corresponding to  $q_{Rw} = 0$  in Eqn. (5.66) (indicated by the line with *no radiation* in Fig. 5.23). Furthermore, Fig. 5.23 shows negligible differences between  $T_w$  and  $T_{w,rad}$ . During the simulations, the same behaviour was observed for variations of other parameters such as the absorption coefficient.

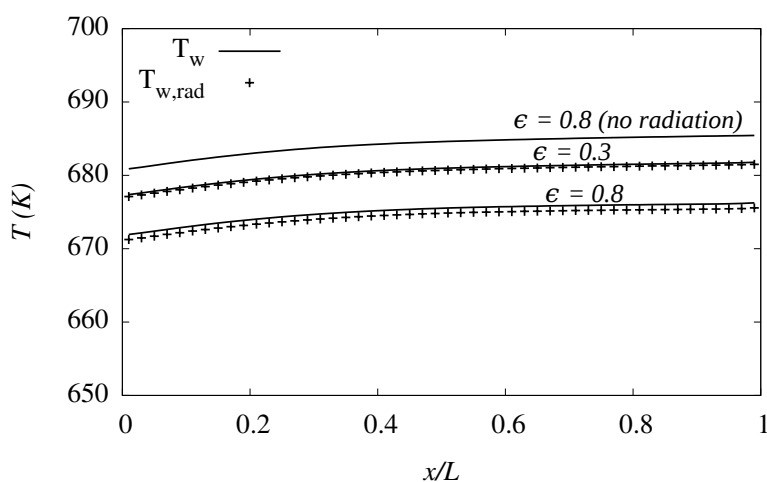


Figure 5.23: Interface temperatures of a heated flat plate (see Fig. 5.5) considering radiation in the treatment of conjugate heat transfer for two different surface emissivities ( $T_{w,rad}$  is calculated using Eqn. (5.65) and *no radiation* corresponds to  $q_{Rw} = 0$  in Eqn. (5.66))

### 5.2.5 Combustion model

It was mentioned in Chapter 2 that the type of combustion encountered in a fire accident is characterised by a buoyancy dominated, turbulent diffusion flame where there is a strong interaction between combustion and turbulence. The heat released by the fire is responsible for the thermal expansion of the fluid and induces the buoyancy driven flow. With an increasing Reynolds number the transition to a turbulent flow happens. On the other hand, the turbulent eddies enhance the mixing of fuel and oxidiser at a molecular level which in turn intensifies the combustion process. In combustion modelling, when the chemical time scales are much smaller than the mixing-time scale, combustion is assumed to be mixing-controlled. Consequently, chemical processes can be considered to happen infinitely fast in a single step where the reaction occurs once fuel and oxidiser mix (*mixed-is-burnt*), reading

$$1 \text{ kg fuel} + s \text{ kg oxidiser} \rightarrow (1 + s) \text{ kg products}, \quad (5.67)$$

with  $s$  representing the stoichiometric mass ratio of oxidiser (air),  $m_o$ , and fuel,  $m_{fu}$ , reading

$$s = \left( \frac{m_o}{m_{fu}} \right)_{st}. \quad (5.68)$$

This assumption significantly simplifies the analysis of combustion avoiding the resolution or modelling of chemical time scales.

In the underlying investigation the fire is modelled by a buoyant turbulent diffusion flame which is fed by a prescribed mass flow of fuel corresponding to a HRR-time curve of the fire (see Chapter 3). The prediction of the effective amount of released heat and the approximate shape of the flame must be reflected by the chosen combustion model, whereas the resolution of chemical processes is not a main focus. A description of different combustion models used in fire engineering can be found in [67, 93, 95]. Based on OpenFOAM's *fireFoam*, the approach of a conserved scalar, the mixture fraction,  $\bar{Z}$ , is followed, similar to most of the codes presented in Tab. 5.1.  $\bar{Z}$  describes the local ratio of fuel and oxidiser, defined as [88]

$$\bar{Z} = \frac{s\bar{Y}_{fu} - \bar{Y}_o + 1}{1 + s}, \quad (5.69)$$

and has to satisfy the respective transport equation, reading

$$\frac{\partial}{\partial t} (\bar{\rho}\bar{Z}) + \frac{\partial}{\partial x_i} (\bar{\rho}u_i\bar{Z}) = \frac{\partial}{\partial x_i} \left[ \left( \bar{\rho}\mathcal{D} + \frac{\mu_t}{\sigma_t} \right) \frac{\partial \bar{Z}}{\partial x_i} \right]. \quad (5.70)$$

$\bar{Z} = 1$  and  $\bar{Z} = 0$  correspond to the case of a CV consisting solely of fuel and oxidiser, respectively. With the simplification of infinitely fast chemical processes, the thermo-chemical state of the fluid can be related to  $\bar{Z}$  as depicted in Fig. 5.24.

The prediction of the mean consumption rate of fuel,  $\bar{R}_{fu}$ , is incorporated in *fireFoam* based on the *Eddy Dissipation Model (EDM)* presented in [57]. The EDM assumes that the reaction occurs at the smallest scales of turbulence, i.e. at the fine structures where the turbulent energy is transferred into heat through viscous dissipation (see Chapter 5.2.1). For the case of a mixing-controlled combustion, the reaction rate is proportional to the time scale of turbulent dissipation,  $k/\varepsilon$ , which is closely related to molecular mixing. Hence, the mean consumption rate of fuel is directly modelled, using [57]

$$\bar{R}_{fu} = -11.2\bar{\rho}\frac{\varepsilon}{k} \frac{\chi}{(1 - \gamma^*\chi)} \min\left(\bar{Y}_{fu}, \frac{\bar{Y}_o}{s}\right). \quad (5.71)$$

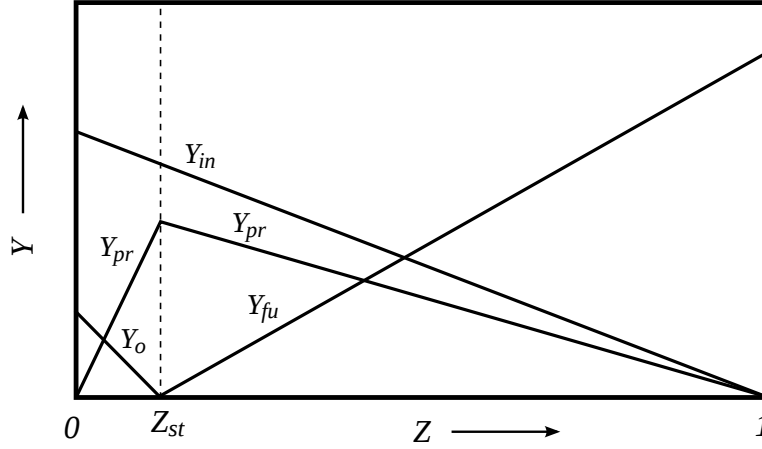


Figure 5.24: State relationships for the limit of infinitely fast, one-step chemical processes (*fu*: fuel, *o*: oxidiser, *pr*: products, *in*: inert, *st*: stoichiometric) [95]

The reaction fraction of fine structures,  $\chi$ , introduces the product mass fraction as a limiting species, reading

$$\chi = \frac{\bar{Y}_{pr}/(1+s)}{\min(\bar{Y}_{fu}, \bar{Y}_o/s) + \bar{Y}_{pr}/(1+s)}, \quad (5.72)$$

where in [95],  $\chi = 1$  is suggested for diffusion flames which is also used hereafter. The mass fraction of the fine structure region,  $\gamma^*$ , is calculated as

$$\gamma^* = 4.6 \left( \frac{\nu \varepsilon}{k^2} \right)^{1/2}. \quad (5.73)$$

Additionally, a transport equation for the fuel-mass fraction  $\bar{Y}_{fu}$  is solved, reading

$$\frac{\partial}{\partial t} (\bar{\rho} \bar{Y}_{fu}) + \frac{\partial}{\partial x_i} (\bar{\rho} u_i \bar{Y}_{fu}) = \frac{\partial}{\partial x_i} \left[ \left( \bar{\rho} \mathcal{D} + \frac{\mu_t}{\sigma_t} \right) \frac{\partial \bar{Y}_{fu}}{\partial x_i} \right] + \bar{R}_{fu}, \quad (5.74)$$

where a unity turbulent Lewis number is assumed in both transport equations (Eqns. (5.70) and (5.74)). With the knowledge of  $\bar{Z}$  and  $\bar{Y}_{fu}$ , the term  $\min(\bar{Y}_{fu}, \bar{Y}_o/s)$  in Eqn. (5.71) can be calculated, finally giving the heat released during the combustion process which is represented by the combustion-source term in Eqn. (5.11), reading

$$q_C = -\bar{R}_{fu} \cdot \Delta h_C, \quad (5.75)$$

where  $\Delta h_C$  denotes the heat of combustion of a specific fuel.

To calculate the turbulent flow field in the fluid region including radiation and combustion, the set of Reynolds-averaged equations and the RTE are extended by the transport

equations for  $\bar{Z}$  and  $\bar{Y}_{fu}$  (Eqns. (5.70) and (5.74)), which needs to be solved for each time step in the following order:

1. Velocity predictor: guess a pressure field and solve the Navier-Stokes equations (Eqn. (5.9)) to compute an intermediate velocity field.
2. Solve the transport equations for  $\bar{Z}$  and  $\bar{Y}_{fu}$  (Eqns. (5.70) and (5.74)) with the intermediate velocity field. Compute the combustion source term according to Eqn. (5.75).
3. If the number of flow iterations is a multiple of *solverFreq*, solve the RTE (Eqn. (5.53)) and compute the radiation heat source term according to Eqn. (5.54).
4. Calculate the field of sensible enthalpy (Eqn. (5.11)) with the intermediate velocity field, and the combustion and radiation source terms. Update the temperature field and the thermo-physical properties (see Chapter 5.2.5.1).
5. Enter the PISO-loop (see Chapter 5.2) to calculate the pressure field and to correct the velocity field for the prescribed number of PISO-corrector steps (typically 2).
6. Solve the transport equations for  $k$  and  $\varepsilon$  (Eqns. (5.17) and (5.18)) with the corrected velocity field. Update the eddy viscosity (Eqn. (5.15)) and calculate the effective diffusion coefficients (Eqn. (5.14)).
7. Calculate the density from the equation of state, i.e. the ideal-gas equation.

Preliminary studies showed, that beside the prescribed mass flux an additional amount of fuel entered the domain through diffusion due to the gradients of  $\bar{Z}$  and  $\bar{Y}_{fu}$  at the fuel inlet. Setting the diffusion coefficient of  $\bar{Z}$  and  $\bar{Y}_{fu}$  (i.e.  $\alpha_{eff}$ ) to zero at the patch of fuel inlet, resulted in numerical instabilities. A more elegant way to overcome this problem, is to set the patch value according to the balance of the desired convective flux of the variable at infinity,  $\phi_\infty$ , and the sum of convective and diffusive fluxes at the considered patch. For the transported variable  $\phi$ , the patch value  $\phi_f$  then reads

$$\phi_f = \phi_\infty \frac{|\Phi_f|}{|\Phi_f| + \alpha_{eff,f} S_f / \delta x_f} + \phi_{int} \frac{\alpha_{eff,f} S_f / \delta x_f}{|\Phi_f| + \alpha_{eff,f} S_f / \delta x_f}, \quad (5.76)$$

with  $\Phi_f$  denoting the face flux,  $\phi_{int}$  the cell value of the cell adjacent to the patch and  $\delta x_f$  the distance from the patch to the cell point adjacent to the patch.



### 5.2.5.1 Thermo-physical properties of the fluid mixture

The temperature dependency of the thermo-physical properties of each species  $i$  (fuel, oxidiser and products,  $N = 3$ ) is considered via the functional relationship of specific heat capacity at constant pressure, reading

$$c_{pi} = \frac{\mathcal{R}}{W_i} \sum_{n=1}^5 d_{ni} T^{n-1} \quad (5.77)$$

where  $\mathcal{R} = 8.314$  J/mol/K is the universal gas constant,  $W_i$  is the molar mass of species  $i$ , and  $d_{ni}$  are coefficients taken from JANAF-tables of thermodynamics for each species  $i$  [58]. The JANAF coefficients of air and methane (used as fuel in the underlying investigation) and its combustion products are listed in Appendix A.1. With the expression for  $c_{pi}$  (Eqn. (5.77)) and Eqn. (4.10), the specific total enthalpy  $h_i$  reads

$$h_i = \frac{\mathcal{R}}{W_i} \sum_{n=1}^5 \frac{d_{ni} T^n}{n} + \frac{\mathcal{R}}{W_i} d_{6i}, \quad (5.78)$$

where the last term represents the heat of formation  $\Delta H_{f,i}^o$  of species  $i$ . Similar to the determination of the enthalpy of the mixture Eqn. (4.6), the mixture-averaged specific heat capacity is calculated, using

$$c_p = \sum_{i=1}^N c_{pi} \bar{Y}_i. \quad (5.79)$$

The mass fractions  $\bar{Y}_i$  in Eqn. (5.79) are derived with  $\bar{Z}$  and  $\bar{Y}_{fu}$  from the state relationships shown in Fig. 5.24. From the solution of the energy equation providing the enthalpy field, the temperature of fluid mixture is calculated with the expression for the temperature dependency of  $h$  through the procedure of a Newton iteration.

The temperature dependency of the laminar dynamic viscosity,  $\mu$ , is described with Sutherland's formula, reading [70]

$$\mu = \frac{A_s \sqrt{T}}{1 + T_s/T}, \quad (5.80)$$

where the constants  $A_s$  and  $T_s$  are set to  $1.072 \cdot 10^{-6}$  kg/(msK<sup>1/2</sup>) and 198 K, respectively, for methane [20], and  $1.458 \cdot 10^{-6}$  kg/(msK<sup>1/2</sup>) and 110.4 K, respectively, for air [16]. A comparison of measured dynamic viscosity for methane and air with Sutherland's formula is shown in Appendix A.2. The laminar thermal conductivity exhibits a similar temperature dependency as the laminar dynamic viscosity [15]. Since its units correspond to those of the product of dynamic viscosity and specific heat, OpenFOAM calculates  $\lambda$ , using

$$\lambda = \mu c_v \left( 1.32 + 1.77 \frac{R}{c_v} \right), \quad (5.81)$$

where  $c_v$  is the specific heat capacity at constant volume and  $R = \mathcal{R}/W$  the individual gas constant.  $c_v$  is derived from the identity  $R = c_p - c_v$ .

### 5.2.5.2 Radiation properties of the fluid mixture

In case of a grey gas for which the RTE was given in Chapter 5.2.4.1, the absorption coefficient  $a$  needs to be determined depending only on the fluid composition. The components mainly contributing to absorption and emission of thermal radiation in a fluid mixture are carbon dioxide (CO<sub>2</sub>) and water vapour (H<sub>2</sub>O). The radiation properties of both gases strongly depend on the wavenumber. Hence, the calculation of a mean absorption coefficient,  $\bar{a}$ , is sought. For small path lengths in the order 10<sup>-4</sup> m, the assumption of a grey gas is applicable and  $\bar{a}$  can be expressed using [95]

$$\bar{a} = \sum_{i=1}^N f_i(T) a_i p, \quad (5.82)$$

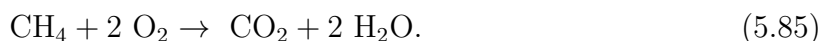
with  $f_i(T)$  as weighting functions describing the temperature dependency,  $a_i$  the  $i$ th grey-gas absorption coefficient and  $p$  the sum of the partial gas pressures. The functions  $f_i(T)$  are estimated by fitting Eqn. (5.82) to experimental data found, e.g. in [17]. In OpenFOAM they are approximated by a 5th-order polynomial, reading

$$f_i(T) = \sum_{n=0}^5 b_{ni} T^n. \quad (5.83)$$

In the present investigation, the considered gases (indicted by index  $i$ ) contributing to absorption are CH<sub>4</sub>, CO<sub>2</sub> and H<sub>2</sub>O ( $N = 3$ ) with the coefficients  $b_{in}$  listed in Appendix A.3. OpenFOAM uses an expression for  $a_i$ , reading

$$a_i = 9.869231 \cdot 10^{-6} M_i, \quad (5.84)$$

in order to calculate the  $i$ th gray-gas absorption coefficient depending on the number of moles of species  $i$ ,  $M_i$ . The corresponding values of  $M_i$  for CH<sub>4</sub>, CO<sub>2</sub> and H<sub>2</sub>O are calculated based on  $\bar{Z}$  from the state relationships of infinitely fast chemical processes, using the reaction equation



### 5.2.5.3 Application of the combustion model to a buoyant diffusion flame

In order to assess the performance of the combustion model presented in the previous chapter, it is applied to purely buoyant diffusion flames and the simulation results are compared with the experimental results presented in [59]. In addition, different buoyancy modifications of the standard  $k$ - $\epsilon$  turbulence model which were analysed in Chapter 5.2.3.1 for a non-reactive flow are employed to investigate their behaviour in a reactive flow.

In the considered experiments [59], the diffusion flames were realised by natural gas exiting a 0.3 m x 0.3 m square burner which sat 0.75 m above the floor (see Fig. 5.25). The fuel-mass flow was varied to obtain flames of different HRR,  $\dot{Q}$ . Velocity and temperature measurements were conducted and semi-empirical correlations were derived for the respective values at the center-line of the flame. These semi-empirical correlations for velocity and temperature read

$$\frac{\bar{w}}{\dot{Q}^{1/5}} = K \left( \frac{z}{\dot{Q}^{2/5}} \right)^m \quad (5.86)$$

and

$$\frac{2g\Delta T}{T_\infty} = \left( \frac{K}{C} \right)^2 \left( \frac{z}{\dot{Q}^{2/5}} \right)^{2m-1}, \quad (5.87)$$

where  $C = 0.9$  and the constants  $K$  and  $m$  are set to different values depending on the considered region, i.e. the flame, intermittent and plume region (see Tab. 5.4).  $\Delta T = \bar{T} - T_\infty$  denotes the temperature rise with respect to ambient temperature. The profiles are scaled with  $\dot{Q}$  so that curves with different HRRs coincide. It has to be mentioned that the temperatures measured in [59] were not corrected with respect to radiative interaction of the thermocouples with the surrounding fluid. As a result, thermocouples showed lower temperatures than the actual gas temperature at the center-line, whereas the measured values were higher than the actual temperatures in the wings of the flame. In [59], the error of flame temperatures was estimated with approximately 300 K. This error decreases further downstream where temperatures are significantly smaller.

3D-simulations were conducted considering radiation via the fvDOM using the numerical set-up described below:

- **Grid:** the computational domain has the dimensions of 2.4 m x 3.75 m x 2.4 m. The grid spacing in the flame region is based on the relationship  $D^*/10$  [6], with  $D^*$  representing a characteristic plume diameter and is calculated, using

$$D^* = D\dot{Q}^{*2/5}, \quad (5.88)$$

where 0.3 m is taken for the characteristic source diameter,  $D$ . For a HRR of 35 kW this gives a grid size of approximately 0.02 m which is also used for higher HRRs. The grid size is gradually increased with increasing distance from the flame, both in vertical and lateral direction, resulting in a total number of cells of approximately 214,600 cells.

- **Boundary conditions:** at the open boundaries of the domain, *pressureNormalInletOutletVelocity* for velocity and a *totalPressure* of 101325 Pa for pressure  $p_{rgh}$  are prescribed at the sides, and *inletOutlet* with zero as *inletValue* for velocity and the *buoyantPressure* for  $p_{rgh}$  are considered at the top. BCs for temperature, the turbulence parameters ( $k$  and  $\varepsilon$ ), mixture fraction and fuel-mass fraction are set to *inletOutlet* with *inletValues* of 293 K,  $1 \cdot 10^{-6} \text{ m}^2/\text{s}^2$ ,  $1 \cdot 10^{-9} \text{ m}^2/\text{s}^3$  and zero, respectively, at the open boundaries. At the patch of the fuel inlet, *buoyantPressure* is prescribed for  $p_{rgh}$ , a fixed value of 293 K for temperature, and the values for mixture fraction and fuel-mass fraction are calculated according to Eqn. (5.76) with 1 as value at infinity.
- **Initial conditions:** the ambient has a temperature of 293 K and is at rest.
- **Heat source:** numerical results of center-line distributions for  $\dot{Q}$  of 35, 45, and 55 kW are compared with the semi-empirical correlations of Eqns. (5.86) and (5.87). The different burning rates are realised by varying the fuel-mass flux at the inlet assuming a heat of combustion of  $\Delta h_C = 50 \text{ MJ/kg}$ . The inlet values for  $k_{in}$  and  $\varepsilon_{in}$  are calculated with  $Tu_{in} = 0.5 \%$  and  $l_m = 0.3/15 \text{ m}$  applying Eqns. (5.33) and (5.34).
- **Thermo-physical properties:** the fluid properties  $c_p$  and  $\mu$  are calculated according to the procedure presented in Chapter 5.2.5.1, where the JANAF coefficients for methane and its products listed in Appendix A.1 are used. For the calculation of the mean absorption coefficient, the method described in Chapter 5.2.5.2 is applied with the coefficients listed in Appendix A.3.
- **Discretisation:** the solid-angle is discretised with 12 discrete rays for the fvDOM, and as discretisation schemes, *linearUpwind* and *central-difference* are used for the convection terms and diffusion terms, respectively.

To obtain a steady-state solution, a transient calculation is conducted until all flow parameters are constant. The calculation is parallelised on 4 CPUs using domain decomposition (scotch method) which results in approximately 54000 cells per CPU.

Figs. 5.26 to 5.29 depict mean vertical velocity and temperature rise at the center-line. While for the buoyant plume (Chapter 5.2.3.1) no difference in results was observed depending on how  $G_{SGDH}$  was introduced into the  $\varepsilon$ -equation (Eqn. (5.39)) with the SGDH, results with both methods mentioned in Chapter 5.2.3 are shown here. SGDH<sub>1</sub> indicates

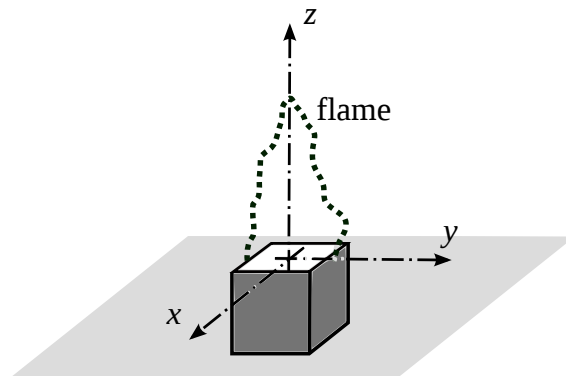


Figure 5.25: Investigated experiment of a turbulent buoyant diffusion flame [59]

	flame	intermittent region	plume
$m$	0.5	0	-1/3
$K$	6.8 (m <sup>1/2</sup> /s)	1.9 (m/s/kW <sup>1/5</sup> )	1.1 (m <sup>4/3</sup> /s/kW <sup>1/3</sup> )

Table 5.4: Constants  $m$  and  $K$  for the correlations given in Eqns. (5.86) and (5.87) in the different regions of the diffusion flame [59]

the consideration of  $G_{SGDH}$  in the  $\varepsilon$ -equation independently of the sign of  $G_{SGDH}$  with  $C_3 = 0.8$ , whereas  $SGDH_2$  neglects negative  $G_{SGDH}$  in the  $\varepsilon$ -equation with  $C_3 = 0$ . For both velocity and temperature distributions, the standard model and both  $SGDH$  approaches show qualitatively good agreement with the correlations (Eqns. (5.86) and (5.87)). The  $SGDH_2$  approach shows very similar results to those obtained with the standard model. Compared with the semi-empirical correlations, both models over-estimate the quantities at the center-line. This is equivalent to an over-estimation of the peak values and an under-estimation of the plume widths above the flame as shown in Fig. 5.30 for the radial velocity profile scaled with the center-line value,  $\bar{w}_c$ , compared to a best fit of experimental results. The same behaviour was observed in the non-reactive case as a result of lower turbulent viscosity and turbulent thermal diffusivity predicted by the turbulence models (see Chapter 5.2.3.1).

With  $SGDH_1$ , center-line distributions for different HRRs do not coincide as well, as it is observed with the standard model and the  $SGDH_2$  approach (see Figs. 5.26 and 5.28). Velocity distributions are slightly underestimated in all regions (see Figs. 5.26). The temperature distributions in the flame region are higher for the  $SGDH_1$  than the  $SGDH_2$  approach (compare Figs. 5.28 and 5.29). Keeping in mind that the temperature measurements are underestimated in the flame region due to radiation errors, the

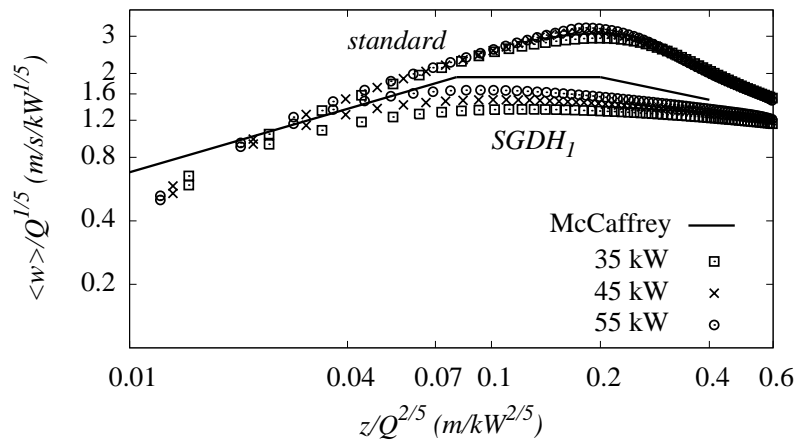


Figure 5.26: Mean vertical velocity at center-line with different turbulence models compared with McCaffrey's correlations (Eqns. (5.86) and (5.87),  $\langle w \rangle = \bar{w}$ ,  $Q = \dot{Q}$ )

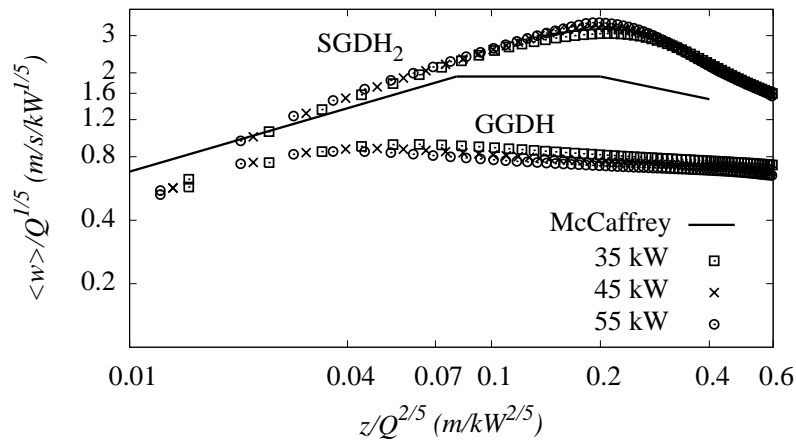


Figure 5.27: Mean vertical velocity at center-line with different turbulence models compared with McCaffrey's correlations (Eqns. (5.86) and (5.87),  $\langle w \rangle = \bar{w}$ ,  $Q = \dot{Q}$ )

prediction of flame temperatures is slightly improved compared to the  $\text{SGDH}_2$ . On the other hand, an underestimation of the temperature rise in the plume region is observed, which will be higher considering radiation errors in measurements. The reason for wider plume widths with the  $\text{SGDH}_1$  (see also Fig. 5.30) can be seen in the vertical distribution of the turbulence production (see Fig. 5.31), where higher values are exhibited in the vicinity of the burner outlet resulting in higher turbulence, and thus in higher spreading rates. Furthermore, during the simulations of the experiments, numerical instabilities are observed when applying the  $\text{SGDH}_1$  approach. The GGDH buoyancy-modification exhibited promising behaviour for a non-reactive flow (see Chapter 5.2.3.1), whereas its application to the diffusion flame shows a strong under-estimation of the center-line quan-

tities. This is attributed to the fact that near the burner outlet, where in the experiment a laminar region is observed, the model over-predicts the turbulence due to great lateral density gradients encountered in the flame region, as seen in Fig. 5.31. As a consequence, thermal energy and fuel are stronger diffused in lateral direction resulting in a wider and shorter flame region than observed in the experiment. Hence, the beginning of the plume region is predicted much closer to the burner outlet as also seen in Fig. 5.29, where the slope of the plume region corresponds well to the experiment but starts far more upstream. This behaviour is not in agreement with the results presented in [94], where the application of the GGDH buoyancy-modified  $k-\varepsilon$  model to a buoyant diffusion flame reproduced experimental data very well. In [94], a different combustion model was used based on the flamelet concept [74] which is of higher complexity, and thus computationally more expensive than the method used here. This highlights the great influence of how combustion is treated in fire modelling. Additionally, in [94]  $G_{GGDH}$  was introduced into the  $\varepsilon$ -equation (Eqn. (5.39)) through a modified flux Richardson number (which is not further specified in the work) and all turbulent scalar fluxes (Eqn. (5.7)) were modelled with the GGDH instead of the SGDH.

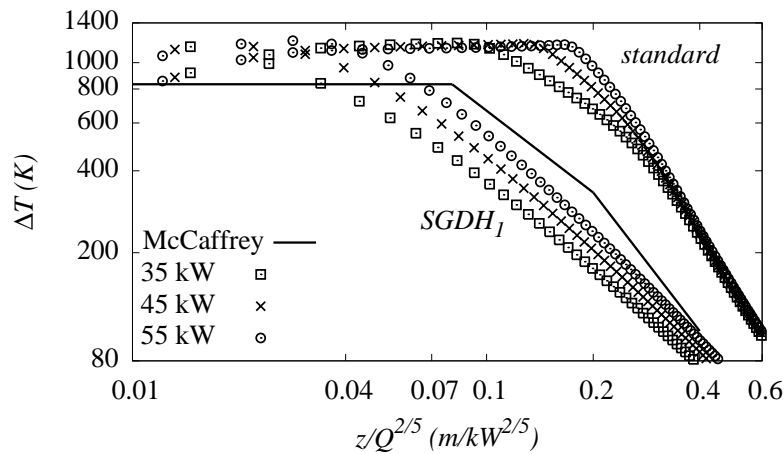


Figure 5.28: Temperature rise at center-line with different turbulence models compared with McCaffrey's correlations (Eqns. (5.86) and (5.87),  $Q = \dot{Q}$ )

From the results of the presented analysis (for a summary see Tab. 5.5) it can be concluded that even though the GGDH approach shows improvements over the standard model for buoyant plumes, it cannot be suggested in combination with the used combustion model for the simulation of fire scenarios. The  $SGDH_1$  buoyancy modification shows higher spreading rates for velocity and temperatures than seen with the  $SGDH_2$  approach, but underestimates velocities in all regions. The numerical instabilities observed when applying the  $SGDH_1$  approach did not allow convergence of the solver in cases of more complex conditions such as transient HRRs. The standard model and the  $SGDH_2$  approach show qualitatively good correspondence with the correlations and quantitatively

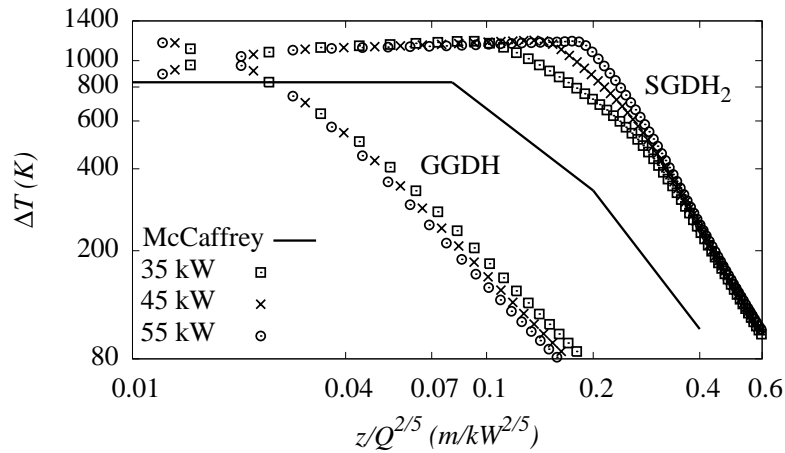


Figure 5.29: Temperature rise at center-line with different turbulence models compared with McCaffrey's correlations (Eqns. (5.86) and (5.87),  $Q = \dot{Q}$ )

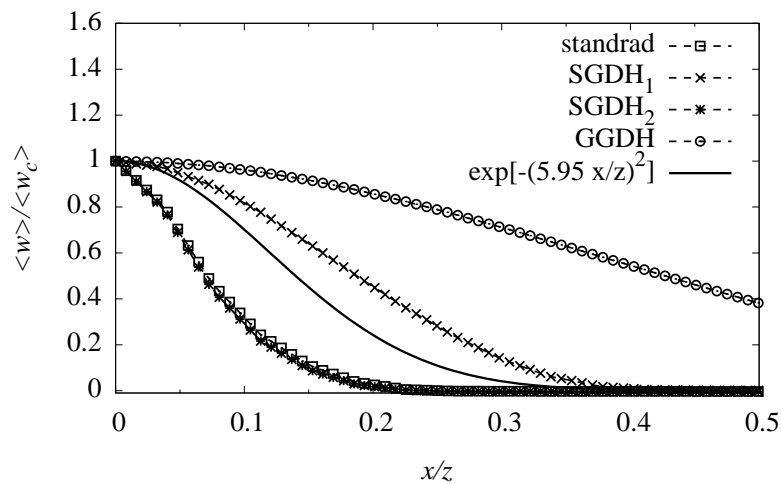


Figure 5.30: Radial distribution of mean vertical velocity in the plume region ( $z = 1.065$  m) for  $\dot{Q} = 45$  kW with different buoyancy-augmentations compared with a best-fit from [59] ( $\langle w \rangle = \bar{w}$  and  $\langle w_c \rangle = \bar{w}_c$ )

good agreement with temperatures in the flame region when considering radiation errors, whereas plume widths are underestimated. Whilst the SGD<sub>2</sub> approach exhibits no advantage over the standard  $k-\varepsilon$  model, it does not lead to a significant increase in computational time and is thus adopted for the underlying investigation of modelling fires in underground structures as it can offer benefits in other flows such as in the presence of walls (see Chapter 6.2). Finally, it can be concluded from the analysis results and the observations published in the literature, that the choice of a turbulence model represents an uncertainty in fire modelling.



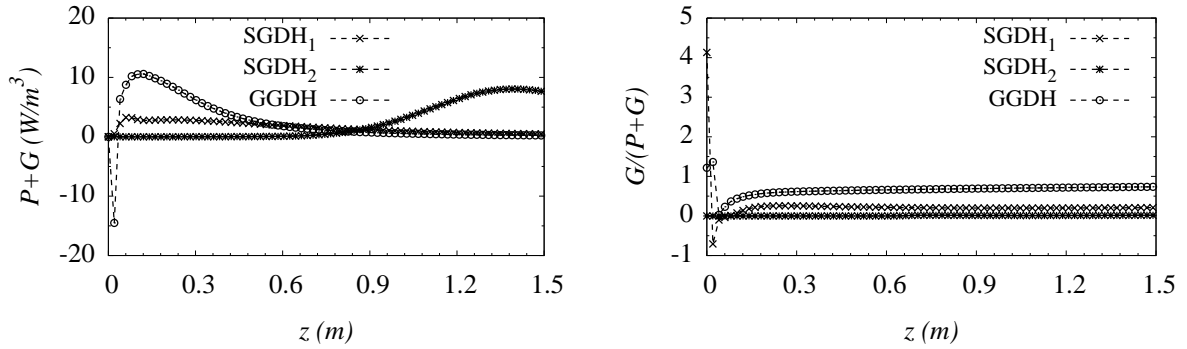


Figure 5.31: Absolute (*left*) and relative (*right*) turbulence production at center-line with different buoyancy-augmentations for  $\dot{Q} = 45$  kW

	<i>standard</i>	<i>SGDH<sub>1</sub></i>	<i>SGDH<sub>2</sub></i>	<i>GGDH</i>
<i>velocities at center-line</i>	overestimated in all regions	good agreement in all regions	overestimated in all regions	underestimated in all regions
<i>temperatures at center-line</i>	overestimated in plume region	underestimated in plume region	overestimated in plume region	underestimated in all regions
<i>plume width at z = 1.065 m</i>	underestimated	good agreement	underestimated	overestimated
<i>distinction of flame and plume region</i>	yes	yes	yes	no
<i>numerically stable</i>	yes	no	yes	yes

Table 5.5: Behaviour of analysed buoyancy modifications of the  $k$ - $\varepsilon$  turbulence model in simulations of buoyant diffusion flames compared with McCaffrey's correlations (Eqns. (5.86) and (5.87))

# Chapter 6

---

## Application of the fire code on realistic geometries

On the basis of the *chtMultiRegionFoam* solver the different sub models which were analysed in the previous sections, i.e. the conjugate heat transfer, the buoyancy-modifications of the standard  $k-\varepsilon$  turbulence model, the treatment of radiative heat transfer and the combustion model, are assembled to a single fire code. Before the code is applied to realistic tunnel configurations, its predictive ability is assessed within the re-analysis of two real-scale fire experiments: (i) the Cardington compartment-fire test conducted by the *Building Research Establishment (BRE)* [53, 90], and (ii) a 1:3-scaled tunnel-fire test in the *Buxton Dust Explosion Gallery* [7]. Experimental data of temperatures and velocities at various locations are compared with simulation results. Additionally, analyses are conducted in order to work out the influence of different approaches in modelling the fire source: (i) a non-reactive, and (ii) a reactive description of the fire source. In the first case, the fire is modelled by a volumetric heat source, only considering the convective portion of the total HRR. Thus, radiative heat transfer is neglected and no combustion model is applied. This approach represents a procedure to avoid the computationally expensive modelling of radiation and combustion. The second approach includes combustion and takes radiative heat transfer into account by modelling the fire as a buoyant diffusion flame, fed by methane. Results obtained from application of the different approaches are compared in terms of computational time and quality of prediction.

## 6.1 The Cardington compartment-fire test

In total, 8 full-scale fire tests were carried out by the *Building Research Establishment (BRE)*, UK in a compartment measuring 12 m x 12 m x 3 m characterised by different opening configurations, compartment linings and composition of fire load [53, 90]. For the CFD-analysis, Test 8 is considered where the compartment comprised 0.3 m thick walls made of concrete blocks and a 0.3 m thick pre-cast concrete roof. In Test 1, the roof was damaged by extensive cracking and spalling after 20 min showing the necessity of protecting the ceiling with a 0.025 m thick thermal insulation. Preliminary simulations of Test 8 omitting the insulation predicted much lower compartment temperatures than observed in the experiment due to absorption of thermal energy by the roof and lower re-radiation, similar to the experimental observations of Test 1. Hence, the sprayed insulation is also considered in the analyses. The floor consisted of sand which covered the concrete floor slab. Two openings were installed at the front of the compartment as depicted in Figs. 6.1 and 6.2, showing the geometry which is used for the CFD-analysis. Each of the openings had a width of 3.6 m and extended over the full height of the compartment. The thermo-physical properties of the wall, roof and insulation materials are summarised in Tab. 6.1.

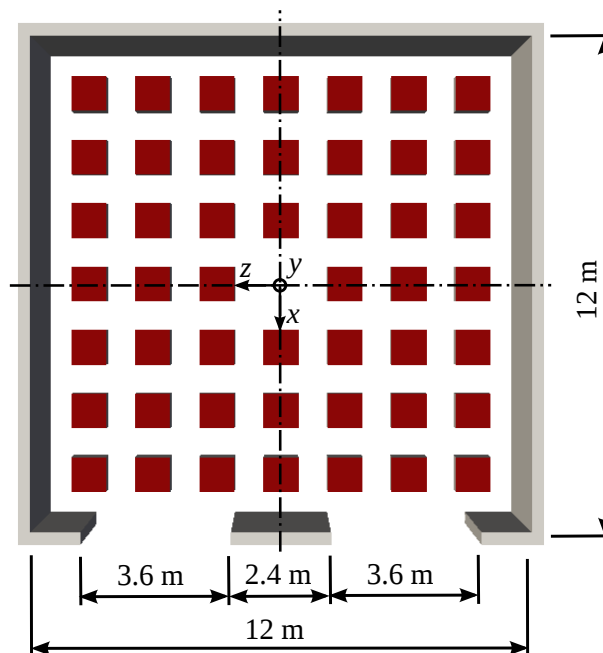


Figure 6.1: Plan view of the Cardington compartment showing the 48 stick cribs

The fire load was modelled by 48 stick cribs of dimensions 1 m x 1 m arranged in a 7 x 7 regular pattern parallel to the walls omitting the central crib due to a supporting column located there (see Fig. 6.1). In Test 8, the stick cribs were composed of 80% wood and 20% plastic by calorific value (with 17 MJ/kg for wood, 34 MJ/kg for polypropylene). In

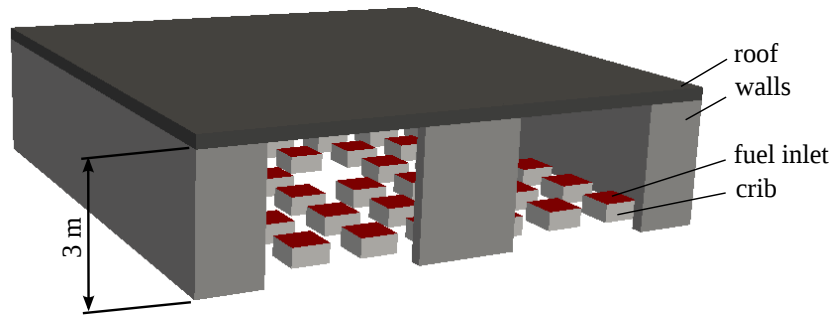


Figure 6.2: 3D-view of the Cardington compartment

<i>Element</i>	$\rho$ (kg/m <sup>3</sup> )	$c_p$ (J/kg/K)	$\lambda$ (W/m/K)
walls	1375	753	0.42
roof	240	1500	1.50
insulation	680	970	0.19

Table 6.1: Thermo-physical properties of Cardington compartment elements

order to estimate the HRR of the fire during the experiment, 8 cribs were positioned on load cells to measure the weight loss in consequence of combustion. A tri-linear HRR-curve was derived from the mass-loss rates with the corresponding values listed in Tab. 6.2. As suggested in [2] for compartment fires, the linear increase of the HRR is replaced by a quadratic fire growth, using

$$\dot{Q} = \alpha_q t^2, \quad (6.1)$$

with  $\alpha_q = 43 \cdot 10^6 / 300^2 = 477 \text{ W/s}^2$ . The difference of released energy between the linear and the quadratic fire growth is added to the linear decay resulting in an increased duration of the fire (see Tab. 6.2). The modified HRR which is used as main input for the CFD-analyses is shown in Fig. 6.3. Hereby, the HRR used for the non-reactive approach is reduced by the radiative fraction to 80 % of the total HRR [2].

Gas temperatures were measured with thermocouples at 64 locations inside the compartment organised in 16 thermocouple trees (G1 – G16, see Fig. 6.4). Each thermocouple tree carried 4 thermocouples at 0.1, 0.3, 0.6 and 1.8 m below the ceiling. At centre line of the openings, temperature and velocity measurements were taken over the full height at 0.05, 0.4, 0.75, 1.1, 1.45, 1.8, 2.15 and 2.5 m below the ceiling. In [90], the measurements of gas temperature used for comparison with the numerical predictions were corrected with respect to radiative interaction of the thermocouples with the surrounding fluid.

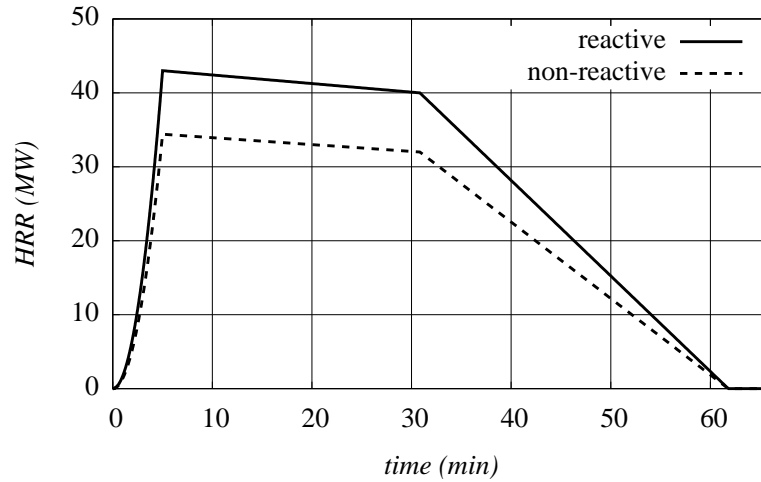


Figure 6.3: HRR-curve of Cardington compartment-fire Test 8 with a quadratic fire growth applied for the reactive (100% of measured HRR) and non-reactive (80% of measured HRR) simulations

<i>time</i> (min)	<i>HRR Cardington fire Test 8 (MW)</i>		
	<i>reactive (linear)</i>	<i>reactive (quadratic)</i>	<i>non-reactive (quadratic)</i>
0.0	0.0	0.0	0.0
5.0	43.0	43.0	34.4
31.0	40.0	40.0	32.0
60.0	0.0		
61.5		0.0	0.0

Table 6.2: HRR values at different time instants corresponding to Fig. 6.3

The numerical set-up used for the CFD simulations is summarised as follows:

- **Grid:** the computational domain is extended beyond the compartment boundaries at the side of the openings in  $x$  and  $y$  direction, resulting in a total domain size of 18 m x 12.6 m x 5.4 m. The cartesian grid is set up with OpenFOAM's *blockMesh*-utility with a grid size of 0.15 m estimated from  $D^*/10$ . The geometry of each crib is set to 0.9 m x 0.45 m x 0.9 m in order to be resolved by the grid size. Grid-refinement is done at burner outlets and in areas adjacent to the floor, walls and ceiling to keep the dimensionless wall distance within  $30 < y^+ < 100$  for a correct application of the wall-function approach [14]. This results in a total cell number of approximately 448,100 with approximately 395,100 cells in the fluid region.
- **Boundary conditions:** a *pressureInletOutletVelocity* BC is prescribed for velocity at all domain openings, *totalPressure* and *buoyantPressure* for  $p_{rgh}$  at vertical domain openings and at the top domain opening, respectively. No-slip BCs for velocity

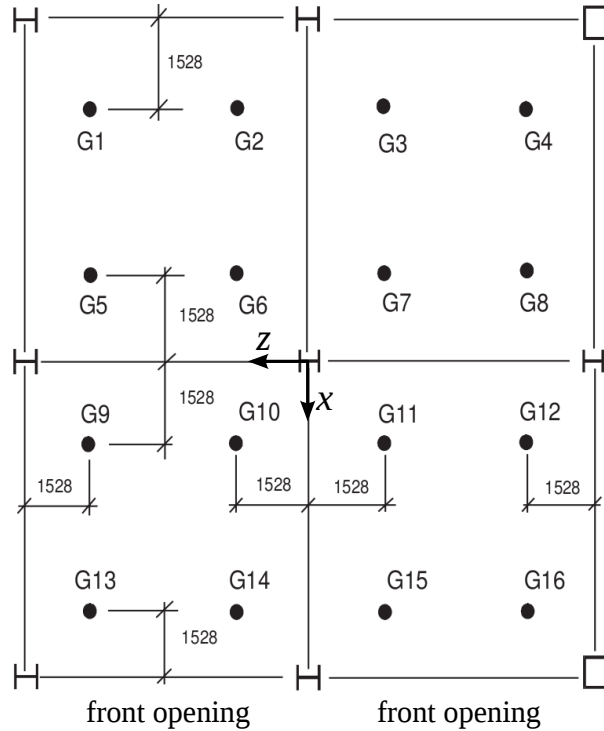


Figure 6.4: Distribution of thermocouple trees (dimensions in mm) [53]

are set at solid surfaces. At the open boundaries an *inletOutlet* BC is prescribed for temperature with an ambient temperature of 293 K as inlet value. The floor is considered adiabatic whereas conjugate heat transfer including radiation and with application of temperature wall-functions are used for the walls, insulation and roof. The cribs are simulated as thermally inert obstacles. BCs for the turbulence parameters ( $k$  and  $\varepsilon$ ), mixture fraction and fuel mass-fraction (reactive case) are set to *inletOutlet* with *inletValues* of 293 K,  $1 \cdot 10^{-6} \text{ m}^2/\text{s}^2$ ,  $1 \cdot 10^{-9} \text{ m}^2/\text{s}^3$  and zero, respectively, at the open boundaries. The surface emissivity,  $\epsilon$ , is set to 0.8 for all surfaces [2].

For the BCs in the solid regions of walls, insulation and roof, the conjugate heat transfer is enabled at the fluid interface, the insulation-roof and roof-walls interface, whereas a constant temperature of 293 K is assumed at the remaining boundary interfaces for the walls, i.e. at the floor and outer surface.

- **Initial conditions:** the ambient has a temperature of 293 K and is at rest.
- **Heat source:** in the non-reactive case, the fire load is represented by a volumetric heat source. It is realised by the source term,  $S_Q$ , in the energy equation (Eqn. (5.10)), where the location and temporal evolution of energy release are implemented with the help of the *swak4Foam* utility [1]. The HRR corresponds to the convective portion of the fire, which depends on its size and the type of fuel. In the underlying investigation, 80% of the measured HRR is applied as suggested in [2] (see Fig. 6.3).

In the reactive simulation, the fire is modelled by a methane diffusion flame. On each crib, a fuel inlet is defined (see Fig. 6.2) and the time-dependent fuel mass-flow rate is specified using the *timeVaryingFlowRateInletVelocity* BC, where a temporal history of mass flux can be prescribed. From the mass flux, an inlet velocity of the fuel is calculated according to the density and the inlet surface. The fuel mass-flow rate is determined with the heat of combustion of methane,  $\Delta h_C = 50$  MJ/kg and the HRR curve,  $\dot{Q}(t)$ , (Fig. 6.3), using

$$\dot{m}(t) = \frac{\dot{Q}(t)}{\Delta h_C}. \quad (6.2)$$

At the patch of fuel inlets, *buoyantPressure* is prescribed for  $p_{rgh}$ , a fixed value of 293 K for temperature and the values for mixture fraction and fuel mass-fraction are calculated according to Eqn. (5.76) with 1 as value at infinity. The inlet values for  $k_{in}$  and  $\varepsilon_{in}$  are calculated with  $Tu_{in} = 0.5$  % and  $l_m = 0.9/15$  m by the BCs *turbulentIntensityKineticEnergyInlet* and *turbulentMixingLengthDissipationRateInlet*, respectively, which apply Eqns. (5.33) and (5.34). These BCs allow to adjust  $k_{in}$  and  $\varepsilon_{in}$  according to the inlet velocity of fuel, changing over time.

- **Thermo-physical properties:** the fluid properties  $c_p$  and  $\mu$  are calculated according to the procedure presented in Chapter 5.2.5.1, where for the non-reactive and reactive simulations the JANAF coefficients of air and methane (and its products), respectively, listed in Appendix A.1 are used. For the calculation of the mean absorption coefficient, the method described in Chapter 5.2.5.2 is applied with the coefficients listed in Appendix A.3. The thermo-physical parameters for the solid materials are assumed independent of temperature and are given in Tab. 6.1.
- **Discretisation:** within the fvDOM radiation model, the solid angle is discretised with 12 rays. For the discretisation schemes, *linearUpwind* and *central-difference* are used for the convection terms and diffusion terms, respectively (detailed discretisation and solver settings see Appendix B).

In both the reactive and non-reactive case, the  $k$ - $\varepsilon$  turbulence model with the SGDH<sub>2</sub> buoyancy modification is used. The control over the time step is effectuated through the *Courant* number  $Co$ , which is calculated for each cell, defined as [70]

$$Co = \frac{\Delta t |u|}{\Delta x}, \quad (6.3)$$

where  $\Delta t$  is the time step,  $|u|$  the magnitude of the velocity through the cell and  $\Delta x$  the cell size in the direction of the velocity. In all simulations  $Co$  is set to 0.8, from which the time step is derived by re-arranging Eqn. (6.3). The calculations are parallelised on 8 CPUs using domain decomposition (scotch method) which results in approximately 56000 cells per CPU.

### 6.1.1 Results and discussion

The simulations showed that for the non-reactive case calculated temperatures are far above realistic values with an overestimation of measurements greater than 500 °C. Even a variation of the representative volume of the heat source, i.e. the power density, until its theoretical maximum (total volume of compartment) resulted in a strong overestimation of compartment temperatures. Furthermore, a reduction of the convective part of the HRR from originally 80% to 60% did not allow to obtain realistic results. Hence, it is concluded that the non-reactive approach to simulate a compartment fire with a high heat output of 43 MW distributed on a surface of 12 m x 12 m is not suitable, and thus results are only shown for the reactive case.

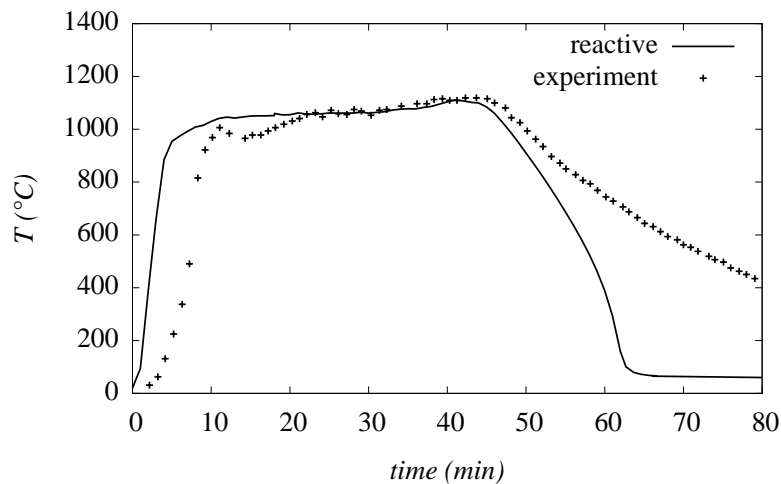


Figure 6.5: Average compartment temperature

The temporal distribution of the average compartment temperature is shown in Fig. 6.5. The temperature distribution predicted by the reactive case shows reasonable correspondence with the experimental data. However, a steep gradient is observed in the first minutes which does not correspond to the observations in the experiment. During the phase of fire growth the quadratic increase of the ejected fuel mass of the diffusion flame burns immediately (mixed-is-burnt) and leads to a steep temperature rise, which does not reproduce the measurements. This behaviour might be related to the fact that the combustion model in combination with the assumption of mixing-controlled combustion is mainly applicable to well-ventilated fires [95]. Well-ventilated conditions can be expected close to the front openings whereas at the rear part of the compartment, conditions allowing complete combustion of available oxidiser are unlikely. Consequently, the current model predicts reasonable magnitudes of gas temperature close to the opening depicted in Figs. 6.6 and 6.7 for the positions G14 and G10 and overestimates temperature levels at the beginning of the fire in under-ventilated regions, as seen at positions G6 and G2 in Figs. 6.8 and 6.9, where this overestimation is observed until approximately 15 min.



Similar conclusions can be drawn for the decay phase where the average temperature is underestimated by the simulation. Moreover, the fire decay is also influenced by the heat released by the residues of the burnt cribs which is not considered in the simulation (the same was mentioned in [76]).

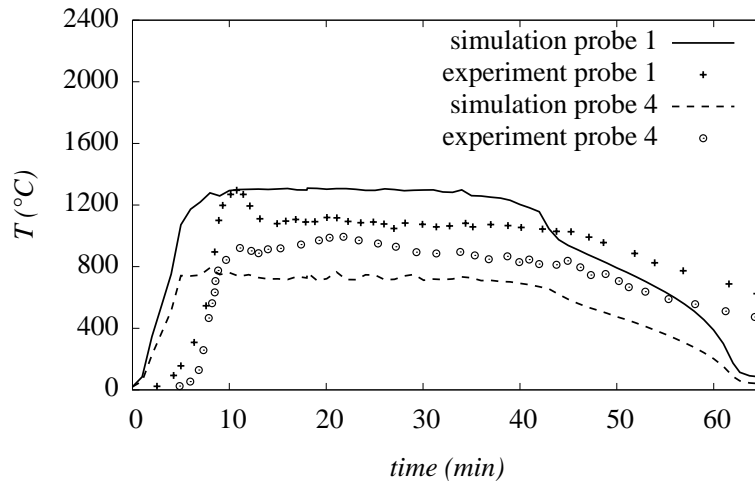


Figure 6.6: Temperatures at thermocouple trees G14 (probe 1:  $y = 2.9$  m, probe 4:  $y = 1.2$  m)

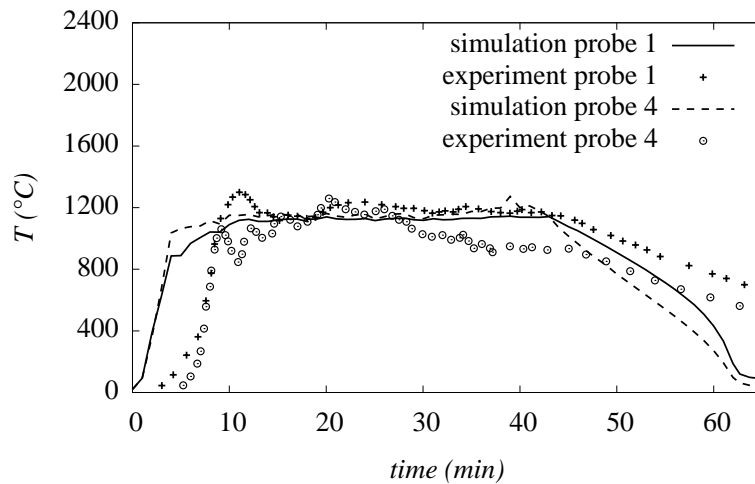


Figure 6.7: Temperatures at thermocouple trees G10 (probe 1:  $y = 2.9$  m, probe 4:  $y = 1.2$  m)

The results of the individual measurement positions G2 and G6 (see Figs. 6.9 and 6.8) show an underestimation of the temperature with longer duration of the fire. Furthermore, similar temperatures are predicted for heights  $y = 2.9$  m (probe 1) and  $y = 1.2$  m (probe 4) except for thermocouple tree G14 (see Fig. 6.6), not reproducing the temperature stratification observed in the experiment. This can also be seen in the contour plot shown

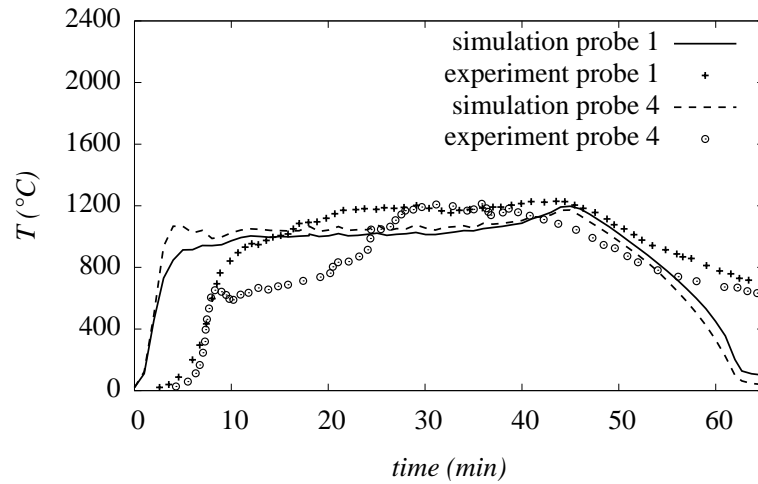


Figure 6.8: Temperatures at thermocouple tree G6 (probe 1:  $y = 2.9$  m, probe 4:  $y = 1.2$  m)

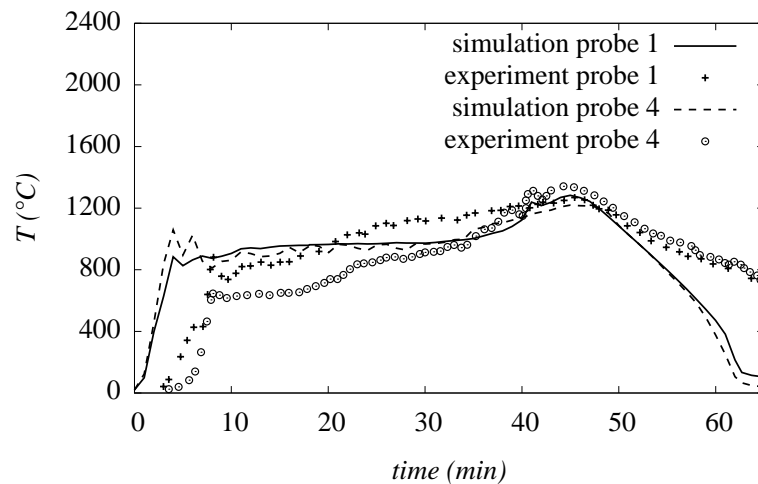


Figure 6.9: Temperatures at thermocouple tree G2 (probe 1:  $y = 2.9$  m, probe 4:  $y = 1.2$  m)

in Fig. 6.10, including the measurement positions G2, G6, G10 and G14. The numerical results (see Fig. 6.10) show a homogeneous temperature distribution in two thirds of the domain except in the front part of the domain (close to the openings), where the highest temperatures as well as the highest density of released heat is observed in the simulation (a time series of contour plots of temperature at  $z = 1.53$  m is depicted in Appendix C). Interestingly, the simulation results show good agreement with the experiment at position G14 (see Fig. 6.6), confirming the better behaviour of the used combustion model for well-ventilated conditions, which is still applicable at position G10 (see Fig. 6.7).

Distributions of flow parameters at various heights at the center line of the right-hand opening ( $z < 0$ , see Fig. 6.1) are shown in Figs. 6.11 and 6.12. Calculated temperatures

slightly overestimate the experimental values but exhibit qualitatively good correspondence with the measurements. The velocity distributions reproduce the experimental results qualitatively good but absolute values are underestimated by the simulation for all probes, especially at  $y = 2.25$  m. The underestimation of the velocities may be explained by less expansion of the fluid due to lower temperatures as seen for some local measurements at the rear of the compartment starting at approximately 20 min (see, e.g. Fig. 6.8). On the other hand, the predicted position of the neutral plane of velocity at the right-hand opening (see Figs. 6.13, 6.15 and 6.16), giving a ratio of  $h_0/H \approx 0.5$  (with  $h_0$  as the height of the neutral plane and  $H$  the total opening height), is in the typical range of 0.3 – 0.5 [26].

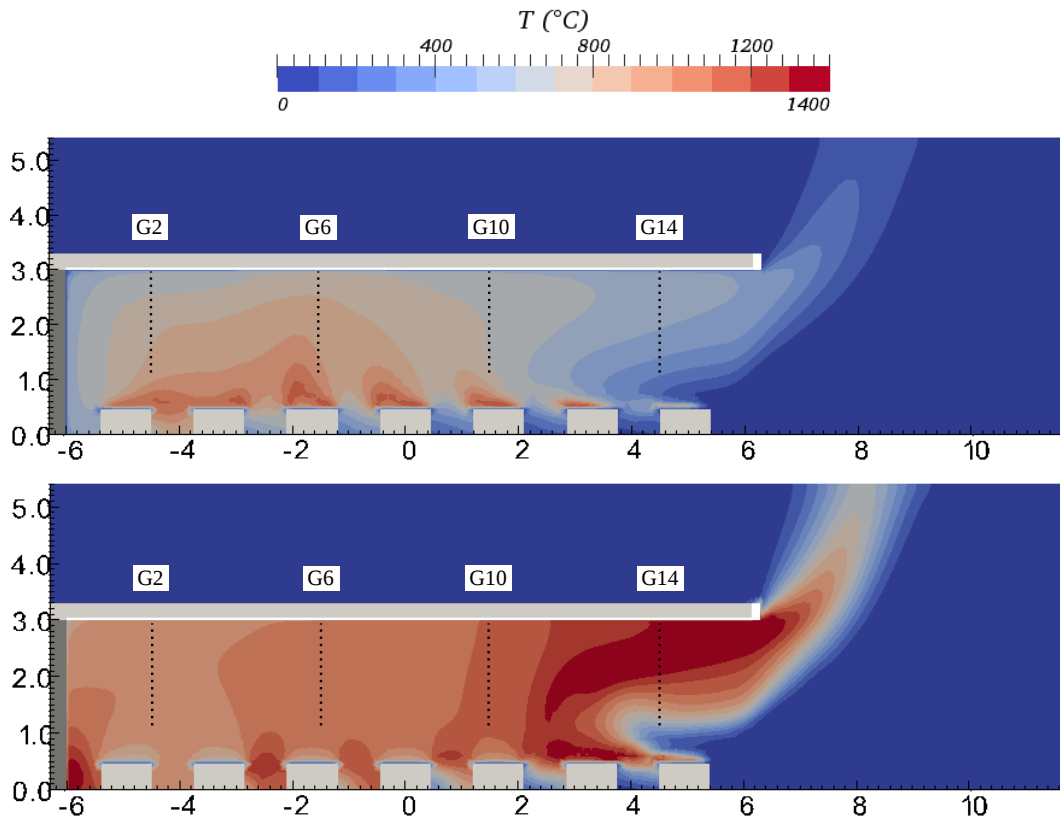


Figure 6.10: Contour plots of temperature at  $z = 1.53$  m including thermocouple trees G2, G6, G10 and G14 (dotted lines) for time instants  $t = 3$  min (*top*) and  $t = 30$  min (*bottom*) (dimensions in m)

In Fig. 6.17, the averaged specific heat fluxes,  $q_w$ , at the compartment's inner surfaces (i.e. walls and insulation) are depicted, divided into their convective and radiative fractions. The results for the specific heat fluxes at the inner surfaces of the compartment exhibit the expected strong dominance of radiative heat transfer. This fact did not allow to obtain reasonable results with the non-reactive approach (as earlier mentioned) where radiation was not taken into account. After an increase during the stage of fire growth, heat fluxes decrease as solid temperatures approach the fluid temperature in the course

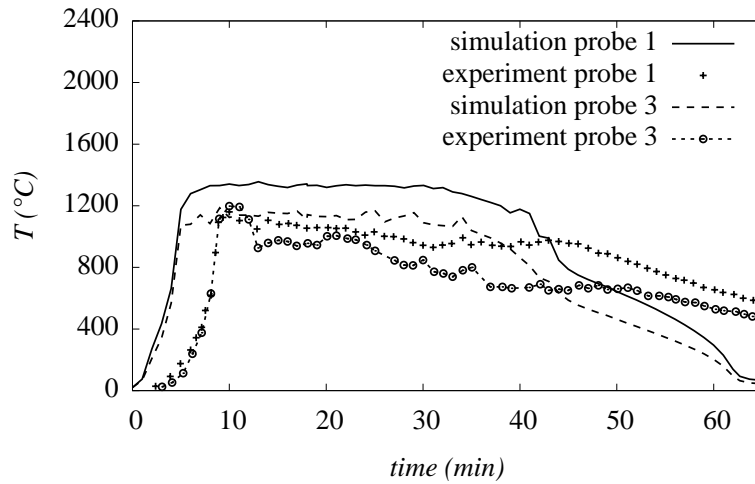


Figure 6.11: Temperature at center line of the right-hand opening ( $z < 0$ , probe 1:  $y = 2.95$  m, probe 3:  $y = 2.25$  m)

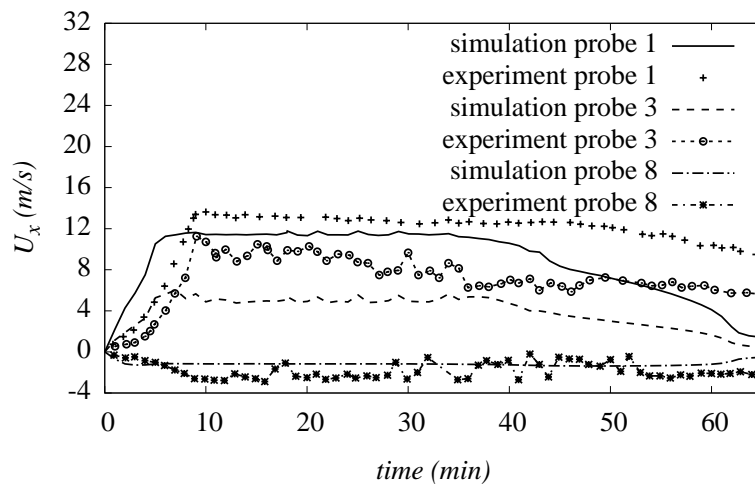


Figure 6.12: Velocity at center line of the right-hand opening ( $z < 0$ , probe 1:  $y = 2.95$  m, probe 3:  $y = 2.25$  m, probe 8:  $y = 0.5$  m)

of the fire, leading to a negligible convective heat transfer and increasing re-radiation of heated surfaces. During the fire decay, the fluid temperatures decrease and the solid surfaces cool down, releasing heat indicated by the negative heat fluxes for  $t > 50$  min (see Fig. 6.17).

### 6.1.2 Conclusions

The displayed results show, that apart from the period of fire growth and decay, the distribution of the average compartment temperature shows good agreement with the

measurements (see Fig. 6.5). On the other hand, discrepancies between predictions and experimental data are observed for variations of local velocities and temperatures (see, e.g. Fig. 6.8). A similar conclusion was drawn in [76], where experiments of the same series (though Test 8 was not included) were analysed with FDS [27]. The observed deviations of the numerical results exhibit the complexity of the mechanisms which occur throughout the development of a compartment fire such as the change of ventilation conditions in different parts of the domain. Furthermore, the applied representation of 48 wood cribs by 48 gas burners with a uniform mass flux of fuel obviously cannot reproduce the burning of the individual cribs where the ignition of the cribs may not have been as uniform as suggested by the prescribed HRR curve in the simulation. However, the presented application showed reasonable agreement concerning fluid temperatures in well-ventilated regions (see, e.g. Fig. 6.7). Moreover, it allowed to identify limitations of the used model assumptions of the fire code, such as in the simple combustion model.

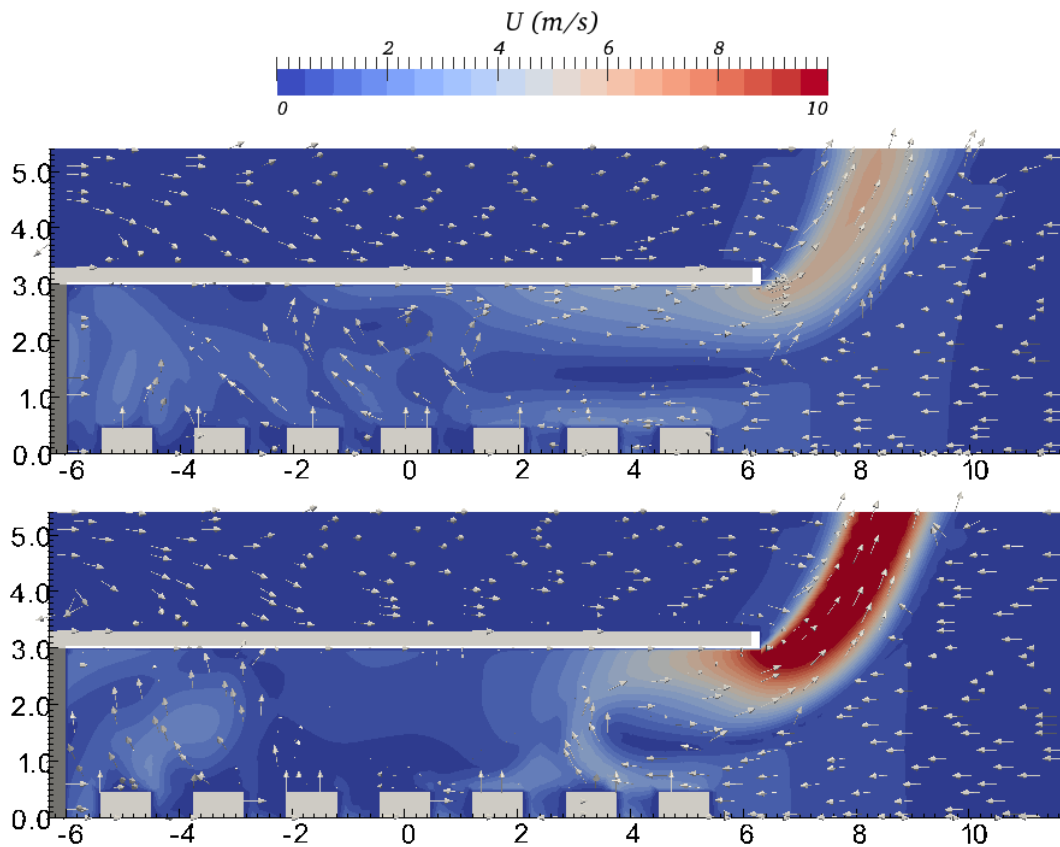


Figure 6.13: Contour plots of velocity magnitude at  $z = 3$  m for time instants  $t = 3$  min (*top*) and  $t = 30$  min (*bottom*) (dimensions in m)

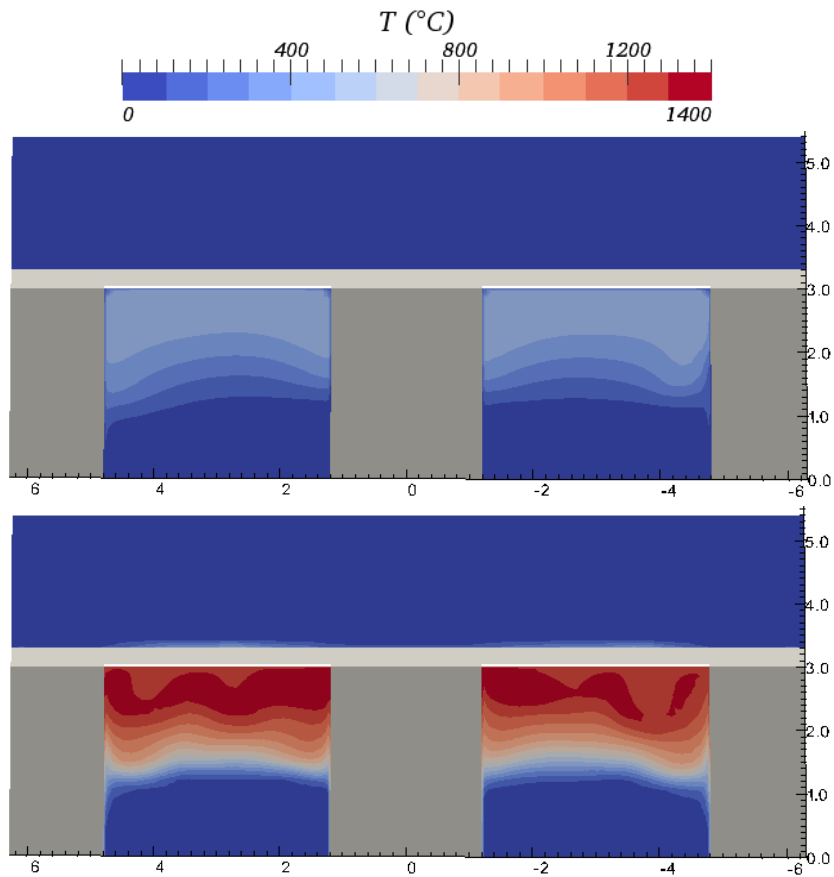


Figure 6.14: Contour plots of temperature at  $x = 6.3$  m (openings) for time instants  $t = 3$  min (top) and  $t = 30$  min (bottom) (dimensions in m)

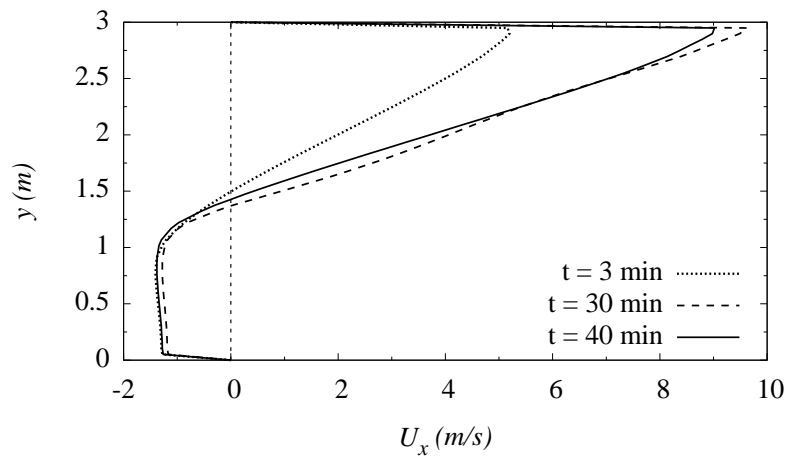


Figure 6.15: Horizontal velocity profile at the center line of the right-hand opening at different time instants

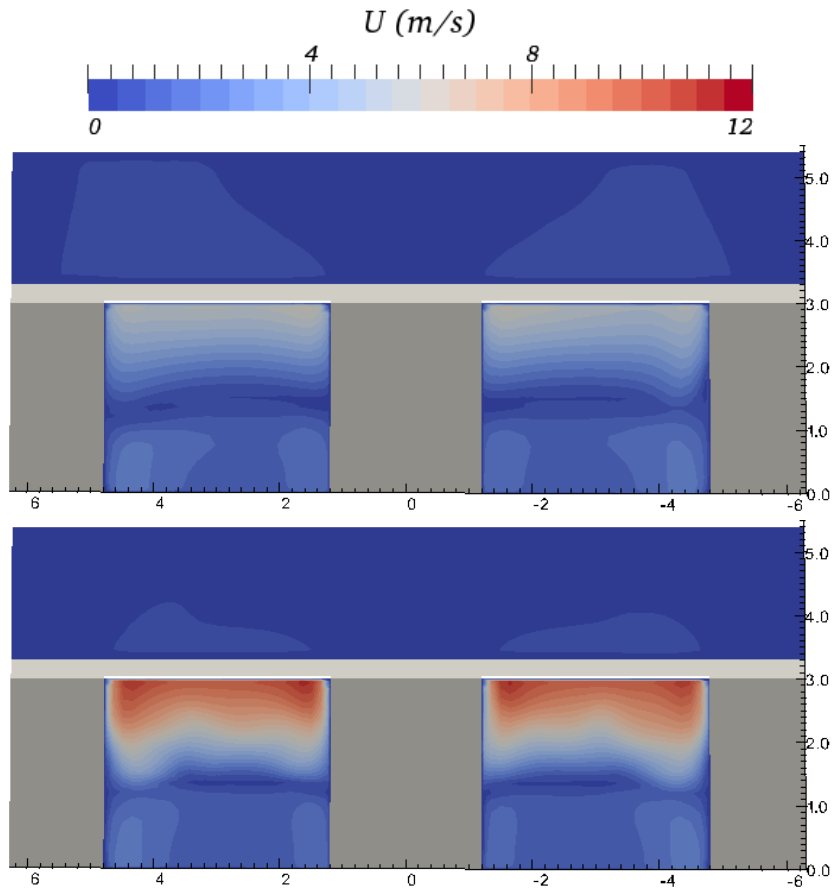


Figure 6.16: Contour plots of velocity magnitude at  $x = 6.3$  m (openings) for time instants  $t = 3$  min (top) and  $t = 30$  min (bottom) (dimensions in m)

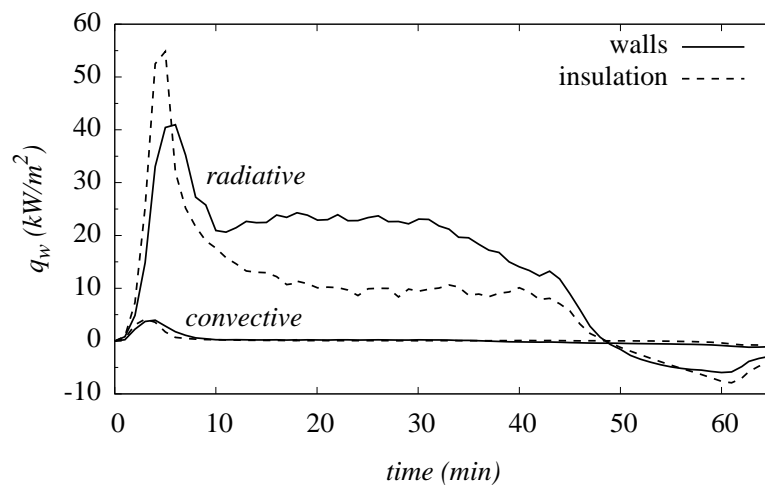


Figure 6.17: Averaged specific heat fluxes at the surfaces of walls and insulation divided into convective and radiative part

## 6.2 The Buxton tunnel-fire test

Within this work, Test 2 of in total 9 tunnel-fire tests in the 366 m long *Buxton Dust Explosion Gallery* [7] is considered for re-analysis. In order to examine a fire event in the Channel Tunnel, the experiments involved a 1:3-scaled model of a train used to carry heavy-goods vehicles (HGV). The modelled train section consisted of the pulling locomotive, the amenity coach, the HGV-loader waggon and a HGV-carrier vehicle carrying two tractor units. The geometry of the tunnel cross-sectional area and the scaled train section are depicted in Figs. 6.18 (*left*) to 6.20. In order to protect the lining of the test tunnel, an insulation was applied in the vicinity of the fire source. Tab. 6.3 lists the thermo-physical properties of the 0.48 m thick concrete tunnel lining and the insulation specified for the CFD simulation.

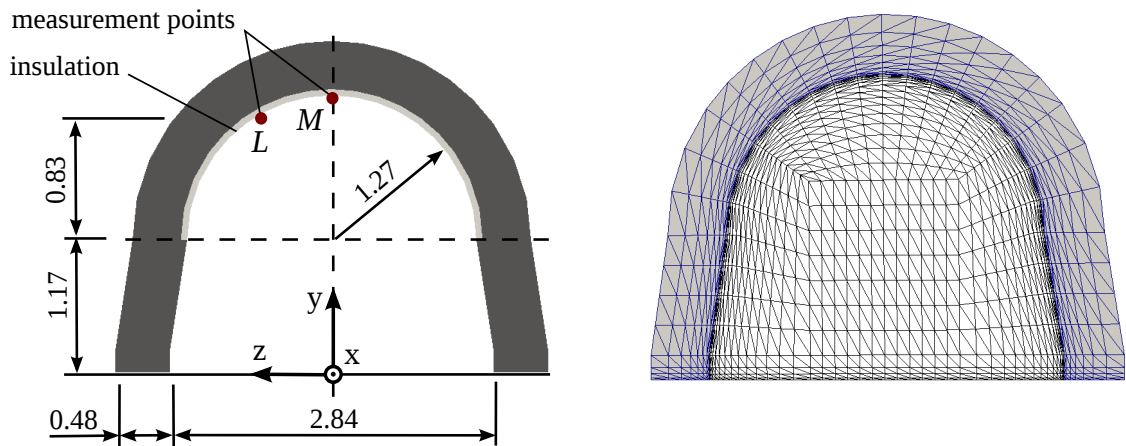


Figure 6.18: Geometry of tunnel cross-section indicating two measurement points ( $M$  and  $L$ ) for surface temperatures (*left*, dimensions in m), and solid and fluid grid at a cross-section far downstream of the fire (*right*)

<i>Element</i>	$\rho$ (kg/m <sup>3</sup> )	$c_p$ (J/kg/K)	$\lambda$ (W/m/K)
concrete lining	2775	900	1.900
insulation	150	800	0.033

Table 6.3: Thermo-physical properties of the Buxton tunnel lining

Throughout the test, the gallery was ventilated with a constant average velocity of 1.1 m/s. The fire source was realised by a 0.94 m<sup>2</sup> kerosene pool fire located at the position  $x = 0$  m (see Fig. 6.19). *Oxygen Consumption Calorimetry* was used to estimate the HRR over



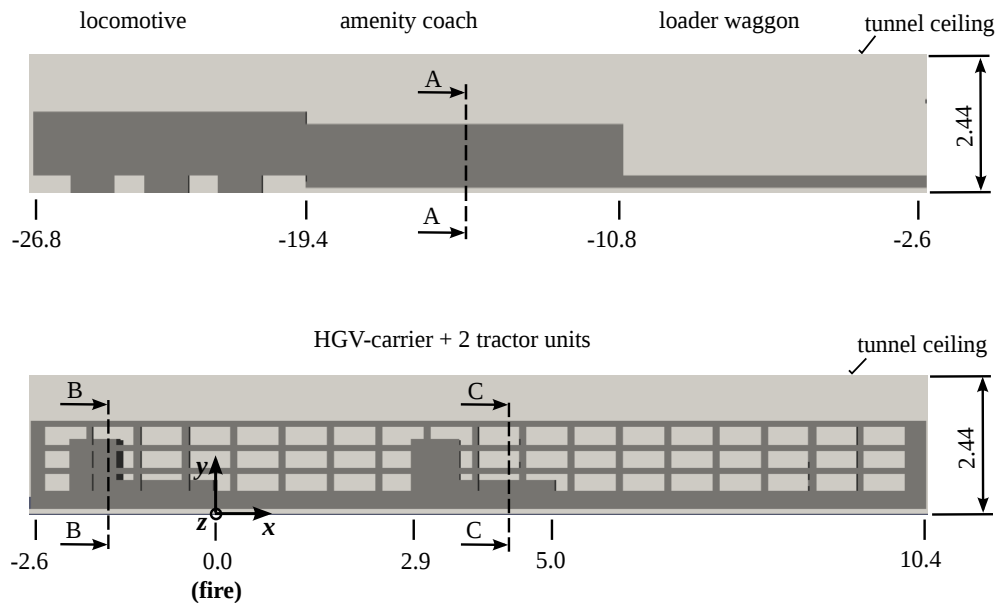


Figure 6.19: Geometry of modelled train section (dimensions in m,  $x = 0$  m corresponds to the location of the fire source)

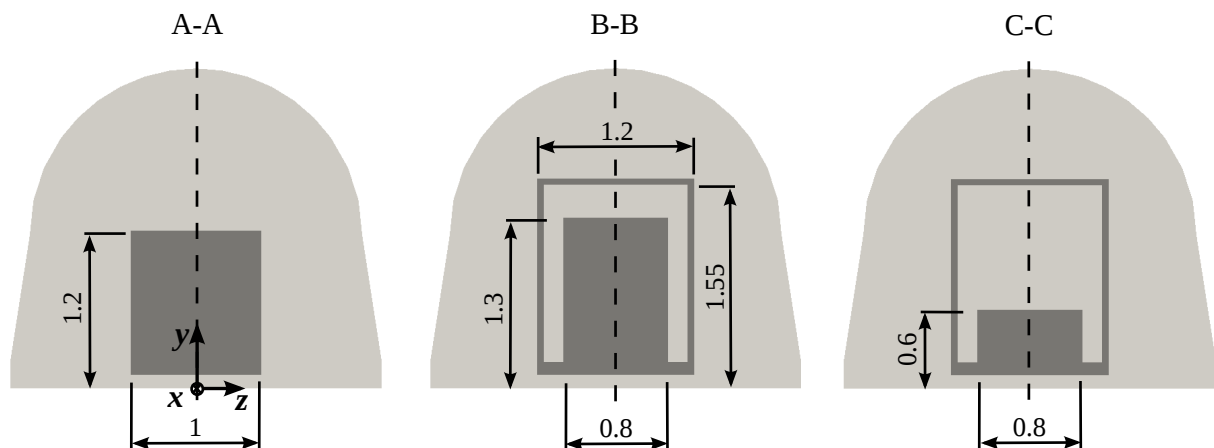


Figure 6.20: Cross-sections A-A, B-B and C-C as indicated in Fig. 6.19 (dimensions in m)

time shown in Fig. 6.21 with a maximum HRR of 2 MW. An additional measurement of the mass-loss rate of kerosene with a load cell allowed to derive the combustion efficiency. Available measurements relevant for the current study are temperatures around the amenity coach, above the HGv-carrier roof, in the vicinity of the fire and 44.5 m and 111.5 m downstream of the fire, respectively. Additionally, the temporal evolution of the back-flow of hot combustion gases at the tunnel ceiling was monitored. Velocity measurements for the considered test presented in [7] are only available for locations around the amenity coach, where the values do not change significantly in the course of fire. Hence, they are not used here. The coordinates of the measurement points used for comparison with the CFD simulations are given in Tab. 6.4. The fluid temperatures given in [7]

were not corrected with respect to radiative interaction of the thermocouples with the surrounding fluid.

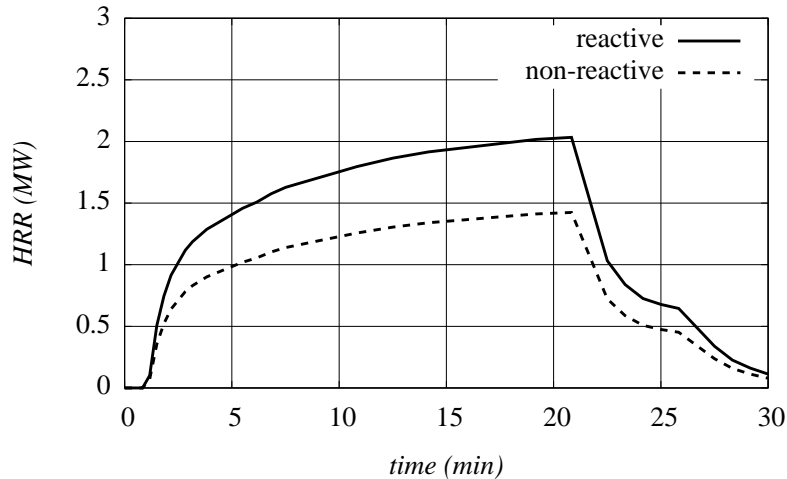


Figure 6.21: HRR-curve of the Buxton tunnel-fire Test 2 [7] applied for the reactive (100% of measured HRR) and non-reactive (70% of measured HRR) simulations

<i>Temperature measurements</i>			
<i>location</i>	<i>x (m)</i>	<i>y (m)</i>	<i>z (m)</i>
above HGV-carrier roof 2 m upstream	-2.0	2.17	0.0
fire below HGV-carrier roof	0.0	1.5	0.0
fire above HGV-carrier roof	0.0	2.17	0.0
above HGV-carrier roof 3 m downstream	3.0	2.22	0.0
44.5 m downstream	44.5	2.21	0.0
111.5 m downstream	111.5	1.75	0.0

Table 6.4: Coordinates of measurement points in the Buxton tunnel used for comparison

The CFD simulations were conducted with the following numerical set-up:

- **Grid:** the computational grid extends from 45 m upstream to 149 m downstream of the fire source neglecting the 1:1000 slope of the test tunnel. The simulated insulation extends over the whole arc of the tunnel cross-section (see Fig. 6.18 (*left*)) and has a thickness of 0.05 m for  $-2.6 \text{ m} \leq x \leq 5 \text{ m}$ , and 0.025 m for  $5 \text{ m} < x \leq 15 \text{ m}$ . The hexahedral grid (see Fig. 6.18 (*right*)) is generated with the *blockMesh*-utility where the train section is modelled by cuboids according to the blocked tunnel area of each part of the train reported in [7]. A grid size of 0.1 m, estimated from  $D^*/10$ , is used in the region close to the fire until 10 m downstream, whereas 0.2 m is used in the remaining region. The fluid grid is refined around the blockage and adjacent to the tunnel lining to keep the dimensionless wall distance

to  $30 < y^+ < 100$  for a correct application of the wall-function approach [14]. This results in a total cell number of approximately 915,000 with approximately 652,000 cells in the fluid region.

- **Boundary conditions:** at the tunnel inlet, a developed velocity profile corresponding to the ventilation condition of 1.1 m/s is prescribed, which was obtained from a previous incompressible simulation with *simpleFoam* excluding the blockage. Pressure is set to *zeroGradient*, temperature, mixture fraction and fuel-mass fraction (reactive case) to *fixedValues* of 281 K and zero, respectively, at the inlet.  $k$  and  $\varepsilon$  at the inlet are estimated with  $Tu = 0.5\%$  and  $l_m = 2.47/15$  m from Eqns. (5.33) and (5.34), where 2.47 m is the hydraulic diameter of the tunnel cross-section. At the outlet, *zeroGradient* for velocity, a *fixedValue* of 101325 Pa for  $p_{rgh}$  and *inletOutlet* for temperature,  $k$  and  $\varepsilon$ , mixture fraction and fuel-mass fraction are specified with *inletValues* of 281 K,  $1 \cdot 10^{-6}$  m<sup>2</sup>/s<sup>2</sup>,  $1 \cdot 10^{-9}$  m<sup>2</sup>/s<sup>3</sup> and zero, respectively. The floor is considered as adiabatic, whereas conjugate heat transfer including radiation with application of temperature wall-functions are applied at the fluid and tunnel-lining interface. In preliminary simulations, the conjugate heat transfer between fluid and blockage was enabled, resulting in high absorption of heat by the blockage leading to a delayed increase of fluid temperatures. Based on the fact that no detailed information on the thermo-physical properties of the blockage is available, these predictions are not considered reliable. Thus, the case with an adiabatic blockage is analysed in the following. The surface emissivity  $\epsilon$  of all surfaces is set to 0.8 [2].

For the BCs in the solid regions of concrete tunnel lining and insulation, the conjugate heat transfer is enabled at the fluid interface and the concrete-insulation interface, whereas a constant temperature of 281 K is assumed at the remaining boundary interfaces for the concrete lining, i.e. at the floor, inlet, outlet and outer surface.
- **Initial conditions:** the initial velocity field is obtained from an incompressible simulation with the developed velocity profile at the inlet including the blockage using *simpleFoam*. The initial temperature field is set to 281 K.
- **Heat source:** the heat source is located inside the HGV-carrier and its extension starts at  $x = 0$  m. For the non-reactive case, a volumetric heat source is used in the same way as explained for the Cardington test (see Chapter 6.1) only considering the convective portion of the HRR. Preliminary simulations showed that considering 80% of the total HRR, as recommended in [2], resulted in a strong overestimation of temperature measurements. Hence, only 70% of the measured HRR with a total volume of the heat source of 3 m<sup>3</sup> are considered (see Fig. 6.21). In the reactive simulation, the fire is modelled in the same way as for the Cardington test (see Chapter 6.1) by a methane diffusion flame. The gas burner has a quadratic inlet of 1 m side length and the time-dependent fuel-mass flow rate is prescribed using

the *timeVaryingFlowRateInletVelocity* BC in order to realise the HRR-time curve depicted in Fig. 6.21. At the patch of fuel inlets, *buoyantPressure* is prescribed for  $p_{rgh}$ , a fixed value of 281 K for temperature, and the values for mixture fraction and fuel mass-fraction are calculated according to Eqn. (5.76) with 1 as value at infinity. The inlet values for  $k$  and  $\varepsilon$  are calculated with  $Tu_{in} = 0.5\%$  and  $l_m = 1/15$  m by the BCs *turbulentIntensityKineticEnergyInlet* and *turbulentMixingLengthDissipationRateInlet*.

- **Thermo-physical properties:** the fluid properties for the non-reactive and reactive case are determined in the same way as for the Cardington simulations (see Chapter 6.1). The thermo-physical parameters for the solid materials are assumed independent of temperature and are given in Tab. 6.3.
- **Discretisation:** the same settings as in the Cardington test (see Chapter 6.1) are used.

In both the reactive and non-reactive case, the  $k$ - $\varepsilon$  turbulence model with the SGDH<sub>2</sub> buoyancy modification is used. The time step is calculated from a constant  $Co = 0.8$  (Eqn. (6.3)). The calculations are parallelised on 16 CPUs using domain decomposition (scotch method) which results in approximately 57000 cells per CPU.

### 6.2.1 Results and discussion

During preliminary simulations, it was observed that the pressure BC at the tunnel outlet played a crucial role in the reactive case. Serious numerical instabilities in the flow field including back-flow at the outlet were caused when fixing the pressure to 101325 Pa. A thorough investigation of the phenomena revealed pressure waves as the origin of these instabilities. The pressure waves moved downstream from the upstream end of the train and were reflected at the outlet. The application of a non-reflective BC, the *waveTransmissive* BC, allowed the pressure waves to leave the domain and avoided these instabilities. Applied on the pressure field, the *waveTransmissive* BC determines the boundary value by solving an advection equation for pressure as described in [75]. The relaxation of the value at the boundary to a specified far-field value,  $p_\infty$ , is accomplished by specifying a relaxation length scale,  $l_\infty$ . In the present case,  $p_\infty$  is set to 101325 Pa, whereas numerical simulations showed best results with  $l_\infty$  equal to two times the tunnel length, leading to  $l_\infty = 388$  m in the presented simulations.

Figs. 6.22 to 6.27 show evolutions of fluid temperatures at the locations mentioned in Tab. 6.4 at the symmetry axis of the tunnel cross-section ( $z = 0$  m; time series of contour plots of temperature at  $z = 0$  m for the reactive and non-reactive case are depicted in Appendix D). The results at 2 m upstream of the fire (see Fig. 6.22) show a faster increase and an overestimation of temperature compared to the experiment with both the non-reactive

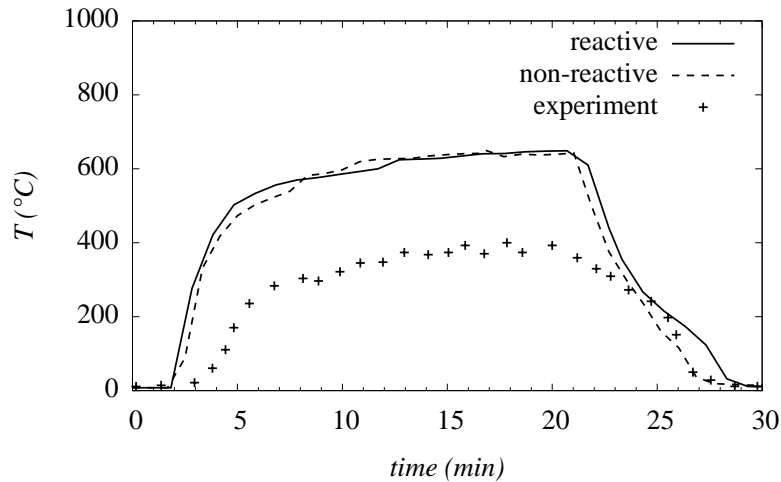


Figure 6.22: Temperature evolution 2 m upstream of the fire above the HGV-carrier roof ( $y = 2.17$  m)

and reactive approach. At this position, the temperature is mainly influenced by the hot gases which originate from the back-flow under the carrier roof (see Fig. 6.28). The gas portion which is in constant contact with the carrier roof flows upstream without exchanging heat with the blockage, as the latter is assumed adiabatic in the simulations. Hence, the predicted temperatures are higher than the values observed in the experiment. A similar explanation can be given for the overestimation of temperatures at the fire below the HGV-carrier roof (see Fig. 6.23), whereas the overshoot for the reactive case between  $t = 5$  and 12 min is caused numerically from the combination of the  $\text{SGDH}_2$  turbulence model and the EDM combustion model<sup>1</sup>. It is worth mentioning, that the instability in the flame region is not affecting the results significantly at other measurement points. The effect of the adiabatic blockage is reduced for the other positions located above the HGV-carrier roof (see Figs. 6.24 and 6.25). At the fire source above the HGV-carrier (see Fig. 6.24), the hot gases come from positions where they immediately escape the carrier without touching a great portion of the roof (see Figs. 6.31 and 6.32). Similarly, at the measurement point 3 m downstream (see Fig. 6.25), the flow below the roof is stronger directed in longitudinal direction by the ventilation than observed further upstream (see Figs. 6.31 and 6.32). Consequently, the hot gases are pushed downstream under the carrier roof and a smaller amount escapes from the lateral openings to the upper part of the tunnel. However, the influence of the thermal inertia of the blockage is exhibited at the position 3 m downstream of the fire during the decay phase ( $t > 20$  min, see Fig. 6.25). In the stage of fire decay, the blockage which was heated during the experiment releases thermal energy resulting in a slower decrease of temperature measurements than predicted by the simulations.

<sup>1</sup>This behaviour is not observed when applying the standard  $k-\varepsilon$  model in combination with the EDM combustion model.

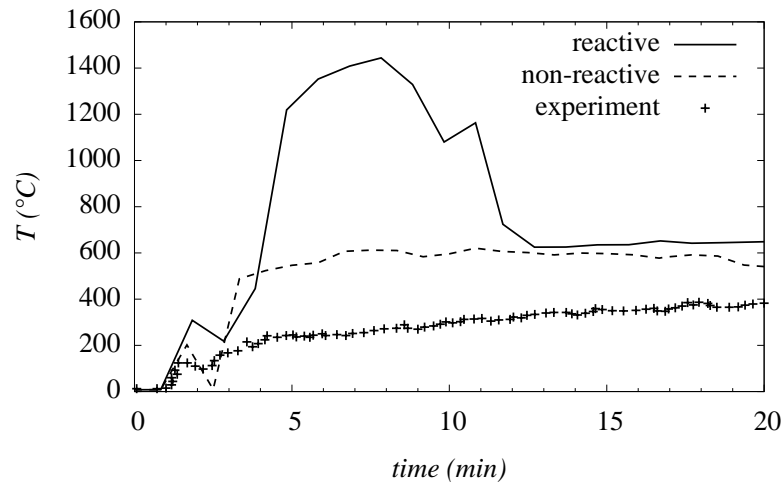


Figure 6.23: Temperature evolution at the fire source below the HGV-carrier roof ( $y = 1.5$  m)

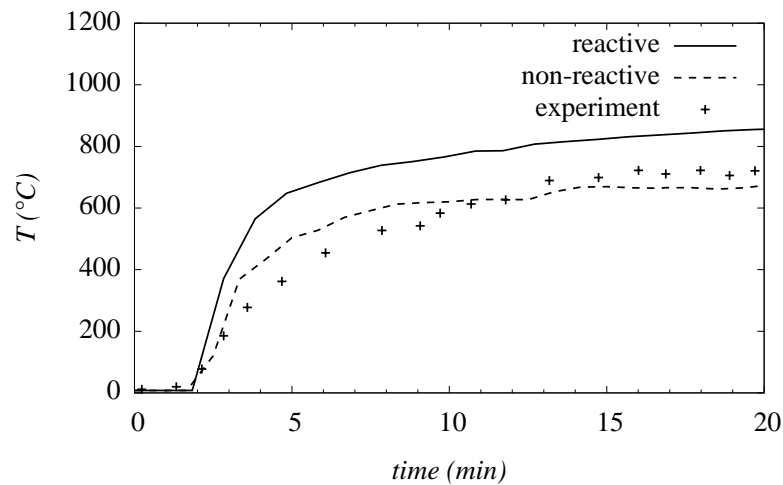


Figure 6.24: Temperature evolution at the fire source above the HGV-carrier roof ( $y = 2.17$  m)

In the contour plots of velocity depicted in Fig. 6.32, the typical vortices at the tunnel ceiling in the vicinity of the fire source can be identified. The temperature distribution depicted in Fig. 6.29 follows the vortex-shape for the non-reactive case, whereas in case of the reactive simulation, a more homogeneous fluid temperature is predicted (see Fig. 6.29 (*top*)). This comes from the homogeneous field of incident radiation,  $G$ , in consequence of radiation which is absorbed by the fluid. The predictions of similar temperature levels in the vicinity of the fire source for the reactive and the non-reactive approach, supports the assumption, that 30 % of the fire's HRR is transported via radiation in this region. However, greater deviations between results produced with the two approaches are observed

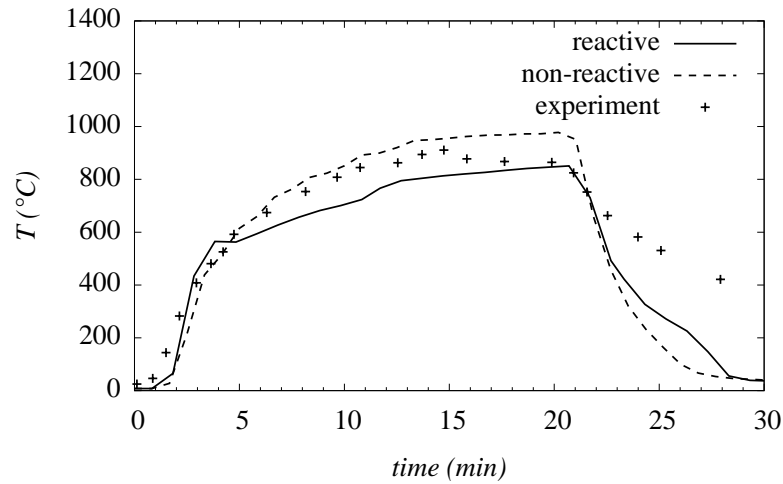


Figure 6.25: Temperature evolution 3 m downstream of the fire above the HGV-carrier roof ( $y = 2.22$  m)

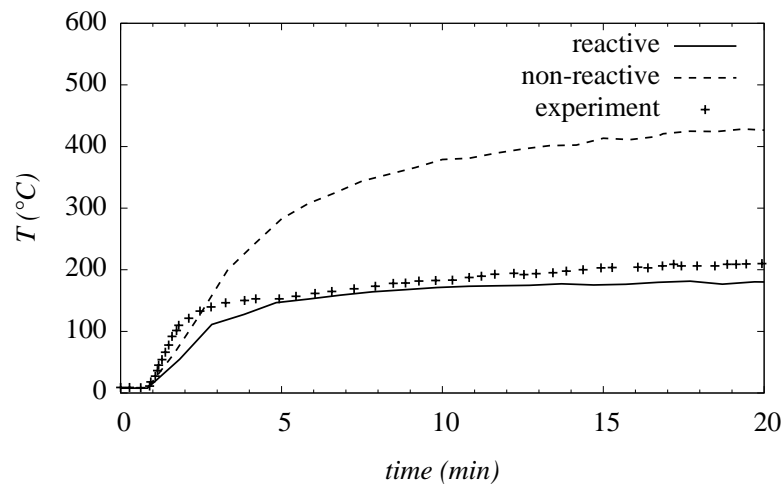


Figure 6.26: Temperature evolution 44.5 m downstream of the fire ( $y = 2.21$  m)

far more downstream of the fire (see Figs. 6.26, 6.27 and 6.30), where the non-reactive case overestimates the measured temperatures, also leading to higher velocities than in the reactive case (see Fig. 6.33). Radiation errors in the temperature measurements which were not considered in [7] are expected to be negligible due to low temperature levels ( $< 200$  °C) at these locations.

Discrepancies between results obtained with the two approaches are mainly a consequence of the fact that within the non-reactive approach, radiative heat transfer in the fluid and between the fluid and the tunnel lining is not taking into account. Tab. 6.5 lists the averaged specific wall-heat fluxes of the insulation and concrete lining at 15 min, where in total more energy is absorbed by the concrete tunnel lining in the reactive case. The dominance of radiative heat transfer in the reactive case can also be seen in

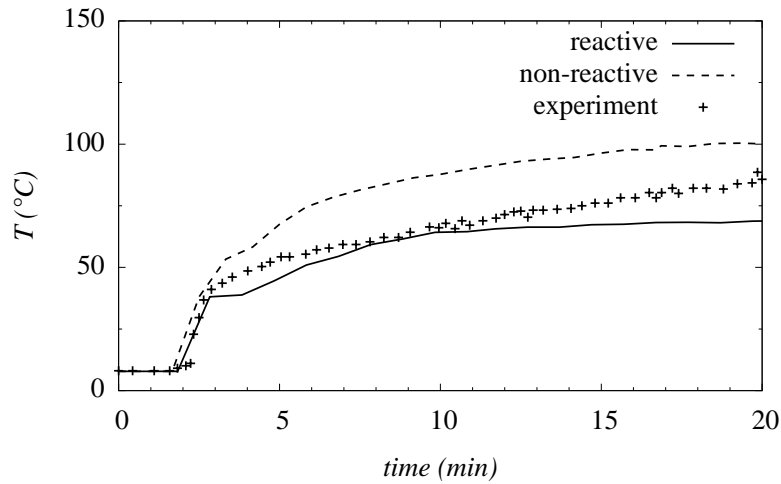


Figure 6.27: Temperature evolution 111.5 m downstream of the fire ( $y = 1.75$  m)

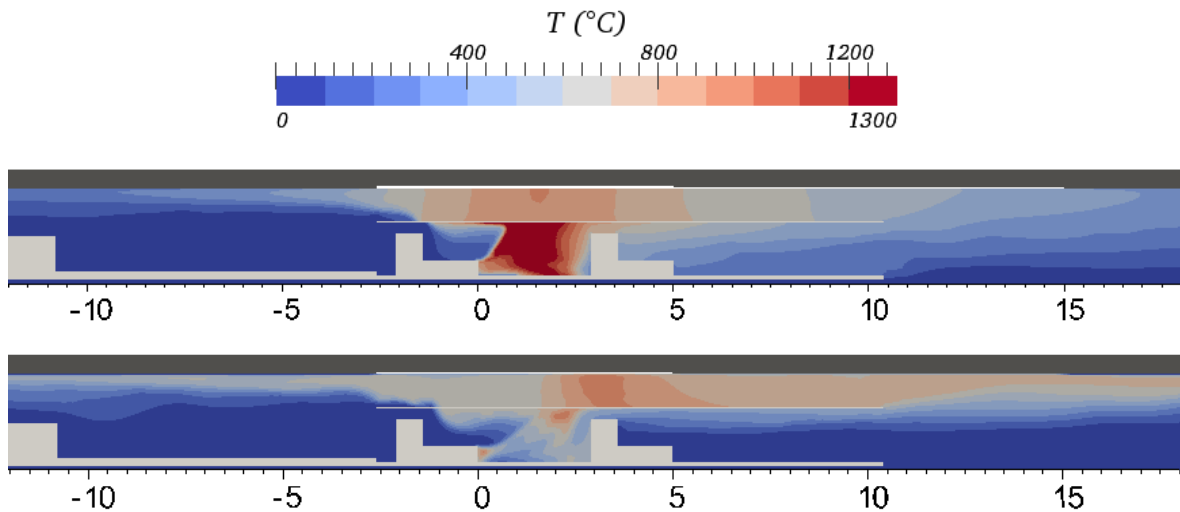


Figure 6.28: Contour plots of temperature at  $z = 0$  m for  $t = 15$  min for the reactive (*top*) and non-reactive case (*bottom*) (dimensions in m)

Fig. 6.34 with its peak in the vicinity of the fire where the highest temperatures are encountered. Fig. 6.34 shows, that in average only the insulation releases heat during the decay-phase. However, contour plots of the wall-heat fluxes indicate a local heat release of the concrete lining near the fire source due to high surface temperatures. The temperature field over the tunnel cross-section at the downstream positions depicted in Fig. 6.30, show a more homogeneous distribution for the reactive case, which can be attributed to the absorption of radiation by the fluid not taken into account by the non-reactive simulation. The difference of predictions between the two approaches decreases with increasing downstream distance from the fire as a result of lower temperature levels (compare Figs. 6.26 and 6.27). The decreasing influence of radiative heat transfer is shown by the contour plot of specific radiative wall-heat flux in Fig. 6.35.



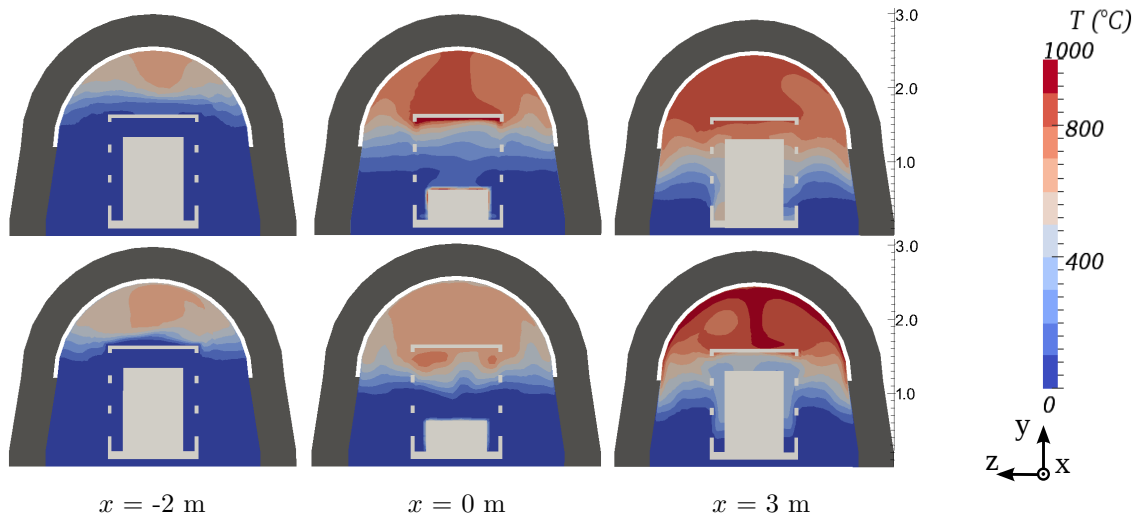


Figure 6.29: Contour plots of temperature at  $x = -2, 0$  and  $3$  m for  $t = 15$  min for the reactive (*top*) and non-reactive (*bottom*) case (dimensions in m)

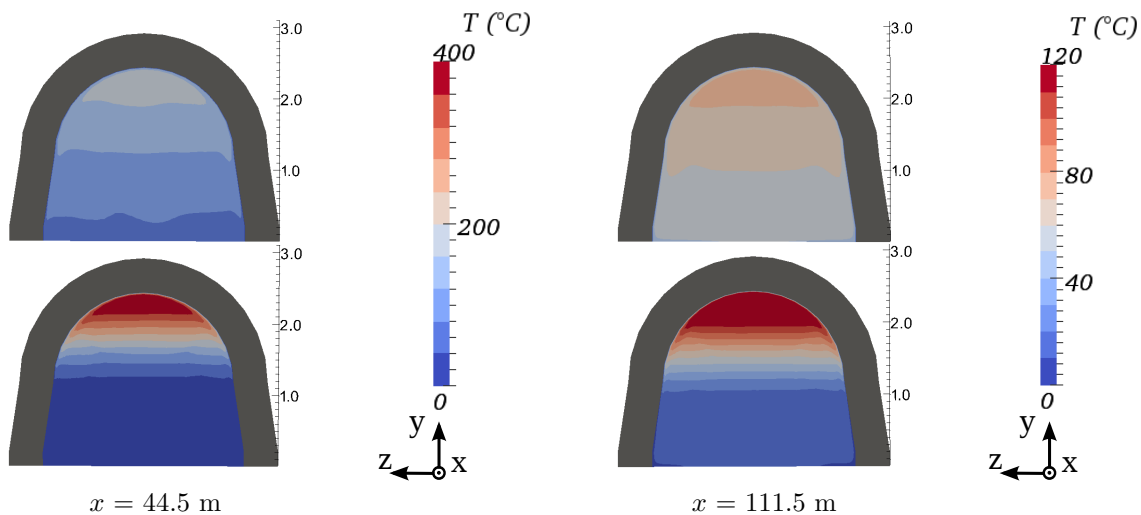


Figure 6.30: Contour plots of temperature at  $x = 44.5$  and  $111.5$  m for  $t = 15$  min for the reactive (*top*) and non-reactive (*bottom*) case (dimensions in m)

In Fig. 6.36, the surface temperature of the insulation along the longitudinal direction of the tunnel at a height of approximately 2 m (point  $L$  in Fig. 6.18 (*left*)) is depicted. At this height and between a longitudinal distance of  $1 \text{ m} \leq x \leq 2 \text{ m}$ , the hot combustion gases exit the HGV-carrier and therefore the highest temperatures are obtained. In this area, the reactive case predicts higher temperatures but a faster decrease in downstream direction than the non-reactive case. The same behaviour is observed for the surface temperatures at the concrete tunnel ceiling (point  $M$  in Fig. 6.18 (*left*) with  $x \leq -2.6 \text{ m}$  and  $x \geq 15 \text{ m}$ , see Figs. 6.37 and 6.38) as a result of additional radiative heat transfer to colder lining surfaces and colder fluid regions in the reactive case.

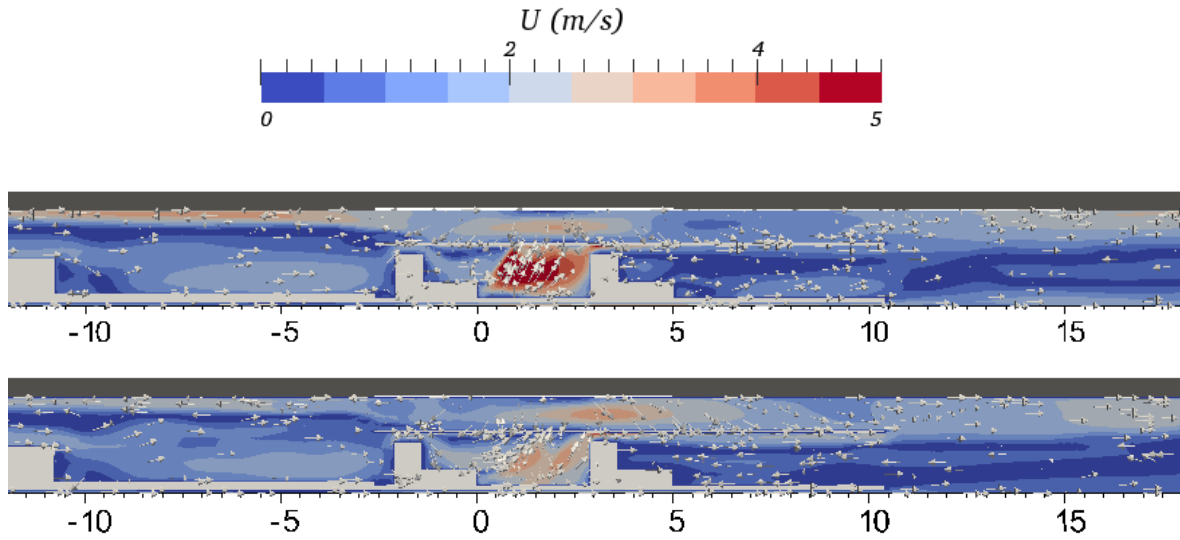


Figure 6.31: Contour plots of velocity magnitude at  $z = 0$  m for  $t = 15$  min for the reactive (*top*) and non-reactive (*bottom*) case (dimensions in m)

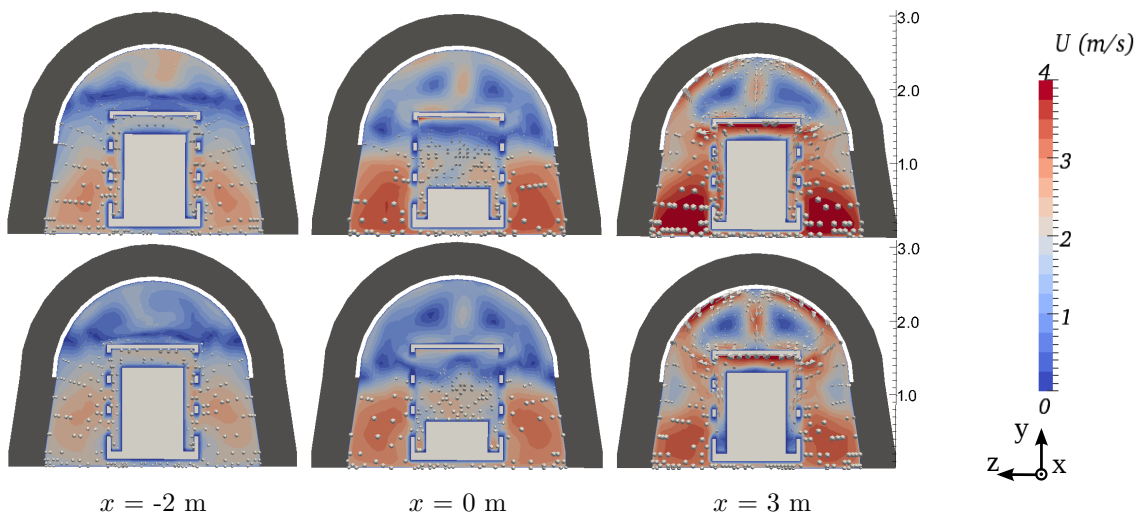


Figure 6.32: Contour plots of velocity magnitude at  $x = -2, 0$  and  $3$  m for  $t = 15$  min for the reactive (*top*) and non-reactive (*bottom*) case (dimensions in m)

In the experiment, the upstream movement of hot combustion gases was monitored in order to determine the back-layering distance. It was observed that the back-flow stopped above the middle of the locomotive, i.e. at  $x \approx -23$  m. The predicted temporal evolution of the back-layering distance is depicted in Fig. 6.39. In order to study the difference between the application of the standard and the  $\text{SGDH}_2$   $k-\varepsilon$  turbulence model in a tunnel geometry, the reactive case was also simulated with the standard model. Whereas similar results for velocity and temperatures were obtained with the two approaches, the only significant difference in the results is seen in the back-flow of the hot gases. While the standard model shows good agreement with the experiment at the beginning of the fire,

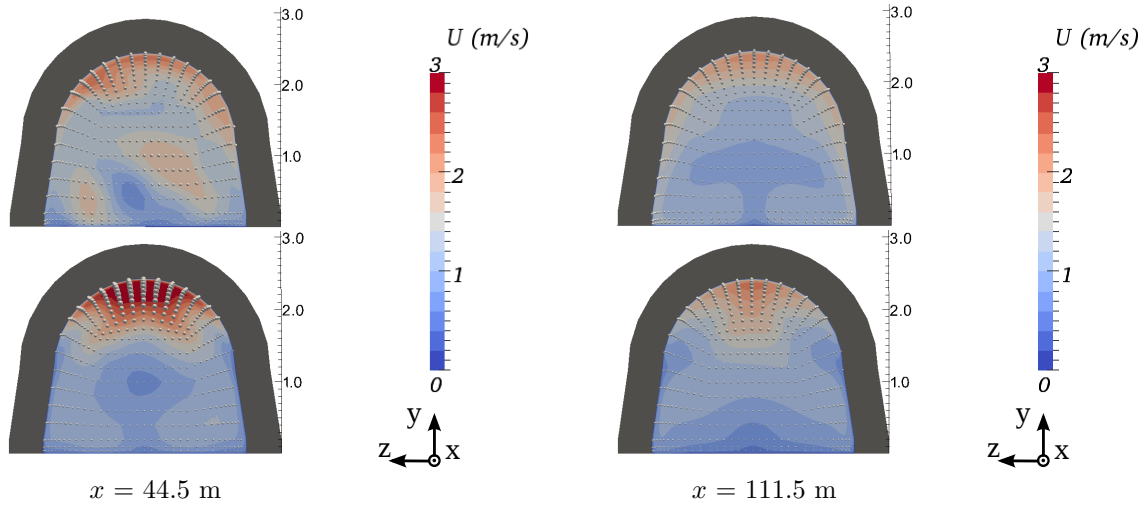


Figure 6.33: Contour plots of velocity magnitude at  $x = 44.5$  and  $111.5$  m for  $t = 15$  min for the reactive (*top*) and non-reactive (*bottom*) case (dimensions in m)

<i>wall-heat flux</i> (W/m <sup>2</sup> )	<i>reactive case</i>		<i>non-reactive case</i>	
	<i>insulation</i>	<i>concrete</i>	<i>insulation</i>	<i>concrete</i>
convective	140	600	970	930
radiative	860	850	0	0
total	1000	1450	970	930

Table 6.5: Averaged specific wall-heat fluxes of concrete lining and insulation at  $t = 15$  min for the reactive and non-reactive case

the back-layering distance is underestimated with increasing duration of the fire. The  $SGDH_2$  predicts a faster back-flow of the hot gases but this overestimation significantly decreases with increasing fire duration, suggesting good correspondence in later stages (since the tendency of the measured back-layering distance is still increasing at the end of measurements). The reason for the discrepancies between the standard and  $SGDH_2$  model in the current case is a negative production of turbulence due to buoyancy,  $G_{SGDH}$ , in the  $k$ -equation (Eqn. (5.38)) for the  $SGDH_2$  model close to the tunnel ceiling in consequence of a negative density gradient. This in turn leads to a lower eddy viscosity,  $\mu_t$ , and thus to a lower resistance for the back-flow. In the non-reactive simulation, the hot gases move back to the tunnel inlet due to the higher temperatures resulting in a greater expansion of the fluid against the ventilation direction. This leads to an unreasonable prediction of the back-layering phenomena by the non-reactive simulation.

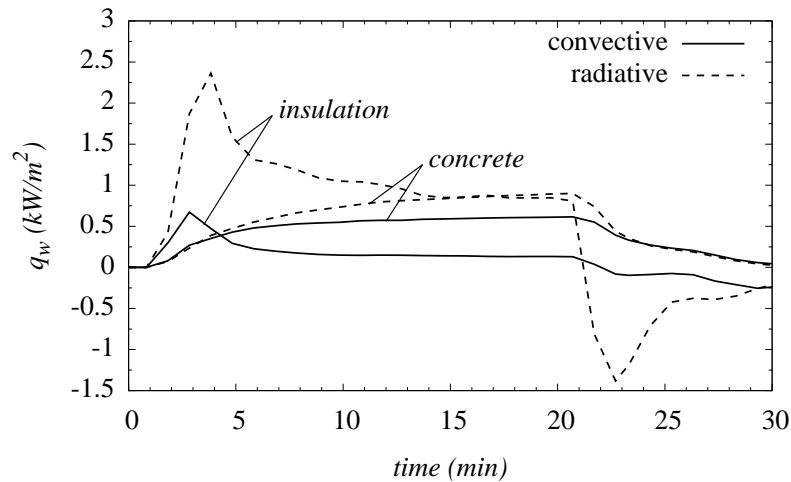


Figure 6.34: Evolution of averaged specific wall-heat fluxes at concrete lining and insulation divided into convective and radiative part for the reactive case

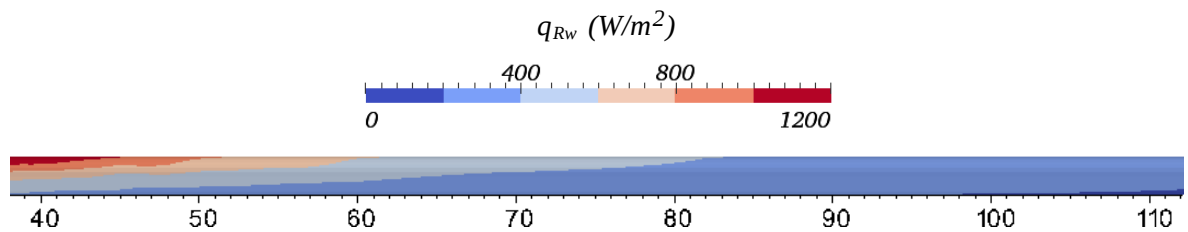


Figure 6.35: Contour plot of specific radiative wall-heat flux,  $q_{Rw}$ , downstream of the fire source at  $t = 15$  min (dimensions in m)

## 6.2.2 Conclusions

From the obtained numerical results it can be concluded that the reactive simulation exhibited satisfactory agreement with the experimental data in terms of fluid temperatures. With the non-reactive approach, reasonable temperature levels were obtained above the fire but gas temperatures upstream and far downstream of the fire were overestimated, which is attributed to neglecting radiative heat transfer. As a result of these discrepancies, the back-flow of hot gases was strongly overestimated. A further drawback of the non-reactive approach is the influence of choosing the radiative fraction of the total HRR which depends on the type of fuel and the fire size. Although, none of the applied turbulence models, i.e. the standard and the  $\text{SGDH}_2$   $k$ - $\varepsilon$  model, was able to predict the development of the back-flow distance accurately, the  $\text{SGDH}_2$  approach showed by trend the best agreement with the measured final back-layering distance. From the plots of surface temperatures it can be seen that the reactive approach predicts higher peak temperatures than the non-reactive approach which locally differ up to  $150$  °C. Even though the lining absorbs in total more energy in case radiation is taken into account, the shown surface temperatures decrease faster with increasing distance from the fire source than

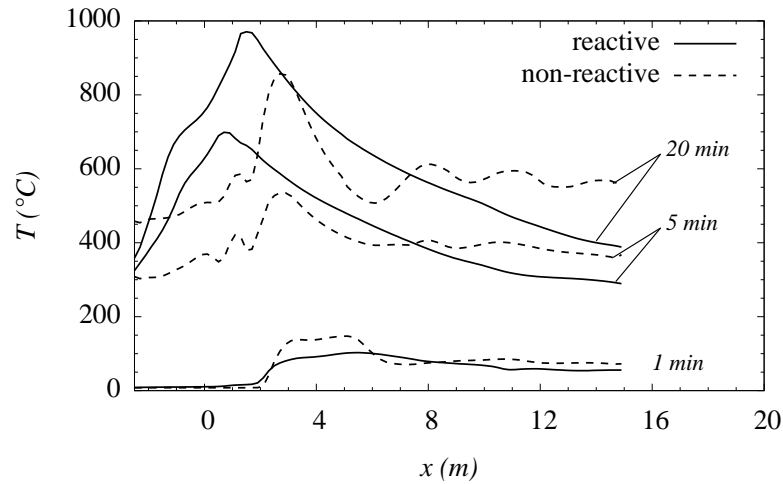


Figure 6.36: Surface temperatures of the insulation along the longitudinal direction of the tunnel (point  $L$  in Fig. 6.18 (left)) at different time instants for the reactive and non-reactive case

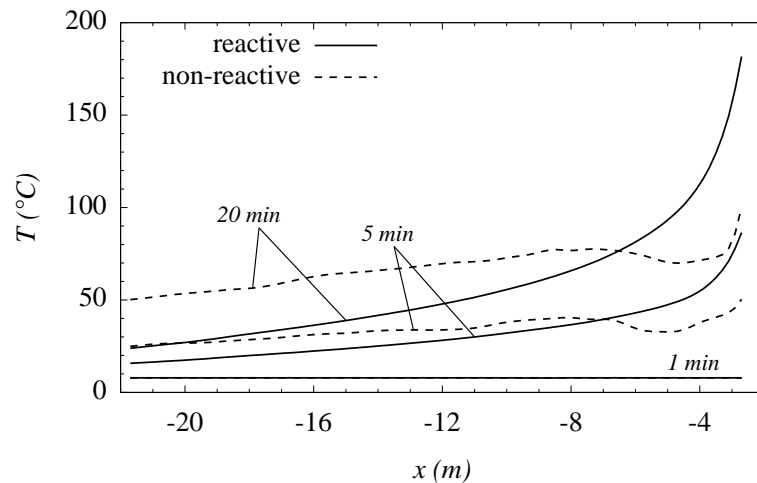


Figure 6.37: Surface temperatures at the highest regions of the concrete lining (point  $M$  in Fig. 6.18 (left)) upstream of the fire at different time instants for the reactive and non-reactive case

for the non-reactive case as a result of radiative heat exchange with colder lining regions. Thus, it can be concluded that radiative heat transfer has a non-negligible influence on both solid and fluid temperatures.

A comparison of CPU-time spent for the non-reactive and the reactive analysis showed a ratio of 1:1.5. The 1.5-times longer simulation time for the reactive case is due to the computation of additional equations for radiation (12 directions) as well as the mixture fraction and fuel-mass fraction for the combustion model. As can be seen in the results, the longer simulation time is justified by predictions of better quality.

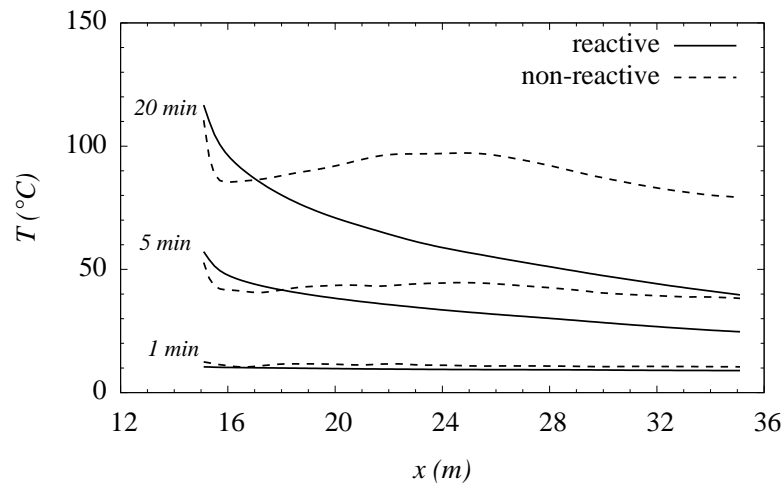


Figure 6.38: Surface temperatures at the highest regions of the concrete lining (point *M* in Fig. 6.18 (left)) downstream of the fire at different time instants for the reactive and non-reactive case

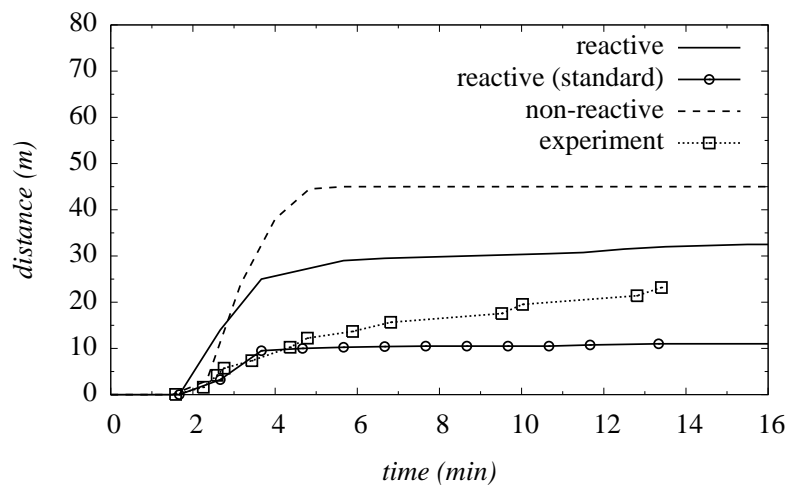


Figure 6.39: Evolution of back-layering distance

### 6.3 Real-scale tunnel configurations

Two types of double-track railway-tunnel cross-sections are investigated, i.e. a rectangular and an arced cross-section depicted in Figs. 6.40 and 6.41 with the same cross-sectional area of approximately  $79 \text{ m}^2$ . The blockage's geometry complies with the railway-loading gauge GC, defined by the *International Union of Railways (UIC)* [85] representing a double-decker coach as used, e.g. by the Austrian Federal Railways (*Österreichische Bundesbahnen (ÖBB)*). The fire source (corresponding to  $x = 0 \text{ m}$ ) is placed 5 m upstream of the upstream end of the train at a height of 2 m (see Fig. 6.42). The evolution of the fire's HRR is derived from the HRR-time curve of a passenger carrier with a peak value of 25 MW, given by the *Deutsche Bahn* [3] presented in Chapter 3.2. In the underlying case, periodic fire spread to waggons at downstream positions is assumed, temporarily leading to a maximum HRR of 34 MW which after averaging gives a constant peak value of 28 MW. Furthermore, a faster fire growth is prescribed, taking into account the excess oxygen in case of fire in a moving train. Hence, a fully developed fire is attained at 15 min corresponding to a growth rate of  $\alpha_q = 31 \text{ W/s}^2$ , whereas an exponential decay starting at 60 min with a coefficient of  $\alpha_d = 0.001 \text{ s}^{-1}$  [42] is assumed, representing the combustion of two waggons (see Fig. 6.43). The same assumptions (except for fire duration and decay) were used to develop a design fire scenario for ventilation design in the *Semmering-Basistunnel Neu, Austria* [51].

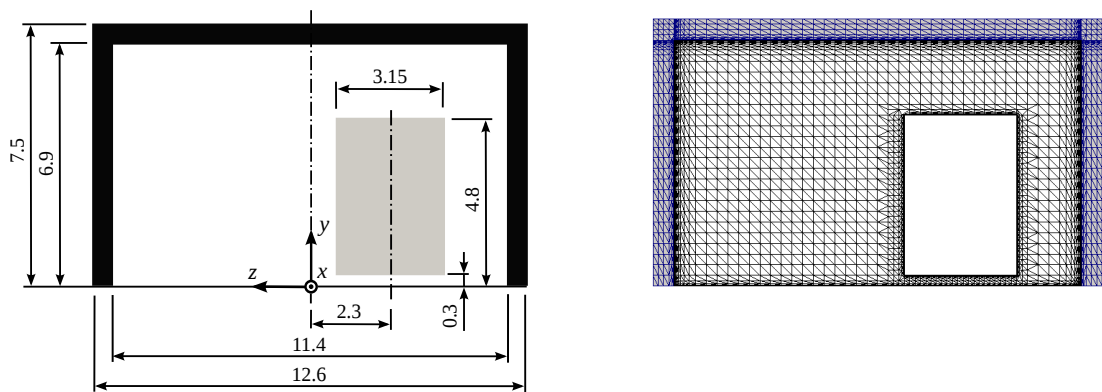


Figure 6.40: Geometry of the rectangular tunnel cross-section (*left*, dimensions in m) and solid and fluid grids at a cross-section far downstream of the fire (*right*)

The fires in the rectangular and arced tunnel cross-section are studied assuming two ventilation velocities (0.5 m/s and 3 m/s, respectively) covering the range of typical velocities in tunnels. The ventilation velocity of 0.5 m/s represents the case of natural ventilation which can be caused by the pressure difference between inlet and outlet of the tunnel due to meteorological effects. On the other hand, the ventilation velocity of 3 m/s represents an upper limit of the critical velocity needed to avoid back-layering. In [56], different correlations for the critical velocity are studied as well as different experiments aiming to identify the critical velocity as a function of the HRR, also suggesting 3 m/s as

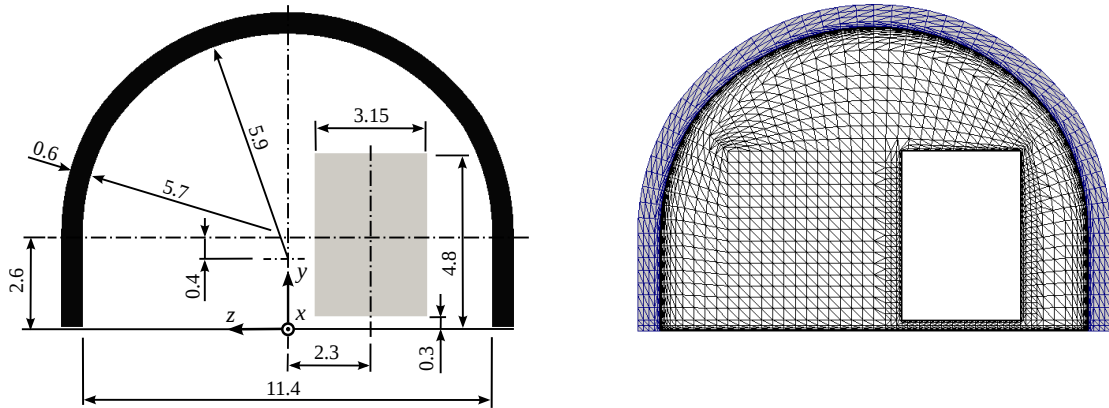


Figure 6.41: Geometry of the arced tunnel cross-section (*left*, dimensions in m), and solid and fluid grids at a cross-section far downstream of the fire (*right*)

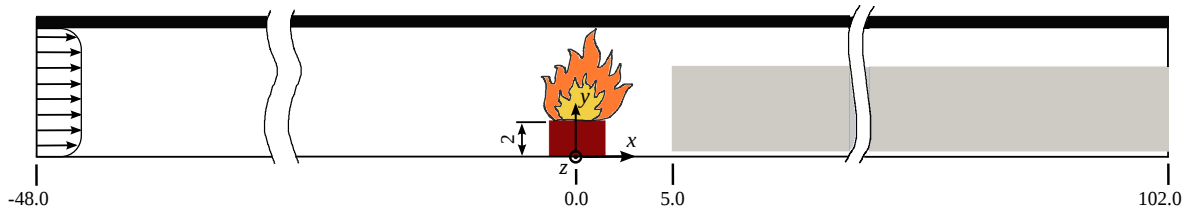


Figure 6.42: Section at  $z = -2.3$  m indicating the tunnel ventilation at the tunnel inlet (dimensions in m,  $x = 0$  m corresponds to the location of the fire source)

upper limit for the critical velocity. The main focus of the underlying CFD-analyses lays on the following issues and their dependency on the used cross-section and ventilation velocity:

- Temperature stratification in cross-sections at the longitudinal positions  $x = -20, 0, 13, 25, 50$  and  $100$  m. The cross-section at  $x = 13$  m corresponds to a downstream distance from the fire source of half a waggon length, representing the closest position to the fire, firefighters might be able to approach. The focus lays on the identification of the hot gas layer at the center-line of the tunnel ( $z = 0$  m) which radiates a heat flux of approximately  $4 - 5$  kW/m<sup>2</sup> downwards to the floor, representing the tenability limit of thermal radiation for firefighters [10, 28]. Assuming  $\epsilon = 1$  for the hot layer and a view-factor from a point at the floor of one, this would correspond to a temperature limit of approximately  $240 - 270$  °C. As both the assumptions are conservative and the absorption of radiation by the participating medium is not taken into account, a temperature limit of  $300$  °C is considered here.
- Development of maximum fluid temperature compared to standard temperature-time curves.
- Development of radiative and convective wall-heat fluxes and lining temperatures.



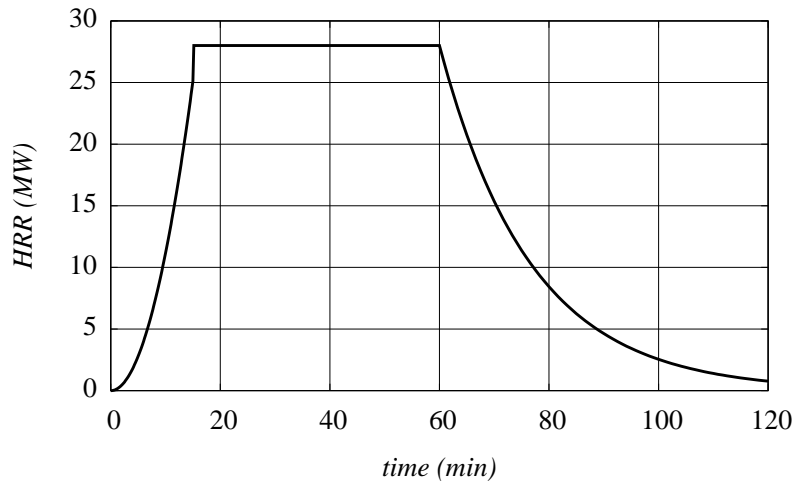


Figure 6.43: Evolution of the HRR for the real-scale tunnel fires

Determination of the convective heat-transfer coefficient,  $\alpha_c$ , and comparison with recommendations in respective standards.  $\alpha_c$  is obtained from the simulations using the definition

$$\alpha_c := \frac{q_w}{T_f - T_w}, \quad (6.4)$$

where  $T_f$  is the fluid temperature at the grid point adjacent to the wall.

- Temperature development across the thickness of concrete lining.

For all the CFD simulations, the following numerical set-up is employed:

- **Grid:** the computational grid extends from 48 m upstream to 102 m downstream of the fire source (see Fig. 6.42). The hexahedral grids (see Figs. 6.40 (*right*) and 6.41 (*right*)) are generated with the *blockMesh*-utility with a grid size of 0.3 m, estimated from  $D^*/10$ . The grids are refined at the burner outlet, around the blockage and in areas adjacent to the tunnel lining to keep the dimensionless wall distance to  $30 < y^+ < 100$  for a correct application of the wall-function approach [14], and is coarsened towards the outlet. This results in approximately 1,686,000 cells in the fluid region and 342,000 cells in the tunnel-lining region for the rectangular cross-section, and 1,355,000 cells in the fluid region and 210,000 cells in the tunnel-lining region for the arced cross-section.
- **Boundary conditions:** at the tunnel inlet, a developed velocity profile corresponding to the desired ventilation condition of 0.5 m/s and 3 m/s is prescribed. Pressure is set to *zeroGradient*, temperature, mixture fraction and fuel-mass fraction to *fixedValues* of 291 K and zero, respectively, at the inlet.  $k$  and  $\varepsilon$  at the

inlet are estimated with  $Tu = 0.5 \%$  and  $l_m = d_h/15$  m from Eqns. (5.33) and (5.34), with a hydraulic diameter of the tunnel cross-sections,  $d_h$ , of approximately 8.5 m. At the outlet, *zeroGradient* for velocity and *inletOutlet* for temperature,  $k$  and  $\varepsilon$ , mixture fraction and fuel-mass fraction are specified with *inletValues* of 291 K,  $1 \cdot 10^{-6}$  m<sup>2</sup>/s<sup>2</sup>,  $1 \cdot 10^{-9}$  m<sup>2</sup>/s<sup>3</sup> and zero, respectively. For  $p_{rgh}$  at the outlet, the *waveTransmissive* BC is prescribed using  $p_\infty = 101325$  Pa and  $l_\infty$  equal to double of the modelled tunnel length, i.e. 300 m. The floor and the train are considered as ideally insulated, whereas conjugate heat transfer including radiation and the application of temperature wall-functions are applied at the fluid-tunnel lining interface. The surface emissivity,  $\epsilon$ , of all surfaces is set to 0.8 [2].

For the BC at the concrete tunnel lining, the conjugate heat transfer is enabled at the fluid interface, whereas a constant temperature of 291 K is assumed at the remaining boundary interfaces, i.e. at the floor, inlet, outlet and outer surface.

- **Initial conditions:** the initial velocity field is obtained from an incompressible simulation with the developed velocity profile at the inlet and including the blockage using *simpleFoam*. The initial temperature field is set to 291 K.
- **Heat source:** the fire is modelled by a methane burner with a quadratic fuel inlet of 3 m side length at the position depicted in Fig 6.42. The same BCs as in the Buxton case (Chapter 6.2) are prescribed on the fuel inlet in order to realise the HRR-time curve shown in Fig. 6.43.
- **Thermo-physical properties:** the fluid properties are determined in the same way as for the Buxton simulations (Chapter 6.2). Thermo-physical parameters for the solid materials are assumed independent of temperature. Hence, the temperature dependent values presented in [2] are averaged and summarised in Tab. 6.6.
- **Discretisation:** the same settings as in the Buxton case are used (Chapter 6.2).

In all simulations, the  $k$ - $\varepsilon$  turbulence model with the SGDH<sub>2</sub> buoyancy modification is used and the control over the time step is effectuated by keeping  $Co = 0.8$ . The calculations are parallelised on 128 CPUs using domain decomposition (scotch method).

<i>Element</i>	$\rho$ (kg/m <sup>3</sup> )	$c_p$ (J/kg/K)	$\lambda$ (W/m/K)
tunnel lining	2400	1000	1

Table 6.6: Thermo-physical properties of the concrete tunnel lining

### 6.3.1 Results and discussion

#### 6.3.1.1 Ventilation velocity 0.5 m/s

Vertical profiles of temperature and horizontal velocity along the center-line of the tunnel cross-section ( $z = 0$  m) at different longitudinal positions and time instants are depicted in Figs. 6.44 to 6.49 (see Appendices E.2 and E.5 for further results). Though the system cannot be considered in a stationary state as the tunnel lining still absorbs thermal energy, changes in the fluid region decrease from 40 to 60 minutes and are considerably smaller compared to the period shortly after the growth phase. For the temperature profiles it can be seen, that the changes at the downstream positions  $x = 13$  and 25 m (see Fig. 6.46 and 6.47, respectively) are greater than those observed above the fire source (see Fig. 6.45) as close to the fire the tunnel lining heats up fast and thus absorption of thermal energy reduces. Consequently, more energy is transported downstream resulting in a continuing temperature rise with increasing duration of the fire. The vertical profiles of horizontal velocity at  $x = -20$  m (see Fig. 6.48) show back-layering from the beginning of the fire. The back-flow of hot gases reaches the tunnel inlet within the first 10 minutes of the fire for both cross-sections (see Appendix E.4, Fig. E.11). This behaviour is expected as a result of the low ventilation velocity.

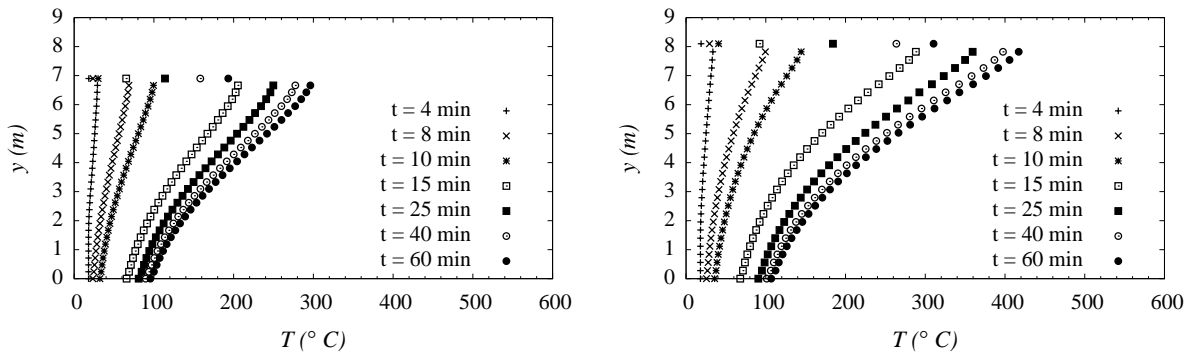


Figure 6.44: Vertical temperature profiles along the center-line of the tunnel ( $z = 0$  m) at  $x = -20$  m for the rectangular (*left*) and arced (*right*) cross-section for different time instants

For both tunnel cross-sections similar temperature levels are predicted (see Figs. 6.50 to 6.52 and Appendix E.1). The maximum temperature is close to 1400 °C and is observed above the fire source after a fire duration of 60 minutes (see, e.g. Fig. 6.51 (*right*)). A comparison with recent tunnel-fire experiments such as presented in [36, 55], where depending on the type of fuel and the ventilation velocity maximum fluid temperatures between 600 °C and 1300 °C were measured, suggests an overestimate of the maximum temperature by the simulations. This was expected as the same behaviour was observed directly above the fire source during the investigation of the combustion model (see Chapter 5.2.5) and the re-analysis of the Buxton tunnel-fire experiment (see Chapter

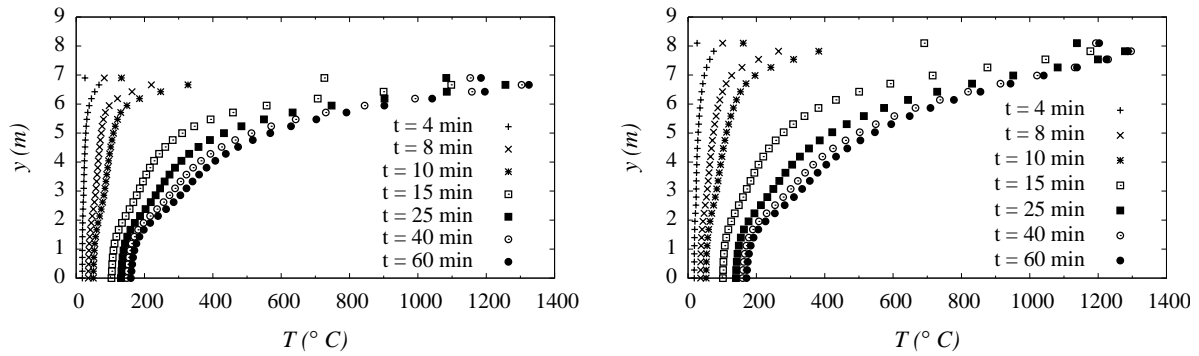


Figure 6.45: Vertical temperature profiles along the center-line of the tunnel ( $z = 0$  m) at  $x = 0$  m for the rectangular (*left*) and arced (*right*) cross-section for different time instants (0.5 m/s ventilation velocity)

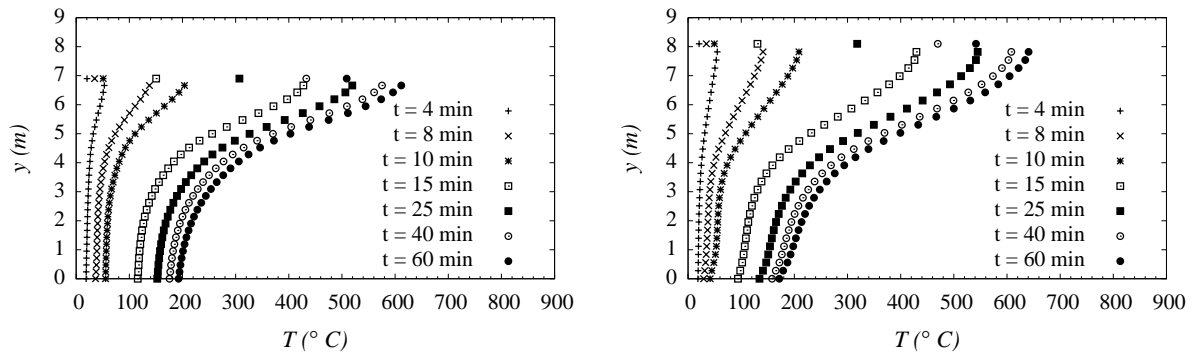


Figure 6.46: Vertical temperature profiles along the center-line of the tunnel ( $z = 0$  m) at  $x = 13$  m for the rectangular (*left*) and arced (*right*) cross-section for different time instants (0.5 m/s ventilation velocity)

6.2). Furthermore, well-ventilated conditions cannot be expected above the fuel outlet ( $y > 2$  m) from the time of a constant HRR, where due to the low ventilation velocity the back-flow of hot gases does not allow fresh air to reach the combustion region (see Figs. 6.48 and 6.53 (*left*) and Appendix E.4, Fig. E.11). Consequently, the applied combustion model most likely overestimates temperatures in under-ventilated areas as discussed for the Cardington compartment-fire experiment (see Chapter 6.1). Therefore it can be concluded, that the estimation of the maximum fluid temperature must be considered as a worst-case scenario, whereas predictions at positions up- and downstream of the fire are more accurate (see also re-analysis of the Buxton tunnel-fire experiment in Chapter 6.2).

The contour plots of temperature at cross-sections  $x = -20$ , 13 and 25 m are depicted in Figs. 6.51 and 6.52 (for positions  $x = 50$  and 100 m, see Appendix E.1, Fig. E.5). Together with the vertical temperature profiles (see Figs. 6.44 to 6.47) they show that in the tunnel's center-line the temperature of hot gases exceeds the tenability limit of thermal radiation for firefighters of 300  $^{\circ}$ C, as observed at all positions  $x = -20$ , 13 and

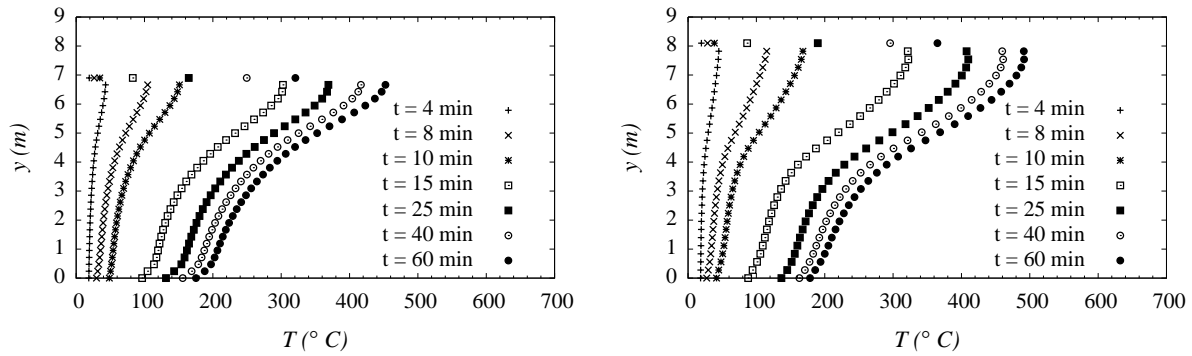


Figure 6.47: Vertical temperature profiles along the center-line of the tunnel ( $z = 0$  m) at  $x = 25$  m for the rectangular (*left*) and arced (*right*) cross-section for different time instants (0.5 m/s ventilation velocity)

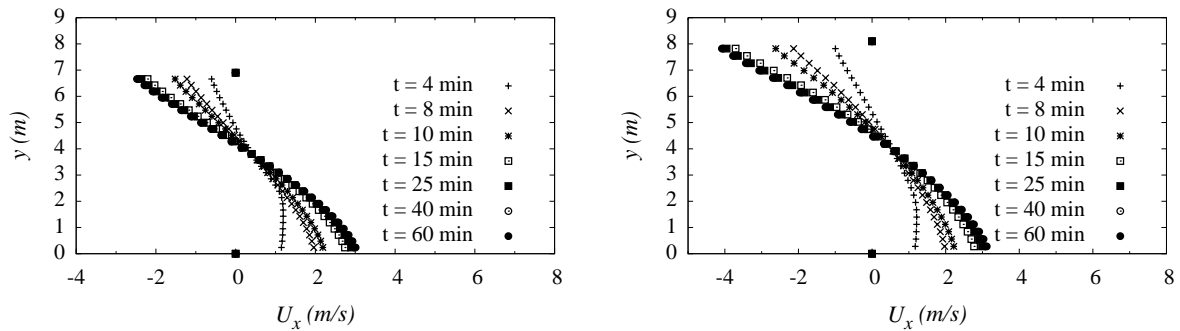


Figure 6.48: Vertical profiles of horizontal velocity along the center-line of the tunnel ( $z = 0$  m) at  $x = -20$  m for the rectangular (*left*) and arced (*right*) cross-section for different time instants (0.5 m/s ventilation velocity)

25 m for both cross-sections close to the end of the growth phase of the fire ( $t = 15$  min). At  $x = -20$  m a temperature of  $300$   $^{\circ}$ C in the tunnel's center-line is seen for the rectangular cross-section only at the beginning of the decay phase ( $t = 60$  min), whereas for the arced cross-section it already appears between  $t = 15$  and  $25$  min due to the concentration of hot gases in the arc (see Fig. 6.51 (*left*)). At the position  $x = 13$  m, the temperature limit is observed between  $t = 10$  and  $15$  min for both cross-sections at the time of greatest increase of the HRR, where at the end of the growth phase of the fire a temperature of  $400$   $^{\circ}$ C is already obtained. At a position  $25$  m downstream of the fire, a fluid temperature of  $300$   $^{\circ}$ C is encountered for  $t > 15$  min for both cross-sections. Hence, the tenability limit of thermal radiation for firefighters is attained at all positions  $x = -20, 13$  and  $25$  m for  $t > 15$  min for both cross-sections, except for the rectangular cross-section at  $x = -20$  m. It has to be mentioned that the simulations do not consider thermal absorption of the train, which is modelled as an adiabatic blockage. Consequently, lower fluid temperatures are expected in reality at  $x = 50$  m where the simulations predict temperatures greater

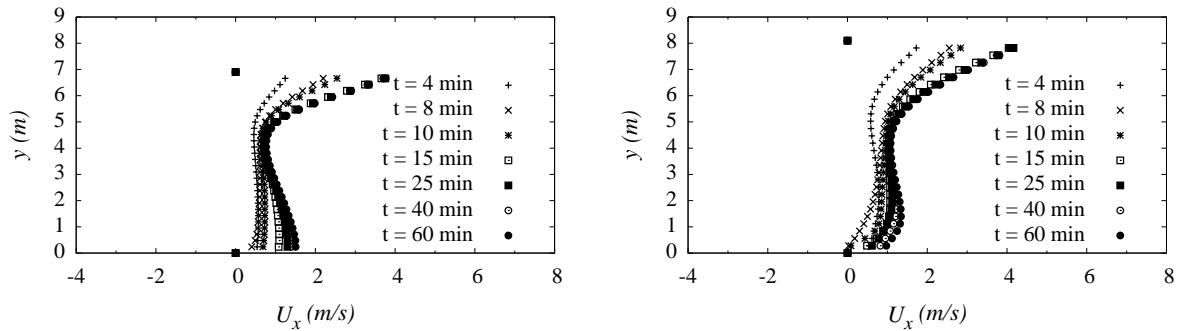


Figure 6.49: Vertical profiles of horizontal velocity along the center-line of the tunnel ( $z = 0$  m) at  $x = 13$  m for the rectangular (*left*) and arced (*right*) cross-section for different time instants (0.5 m/s ventilation velocity)

than 300 °C at  $t = 60$  min (see Appendix E.2, Fig. E.6). Furthermore, the homogeneous temperature distribution observed over the cross-section at  $x = 100$  m is attributed to the fact that the floor is considered adiabatic, and thus higher temperature levels are predicted close to the floor than might occur in reality (see Appendix E.2, Fig. E.7).

It was mentioned before that similar velocity and temperature levels are predicted for both the rectangular and arced cross-section. However, the main differences are seen in the distributions of the flow parameters in the cross-sections. While the typical vortices in the vicinity of the fire source are observed for both cross-sections (see Fig. 6.53 (*right*)), they are more pronounced for the arced cross-section due to the curved shape of the tunnel ceiling. Therefore, the hot gases flow towards the ceiling of the unblocked part of the tunnel ( $z > -0.7$  m) and concentrate in the highest region of the arc where the highest temperatures and velocities in the cross-sections at all longitudinal positions are encountered (see, e.g. Figs. 6.52 (*bottom*) and 6.54 (*bottom*)). On the other hand, in case of the rectangular cross-section the hot gases hit the horizontal ceiling and – driven by buoyancy forces – travel directly up- and downstream of the fire. In consequence of this behaviour, the hot gases stay at the lateral position of the fire source in the cross-section at all longitudinal positions, whereas a trend towards a symmetric temperature distribution is seen for the arced cross-section further downstream of the fire (see Fig. 6.52 (*right*) and Appendix E.1, Fig. E.5). Furthermore, this is the reason why for the arced tunnel a longer area of elevated temperature than for the rectangular tunnel can be identified at the plane  $z = 0$  m for all time instants (compare Appendix E.1, Figs. E.3 and E.4).

In the contour plots of temperature at  $x = 0$  m (see Fig. 6.51 (*right*)), it can be seen that the maximum fluid temperatures appear at similar locations for both types of tunnel cross-section, whereas this is not the case at  $x = 13$  m (see Fig. 6.52 (*left*)). The coordinates of locations where maximum temperatures appear in the cross-sections at  $x = 0$  and 13 m are summarised in Tab. 6.7. The distributions of maximum temperature over time at the

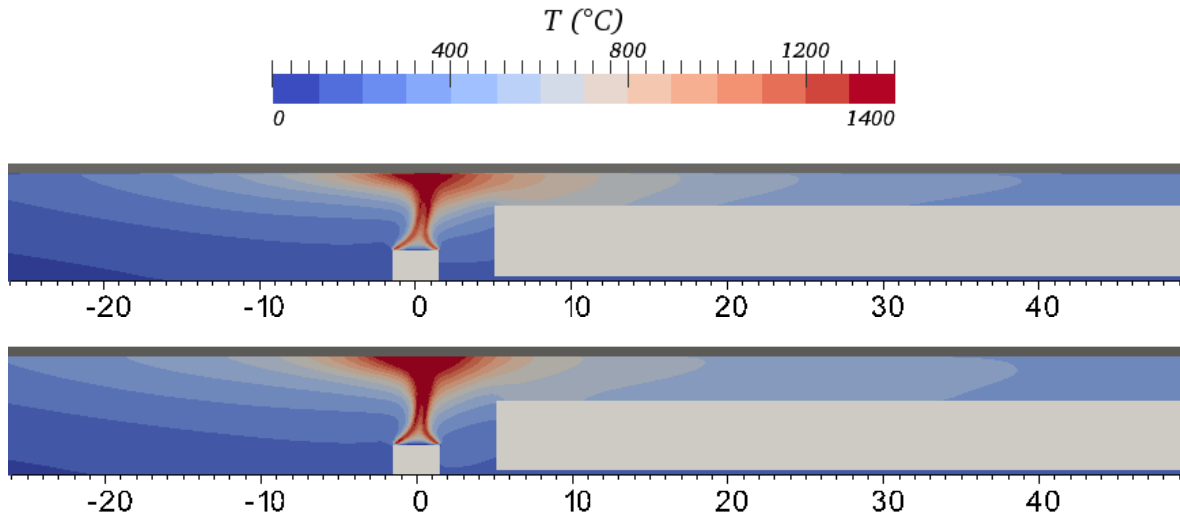


Figure 6.50: Contour plots of temperature at  $z = -2.3$  m for  $t = 60$  min for the rectangular (*top*) and arced (*bottom*) cross-section (dimensions in m, 0.5 m/s ventilation velocity, a time series of contour plots is depicted in Appendix E.1)

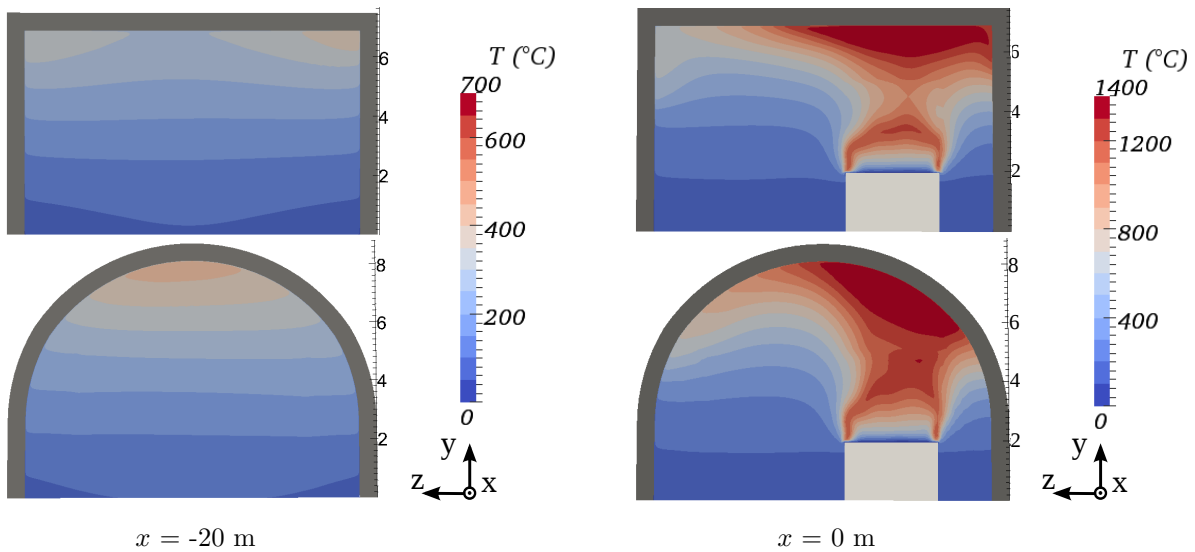


Figure 6.51: Contour plots of temperature at  $x = -20$  and  $0$  m for  $t = 60$  min for the rectangular (*top*) and arced (*bottom*) cross-section (dimensions in m, 0.5 m/s ventilation velocity)

points listed in Tab. 6.7 and the comparison with two standard temperature-time curves, i.e. the RABT-curve and RWS-curve, are depicted in Fig. 6.55. As expected, Fig. 6.55 shows very similar temperature evolutions for both types of cross-section due to the same cross-sectional area of the tunnels. The comparison with the two standard temperature-time curves exhibit the already-mentioned overestimation of the maximum temperature by the simulation. Furthermore, the simulation predicts a slower increase of temperature during the growth phase which can be attributed to the relatively low maximum HRR of

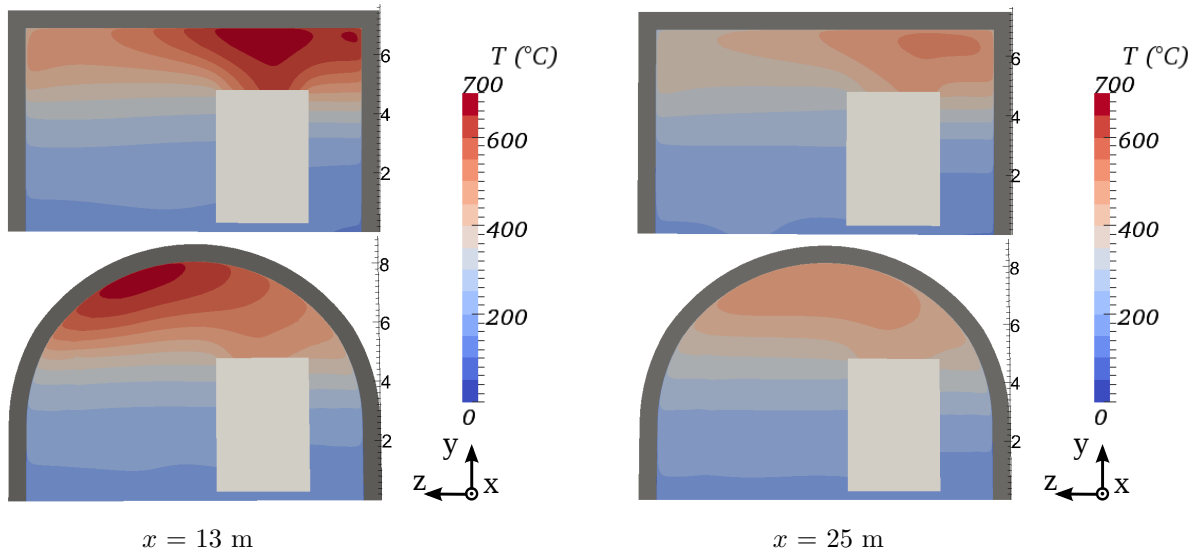


Figure 6.52: Contour plots of temperature at  $x = 13$  and  $25$  m for  $t = 60$  min for the rectangular (*top*) and arced (*bottom*) cross-section (dimensions in m,  $0.5$  m/s ventilation velocity)

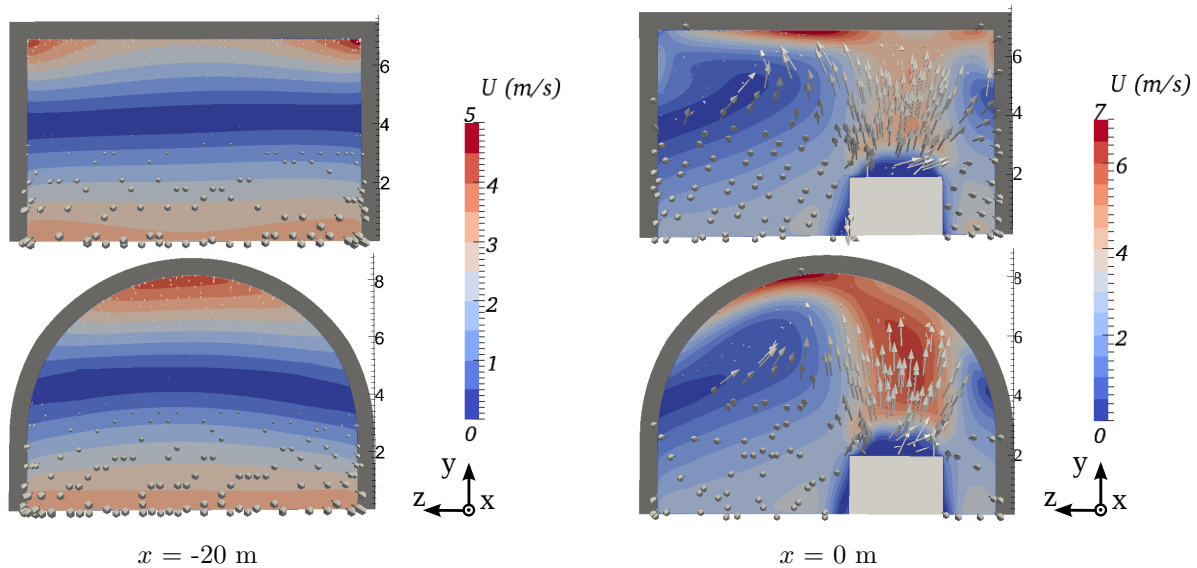


Figure 6.53: Contour plots of velocity magnitude at  $x = -20$  and  $0$  m for  $t = 60$  min for the rectangular (*top*) and arced (*bottom*) cross-section (dimensions in m,  $0.5$  m/s ventilation velocity)

28 MW applied in the simulations. In [55], the temperature measurements of a tunnel-fire experiment with a maximum HRR of 66 MW and a faster increase corresponds well with the RABT-curve and RWS-curve during the growth phase.

Fig. 6.56 shows the evolution of the averaged specific wall-heat fluxes at the concrete tunnel lining where again very similar distributions for the two types of cross-sections



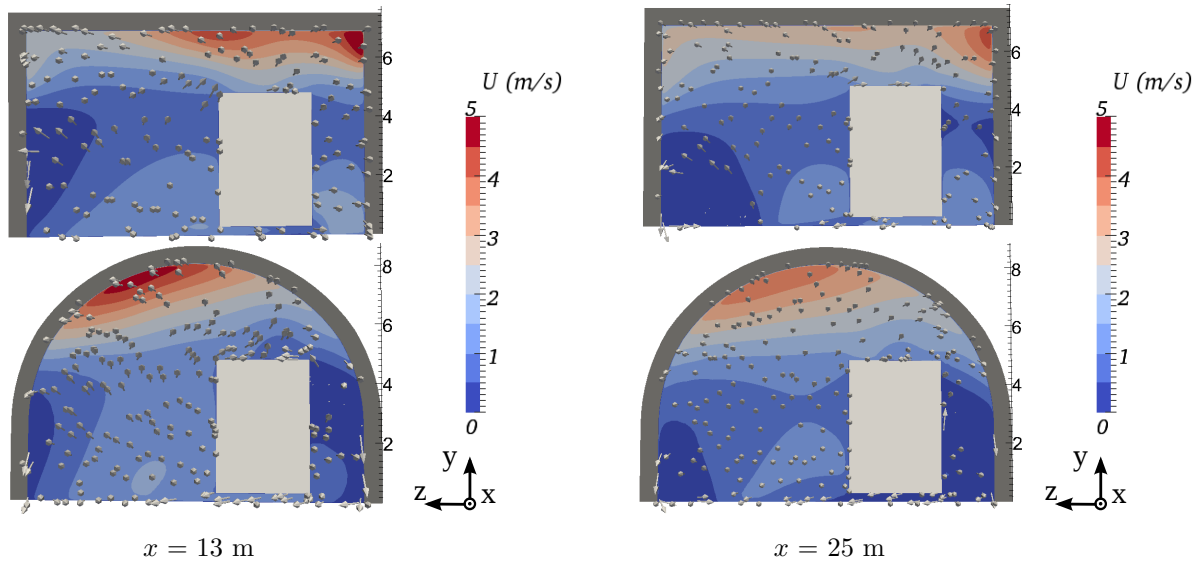


Figure 6.54: Contour plots of velocity magnitude at  $x = 13$  and  $25$  m for  $t = 60$  min for the rectangular (*top*) and arced (*bottom*) cross-section (dimensions in m,  $0.5$  m/s ventilation velocity)

are seen. Like in the case of the Buxton tunnel-fire experiment (see Chapter 6.2, Fig. 6.34), the evolution of the wall-heat fluxes of the concrete lining qualitatively follows the variation of the HRR over time. Furthermore, Fig. 6.56 exhibits the dominance of radiative heat transfer to the tunnel lining as already observed for the Cardington and Buxton experiments. In consequence of the increase in temperature of the tunnel lining during the fire, a decrease of both the convective and radiative wall-heat fluxes is observed from the moment the HRR reaches the constant value of  $28$  MW. The decrease in absorption of thermal energy by the lining in turn leads to a constant temporal increase of the fluid temperatures, which is more pronounced at downstream positions of the fire (compare Figs. 6.46 and 6.47 with Fig. 6.45). Figs. 6.57 and 6.58 depict the surface plots of the convective heat-transfer coefficient,  $\alpha_c$ , at  $t = 8$  and  $60$  min, respectively. For both tunnel cross-sections,  $\alpha_c$  reaches a maximum of approximately  $50$  W/m<sup>2</sup>/K at  $t =$

<i>coordinate</i>	<i>x = 0 m</i>		<i>x = 13 m</i>	
	<i>rectangular</i>	<i>arced</i>	<i>rectangular</i>	<i>arced</i>
<i>y</i> (m)	6.5	6.8	6.6	7.6
<i>z</i> (m)	-2.3	-2.3	-2.3	1.9
distance from ceiling (m)	0.4	0.8	0.3	0.2

Table 6.7: Coordinates of points with maximum fluid temperature in the cross-sections at  $x = 0$  and  $13$  m at  $t = 60$  min and their respective distances from the tunnel ceiling (see also Figs. 6.51 (*right*) and 6.52 (*left*), respectively)

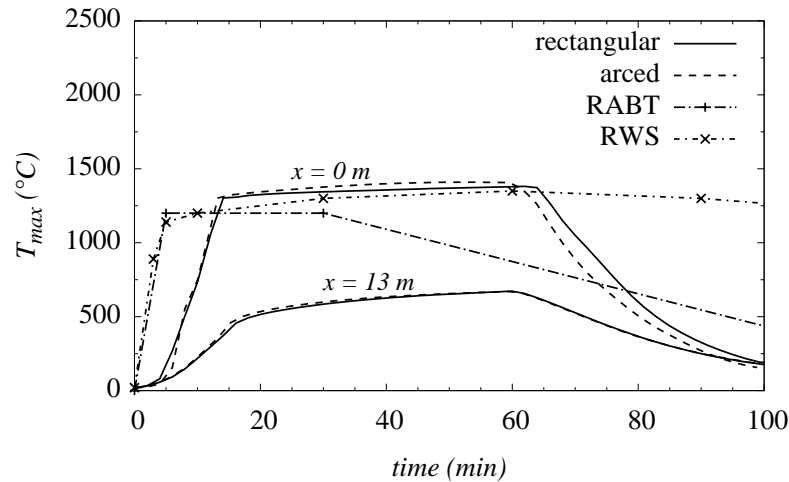


Figure 6.55: Evolution of maximum temperatures at  $x = 0$  and 13 m (see Tab. 6.7 for coordinates of respective points) for a ventilation velocity of 0.5 m/s, compared with the RABT-curve from German guidelines for road tunnels [31] and the RWS-curve from Dutch guidelines (Rijkswaterstaat) for the fire of a fuel tanker [82]

8 min and decreases in the course of the fire to a value of approximately  $25 \text{ W/m}^2/\text{K}$  due to decreasing convective wall-heat fluxes observed in Fig. 6.56. Figs. 6.57 and 6.58 also show the areas of maximum  $\alpha_c$  moving from above the fire source towards the middle of the ceiling during the fire as the tunnel lining is heated up faster above the fire source, and later on absorbs less energy than it is the case at other locations. Depending on the used standard temperature-time curve, a constant value of  $\alpha_c$  is suggested in [2]:  $25 \text{ W/m}^2/\text{K}$  for the standard and the external fire curve, and  $50 \text{ W/m}^2/\text{K}$  in case the hydrocarbon (HC-) curve is used. Hence, the suggestions in the Eurocode correspond well with the obtained simulation results. However, the simulations show  $\alpha_c \approx 50 \text{ W/m}^2/\text{K}$  only during the period of fire growth ( $t = 8$  min) which decreases to approximately  $35 \text{ W/m}^2/\text{K}$  at the end of the growth phase ( $t = 15$  min) and finally drops to approximately  $25 \text{ W/m}^2/\text{K}$  at the beginning of the decay phase ( $t = 60$  min).

Figs. 6.59 to 6.61 depict temperature profiles inside the concrete tunnel lining in the middle of the ceiling ( $z = 0$  m) at positions  $x = 0, 13$  and  $25$  m for different time instants (see Appendix E.3 for positions  $x = -20, 50$  and  $100$  m), where the depth  $d$  is normalised with the thickness of the tunnel lining,  $d_{max}$ . A maximum surface temperature of approximately  $1200 \text{ }^\circ\text{C}$  is seen at  $x = 0$  m and  $t = 60$  min for both types of cross-sections (see Fig. 6.59). The profiles also show that the temperature rise inside the solid mainly effects 1/3 of the lining thickness. For all positions up- and downstream of the fire, higher temperatures for the arced than the rectangular cross-section are predicted by the simulations (see, e.g. Figs. 6.60 and 6.61) as a result of the concentration of hot gases in the arc of the ceiling, which was already discussed before. Thus, similar levels of lining temperature are expected for the rectangular cross-section towards  $z = -2.3$  m (i.e.

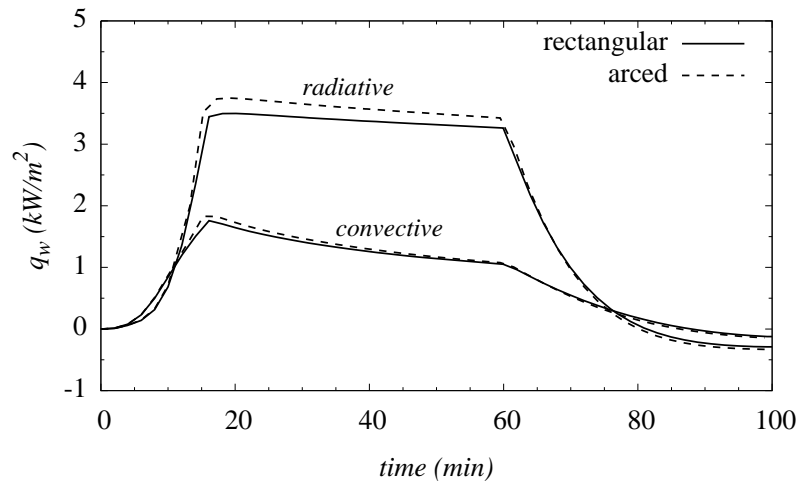


Figure 6.56: Evolution of averaged specific wall-heat fluxes at the concrete lining divided into convective and radiative part for a ventilation velocity of 0.5 m/s

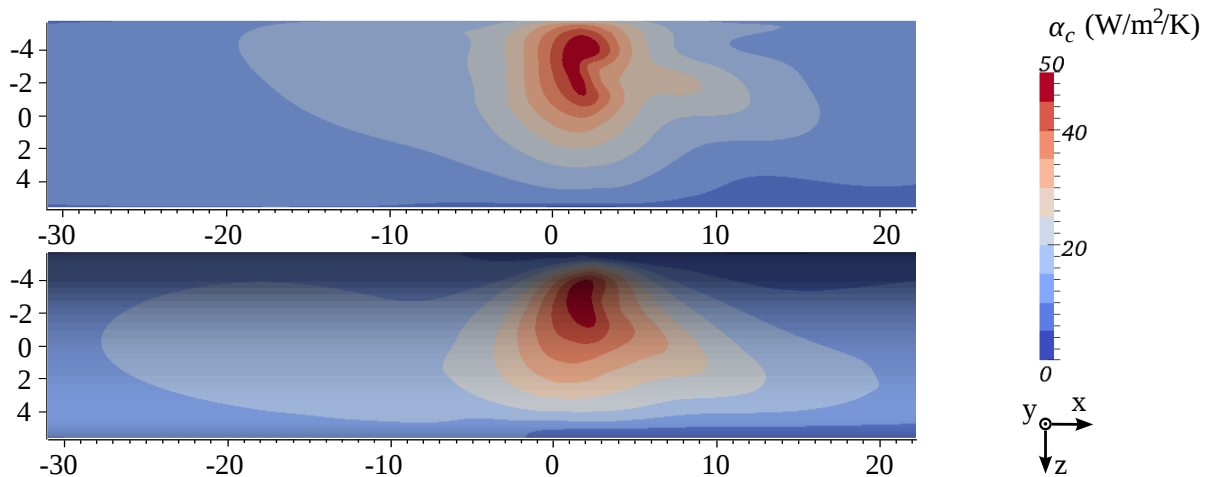


Figure 6.57: Contour plots of convective heat-transfer coefficient,  $\alpha_c$ , (Eqn. (6.4)) at the tunnel ceiling for  $t = 8$  min for the rectangular (*top*) and arced (*bottom*) cross-section (dimensions in m, 0.5 m/s ventilation velocity)

position directly above the fire source). Furthermore, the temperature profiles show that at distances greater than 20 m up- and downstream of the fire, surface temperatures in the range of 200 – 400 °C can occur after a fire duration of 60 minutes (see Figs. 6.61 and Appendix E.3, Figs. E.8 and E.9).

### 6.3.1.2 Ventilation velocity 3 m/s

The time series of temperature-contour plots in the plane  $z = -2.3$  m (see Appendix E.6, Figs. E.15 and E.16) show fluctuations of the flow field around the upstream end of the train for both types of cross sections. These fluctuations are induced by separation

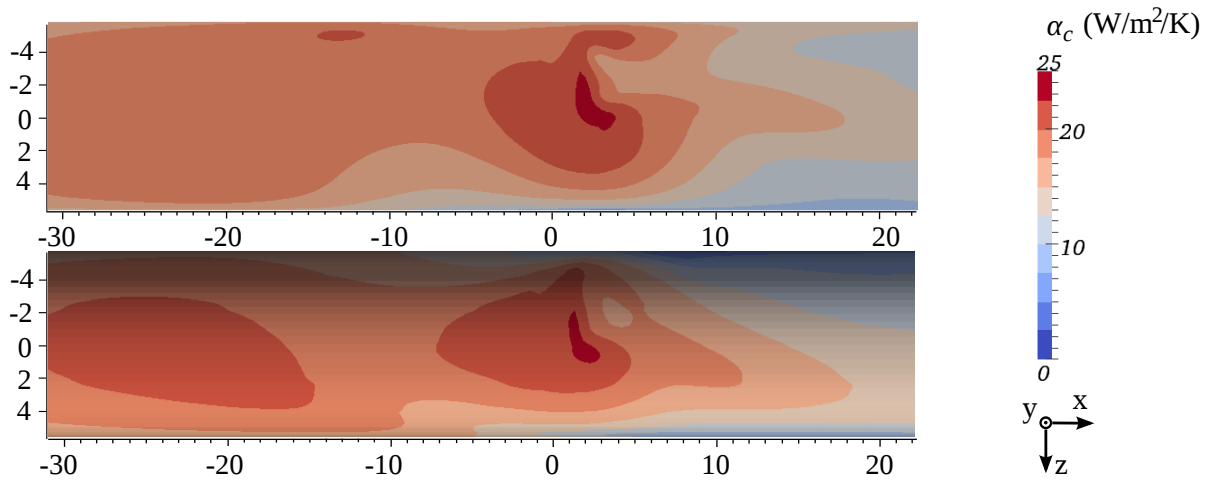


Figure 6.58: Contour plots of the convective heat-transfer coefficient,  $\alpha_c$ , (Eqn. (6.4)) at the tunnel ceiling for  $t = 60$  min for the rectangular (*top*) and arced (*bottom*) cross-section (dimensions in m, 0.5 m/s ventilation velocity)

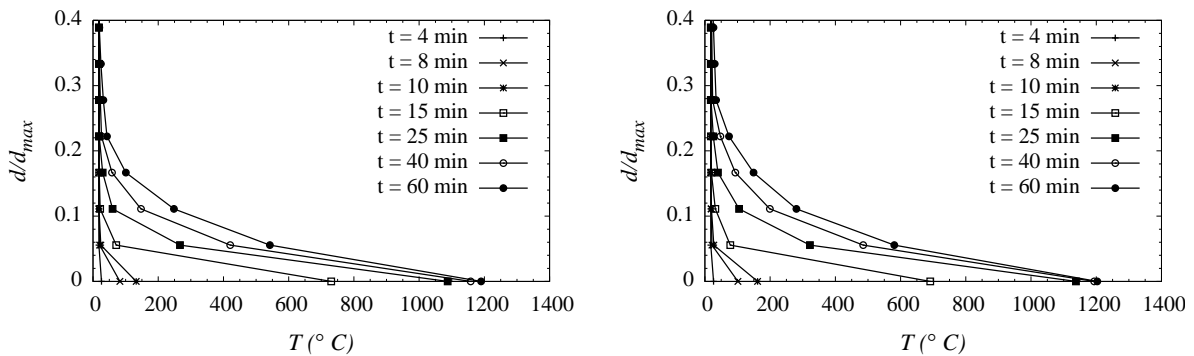


Figure 6.59: Temperature profiles inside the tunnel lining along the center-line ( $z = 0$  m) at  $x = 0$  m for the rectangular (*left*) and arced (*right*) cross-section for different time instants (0.5 m/s ventilation velocity)

of the bulk flow hitting the train at the upstream end, resulting in strong variations of the flow parameter in the vicinity of the fire source (see, e.g. Appendix E.6, Fig. E.15). Furthermore, no back-layering occurs as expected (see Fig. E.23 in Appendix E.9). However, as the applied numerical set-up (turbulence model, grid, etc.) is not meant to resolve flow separation, results are only shown for downstream positions at  $x \geq 13$  m except for the cross-sections where the highest fluid and lining temperatures are observed.

The vertical profiles of temperatures at  $x = 13$  and 25 m for different time instants exhibit the mentioned fluctuations (see Figs. 6.62 and 6.63), whereas the flow becomes more steady at  $x = 50$  and 100 m and no significant changes are observed between  $t = 15$  and 25 min (see Appendix E.7, Figs. E.18 and E.19). Moreover, the temperature levels are strongly reduced compared to the case of 0.5 m/s ventilation velocity which is also

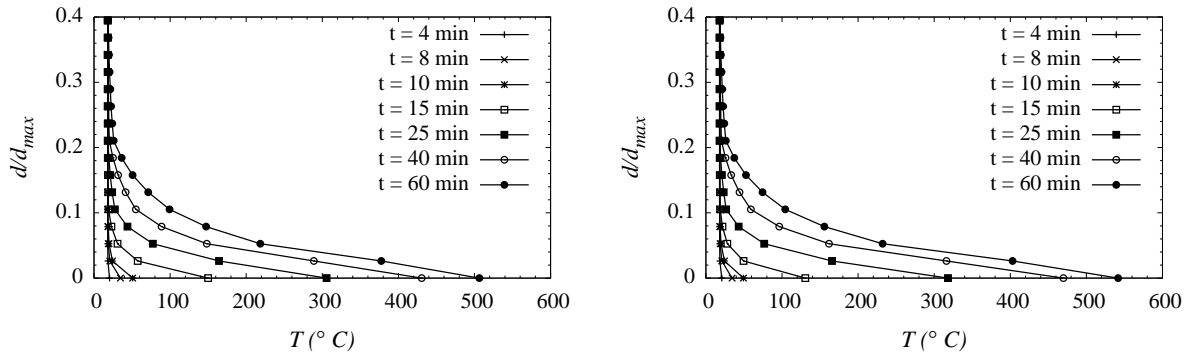


Figure 6.60: Temperature profiles inside the tunnel lining along the center-line ( $z = 0$  m) at  $x = 13$  m for the rectangular (*left*) and arced (*right*) cross-section for different time instants (0.5 m/s ventilation velocity)

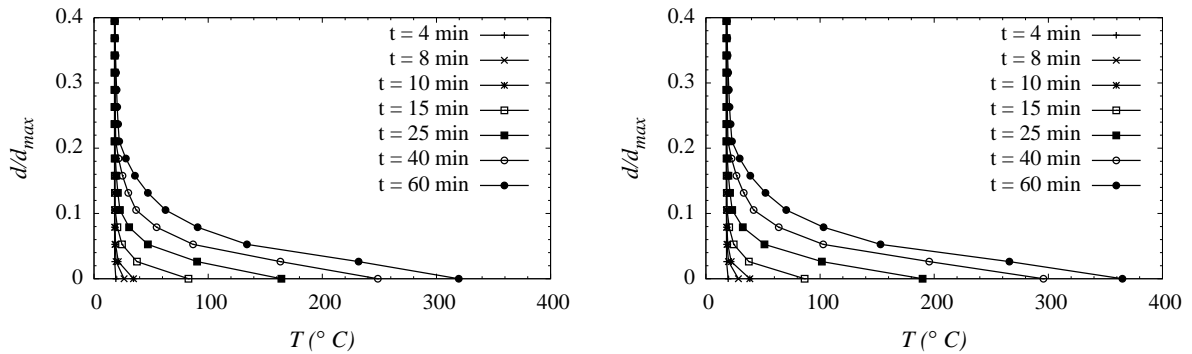


Figure 6.61: Temperature profiles inside the tunnel lining along the center-line ( $z = 0$  m) at  $x = 25$  m for the rectangular (*left*) and arced (*right*) cross-section for different time instants (0.5 m/s ventilation velocity)

seen in the contour plots of temperature (see Fig. 6.64 and Appendix E.6, Fig. E.17), and thus in non of the depicted cross-sections hot gases exceeding a temperature of 300 °C are observed. This is explained with the fact, that the six times higher ventilation velocity introduces a greater mass flux of fresh air, diluting and cooling the hot combustion gases. Additionally, the higher ventilation speed allows faster transport of the hot gases out of the tunnel. The contour plots of velocity magnitude at  $x = 13$  and 25 m exhibit the vortices typically observed close to the fire source. A more distinct structure of the vortices than for a ventilation velocity of 0.5 m/s is seen at these positions due to their faster convection downstream from the position of origin (compare Figs. 6.65 and 6.54).

The maximum fluid temperatures downstream of the fire occur between  $x = 6$  and 7 m for both cross-sections (for  $x = 6$  m, see Fig. 6.66), never exceeding 1300 °C and 1200 °C for the rectangular and arced cross-section, respectively. While in the case of 0.5 m/s ventilation velocity the arced cross-section showed higher maximum temperatures than for the rectangular tunnel (see Chapter 6.3.1.1), the arced cross-section exhibits a lower

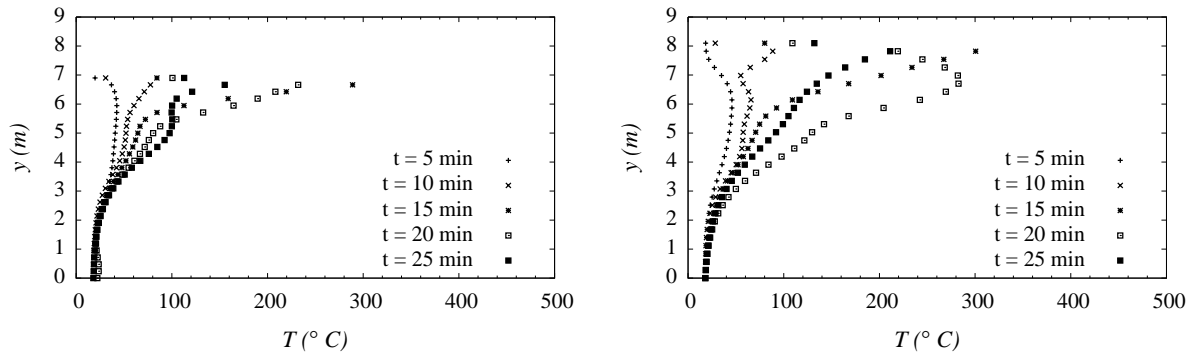


Figure 6.62: Vertical temperature profiles along the center-line of the tunnel ( $z = 0$  m) at  $x = 13$  m for the rectangular (*left*) and arced (*right*) cross-section for different time instants (3 m/s ventilation velocity)

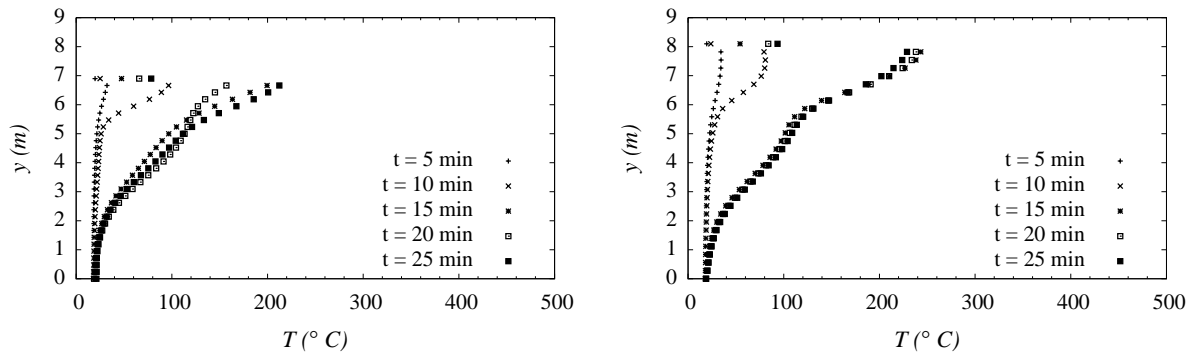


Figure 6.63: Vertical temperature profiles along the center-line of the tunnel ( $z = 0$  m) at  $x = 25$  m for the rectangular (*left*) and arced (*right*) cross-section for different time instants (3 m/s ventilation velocity)

maximum fluid temperature for a ventilation velocity of 3 m/s due to a greater volume above the fire source and the train, allowing more fresh air to mix with the combustion gases. However, at positions further downstream also for the case of 3 m/s ventilation velocity (see, e.g. Fig. 6.63) the hot gases concentrate in the arc of the arced cross-section leading to higher temperatures and more symmetric temperature distributions in the cross-sections than for the rectangular tunnel (see Fig. 6.64 and Appendix E.6, Fig. E.17).

The fluctuations of the flow field are also seen in the evolution of the averaged specific wall-heat fluxes (see Fig. 6.67) where, as already observed in the previous simulations with 0.5 m/s ventilation velocity, a trend of decreasing heat fluxes with increasing duration of the fire is exhibited. The faster transport of hot gases out of the tunnel also reduces the heat transfer to the tunnel lining. Compared with the wall-heat fluxes in the case of a ventilation velocity of 0.5 m/s, the higher ventilation velocity reduces the absorbed thermal energy by approximately 50 % (compare Figs. 6.56 and 6.67). However, it has to

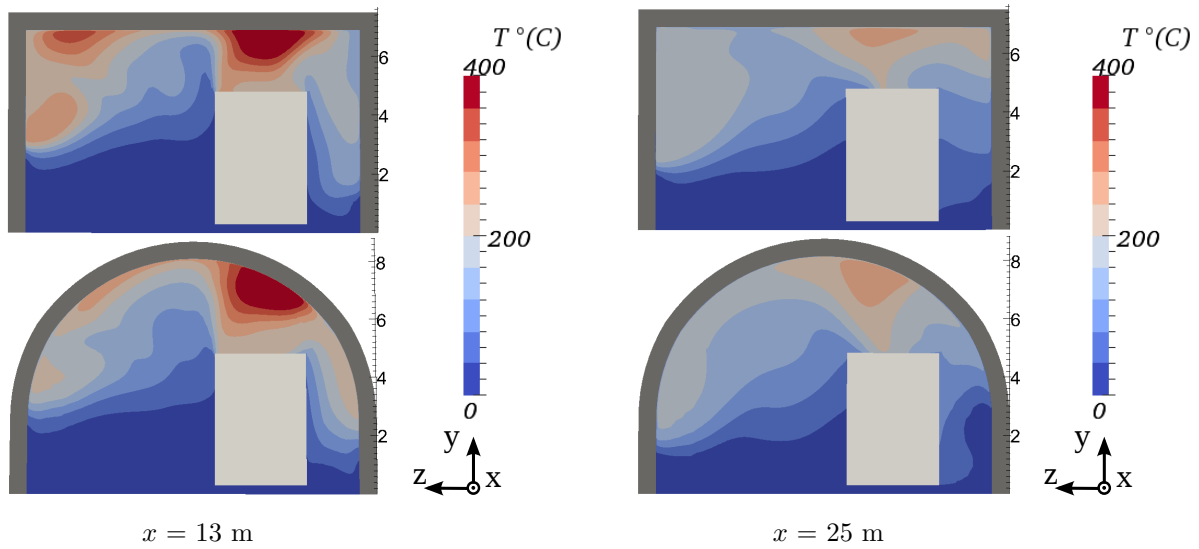


Figure 6.64: Contour plots of temperature at  $x = 13$  and  $25$  m for  $t = 25$  min for the rectangular (*top*) and arced (*bottom*) cross-section (dimensions in m, 3 m/s ventilation velocity)

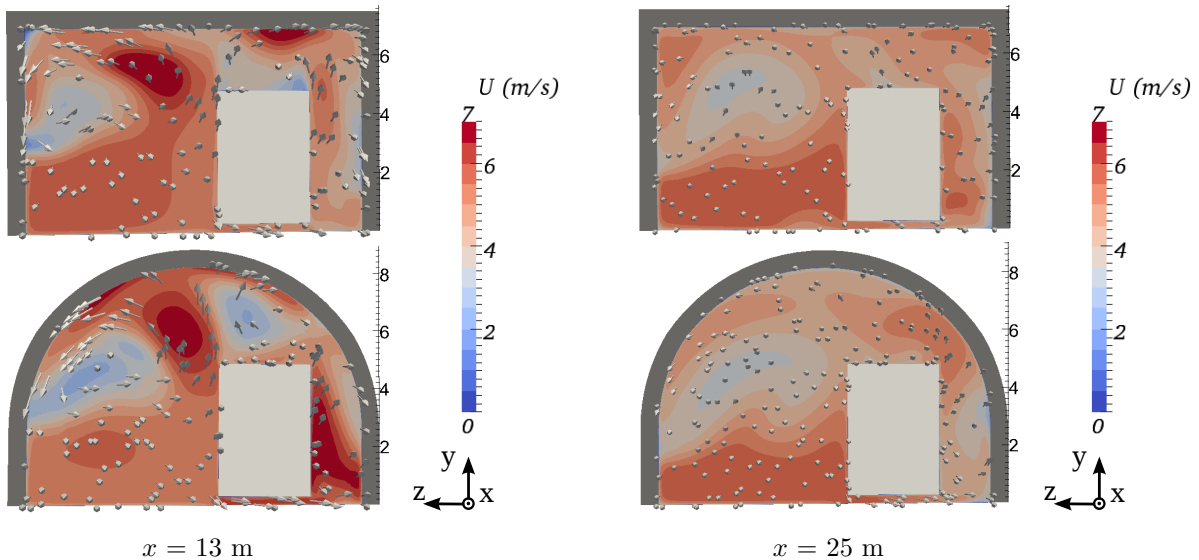


Figure 6.65: Contour plots of velocity magnitude at  $x = 13$  and  $25$  m for  $t = 25$  min for the rectangular (*top*) and arced (*bottom*) cross-section (dimensions in m, 3 m/s ventilation velocity)

be mentioned that the current approach of prescribing the history of the HRR does not allow to reproduce the influence of forced ventilation on the development of the fire's HRR, which was observed in tunnel-fire experiments as discussed in [13, 56] and mentioned in Chapter 3. Unlike in the case of a ventilation velocity of 0.5 m/s, the maximum  $\alpha_c$  is not changing significantly during the fire and lays in the range of 40 – 50 W/m<sup>2</sup>/K (see Fig. 6.68). The areas of high values of  $\alpha_c$  are in the region where the combustion gases are

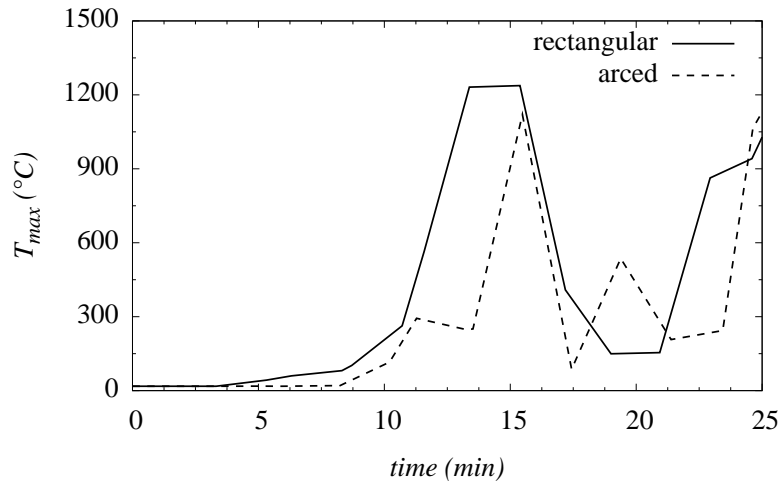


Figure 6.66: Evolution of maximum temperatures in the cross-section at  $x = 6$  m for a ventilation velocity of 3 m/s

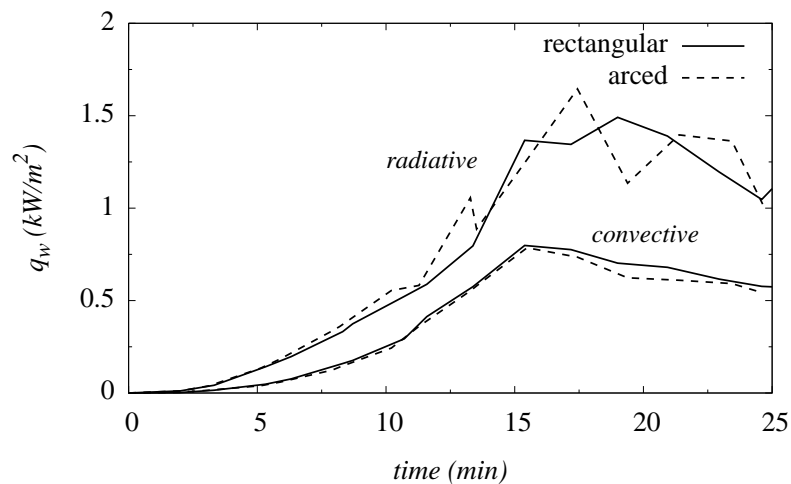


Figure 6.67: Evolution of averaged specific wall-heat fluxes at the concrete lining divided into convective and radiative part for a ventilation velocity of 3 m/s

pushed over the upstream end of the train and are deviated towards the tunnel ceiling as depicted in the contour plots at  $t = 25$  min.

In Figs. 6.69 and 6.70, the evolution of the temperature inside the concrete tunnel lining at the positions of the highest lining temperature in the domain and at  $x = 13$  m in the middle of the ceiling are depicted (for  $x = 25, 50$  and  $100$  m see Appendix E.8). For the rectangular tunnel, the highest lining temperature is seen in the region above the highest fluid temperature, i.e. at  $x = 6$  m,  $z = -1.2$  m. For the arced tunnel, the highest lining temperature occurs on the lateral side of the tunnel lining where the fire source ends ( $x = 1.5$  m) at a height of approximately 3.5 m and is solely a result of radiative heat transfer from the combustion zone. Except for the positions of maximum surface



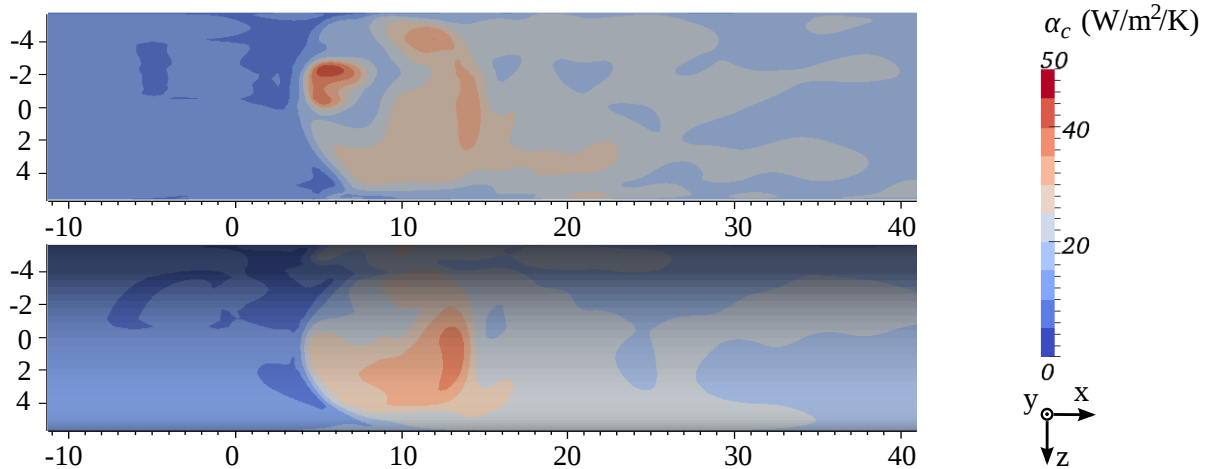


Figure 6.68: Contour plots of the convective heat-transfer coefficient,  $\alpha_c$ , (Eqn. (6.4)) at the tunnel ceiling for  $t = 25$  min for the rectangular (*top*) and arced (*bottom*) cross-section at a ventilation velocity of 3 m/s (dimensions in m)

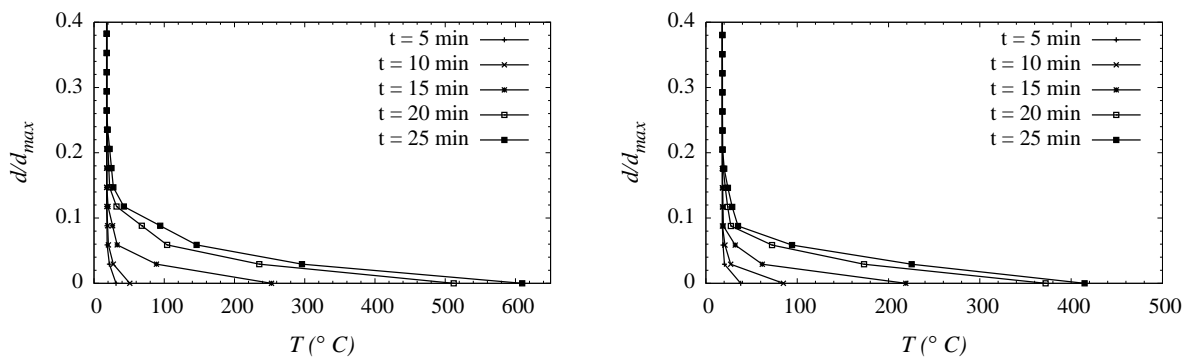


Figure 6.69: Temperature profiles inside the tunnel lining at the point of maximum surface temperature for the rectangular (*left*,  $x = 6$  m,  $z = -1.2$  m) and arced (*right*,  $x = 1.5$  m,  $z = -5.6$  m) cross-section for different time instants (3 m/s ventilation velocity)

temperatures in the vicinity of the fire source, all shown lining temperatures stay below 150 °C. Furthermore, higher lining temperatures are predicted for the arced than the rectangular cross-section at the downstream positions (see, e.g. Fig. 6.70) due to higher fluid temperatures mentioned before which was already discussed for the case of 0.5 m/s ventilation velocity. The temperature distributions inside the concrete lining also show that the temperature rise at  $t = 25$  min mainly effects 1/5 of the lining thickness.

### 6.3.2 Conclusions

The simulations of a train fire inside a double-track railway tunnel exhibit similar levels of temperature and velocity magnitudes for the two types of analysed cross-sections, i.e. a rectangular and an arced cross-section. This behaviour was expected in consequence of

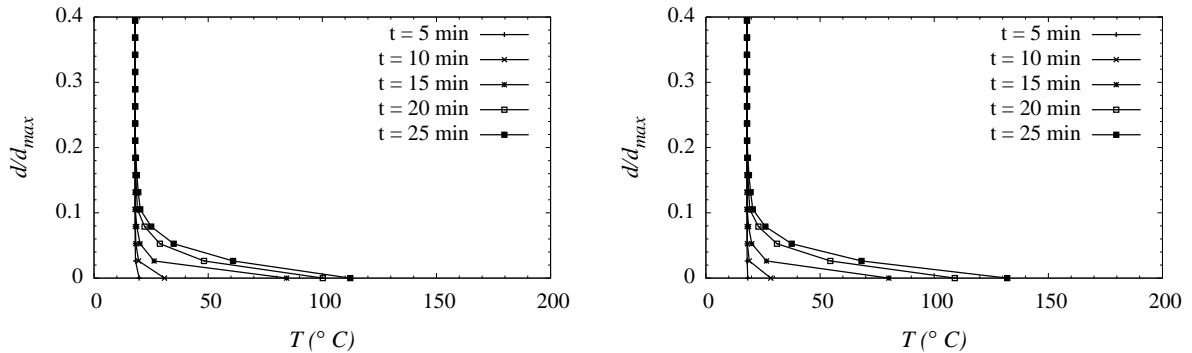


Figure 6.70: Temperature profiles inside the tunnel lining along the center-line ( $z = 0$  m) at  $x = 13$  m for the rectangular (*left*) and arced (*right*) cross-section for different time instants (3 m/s ventilation velocity)

the same cross-sectional area and is observed for both of the applied ventilation velocities of 0.5 m/s and 3 m/s, respectively. The main differences in the flow field of the studied types of cross-sections are seen in the distributions of velocities and temperatures over the cross-sections which might have an implication on the structural stability of the respective tunnel cross-section. While for the rectangular tunnel, the hot gases are concentrated in the nearest corner and up- and downstream of the fire at the lateral position of the fire source, the combustion gases accumulate in the top of the arc for the arced cross-section, where locally higher temperatures than for the rectangular cross-section are observed.

As expected, the tenability limit of thermal radiation for firefighters represented by the gas temperature exceeding 300 °C is not attained in any of the checked cross-sections ( $x = -20, 0, 13, 25, 50$  and  $100$  m)<sup>2</sup> for a ventilation velocity of 3 m/s. On the other hand, it is observed for a ventilation velocity of 0.5 m/s within distances up- and downstream of the fire source of 25 m for both cross-sections within a time period of  $10 \leq t \leq 60$  min. The tenability limit occurs faster for the arced cross-section. For a summary, see Tab. 6.8.

With a ventilation velocity of 0.5 m/s, the predicted maximum fluid temperature close to 1400 °C above the fire overestimates temperatures exhibited during experiments due to the under-ventilated conditions in the combustion zone in reality, where in the course of the fire the access of fresh air is hindered by the strong back-flow of hot gases. This behaviour of the combustion model in under-ventilated conditions was already observed in the re-analysis of fire experiments. As expected, the maximum fluid temperatures drop dramatically for a ventilation velocity of 3 m/s compared to the lower ventilation velocity of 0.5 m/s and occur close to the upstream end of the train. For a ventilation velocity of 3 m/s, the arced tunnel exhibits both a lower maximum fluid and lining temperature than in the case of a rectangular tunnel as a result of a greater volume above the fire source allowing the hot gases to mix with more fresh air. Nevertheless, higher temperatures are

<sup>2</sup>High fluctuations of the fluid temperature are observed at  $x = 6$  m mostly exceeding 300 °C for both cross-sections from  $t = 10$  min (see Fig. 6.66)

observed for the arced cross-section at the middle of the tunnel ceiling further downstream of the fire in the same way as for the case of a ventilation velocity of 0.5 m/s.

As a consequence of the fluid-temperature distribution, the highest lining temperature of approximately 1200 °C is observed above the fire for the case of a ventilation velocity of 0.5 m/s at  $t = 60$  min. For a ventilation velocity of 3 m/s, the six times higher ventilation velocity allows to reduce the averaged specific radiative and convective wall-heat fluxes by approximately 50 %, as the hot combustion gases are transported out of the tunnel faster. The maximum convective heat-transfer coefficient,  $\alpha_c$ , of approximately 50 W/m<sup>2</sup>/K predicted by the simulations corresponds well with the suggestions in the Eurocode [2]. Because of strong absorption of thermal energy by the tunnel lining in case of a ventilation velocity of 0.5 m/s,  $\alpha_c$  decreases fast after the growth phase of the fire. For a ventilation velocity of 3 m/s, on the other hand,  $\alpha_c$  remains almost constant.

$x$ (m)		-20	0	13	25	50	100
0.5 m/s	<i>rectangular</i>	60 min	10 min	10 – 15 min	15 – 25 min	never	never
	<i>arced</i>	15 – 25 min	10 min	10 – 15 min	15 – 25 min	never	never
3 m/s	<i>rectangular</i>	never	never	never	never	never	never
	<i>arced</i>	never	never	never	never	never	never

Table 6.8: Approximate time instants at which the tenability limit for thermal radiation is reached at different longitudinal positions

## Concluding remarks

### 7.1 Conclusions

The main focus of the presented thesis was the development of fires in underground structures and the investigation of the thermal impact on the load-carrying structure. To accomplish this task, a fire code based on *Computational Fluid Dynamics (CFD)* was developed, where the history of the fire's *Heat Release Rate (HRR)* which specifies the fire scenario under consideration, represents the main input parameter for the CFD simulations. Thus, a comprehensive set of previously-estimated or experimentally-obtained HRR-time curves considering different fire loads (i.e. so-called design fires) for road, train and metropolitan tunnels were summarised based on a literature research, including parameters to describe the HRR-time curves by mathematical functions (i.e. linear, quadratic and exponential growth/decay phases). Subsequently, numerous fire codes which have been developed in recent decades were studied and a pre-selection according to specified criteria suggested the development and application of the fire code within the open-source framework of OpenFOAM, a multi-purpose CFD package. Hereby, the following steps were carried out:

1. *Validation of sub models:*

In order to simulate the main characteristics of fires in enclosures, i.e. turbulent buoyancy-driven flows including conductive, convective and radiative heat transfer, suitable sub models accounting for turbulence, radiative heat transfer and combustion were incorporated into OpenFOAM's *chtMultiRegionFoam* solver, which couples the heat transfer between solid and fluid regions. For turbulence modelling, the RANS approach was followed and two methods of modifying the standard  $k-\varepsilon$

turbulence model with respect to additional turbulence production due to buoyancy effects, which were based on (i) the *Simple Gradient Diffusion Hypothesis (SGDH)* and (ii) the *Generalised Gradient Diffusion Hypothesis (GGDH)*, were studied. The re-analysis of a buoyant-plume experiment showed no advantage of the SGDH approach over the standard model (with both models producing numerical results deviating from experimental data), whereas the numerical results obtained with the GGDH approach exhibited very good agreement with experimental data. Two procedures of treating thermal radiation within a participating medium currently implemented in OpenFOAM, i.e. the P1-approximation and the *Finite Volume Discrete Ordinate Method (fvDOM)* were analysed by means of two benchmark tests. The fvDOM exhibited excellent agreement with the reference solutions, and was thus chosen to be included into the fire code. The consideration of the radiative wall-heat flux in the treatment of conjugate heat transfer showed reasonable behaviour and highlighted the importance of including radiation in the conjugate heat transfer. The combustion process in a fire was modelled by a buoyant diffusion flame of a methane gas-burner. The combustion model was based on the mixture-fraction approach applying the *Eddy Dissipation Model (EDM)* to model the mean consumption rate of fuel. An experimentally investigated turbulent diffusion flame was analysed with the EDM combustion model in combination with the buoyancy-modified turbulence models previously studied for a non-reactive flow. The simulations exhibited a strong dependency of the obtained numerical results on the applied buoyancy modifications. The GGDH approach did not allow to reproduce a distinction of flame, intermittent and plume region, whereas they were observed when using the standard model and the SGDH approach, even if these regions were predicted too far downstream of the vertical flame. Furthermore, the influence of how the buoyancy-source terms were introduced into the  $\varepsilon$ -equation on numerical stability and results could be observed. Hence, the SGDH approach, where only the positive contribution of the turbulence production due to buoyancy is considered in the  $\varepsilon$ -equation, was adopted for the fire code.

## 2. *Re-analysis of real-scale fire experiments:*

After the design of the fire code, its predictive ability was assessed by the re-analyses of a compartment-fire test and a tunnel-fire test. Besides the approach of modelling the fire source by a buoyant diffusion flame, i.e. the reactive approach, a non-reactive approach, where the fire is represented by a volumetric heat source only releasing the convective portion of the HRR was investigated. Thus, radiative heat transfer was not considered and no combustion model was applied in the non-reactive case. Re-analysis of the fire experiments showed a strong dominance of radiative heat transfer over convective heat transfer within the fluid as well as towards solid surfaces. Consequently, the non-reactive simulations did not allow to obtain satisfactory agreement with experimental data for the tunnel fire and failed to produce

reasonable results for the case of a compartment fire with a comparable high HRR. Furthermore, numerical results were extremely sensitive on the choice of the convective fraction of the total HRR which, depending on the type of fuel and the fire size, is in the range of 60 – 80 % (where 80 % is recommended in the Eurocode [2]). With a 1.5-times longer simulation time, the reactive approach showed good correspondence with measurements for averaged quantities in the compartment fire and downstream of the fire in the tunnel, whereas numerical results deviated from the measurements at locations directly above the fire source and in under-ventilated regions. This behaviour is a known deficiency of the applied assumptions in the combustion model and has to be considered in further investigations.

### 3. Analysis of a fire in real tunnel geometries:

The developed fire code was applied to simulate a 28 MW fire in real-scale double-track railway tunnels. Two types of cross-sections (i.e. a rectangular and an arced cross-section) with similar cross-sectional area and two different ventilation velocities of 0.5 m/s (low) and 3 m/s (high) were investigated. For each of the ventilation velocities, similar levels of temperature and velocity magnitudes were observed in the rectangular and the arced cross-section. As expected, the influence of the type of cross-section was mainly seen in the distribution of flow parameters over the cross-section. Hot gases propagated up- and downstream of the fire at the lateral position of the fire source for the rectangular tunnel, whereas they concentrated in the arc of the arced tunnel. The simulations showed, that firefighters can only approach the fire source from downstream safely until a distance of 25 m for  $t \leq 15$  min, as the tenability limit of radiation represented by hot-gas temperatures exceeding 300 °C was observed at later time instants for a ventilation velocity of 0.5 m/s. The high ventilation velocity (3 m/s) resulted in a decrease of fluid and tunnel-lining temperatures where the latter was a consequence of the reduced (by 50 %) wall-heat fluxes, and thus the tenability limit of radiation was not attained for  $x \geq 13$  m. For both ventilation velocities, the simulations predicted a maximum convective heat-transfer coefficient of approximately 50 W/m<sup>2</sup>/K corresponding to suggestions found in the Eurocode [2].

## 7.2 Engineering model

Based on the presented results and findings, the suggestions concerning engineering modelling of thermal actions on structures exposed to fire given in standards and guidelines (see, e.g. [2]) are reviewed. A corresponding engineering model should allow to use the presented findings of the CFD simulations for practical applications.

### 7.2.1 Heat transfer

Temperature profiles inside a thermally loaded structure are determined by solving the heat-conduction equation (Eqn. (4.13)) with convective and radiative heat transfer towards the surface exposed to the fire. According to [2], the boundary condition at the exposed surface describing convective and radiative heat transfer is written in terms of a net specific wall-heat flux, reading

$$q_{w,tot} = \alpha_c(T_f - T_w) + \epsilon \sigma_{SB}(T_f^4 - T_w^4), \quad (7.1)$$

where the configuration factor is set to one and a unit emissivity is taken for the flame [2]. The fluid temperature,  $T_f$ , is given by nominal temperature-time curves. The convective heat-transfer coefficient,  $\alpha_c$ , is set to a constant value within the range of 25 – 50 W/m<sup>2</sup>/K depending on the used temperature-time curve, whereas a varying value of  $\alpha_c$  was obtained in the CFD simulations during the growth phase of the fire for a ventilation velocity of 0.5 m/s (see Chapter 6.3.1.1). The surface temperature,  $T_w$ , then results from the solution of the heat-conduction problem for a thermally loaded structure.

The following discussion should allow to work out the influence of a varying  $\alpha_c$  on  $T_w$  in case the approach suggested in [2] is applied. In the respective simulations, the heat-conduction equation is solved in 1D for a wall of 0.6 m thickness with the thermo-physical properties listed in Tab. 6.6. At the back surface of the wall, the temperature is fixed to 291 K, whereas at the fire-loaded surface the boundary condition Eqn. (7.1) is employed considering different values of  $\alpha_c$  including the case of varying  $\alpha_c$  during the growth phase (see Tab. 7.1),  $\alpha_c = 0$  (no convective heat transfer) and  $\alpha_c = \infty$  (corresponding to  $T_w = T_f$ ). The radiative heat transfer is the same for all simulations with a surface emissivity of  $\epsilon = 0.8$  (according to [2]). The evolution of  $T_f$  is taken from the CFD simulation in a rectangular cross-section with a ventilation velocity of 0.5 m/s at a point above the fire source ( $x = 0$  m,  $z = -2.3$  m). The surface temperatures from the 1D calculations are compared with the results from the CFD simulation (see Figs. 7.1 and 7.2).

<i>time</i> (min)	$\alpha_c$ (W/m <sup>2</sup> /K)
0 – 8	50
8 – 15	35
15 – 60	25

Table 7.1: Evolution of  $\alpha_c$  based on numerical results from CFD simulations (see Chapter 6.3.1.1)

Figs. 7.1 and 7.2 show a slight overestimation of  $T_w$  by the 1D calculations with  $\alpha_c$  between 25 and 50 W/m<sup>2</sup>/K compared to the CFD simulation as a result of neglecting the absorption of radiation by the fluid in the 1D case. Furthermore, the results confirm

the already observed dominance of radiative heat transfer for temperatures above 1100 °C as points for different (finite) values of  $\alpha_c$  coincide for  $T_f > 1100$  °C ( $t \geq 15$  min). However, convective and radiative heat transfer are of similar importance during the growth phase of the fire (see also Fig. 6.56 for  $t \leq 10$  min). In the first 12 minutes, a difference of approximately 50 °C is observed between results with  $\alpha_c = 25$  and 50 W/m<sup>2</sup>/K for a temperature level of 200 °C, exhibiting a non-negligible influence of the choice of  $\alpha_c$  at that stage. On the other hand, one would expect best correspondence of the 1D results with the CFD simulation for the case of a varying  $\alpha_c$  which was obtained from the CFD simulation. However,  $\alpha_c$  was calculated using  $T_w$  (see Eqn. (6.4)) which beside convection is also a result of radiation, and hence is higher when compared to the case of pure convection. Consequently, the calculated values for  $\alpha_c$  are overestimated.

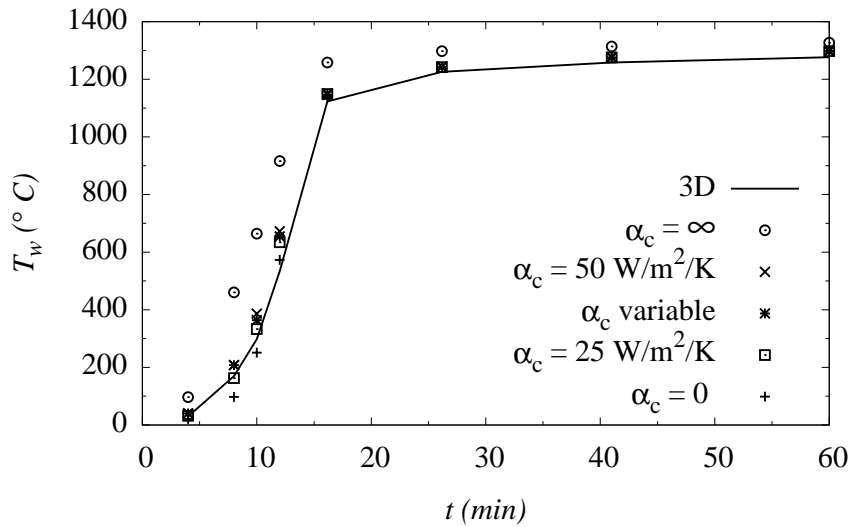


Figure 7.1: Evolution of surface temperature from 1D calculations with different  $\alpha_c$  compared with results from the CFD simulation ( $T_w = T_f$  for the case of  $\alpha_c = \infty$ )

For the 1D model applying the boundary condition in Eqn. (7.1), it can be concluded that 25 and 50 W/m<sup>2</sup>/K according to [2] can be considered as a good approximation for the lower and upper limit of  $\alpha_c$ . Even though the evolution of  $T_w$  with  $\alpha_c = 25$  W/m<sup>2</sup>/K shows best agreement with the CFD simulation during the growth phase of the fire, the constantly increasing difference for  $T_w$  suggests a reduction of  $\alpha_c$  over the period of this stage. For fluid temperatures greater than 1100 °C, the results for  $T_w$  become insensitive to the choice of  $\alpha_c$  and show good agreement with the results from the more complex CFD model. The comparison of  $T_f$  (for  $\alpha_c = \infty$ ,  $T_w = T_f$ ) with the results of  $T_w$  based on finite  $\alpha_c$  highlights the importance of taking the heat transfer between fluid and solid regions into account.



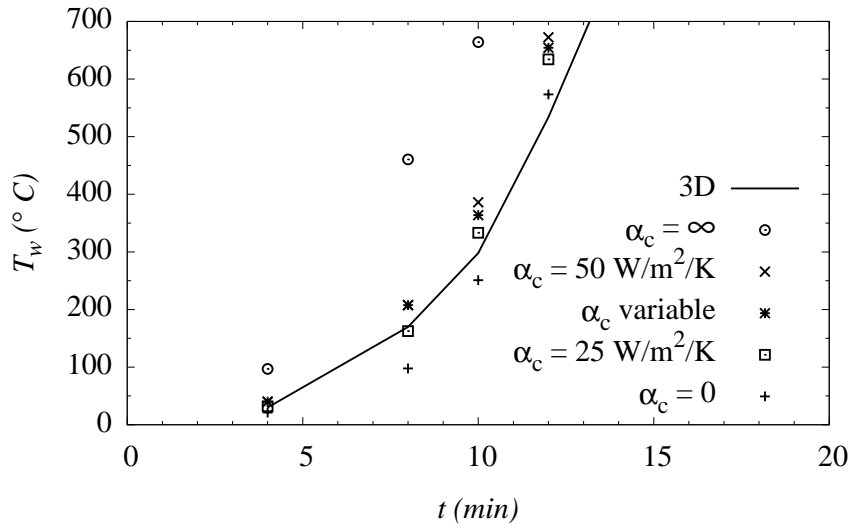


Figure 7.2: Evolution of surface temperature from 1D calculations with different  $\alpha_c$  compared with results from the CFD simulation during the first 12 minutes ( $T_w = T_f$  for the case of  $\alpha_c = \infty$ )

### 7.2.2 Longitudinal and cross-sectional distribution of the thermal load

The presented tunnel-fire simulations as well as experimental studies showed that the maximum thermal load concentrates in a small (compared to the dimensions of the tunnel) region of the tunnel, whereas in practical calculations the thermal load is assumed to be constant over the whole tunnel-lining in longitudinal and circumferential direction (except to the commonly shielded floor). A reduction of the thermal load is observed with increasing distance from the fire source in longitudinal direction. Similarly, the distribution of fluid temperature within the cross-section at which the maximum temperature is found is not constant. In the following, the longitudinal and cross-sectional distributions of tunnel-lining and fluid temperatures obtained from the CFD simulations in tunnels of real dimensions are analysed and approximated by mathematical functions allowing the consideration of the non-uniform distribution of the thermal load within engineering design.

The approximation of the longitudinal distribution of the lining temperature can be expressed with an exponential decay, reading

$$T_w(x) \approx \begin{cases} (T_{w,max} - 100)e^{0.08x} + 100 & \text{for } x < 0 \text{ m} \\ (T_{w,max} - 200)e^{-0.08x} + 200 & \text{for } x \geq 0 \text{ m} \end{cases} \quad (7.2)$$

for a ventilation velocity of 0.5 and

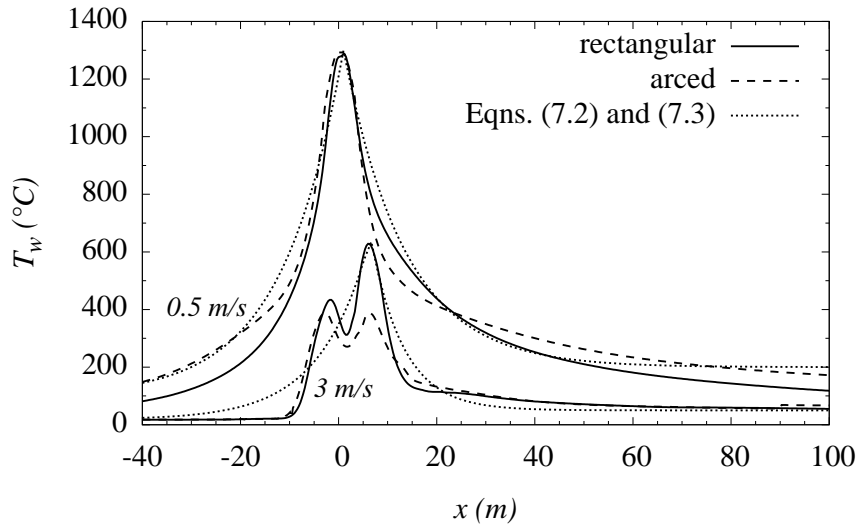


Figure 7.3: Longitudinal distribution of lining temperature of tunnels with rectangular and arced cross-section at  $z = -2.3$  m for a ventilation velocity of 0.5 m/s and at  $z = -1.2$  m for a ventilation velocity of 3 m/s

$$T_w(x) \approx \begin{cases} (T_{w,max} - 18)e^{0.1x} + 18 & \text{for } x < 0 \text{ m} \\ (T_{w,max} - 50)e^{-0.15x} + 50 & \text{for } x \geq 0 \text{ m} \end{cases} \quad (7.3)$$

for a ventilation velocity of 3 m/s (see Fig. 7.3). In Eqns. (7.2) and (7.3), the maximum lining temperature,  $T_{w,max}$ , occurs at  $x = 0$  m and is 1300 °C and 650 °C for a ventilation velocity of 0.5 m/s and 3 m/s, respectively.

For the vertical temperature distribution in the center-line of the rectangular and arced cross-section for a ventilation velocity of 0.5 m/s (see Fig. 7.4 (left)) the respective mathematical relation reads

$$T(y) \approx y^m + C. \quad (7.4)$$

The exponent  $m$  and the constant  $C$  are determined using

$$C = T_{max} - (H_r - 0.1)^{3.7} \quad \text{and} \quad m = \frac{9.8}{\sqrt{H}}, \quad (7.5)$$

respectively, where for  $C$  the tunnel height of the rectangular cross-section,  $H_r$ , is used and  $m$  is defined as a function of the tunnel height of the considered cross-section,  $H$ . The parameters used with the approximation Eqn. (7.4) to describe the vertical temperature distributions in Fig. 7.4 (left) are listed in Tab. 7.2. For a ventilation velocity of 3 m/s, the vertical temperature distribution in the center-line of the rectangular and

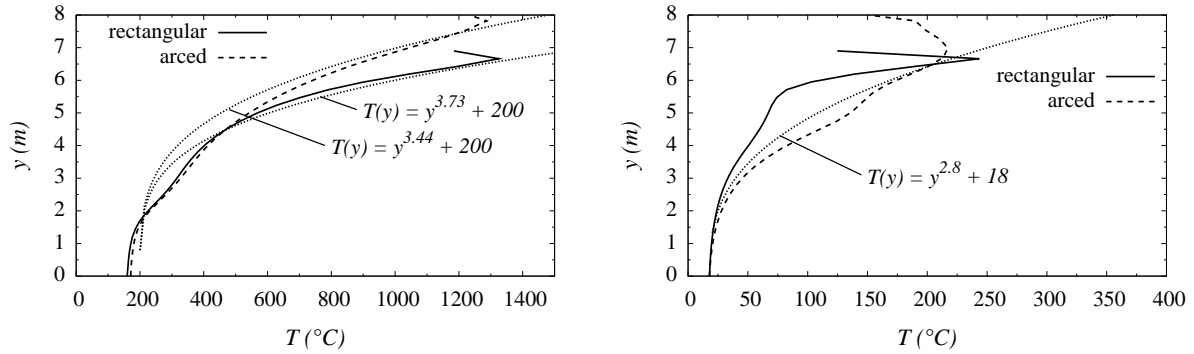


Figure 7.4: Vertical distribution of fluid temperature in tunnels of rectangular and arced cross-section with ventilation velocities of 0.5 (*left*,  $x = 0$  m,  $z = 0$  m) and 3 m/s (*right*,  $x = 6$  m,  $z = 0$  m)

arced cross-section (see Fig. 7.4 (*right*)) can be approximated as a function of the ambient temperature of the ventilation air,  $T_\infty$ , reading

$$T(y) \approx y^{2.8} + T_\infty, \tag{7.6}$$

where  $T_\infty = 18$  °C is used for the underlying example. In all Eqns. (7.2) to (7.6), length scales are inserted in meters and temperatures in degrees Celsius.

The presented mathematical functions for longitudinal and cross-sectional temperature distributions were derived from simulations, where only two types of tunnel cross-section and two ventilation velocities were studied. In order to allow a more general description of the distributions by mathematical functions, more simulations are necessary to work out the influence of different parameters such as cross-sectional area of the tunnel, shape of the tunnel cross-section, heat-release rate and ventilation velocity.

	$T_{max}$ (°C)	$H$ (m)	$C$ (°C)	$m$ (1)
rectangular	1400	6.9	200	3.73
arced	1400	8.1	200	3.44

Table 7.2: Parameters used with the approximation Eqn. (7.4) to describe vertical temperature distributions in Fig. 7.4 (*left*) for the rectangular and arced cross-section

## 7.3 Outlook

From the presented research it could be seen, that the modelling of turbulence and combustion within the developed fire code needs further development in the following areas:

- The combination of the GGDH buoyancy-modified  $k$ - $\varepsilon$  turbulence model with the EDM combustion model did not exhibit satisfactory behaviour. As combination of the same turbulence model with the flamelet-combustion model showed good agreement with experimental data in [94], the implementation of the flamelet-combustion model presents a promising solution. On the other hand, increasing computational performance allows to consider *Large Eddy Simulation (LES)* for modelling of fires in enclosures with realistic dimensions. LES only models the small-scale eddies and resolves the main structure of a turbulent flow, and thus no buoyancy modifications are necessary, which poses a main uncertainty in the RANS approach for buoyant diffusion flames.
- In the re-analyses of fire experiments as well as within the simulations of a fire scenario in real-scale tunnel geometries, overestimation of fluid temperatures in under-ventilated regions by the applied single-step combustion model was observed. This behaviour is a consequence of the assumption that, in case fuel and oxidiser are present in a computational cell, they undergo a stoichiometric combustion with a complete consumption of the limiting species, independently of the fluid temperature. Hence, local extinction effects which are encountered under conditions of excess fuel and are – amongst others – a function of the fuel-oxidiser mixture (i.e. the mixture fraction) and the local fluid temperature, cannot be reproduced. In [8], a simple method is presented to determine the ignition of a layer of products of incomplete combustion, allowing to derive a critical equivalence ratio, i.e.  $s \cdot m_{fu}/m_o$ , as a function of the layer temperature at which the layer begins to burn (see Fig. 7.5 (*left*)). Another possibility to consider local extinction effects without resolving detailed chemical processes is presented in [12, 34] within the framework of the *Eddy Dissipation Concept (EDC)*. Within this model, a pre-calculated chemical time scale,  $\tau_{ch}$ , which depends on the mixture fraction and the fluid temperature (see Fig. 7.5 (*right*)) is compared with the characteristic time scale for the turbulent fine structures,  $\tau^* = 0.41(\nu/\varepsilon)^{1/2}$ . In case of  $\tau_{ch} > \tau^*$ , extinction is predicted.

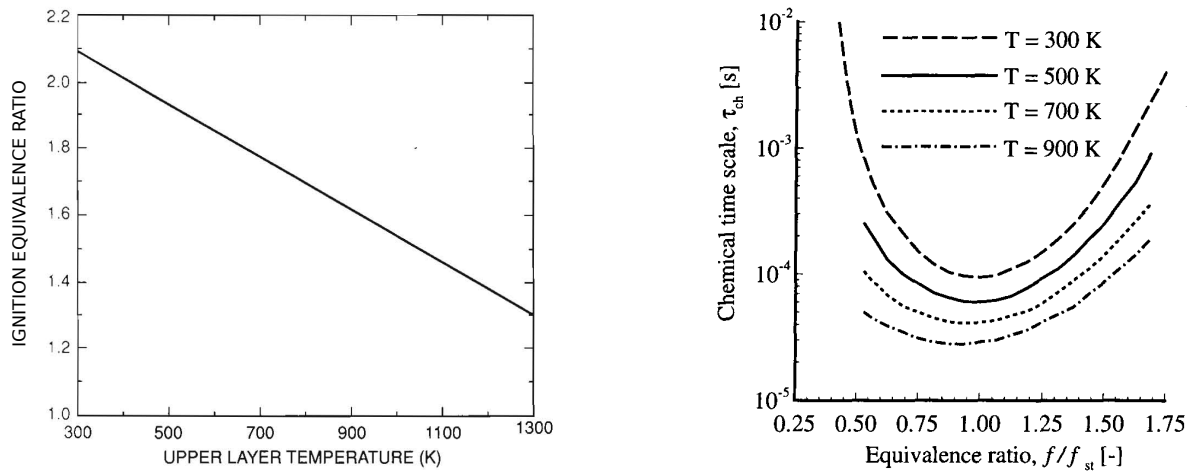


Figure 7.5: Equivalence ratio ( $s \cdot m_{fu}/m_o$ ) required for ignition of a layer of incomplete combustion products as a function of the layer temperature (*left*) [9] and chemical time scale,  $\tau_{ch}$ , of methane for different fluid temperatures and compositions (*right*, with  $f$  representing the mixture fraction) [34]

# Bibliography

- [1] <http://openfoamwiki.net/index.php/Contrib/swak4Foam>. Retrieved June, 2011.
- [2] Eurocode 1 – ONEN 1991-1-2 - Actions on structures – part 1-2: General Actions – Actions on structures exposed to fire, Österreichisches Normungsinstitut, 2004.
- [3] Deutsche Bahn AG. Ergebnisbericht zur Beurteilung von Bränden an Schienenfahrzeugen als Bemessungsbrände zur brandschutztechnischen Auslegung von oberirdischen Personenverkehrsanlagen der Deutschen Bahn AG. Technical report, DB Station & Service, Fachstelle Brandschutz, Frankfurt am Main, September 2000.
- [4] C. Albanakis and D. Bouris. 3D conjugate heat transfer with thermal radiation in a hollow cube exposed to external flow. *International Journal of Heat and Mass Transfer*, 51:6157–6168, 2008.
- [5] V. Babrauskas and D. Peacock. Heat release rate: the single most important variable in fire hazard. *Fire Safety Journal*, 18:255–272, 1992.
- [6] H.R. Baum, K.B. McCratten, and R.G. Rehm. Three dimensional simulation of fire plume dynamics. In Y. Hasemi, editor, *Fire Safety Science, Proceedings of the Fifth International Symposium*. The International Association for Fire Safety Science, 1997. ISBN: 4-9900625-5-5.
- [7] R. S. Bettis, S. F. Jagger, and Y. Wu. Interim validation of tunnel fire consequence models: summary of phase 2 tests. Internal report, Health and safety executive research and laboratory services division, 1993. IR/L/FR/93/11.
- [8] C.L. Beyler. Ignition and burning of a layer of incomplete combustion products. *Combustion Science and Technology*, 39:287–303, 1984.
- [9] C.L. Beyler. Flammability limits of premixed and diffusion flames. In P.J. DiNenno, editor, *SFPE Handbook of Fire Protection Engineering*, chapter 9. National Fire Protection Association, 3rd edition, 2002. ISBN: 087765-451-4.
- [10] Hoschke B.N. Standards and specifications for firefighters’ clothing. *Fire Safety Journal*, 4:125–137, 1981.

- 
- [11] J. Bredberg. On the wall boundary condition for turbulence models. Internal report 00/4, Department of Thermo and Fluid Dynamics, Chalmers University of Technology, 2000.
- [12] S. Byggstoyl and B.F. Magnussen. A model for flame extinction in turbulent flow. *4th International Symposium on Turbulent Shear Flows*, pages 10.32–10.38, 1983.
- [13] R.O. Carvel, A.N. Beard, P.W. Jowitt, and D.D. Drysdale. The influence of tunnel geometry and ventilation on the heat release rate of a fire. *Fire Technology*, 40:5–26, 2004.
- [14] M. Casey and T. Wintergerste. European Research Community on Flow, Turbulence and Combustion: "Best Practice Guidelines", January 2000. Version 1.0.
- [15] S. Chapman and T.G. Cowling. The mathematical theory of non-uniform gases. Cambridge University Press, 1970. ISBN: 0-521-40844.
- [16] T.J. Chung. *Computational fluid dynamics*, chapter 2.2. Cambridge University Press, 2002. ISBN 0-521-59416-2.
- [17] A. Coppalle and P. Vervisch. The total emissivities of high-temperature flames. *Combustion and Flame*, 49:101–108, 1983.
- [18] G. Cox and S. Kumar. Modeling enclosure fires using CFD. In P.J. DiNenno, editor, *SFPE Handbook of Fire Protection Engineering*, chapter 3-8. National Fire Protection Association, 3rd edition, 2002. ISBN: 087765-451-4.
- [19] A. L. Crosbie and R. G. Schrenker. Radiative transfer in a two-dimensional rectangular medium exposed to diffuse radiation. *Journal of Quantitative Spectroscopy & Radiative Transfer*, 31(4):339–372, 1984.
- [20] C.T. Crowe. *Engineering fluid mechanics*, chapter Appendix. John Wiley and Sons, 9th edition, 2009. ISBN-13: 978-0470-25977-1.
- [21] France CTICM. Demonstration of real fire tests in car parks and high buildings. Technical report, CTICM, France; PROFIL-ARBED Recherches, Luxembourg; TNO, The Netherlands, 2002.
- [22] B.J. Daly and F.H. Harlow. Transport equations in turbulence. *Physics of Fluids*, 13:2634–2649, 1970.
- [23] NIST Standard Reference Data. Thermophysical properties of fluid systems. <http://webbook.nist.gov/chemistry/fluid/>. Retrieved February, 2012.
- [24] Centre d'Etuded des Tunnels. Guide to the road tunnel safety documentation – specific hazard investigations, 2003.

- 
- [25] F.J. Diez, L.P. Bernal, and G.M. Faeth. Weakly buoyant turbulent fire plumes in uniform still and crossflowing environments. In B. Sunden and M. Faghri, editors, *Transport phenomena in fires*, chapter 2. WIT Press, 2008. ISBN: 978-1-84564-160-3.
- [26] D. Drysdale. *Introduction to fire dynamics*. John Wiley & Sons, Ltd, 3rd edition, 2011. ISBN: 978-0-470-31903-1.
- [27] McGrattan et al. *Fire Dynamics Simulator (Version 4) Technical Reference Guide*. National Institute of Standards and Technology, Gaithersburg, MD, USA, 2004.
- [28] ABCB Australia FCRC. Fire design guidelines. Technical report, Australian Building Codes Board, 1996.
- [29] J.H. Ferziger and M. Peric. *Computational Methods for Fluid Dynamics*. Springer-Verlag, 3rd edition, 2002. ISBN: 3-540-42074-6.
- [30] D.F. Fletcher, J.H. Kent, V.B. Apte, and A.R. Green. Numerical simulations of smoke movement from a pool fire in a ventilated tunnel. *Fire Safety Journal*, 23:305–325, 1994.
- [31] Forschungsgesellschaft für Straßen- und Verkehrswesen – Arbeitsgruppe Verkehrsführung und Verkehrssicherheit. *Richtlinie für die Ausstattung und den Betrieb von Straßentunnel – RABT*, 2002.
- [32] TU Wien, Institut für Hochbau und Technologie. Verkehrsbauwerk Südtiroler Platz, Einreichung 2006, Gutachterliche Untersuchung, Rauch- und Wärmeabzug in der UstraB Station. Technical report, TU Wien, Institut für Hochbau und Technologie, 2006.
- [33] V. Gnielinski. Wärmeübertragung bei der Strömung längs einer ebenen Wand. In Verein Deutscher Ingenieure, editor, *VDI-Wärmeatlas*, chapter Gd 1. Springer-Verlag, 8th edition, 1997. ISBN: 3-540-62719-7.
- [34] I. R. Gran, M. C. Melaaen, and B. F. Magnussen. Numerical simulation of local extinction effects in turbulent combustor flows of methane and air. *25th Symposium on Combustion/The Combustion Institute*, pages 1283–1291, 1994.
- [35] A. Haack. Technical report part 1 – Design fire scenarios. Technical report, Thematic Network FIT – Fire in Tunnels, 2007.
- [36] A. Haack, W. Meyeroltmanns, and H.P. Cabos. Verhalten von Schienenfahrzeugen in Stahl- bzw. Aluminiumbauweise bei Tunnelbränden. Forschungsbericht P 570, Studiengesellschaft Stahlanwendung e.V., Düsseldorf, 2001.
- [37] Y. Hasemi and T. Togunaga. Flame geometry effects on the buoyant plumes from turbulent diffusion flames. *Fire Science and Technology*, 4(1):15–26, 1984.



- 
- [38] G. Heskestad. *Fire Plumes. SFPE Handbook*. National fire protection association, 2nd edition, 1995.
- [39] C. Huggett. Estimation of rate of heat release by means of oxygen consumption measurements. *Fire and Materials*, 4(2):61–65, 1980.
- [40] H. Ingason. Heat release rate measurements in tunnel fires. SP Report 1994:08, Swedish National Testing and Research Institute, 1994.
- [41] H. Ingason. Design fires in tunnels. Second International Symposium on Safe&Reliable Tunnels, Lausanne, 2006.
- [42] H. Ingason. Design fire curves for tunnels. *Fire Safety Journal*, 49(4):259–265, 2009.
- [43] H. Ingason and A. Lönnemark. Heat release rates from heavy goods vehicle trailer fires in tunnels. *Fire Safety Journal*, 40:646–668, 2005.
- [44] R.I. Issa. Solution of the implicitly discretised fluid flow equations by operator-splitting. *Journal of Computational Physics*, 62:40–65, 1985.
- [45] H. Jasak. *Error analysis and estimation for the finite volume method with applications to fluid flows*. PhD thesis, Imperial College of Science, Technology and Medicine, 1996.
- [46] H. Jasak, H.G. Weller, and A.D. Gosman. High resolution NVD differencing scheme for arbitrarily unstructured meshes. *International Journal for Numerical Methods in Fluids*, 31:431–449, 1999.
- [47] C.L.V. Jayatilaka. The influence of Prandtl number and surface roughness on the resistance of the laminar sublayer to momentum and heat transfer. *Progress in Heat and Mass Transfer*, 1:193, 1969.
- [48] W.P. Jones and B.E. Launder. The prediction of laminarization with a two-equation model of turbulence. *Int. Journal of Heat and Mass Transfer*, 15(301-314), 1972.
- [49] W.W. Jones. A review of compartment fire models. NBSIR 83-2684, National Bureau of Standards, 1983.
- [50] W.W. Jones, R.D. Peacock, G.P. Forney, and P.A. Reneke. *CFAST – Consolidated Model of Fire Growth and Smoke Transport (Version 6) – Technical Reference Guide*. National Institute of Standards and Technology, 2009.
- [51] V. Langner and R. Bopp. Semmering-Basistunnel Neu – Technischer Bericht Lüftungskonzept. Technical report, Gruner GmbH Ingenieure und Planer, 2010. Plannummer: 5510-EB-0600AL-00-0001-F02.

- [52] B.E. Launder and D.B. Spalding. The numerical calculation of turbulent flows. *Computer Methods in applied Mechanics and Engineering*, 3(269-289), 1974.
- [53] T. Lennon and B. Moore. The natural fire safety concept – full-scale tests at Cardington. *Fire Safety Journal*, 38(7):623–643, 2003.
- [54] X. Li and P. Durbetaki. The conjugate formulation of a radiation induced transient natural convection boundary layer. *International Journal for Numerical Methods in Engineering*, 35:853–870, 1992.
- [55] A. Lönnemark and H. Ingason. Gas temperatures in heavy goods vehicle fires in tunnels. *Fire Safety Journal*, 40:506–527, 2005.
- [56] Anders Lönnemark. *On the Characteristics of Fires in Tunnels*. PhD thesis, Department of Fire Safety Engineering, Lund Institute of Technology, Lund University, 2005.
- [57] B.F. Magnussen. The Eddy Dissipation Concept – a Bridge between Science and Technology. *Proceedings of the ECCOMAS Thematic Conference on Computational Combustion, Lisbon, Portugal, 21-24 June, 2005*.
- [58] B.J. McBride, S. Gordon, and M.A. Reno. Coefficients for calculating thermodynamic and transport properties of individual species. NASA Technical Memorandum 4513, National Aeronautics and Space Administration, 1993.
- [59] B.J. McCaffrey. Purely buoyant diffusion flames: some experimental results. Report NBSIR 79-1910, National Bureau of Standards, Washington D.C., 1976.
- [60] K. McGrattan, B. Klein, S. Hostikka, and J. Floyd. *Fire Dynamics Simulator (Version 5) Users Guide*. National Institute of Standards and Technology, 2008.
- [61] B. Merci, E. Dick, J. Vierendeels, and C. Langhe. Determination of  $\varepsilon$  at inlet boundaries. *Int Journal of Num Methods for Fluid & Heat Flow*, 12(1):65–80, 2002.
- [62] M. Modest. *Radiative Heat Transfer*. Academic Press, 2nd edition, 2003.
- [63] S. Murakami, S. Kato, and H. Nakagawa. Numerical prediction of horizontal non-isothermal 3-D jet in a room based on the k- $\varepsilon$  model. *American Society of Heating, Refrigerating, and Air-Conditioning Engineers*, 1991.
- [64] S. Nam and R.G. Bill. Numerical simulation of thermal plumes. *Fire Safety Journal*, 21(3):231–256, 1993.
- [65] E.E.A. Nilsson, A. Sunden, Z. Yan, and Faghri. Mathematical modelling and numerical simulation of fires. In B. Sunden and M. Faghri, editors, *Transport phenomena in fires*, chapter 1. WIT Press, 2008. ISBN: 978-1-84564-160-3.

- [66] B. Noll. *Numerische Strömungsmechanik. Grundlagen*. Springer-Verlag Berlin Heidelberg New York, 1983. ISBN: 3-540-56712-7.
- [67] V. Novozhilov. Computational fluid dynamics modeling of compartment fires. *Progress in Energy and Combustion Science*, 27:611–666, 2001.
- [68] S.M. Olenick and D.J. Carpenter. An updated international survey of computer models for fire and smoke. *Journal of Fire Protection Engineering*, 13(2):87–110, 2003.
- [69] CFD online forum – OpenFoam. [www.cfd-online.com/forums/openfoam-solving/59636-why-say-uses-e2-80-98pseudostaggered-e2-80-99-finite-volume-numerics.html](http://www.cfd-online.com/forums/openfoam-solving/59636-why-say-uses-e2-80-98pseudostaggered-e2-80-99-finite-volume-numerics.html). Retrieved July, 2010.
- [70] OpenCFD. OpenFOAM 1.7.1 – the open source CFD toolbox – User Guide. *OpenCFD Limited*, 2010. [www.openfoam.com](http://www.openfoam.com).
- [71] W.J. Parker. Calculations of the heat release rate by oxygen consumption for various applications. NBSIR 81-2427-1, National Bureau of Standards, 1982.
- [72] S.V. Patankar. *Numerical Heat Transfer and Fluid Flow*. Hemisphere Publishing Corporation, 1980. ISBN: 0-89116-522-3.
- [73] R.D. Peacock et al. Defining flashover for fire hazard calculations. *Fire Safety Journal*, 32(331-345), 1999.
- [74] N. Peters. Laminar diffusion flamelet models in non-premixed turbulent combustion. *Progress in Energy and Combustion Science*, 10(3):319–339, 1984.
- [75] T.J. Poinsot and S.K. Lele. Boundary conditions for direct simulations of compressible viscous flows. *Journal of Computational Physics*, 101:104–129, 1992.
- [76] N.D. Pope and C.G. Bailey. Quantitative comparison of FDS and parametric fire curves with post-flashover compartment fire test data. *Fire Safety Journal*, 41:99–110, 2006.
- [77] G.D. Raithby. Discussion of the finite-volume method for radiation, and its application using 3-D unstructured mesh. *Numerical Heat Transfer*, 35(4):389–405, 1999.
- [78] M. A. Ramankutty and A. L. Crosbie. Modified discrete-ordinates solution of radiative transfer in three-dimensional rectangular enclosures. *Journal of Quantitative Spectroscopy & Radiative Transfer*, 60(1):103–134, 1998.
- [79] S.S. Sazhin, E.M. Sazhina, O. Faltsi-Saravelou, and P. Wild. The P-1 model for thermal radiation transfer: advantages and limitations. *Fuel*, 75(3):289–294, 1995.

- [80] A. Shabbir and W. K. George. Experiments on a round turbulent buoyant plume. *Journal of Fluid Mechanics*, 275:1–32, 1994.
- [81] R. Siegel and J. Howell. *Thermal Radiation Heat Transfer*. Taylor & Francis, 4th edition, 2002.
- [82] G.L. Tan. Fire protection in tunnels open to hazardous goods transport experience in the netherlands. *La Securite Dans Les Tunnels Routiers, Paris*, 1997.
- [83] P.H. Thomas. The movement of smoke in horizontal passages against an air flow. Fire research note no. 723, Fire Research Station, 1968.
- [84] S.R. Tieszen and L.A. Gritzko. Transport phenomena that affect heat transfer in fully turbulent fires. In B. Sunden and M. Faghri, editors, *Transport phenomena in fires*, chapter 2. WIT Press, 2008. ISBN: 978-1-84564-160-3.
- [85] Union International des Chemins de Fer (UIC). Rules governing application of the enlarged GA, GB, GB1, GB2, GC and GI3 gauges. Codex 506 VE, Union International des Chemins de Fer, 2008. ISBN 2-7461-1374-0.
- [86] K. van Maele and B. Merci. Application of two buoyancy-modified  $k-\varepsilon$  turbulence models to different types of buoyant plumes. *Fire Safety Journal*, 41:122–138, 2006.
- [87] O. Vassart, L.G. Cajot, and M. Brasseur. WP 1 – thermal & mechanical actions. Technical report, Dissemination of Fire Safety Engineering Knowledge. [www.difisek.eu/UK/Menudata/documents.htm](http://www.difisek.eu/UK/Menudata/documents.htm). Retrieved January, 2012.
- [88] D. Veynante and L. Vervisch. Turbulent combustion modeling. *Progress in Energy and Combustion Science*, 28(3):193–266, 2002.
- [89] J.R. Viegas, M.W. Rubesin, and C.C. Horstman. On the use of wall functions as boundary conditions for two-dimensional separated compressible flows. AIAA-85-0180, AIAA 23rd Aerospace Sciences Meeting, Reno, Nevada, 1985.
- [90] S. Welch, A. Jowsey, S. Deeny, R. Morgan, and J.L. Torero. BRE large compartment fire tests – characterising post-flashover fires for model validation. *Fire Safety Journal*, 42:548–567, 2007.
- [91] K. William and JR. George. Turbulence measurements in an axisymmetric buoyant plume. *International Journal of Heat and Mass Transfer*, 20:1145–1154, 1977.
- [92] J. Worthy, V. Sanderson, and P. Rubini. Comparison of modified  $k-\varepsilon$  model turbulence models for buoyant plumes. *Numerical Heat Transfer*, 39:151–165, 2001.
- [93] Z. Yan. CFD fire simulation and its recent development. In B. Sunden and M. Faghri, editors, *Transport phenomena in fires*, chapter 2. WIT Press, 2008. ISBN: 978-1-84564-160-3.

- 
- [94] Z. Yan and G. Holmstedt. A two-equation turbulence model and its application to a buoyant diffusion flame. *International Journal of Heat and Mass Transfer*, 42:1305–1315, 1999.
- [95] G. H. Yeoh and K. K. Yuen. *Computational Fluid Dynamics in Fire Engineering*, chapter 3. Elsevier, 2008. ISBN: 978-0-7506-8589-4.
- [96] G. H. Yeoh and K. K. Yuen. *Computational Fluid Dynamics in Fire Engineering*, chapter 2. Elsevier, 2008. ISBN: 978-0-7506-8589-4.
- [97] M. Zeiml, R. Lackner, F. Pesavento, and B. A. Schrefler. Thermo-hydro-chemical couplings considered in safety assessment of shallow tunnels subjected to fire load. *Fire Safety Journal*, 43(2):83–95, 2008.

# Appendix **A**

---

## Parameters to describe the temperature dependency of fluid properties

### A.1 JANAF-coefficients

#### A.1.1 Methane (CH<sub>4</sub>)

stoichiometric air fuel mass ratio: 17.1271  
stoichiometric oxygen fuel mass ratio: 4.0  
heat of combustion:  $5.00264 \cdot 10^7$  J/kg

<i>Low temperature coefficients (<math>200\text{ K} \leq T &lt; 1000\text{ K}</math>)</i>					
	fuel (CH <sub>4</sub> )	oxidiser (air)	reactants	burntProducts	products
$d_1$	1.63543	3.10131	2.95825	3.0602	3.05615
$d_2$	0.0100844	0.00124137	0.00210441	0.00182422	0.0018477
$d_3$	-3.36924e-06	-4.18816e-07	-7.06762e-07	-5.93878e-07	-6.01767e-07
$d_4$	5.34973e-10	6.64158e-11	1.12145e-10	8.93807e-11	9.06474e-11
$d_5$	-3.15528e-14	-3.91274e-15	-6.61028e-15	-4.97595e-15	-5.05149e-15
$d_6$	-10005.6	-985.266	-1865.61	-10998.7	-10995.9

Table A.1: Coefficients from JANAF-tables of thermodynamics [58] for the calculation of the specific heat capacity at constant pressure in the range  $200\text{ K} \leq T < 1000\text{ K}$

<i>High temperature coefficients (1000 K ≤ T ≤ 6000 K)</i>					
	fuel (CH <sub>4</sub> )	oxidiser (air)	reactants	burntProducts	products
$d_1$	5.14988	3.58378	3.73662	3.54628	3.55084
$d_2$	-0.013671	-0.000727005	-0.00199028	0.000378279	0.000338343
$d_3$	4.91801e-05	1.67057e-06	6.30727e-06	2.02797e-07	3.42018e-07
$d_4$	-4.84744e-08	-1.09203e-10	-4.82941e-09	9.31602e-10	7.91162e-10
$d_5$	1.66694e-11	-4.31765e-13	1.23723e-12	-6.84016e-13	-6.34688e-13
$d_6$	-10246.6	-1050.53	-1948.03	-11102.1	-11099.7

Table A.2: Coefficients from JANAF-tables of thermodynamics [58] for the calculation of the specific heat capacity at constant pressure in the range  $1000 \text{ K} \leq T \leq 6000 \text{ K}$

<i>Molecular weight (kg/mol)</i>					
	fuel (CH <sub>4</sub> )	oxidiser (air)	reactants	burntProducts	products
$W_i$	16.0428	28.8504	27.6004	27.6334	27.6004

Table A.3: Molecular weight of different compositions

### A.1.2 Air

<i>Low and high temperature coefficients</i>		
	200 K ≤ T < 1000 K	1000 K ≤ T ≤ 6000 K
$d_1$	3.10131	3.58378
$d_2$	0.00124137	-0.000727005
$d_3$	-4.18816e-07	1.67057e-06
$d_4$	6.64158e-11	-1.09203e-10
$d_5$	-3.91274e-15	-4.31765e-13
$d_6$	-985.266	-1050.53

Table A.4: Coefficients from JANAF-tables of thermodynamics [58] for the calculation of the specific heat capacity at constant pressure of air in the ranges of  $200 \text{ K} \leq T < 1000 \text{ K}$  and  $1000 \text{ K} \leq T \leq 6000 \text{ K}$

## A.2 Constants for Sutherland's formula of dynamic viscosity

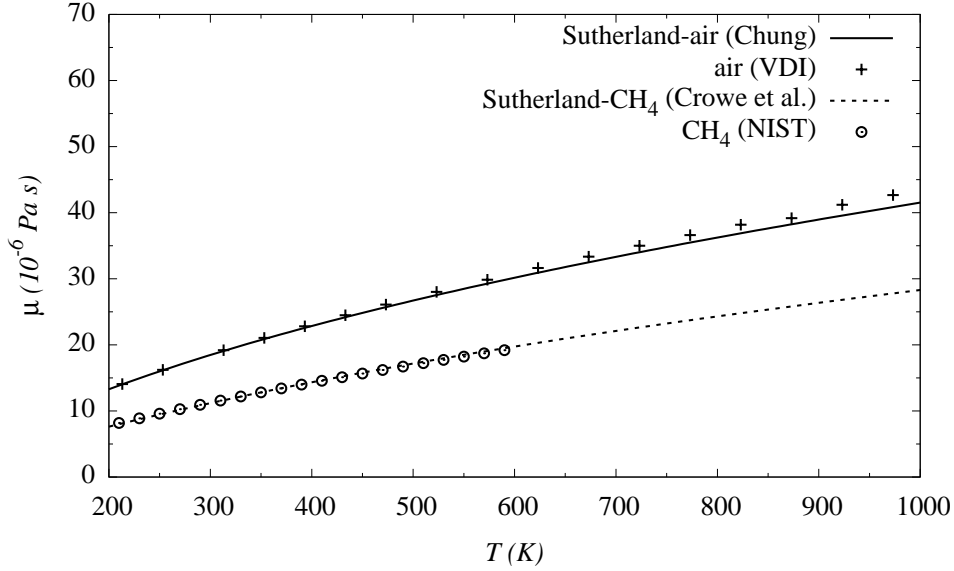


Figure A.1: A comparison of measured dynamic viscosity for methane (NIST [23]) and air (VDI [33]) with Sutherland's formula Eqn. (5.80), using  $A_s = 1.072 \cdot 10^{-6}$  kg/(msK<sup>1/2</sup>) and  $T_s = 198$  K for methane (Crowe et al. [20]), and  $A_s = 1.458 \cdot 10^{-6}$  kg/(msK<sup>1/2</sup>) and  $T_s = 110.4$  K for air (Chung [16])

## A.3 Coefficients of weighting functions for the mean absorption coefficient

<i>High temperature coefficients (<math>300\text{ K} \leq T \leq 2500\text{ K}</math>)</i>			
	CH <sub>4</sub>	CO <sub>2</sub>	H <sub>2</sub> O
$b_0$	6.6334	18.741	-0.23093
$b_1$	-0.0035686	-121.31e3	-1.12390e3
$b_2$	1.6682e-8	273.5e6	9.4153e6
$b_3$	2.5611e-10	-194.05e9	-2.99885e9
$b_4$	-2.6558e-14	56.31e12	0.51382e1
$b_5$	0	-5.8169e15	-1.868e10

Table A.5: Coefficients for the weighting functions describing the temperature dependency of the mean absorption coefficient in the range  $300\text{ K} \leq T \leq 2500\text{ K}$



# Appendix **B**

---

## Discretisation schemes and solver settings for real-scale simulations

### B.1 Discretisation schemes (*fvSchemes*)

#### B.1.1 Fluid regions

ddtSchemes

```
{  
  default      Euler;  
}
```

gradSchemes

```
{  
  default      Gauss linear;  
}
```

divSchemes

```
{  
  default      none;  
  div(phi,U)   Gauss linearUpwindV cellMDLimited Gauss linear 1;  
  div(phiU,p)  Gauss linear;  
  div(phi,k)   Gauss upwind;  
  div(phi,epsilon) Gauss upwind;  
  div(phi,fo)  linearUpwind cellLimited Gauss linear 1;
```

```

div(phi,ft)      linearUpwind cellLimited Gauss linear 1;
div(phi,hs)      linearUpwind cellMDLimited Gauss linear 1;
div(phi,R)       Gauss upwind;
div(R)           Gauss linear;
div((muEff*dev2(grad(U).T()))) Gauss linear;
div(Ji,Ii_h)     Gauss upwind;
}

```

laplacianSchemes

```

{
  default          none;
  laplacian(muEff,U)      Gauss linear limited 0.333;
  laplacian((rho*(1|A(U))),p_rgh) Gauss linear limited 0.333;
  laplacian(alphaEff,hs)  Gauss linear limited 0.333;
  laplacian(DkEff,k)      Gauss linear limited 0.333;
  laplacian(DepsilonEff,epsilon) Gauss linear limited 0.333;
  laplacian(alphaEff,fu)  Gauss linear limited 0.333;
  laplacian(alphaEff,ft)  Gauss linear limited 0.333;
  laplacian(DREff,R)      Gauss linear limited 0.333;
}

```

interpolationSchemes

```

{
  default          linear;
}

```

snGradSchemes

```

{
  default          limited 0.333;
}

```

### B.1.2 Solid regions

ddtSchemes

```

{
  default          Euler;
}

```

```
gradSchemes
{
  default          Gauss linear;
}

divSchemes
{
  default          none;
}

laplacianSchemes
{
  default          none;
  laplacian(K,T)  Gauss linear uncorrected;
}

interpolationSchemes
{
  default          linear;
}

snGradSchemes
{
  default          uncorrected;
}
```

## B.2 Solver settings (*fvSolution*)

### B.2.1 Fluid regions

```
rho
{
  solver          PCG;
  preconditioner  DIC;
  tolerance       0;
  relTol          0;
};
```

```
p_rgh
{
  solver          GAMG;
  tolerance        1e-7;
  relTol          0.01;
  smoother         GaussSeidel;
  cacheAgglomeration true;
  nCellsInCoarsestLevel 10;
  agglomerator     faceAreaPair;
  mergeLevels      1;
};
```

```
p_rghFinal
{
  solver          GAMG;
  tolerance        1e-7;
  relTol          0;
  smoother         GaussSeidel;
  cacheAgglomeration true;
  nCellsInCoarsestLevel 10;
  agglomerator     faceAreaPair;
  mergeLevels      1;
};
```

```
U
{
  solver          smoothSolver;
  smoother         GaussSeidel;
  tolerance        1e-7;
  relTol          0.1;
  nSweeps          1;
};
```

```
UFinal
{
  solver          smoothSolver;
  smoother         GaussSeidel;
  tolerance        1e-7;
  relTol          0;
  nSweeps          1;
};
```

```
fu|ft|k|epsilon|hs
{
  solver          smoothSolver;
  smoother        GaussSeidel;
  tolerance        1e-7;
  relTol          0;
  nSweeps         1;
};
```

```
li
{
  solver          GAMG;
  tolerance        1e-4;
  relTol          0;
  smoother        DILU;
  cacheAgglomeration true;
  nCellsInCoarsestLevel 10;
  agglomerator    faceAreaPair;
  mergeLevels     1;
}
```

## B.2.2 Solid regions

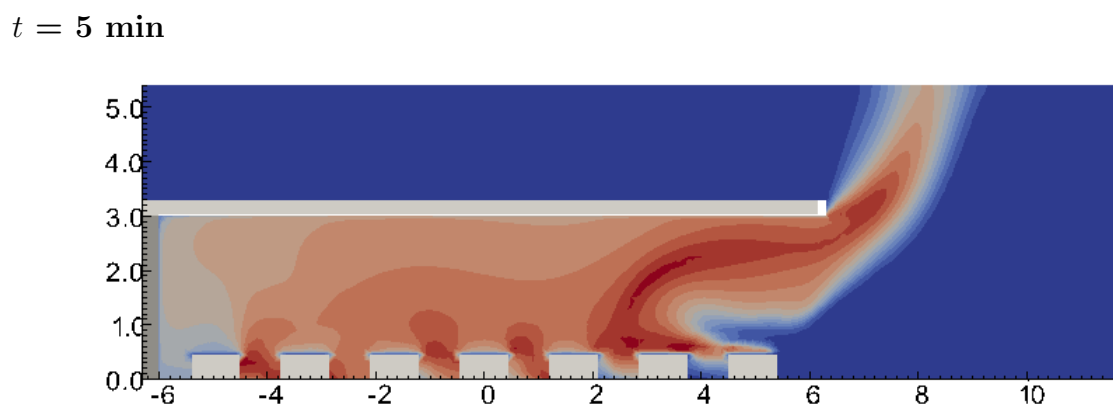
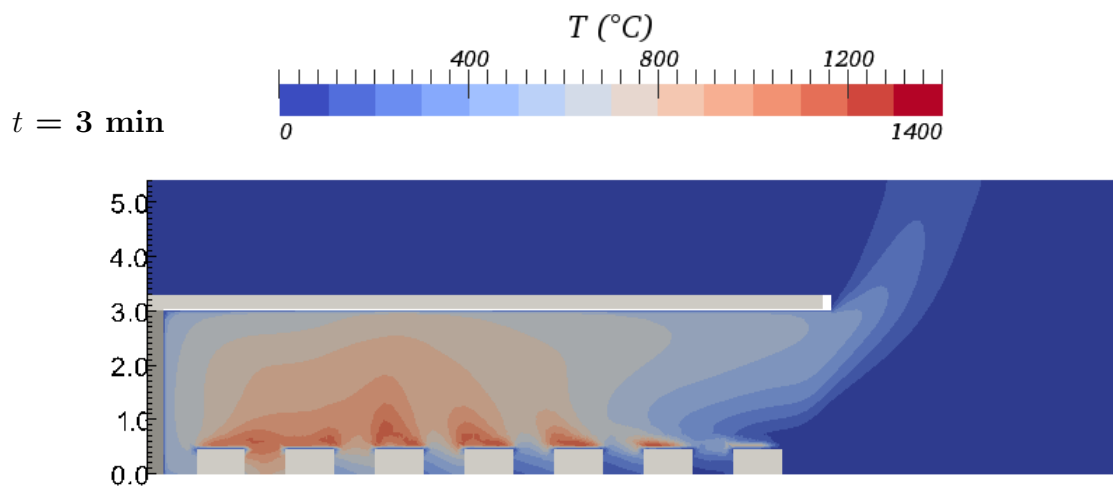
```
T
{
  solver          PCG;
  preconditioner  DIC;
  tolerance        1e-10
  relTol          0.0;
};
```

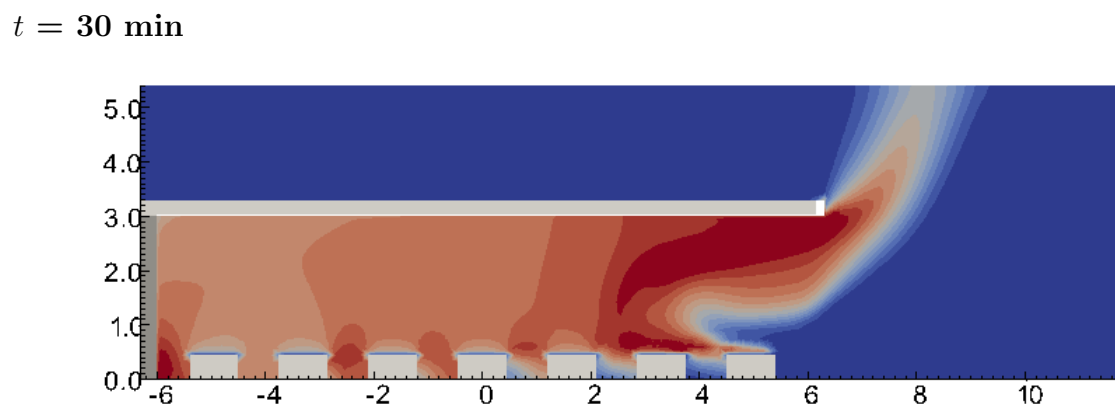
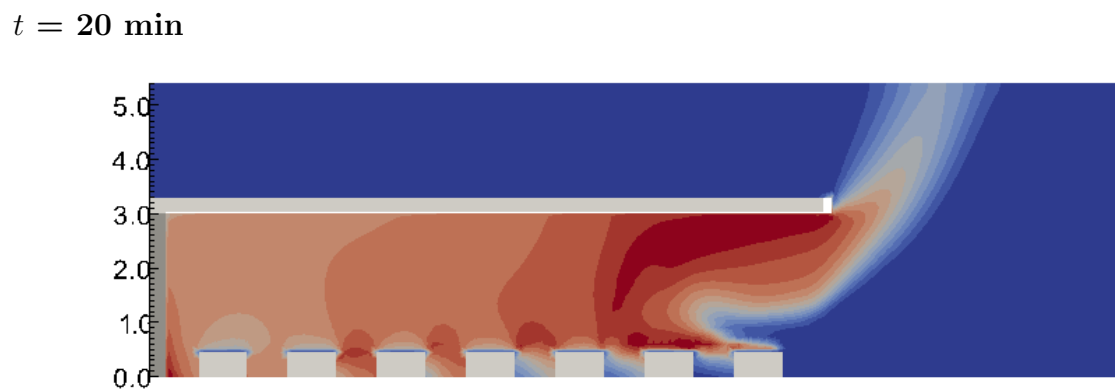
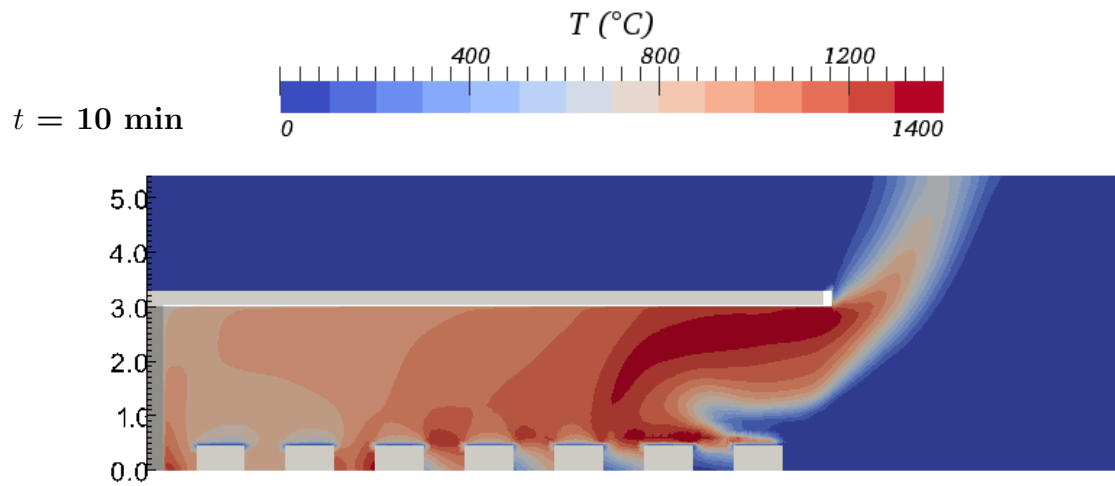
# Appendix C

---

## Simulation results: Cardington

### C.1 Contour plots of temperature at $z = 1.53$ m





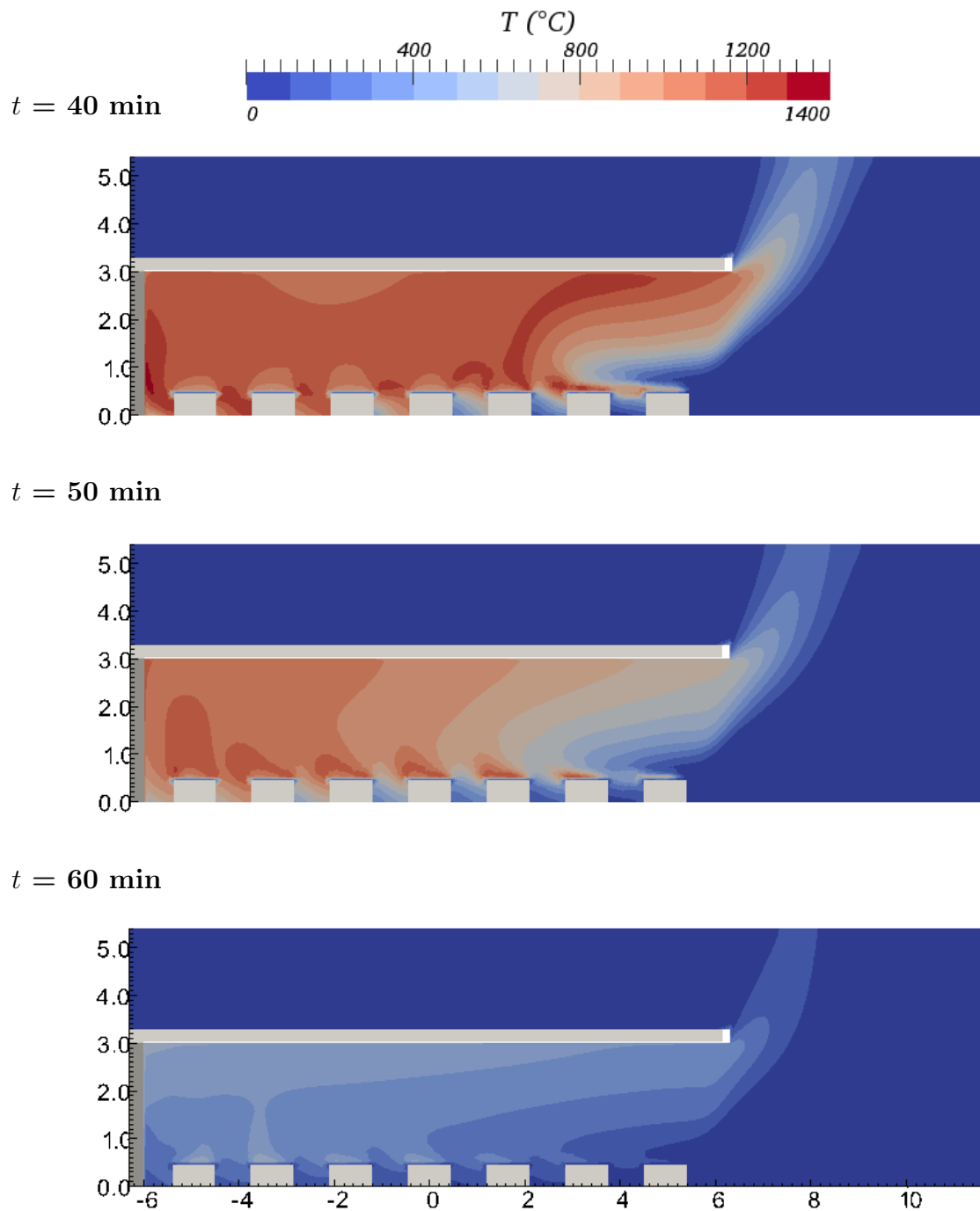


Figure C.1: Contour plots of temperature at  $z = 1.53$  m for different time instants (dimensions in m)



# Appendix **D**

---

**Simulation results: Buxton**

## D.1 Contour plots of temperature at $z = 0$ m (reactive)

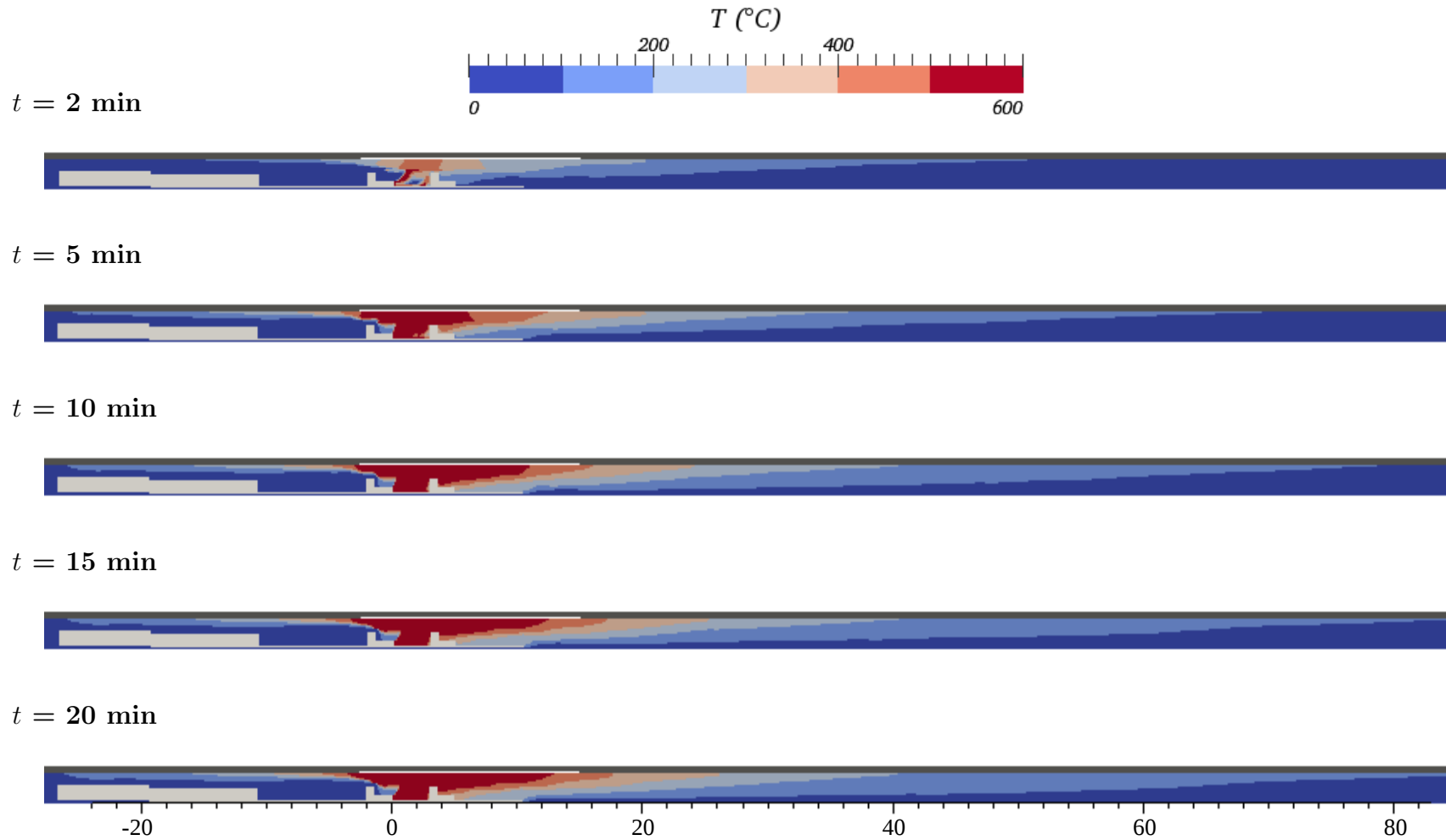


Figure D.1: Contour plots of temperature at  $z = 0$  m for different time instants for the reactive case (dimensions in m)

## D.2 Contour plots of temperature at $z = 0$ m (non-reactive)

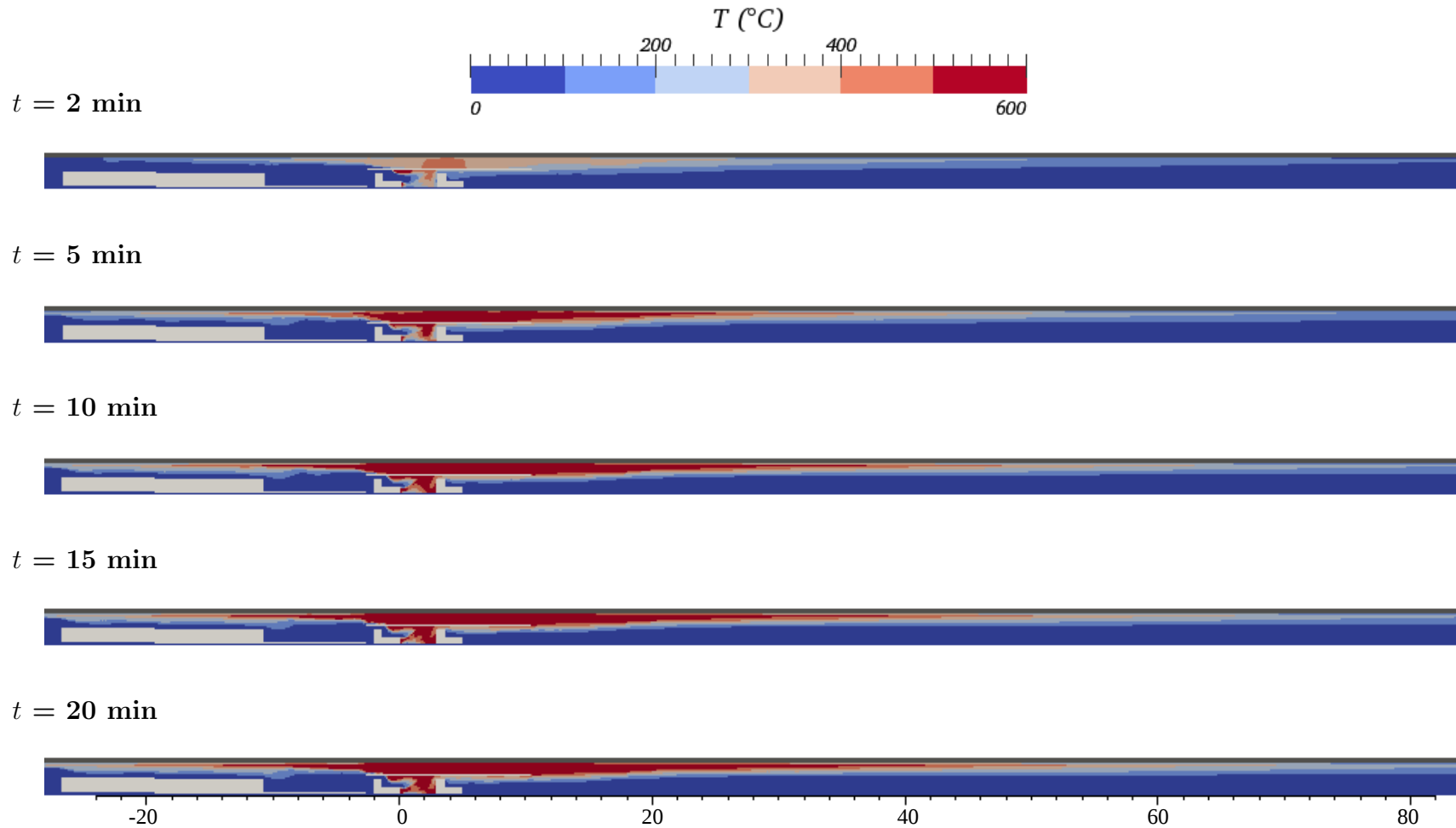


Figure D.2: Contour plots of temperature at  $z = 0$  m for different time instants for the non-reactive case (dimensions in m)

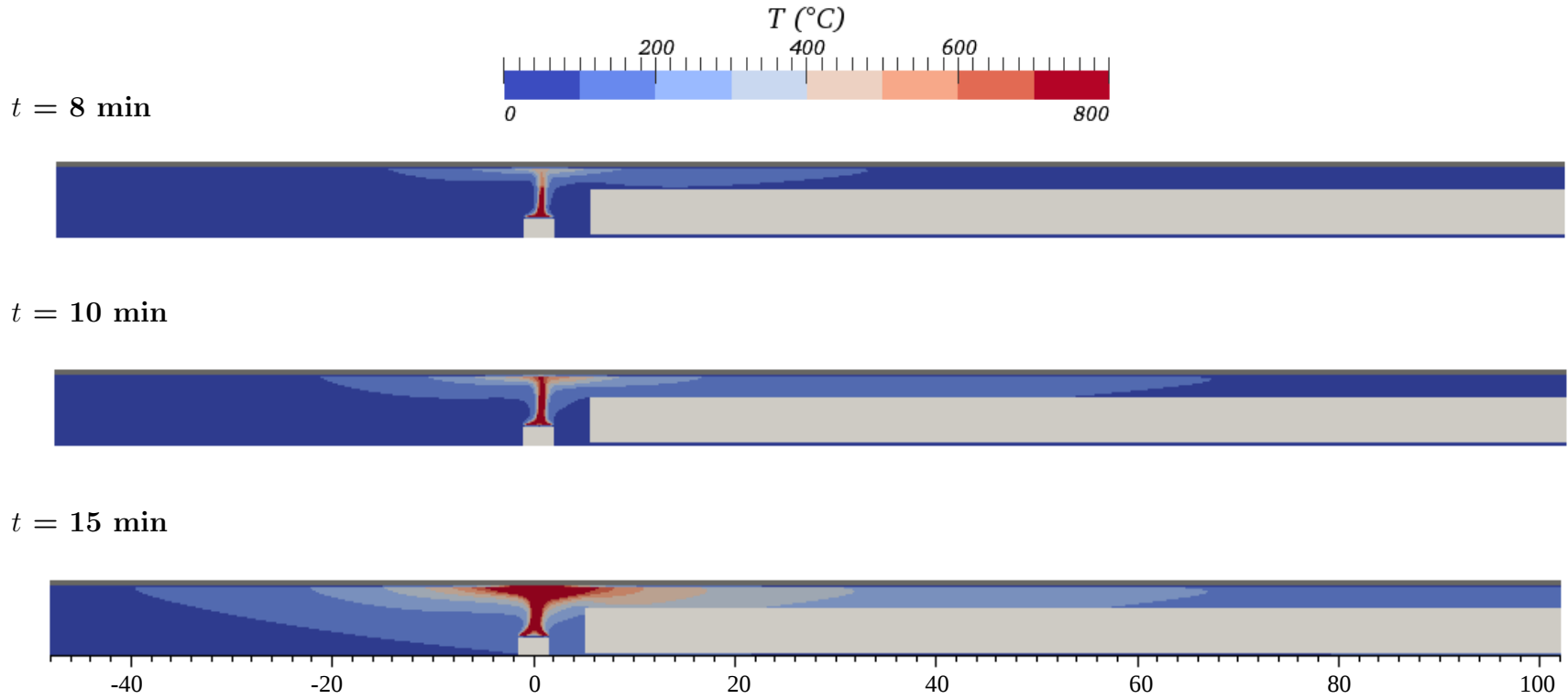
# Appendix **E**

---

**Simulation results: real-scale tunnels**

## E.1 Contour plots of temperature for a ventilation velocity of 0.5 m/s

### E.1.1 Rectangular cross-section ( $z = -2.3$ m)



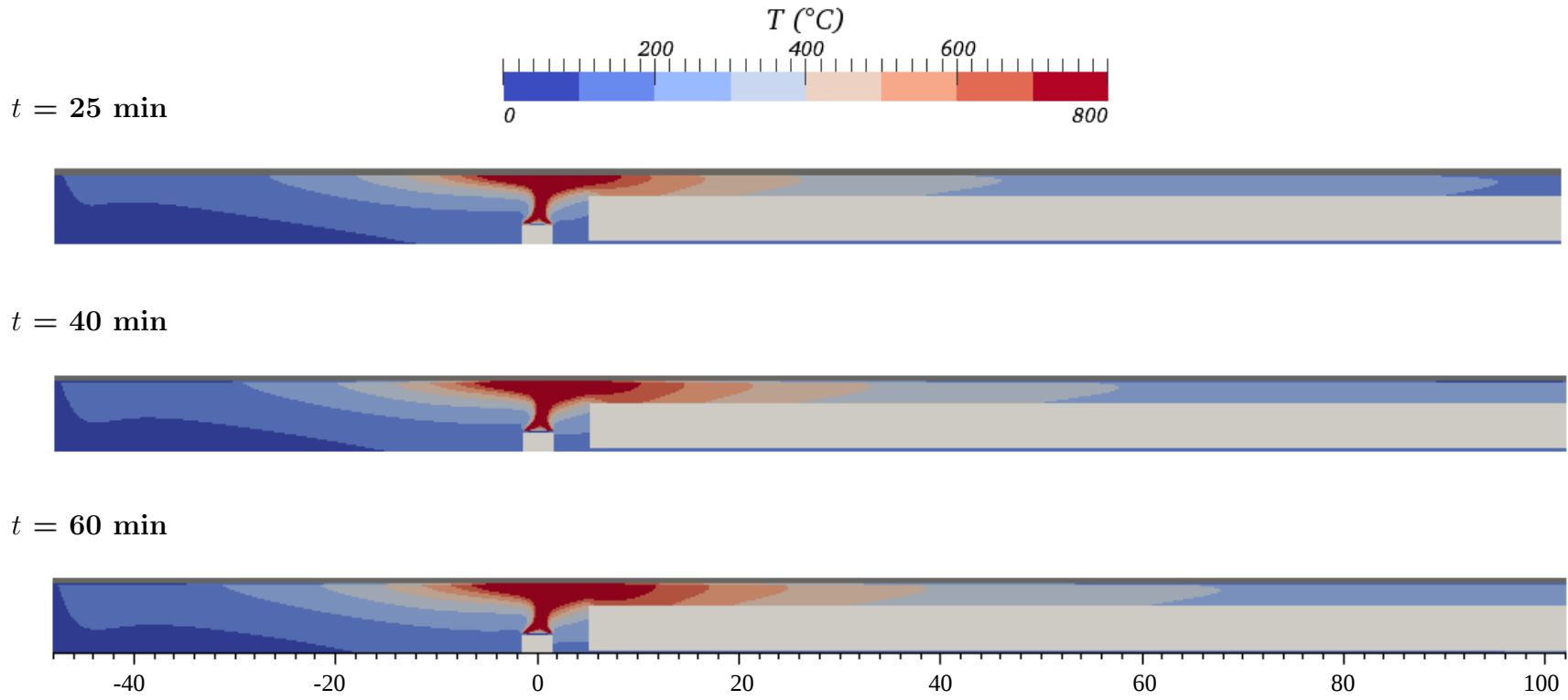
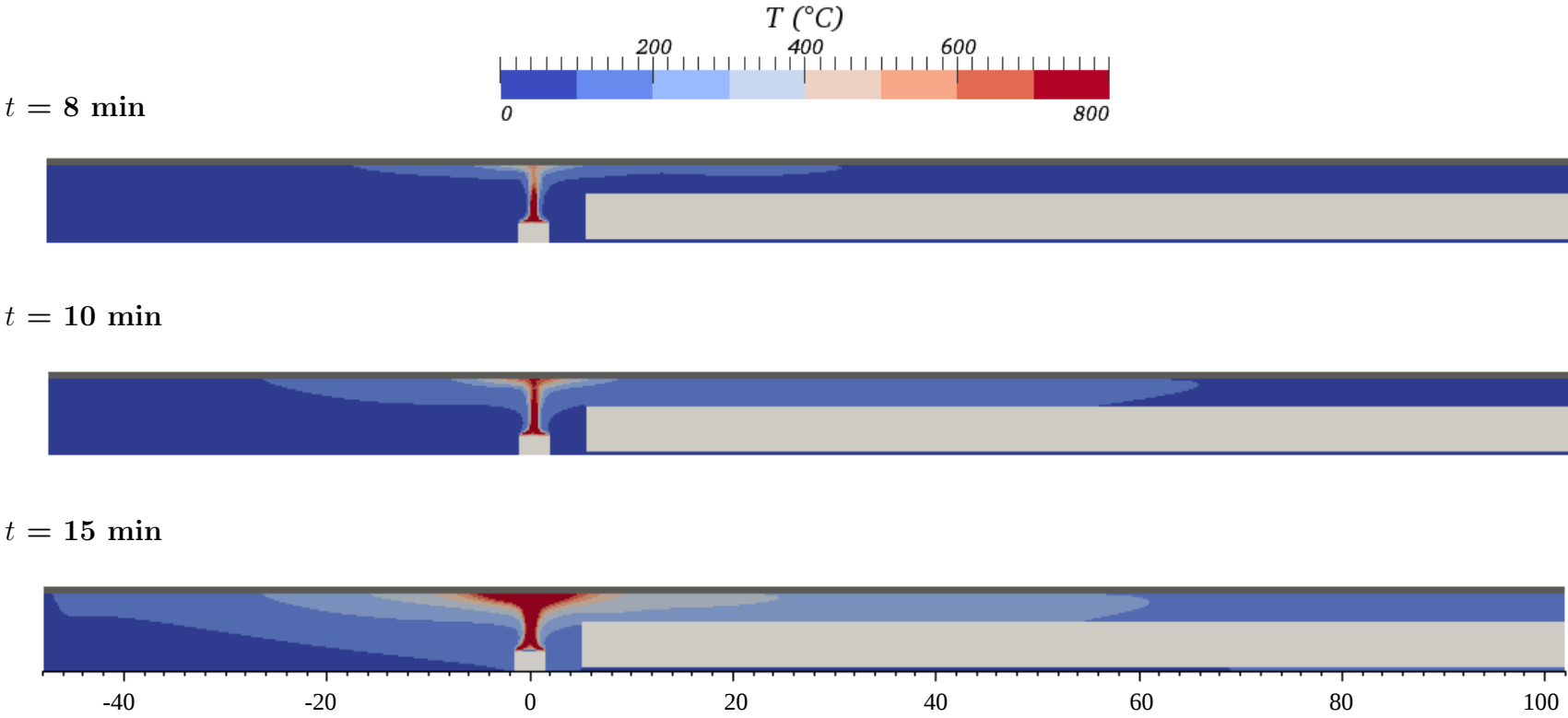


Figure E.1: Contour plots of temperature at  $z = -2.3$  m for the rectangular cross-section for different time instants (dimensions in m)

E.1.2 Arced cross-section ( $z = -2.3$  m)



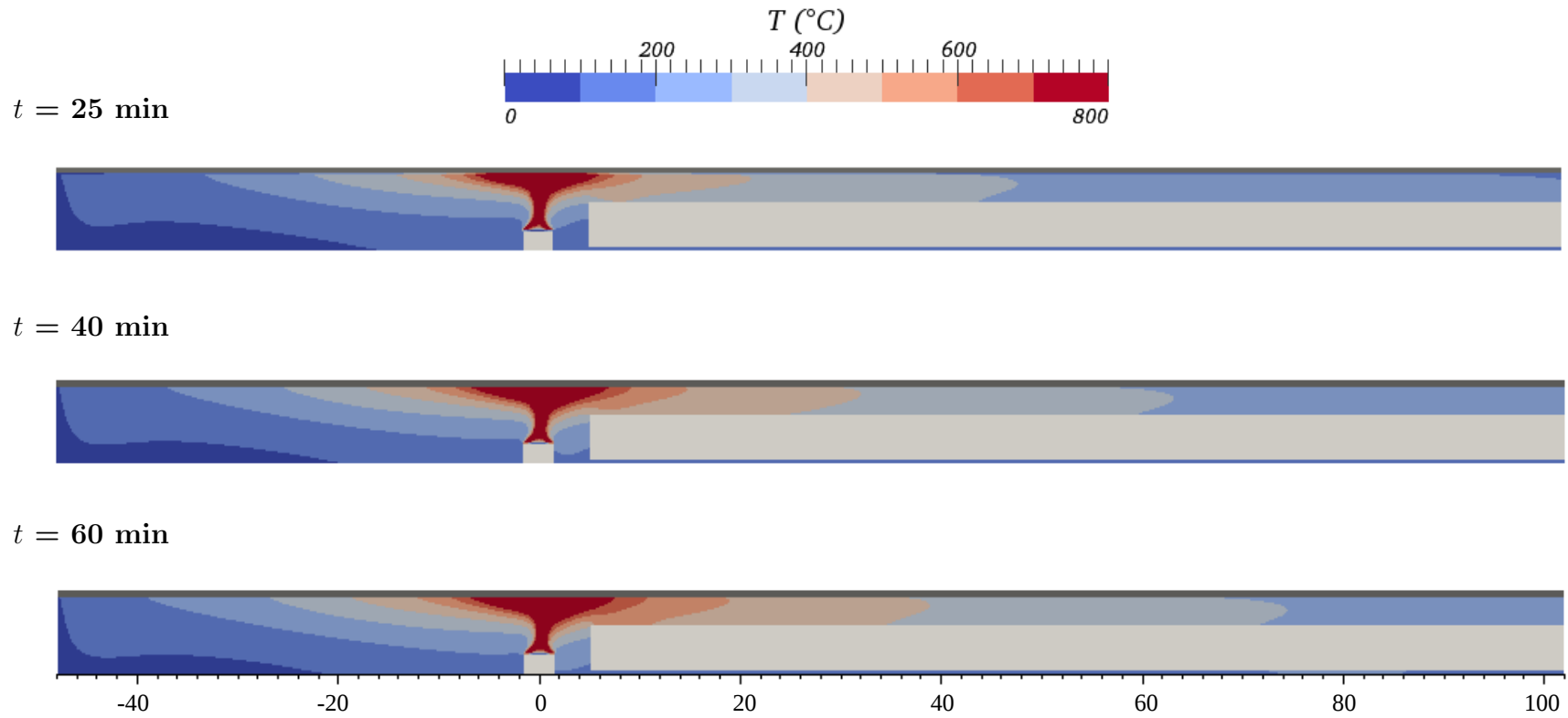
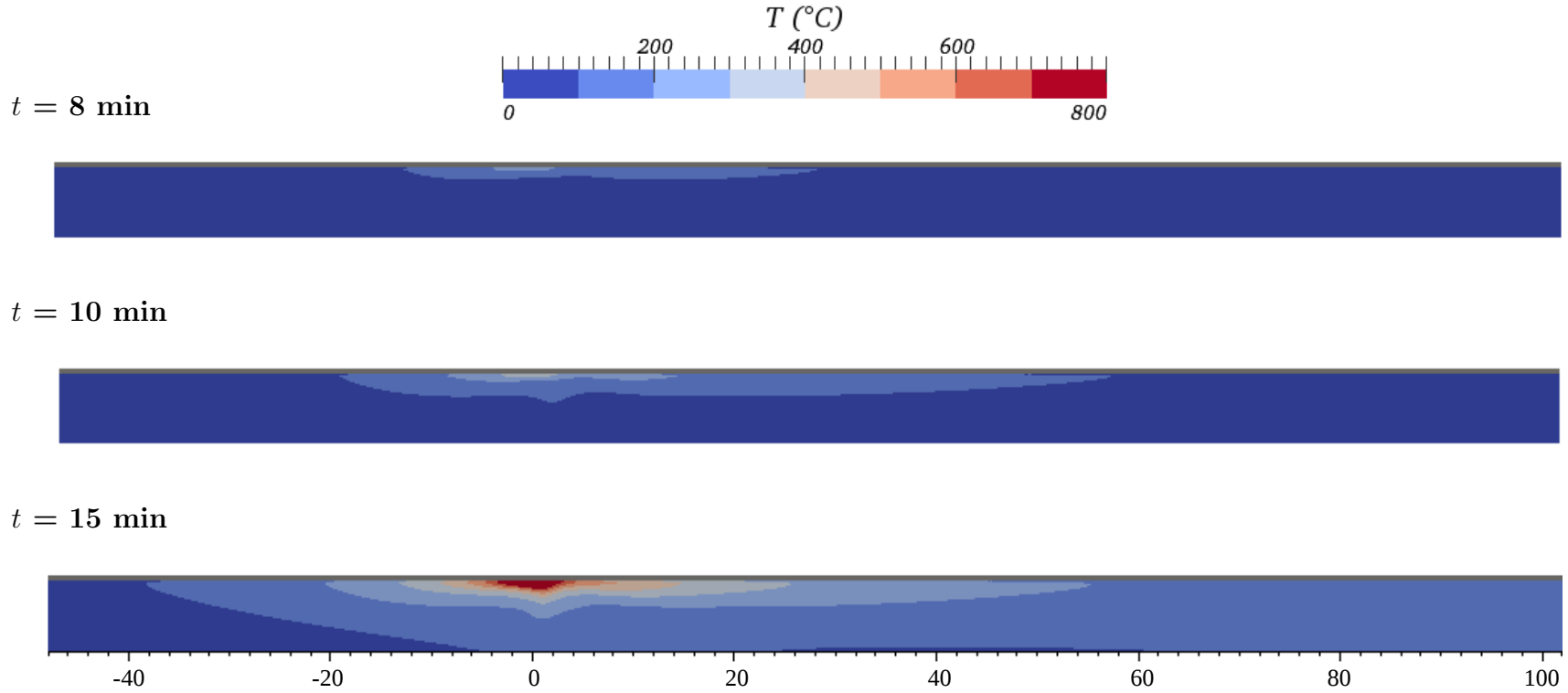


Figure E.2: Contour plots of temperature at  $z = -2.3$  m for the arced cross-section for different time instants (dimensions in m)



### E.1.3 Rectangular cross-section ( $z = 0$ m)



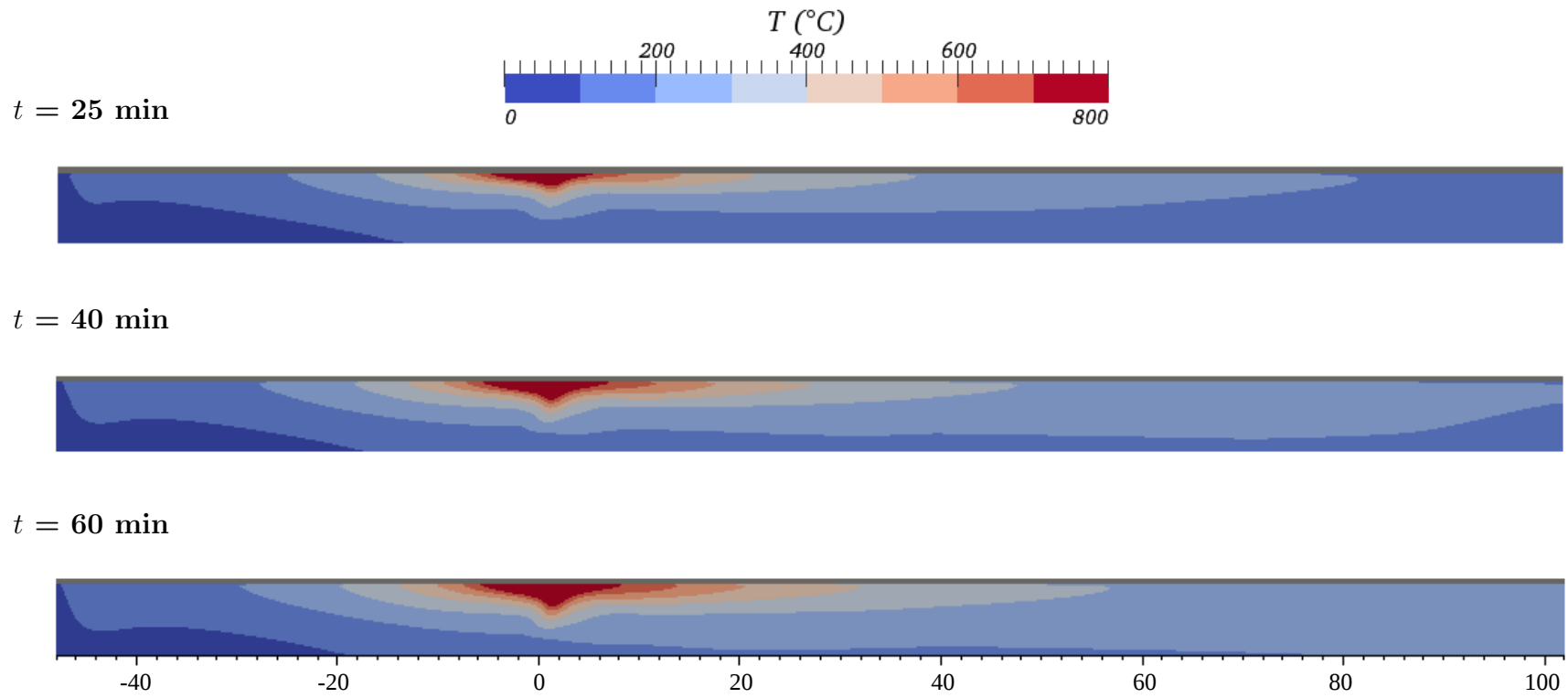
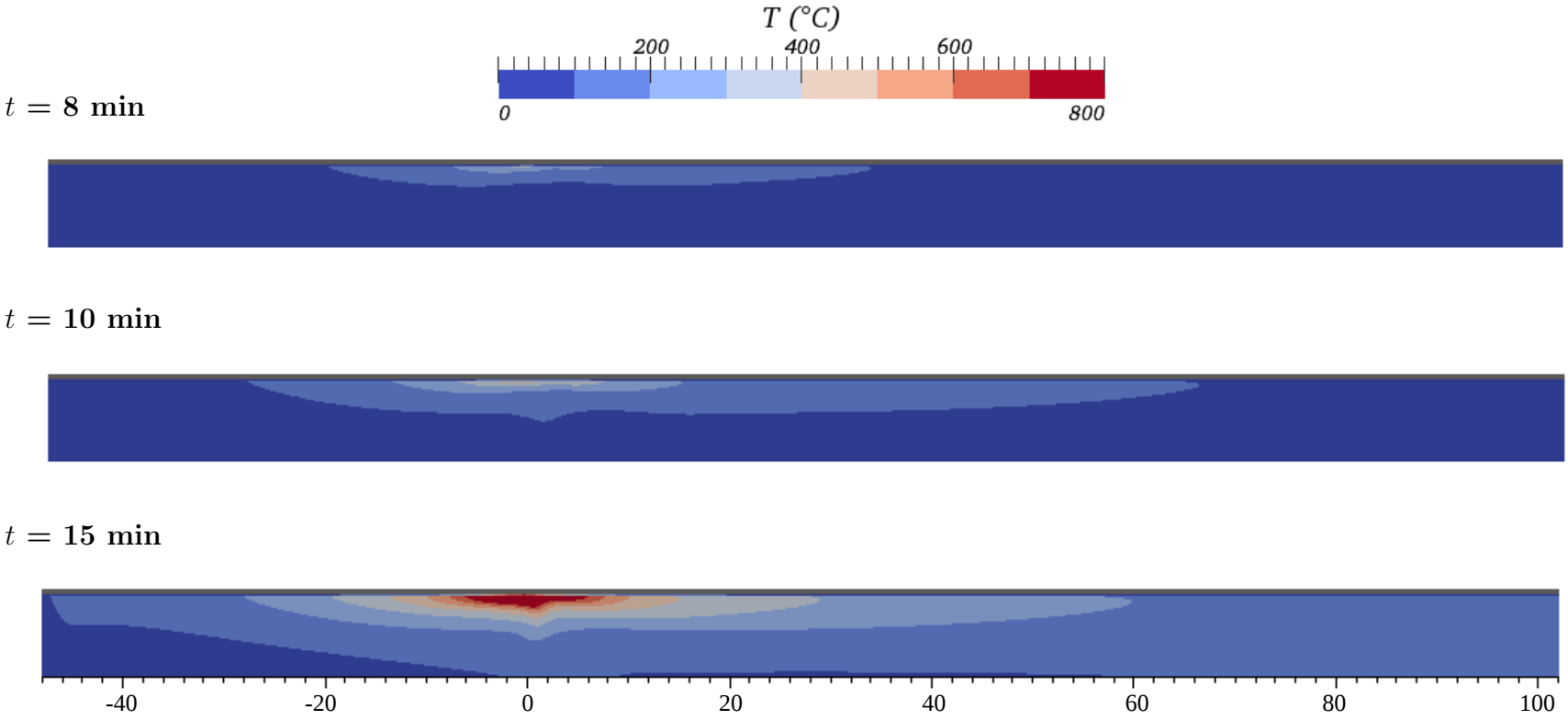


Figure E.3: Contour plots of temperature at  $z = 0$  m for the rectangular cross-section for different time instants (dimensions in m)

E.1.4 Arced cross-section ( $z = 0$  m)



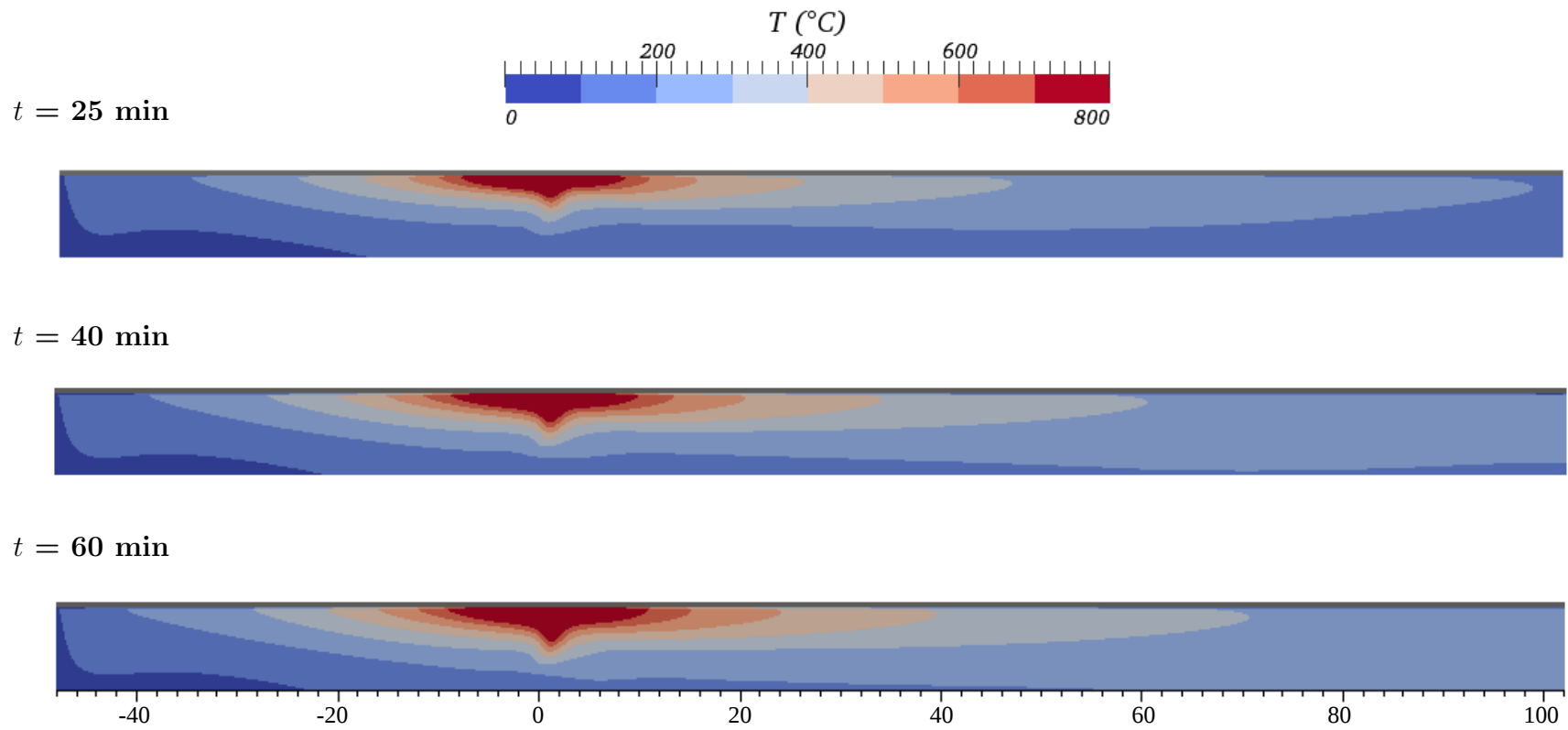


Figure E.4: Contour plots of temperature at  $z = 0$  m for the arced cross-section for different time instants (dimensions in m)

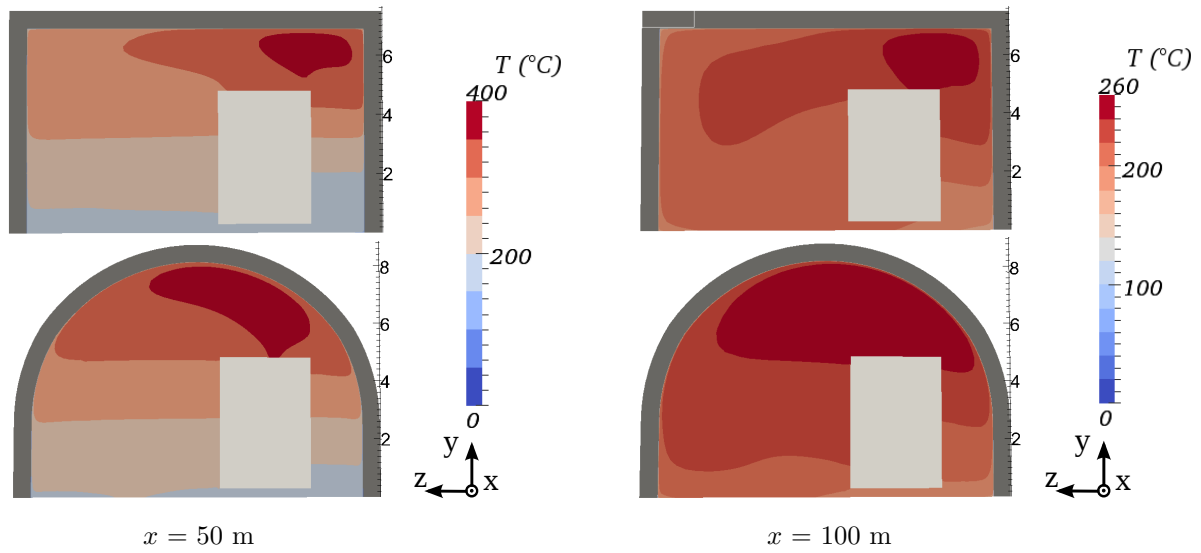
E.1.5 Arced and rectangular cross-section ( $x = 50$  and  $100$  m)

Figure E.5: Contour plots of temperature at  $x = 50$  and  $100$  m for  $t = 60$  min for the rectangular (*top*) and arced (*bottom*) cross-section (dimensions in m)

## E.2 Vertical temperature profiles for a ventilation velocity of 0.5 m/s

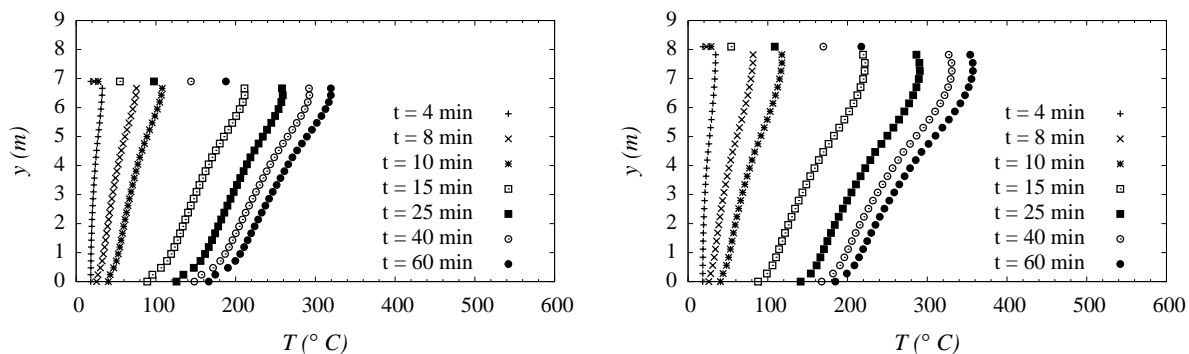


Figure E.6: Vertical temperature profiles along the center-line of the tunnel ( $z = 0$  m) at  $x = 50$  m for the rectangular (*left*) and arced (*right*) cross-section for different time instants

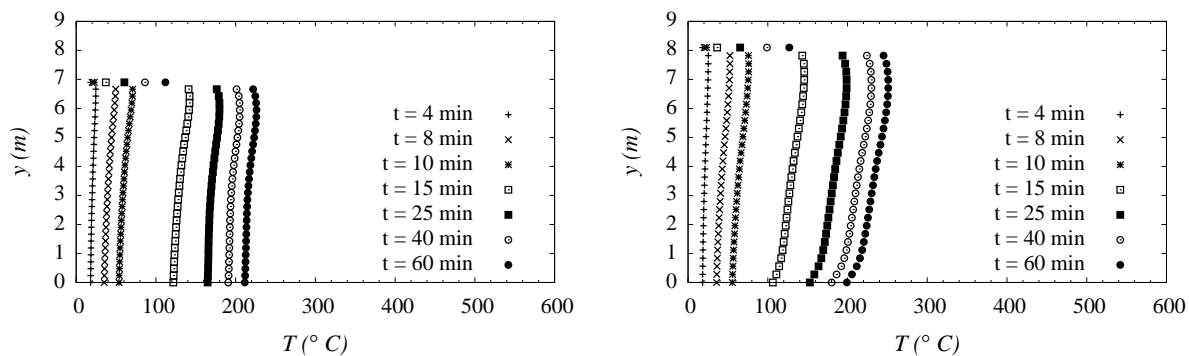


Figure E.7: Vertical temperature profiles along the center-line of the tunnel ( $z = 0$  m) at  $x = 100$  m for the rectangular (*left*) and arced (*right*) cross-section for different time instants

### E.3 Temperature profiles inside tunnel lining for a ventilation velocity of 0.5 m/s

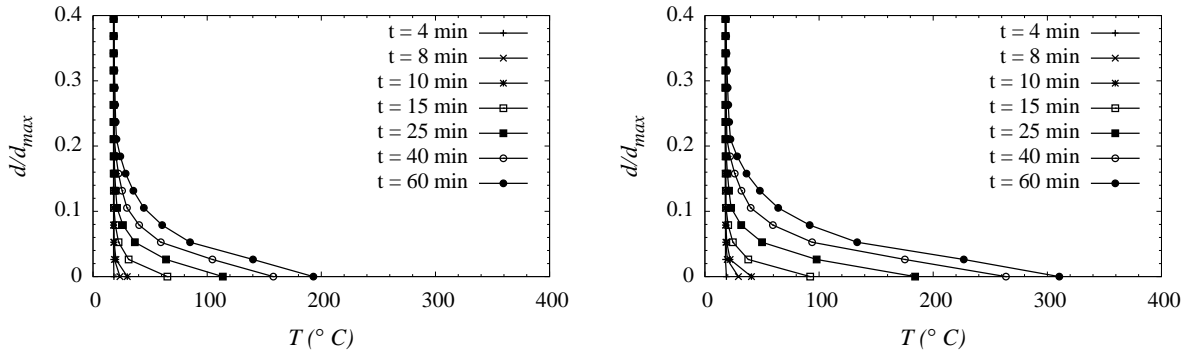


Figure E.8: Temperature profiles inside the tunnel lining along the center-line ( $z = 0$  m) at  $x = -20$  m for the rectangular (*left*) and arced (*right*) cross-section for different time instants

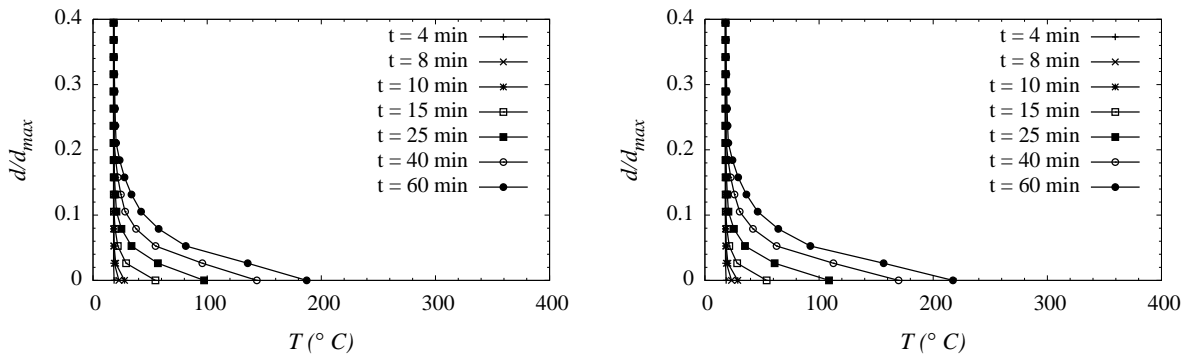


Figure E.9: Temperature profiles inside the tunnel lining along the center-line ( $z = 0$  m) at  $x = 50$  m for the rectangular (*left*) and arced (*right*) cross-section for different time instants

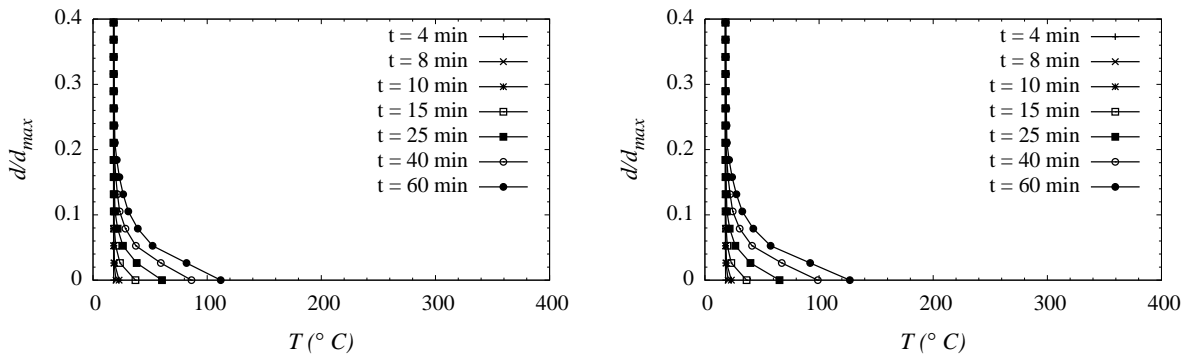


Figure E.10: Temperature profiles inside the tunnel lining along the center-line ( $z = 0$  m) at  $x = 100$  m for the rectangular (*left*) and arced (*right*) cross-section for different time instants

## E.4 Contour plots of velocity magnitude for a ventilation velocity of 0.5 m/s

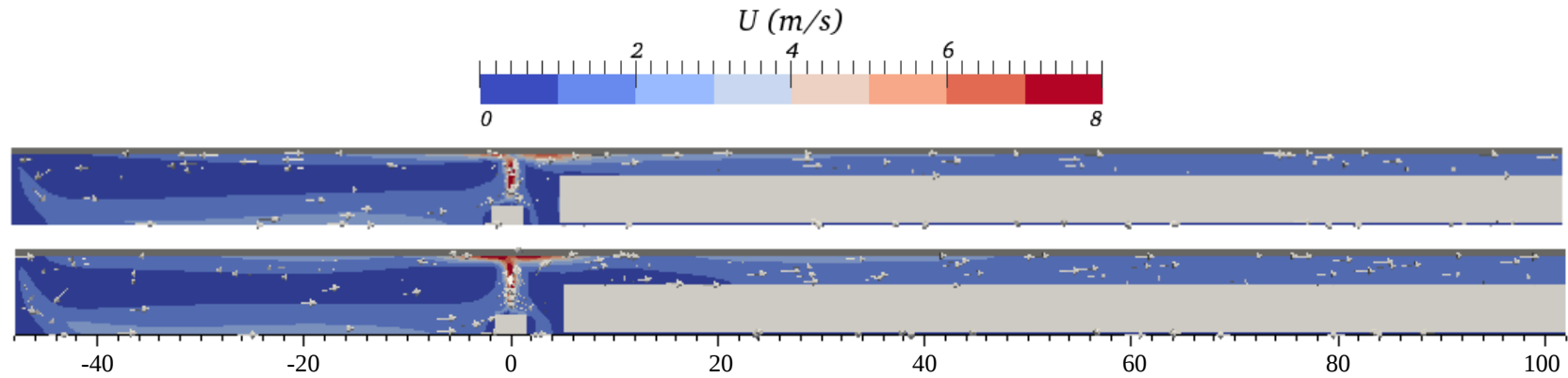


Figure E.11: Contour plots of velocity magnitude at  $z = -2.3$  m for the rectangular (*top*) and arced (*bottom*) cross-section for  $t = 10$  min (dimensions in m)



## E.5 Vertical profiles of horizontal velocity for a ventilation velocity of 0.5 m/s

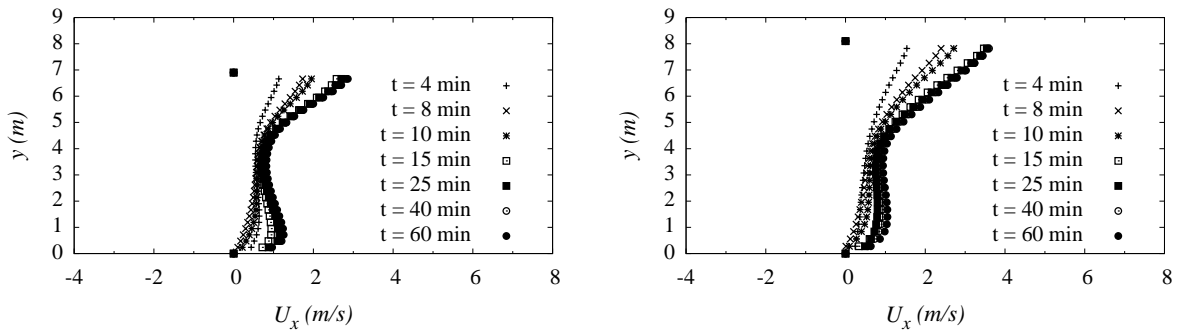


Figure E.12: Vertical profiles of horizontal velocity along the center-line of the tunnel ( $z = 0$  m) at  $x = 25$  m for the rectangular (*left*) and arced (*right*) cross-section for different time instants

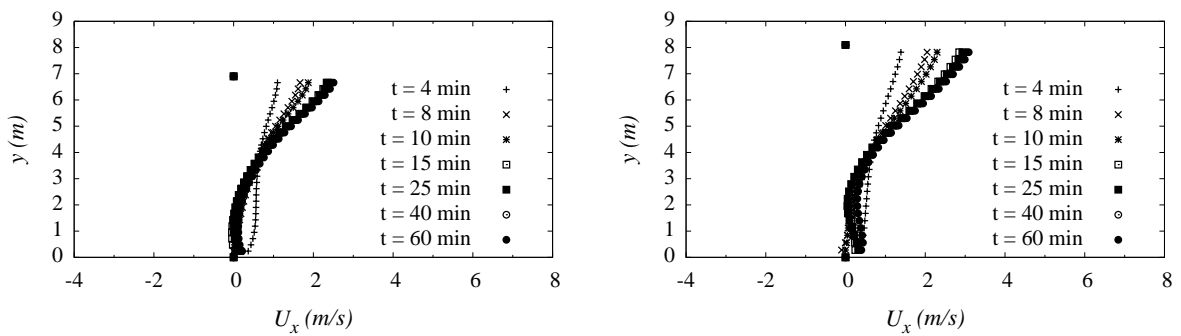


Figure E.13: Vertical profiles of horizontal velocity along the center-line of the tunnel ( $z = 0$  m) at  $x = 50$  m for the rectangular (*left*) and arced (*right*) cross-section for different time instants

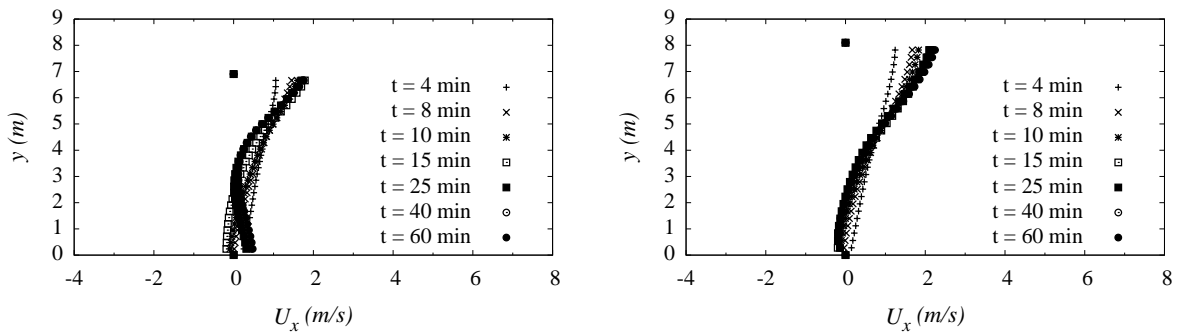
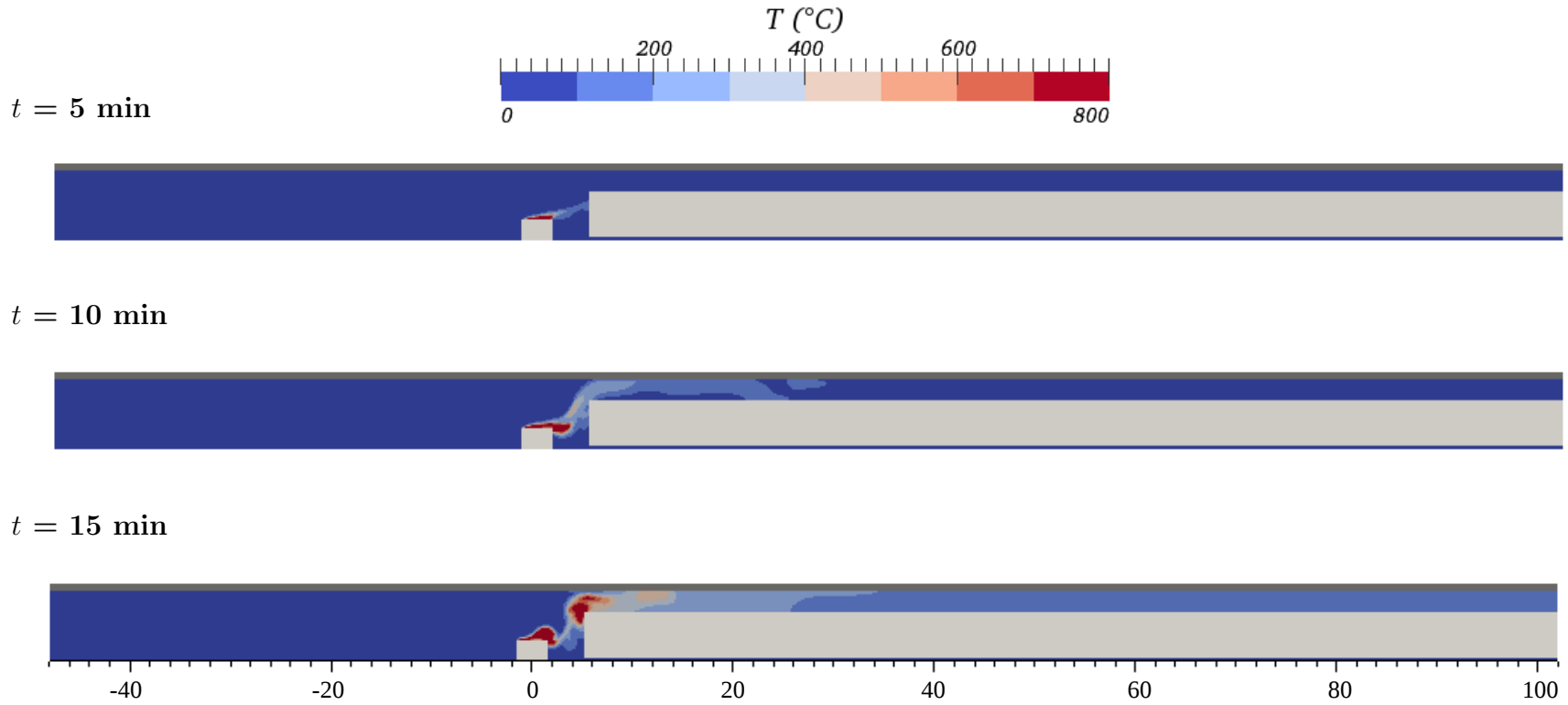


Figure E.14: Vertical profiles of horizontal velocity along the center-line of the tunnel ( $z = 0$  m) at  $x = 100$  m for the rectangular (*left*) and arced (*right*) cross-section for different time instants

## E.6 Contour plots of temperature for a ventilation velocity of 3 m/s

### E.6.1 Rectangular cross-section ( $z = -2.3$ m)



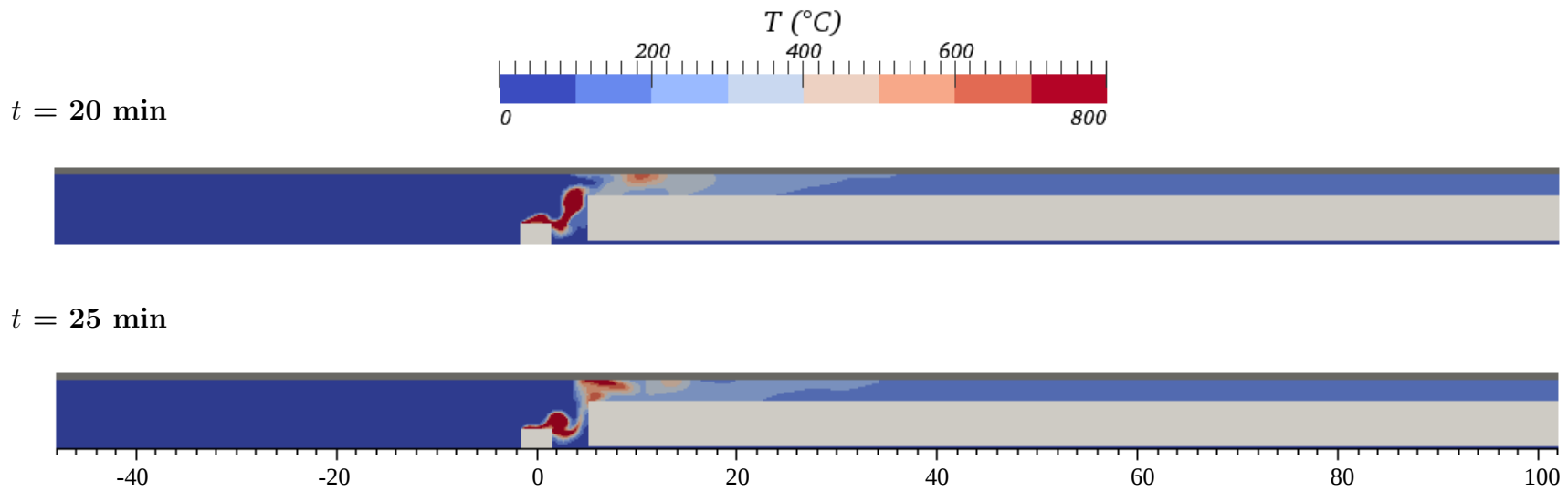
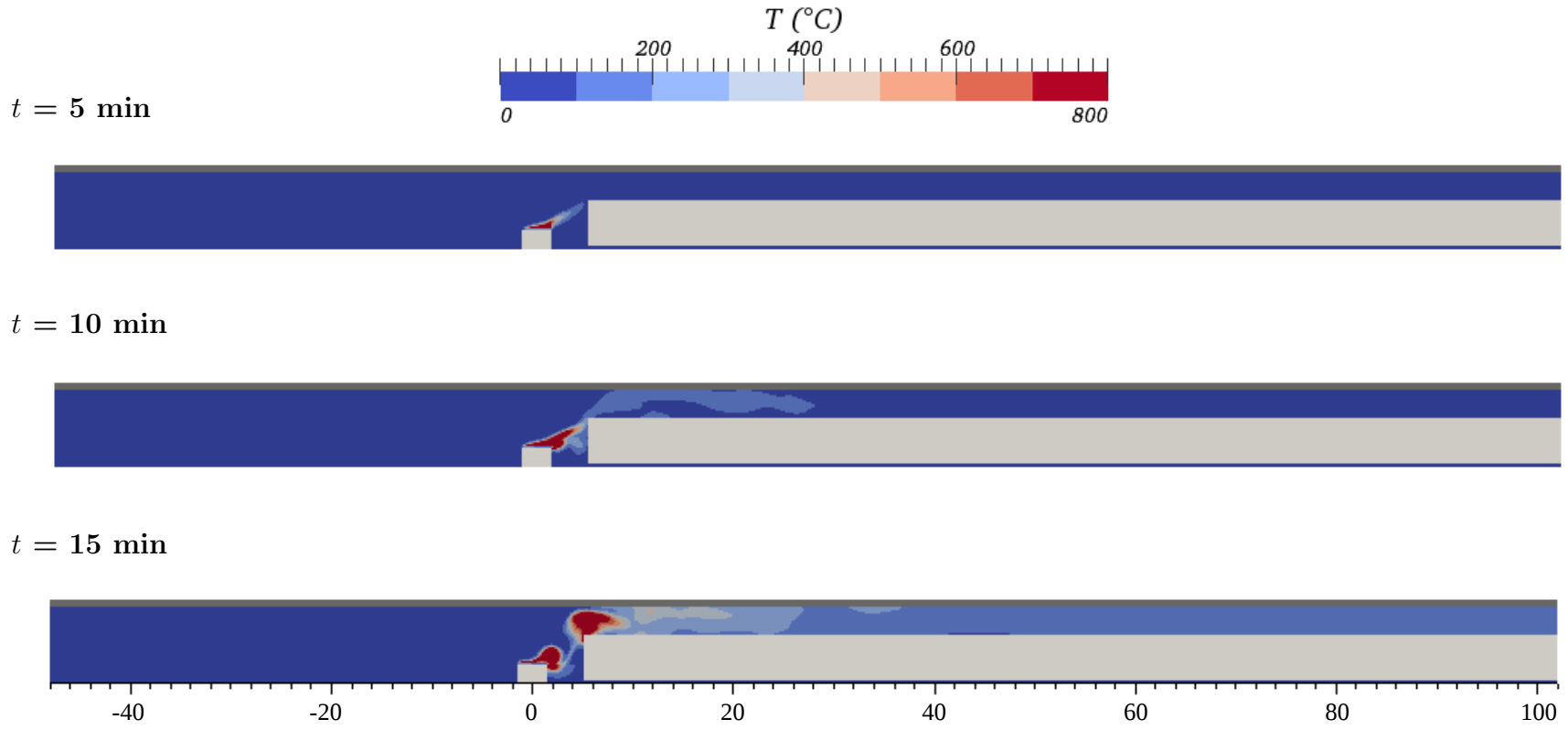


Figure E.15: Contour plots of temperature at  $z = -2.3$  m for the rectangular cross-section for different time instants (dimensions in m)

### E.6.2 Arced cross-section ( $z = -2.3$ m)



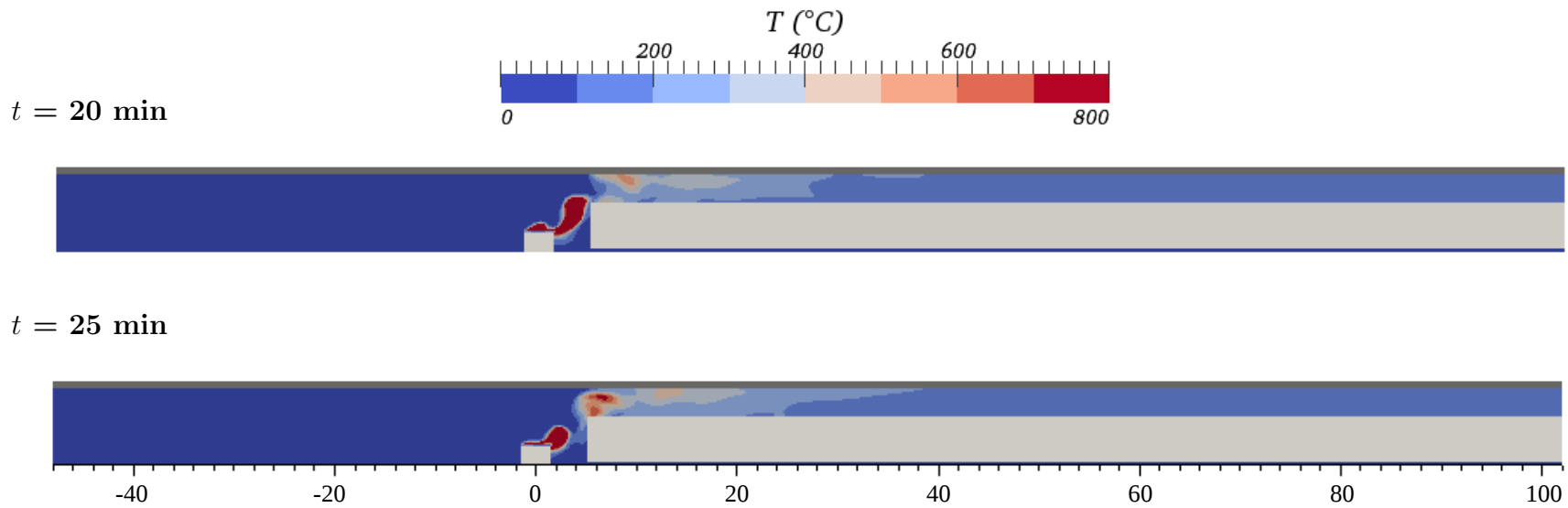


Figure E.16: Contour plots of temperature at  $z = -2.3$  m for the arced cross-section for different time instants (dimensions in m)

### E.6.3 Arced and rectangular cross-section ( $x = 50$ and $100$ m)

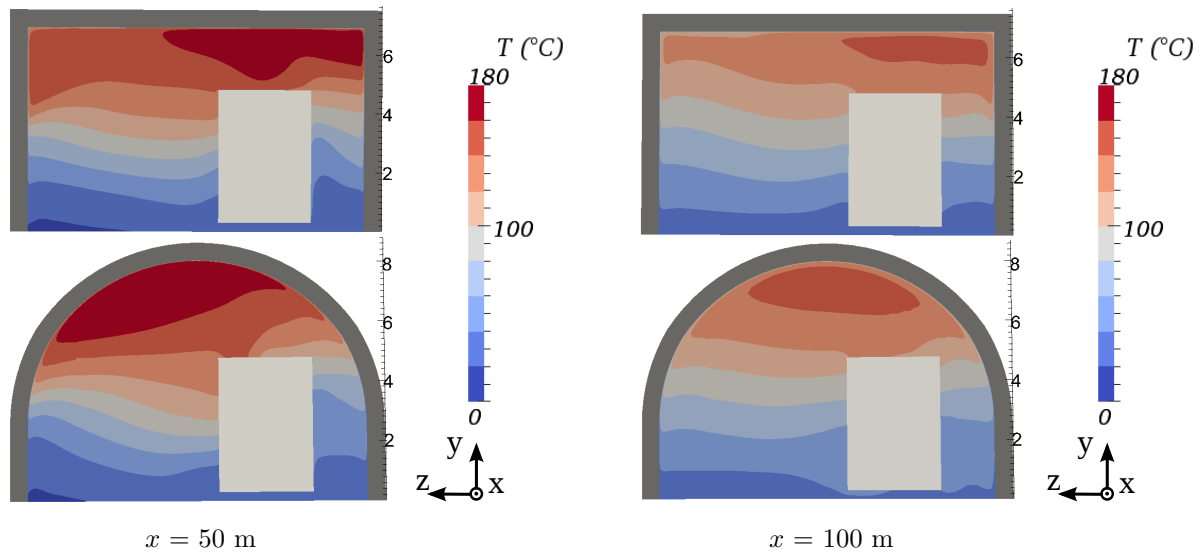


Figure E.17: Contour plots of temperature at  $x = 50$  and  $100$  m for  $t = 25$  min for the rectangular (*top*) and arced (*bottom*) cross-section (dimensions in m)

## E.7 Vertical temperature profiles for a ventilation velocity of 3 m/s

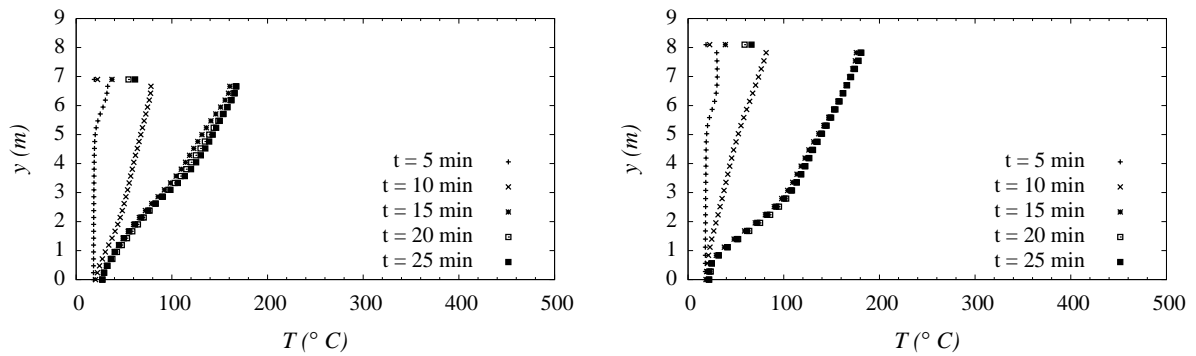


Figure E.18: Vertical temperature profiles along the center-line of the tunnel ( $z = 0$  m) at  $x = 50$  m for the rectangular (*left*) and arced (*right*) cross-section for different time instants

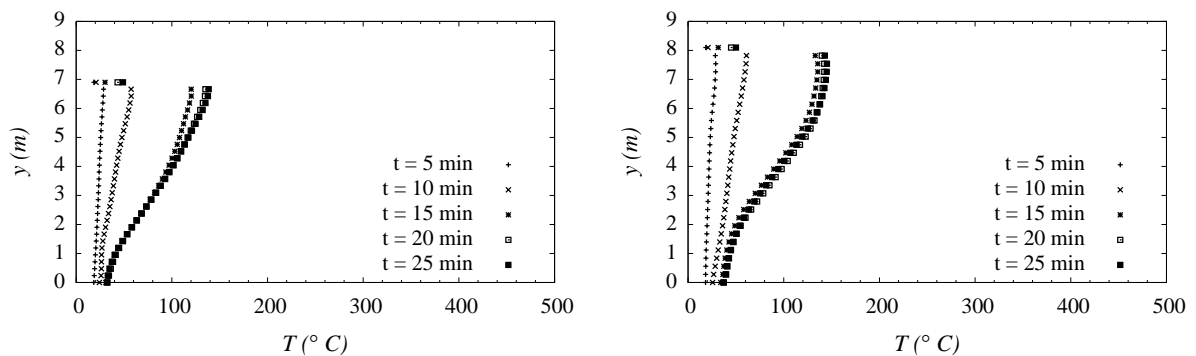


Figure E.19: Vertical temperature profiles along the center-line of the tunnel ( $z = 0$  m) at  $x = 100$  m for the rectangular (*left*) and arced (*right*) cross-section for different time instants

## E.8 Temperature profiles inside tunnel lining for a ventilation velocity of 3 m/s

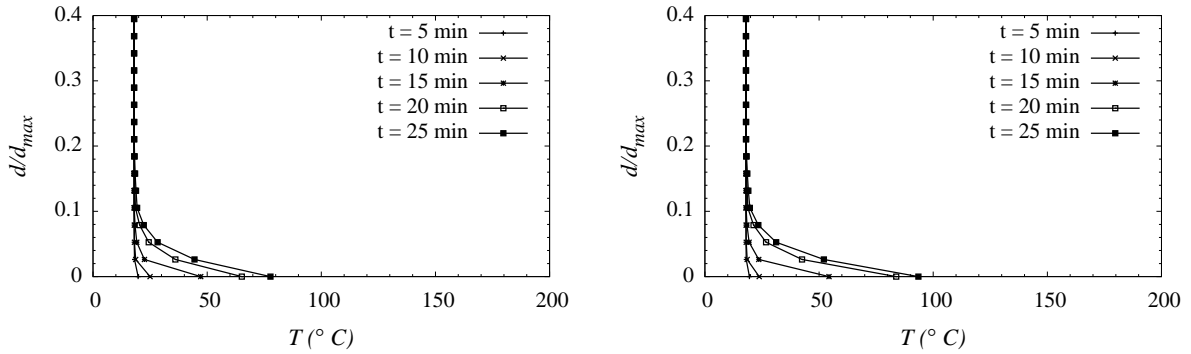


Figure E.20: Temperature profiles inside the tunnel lining along the center-line ( $z = 0$  m) at  $x = 25$  m for the rectangular (*left*) and arced (*right*) cross-section for different time instants

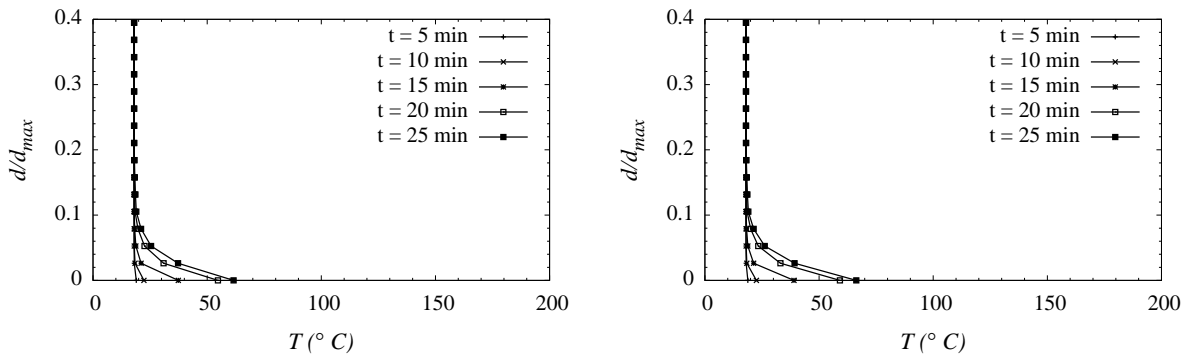


Figure E.21: Temperature profiles inside the tunnel lining along the center-line ( $z = 0$  m) at  $x = 50$  m for the rectangular (*left*) and arced (*right*) cross-section for different time instants

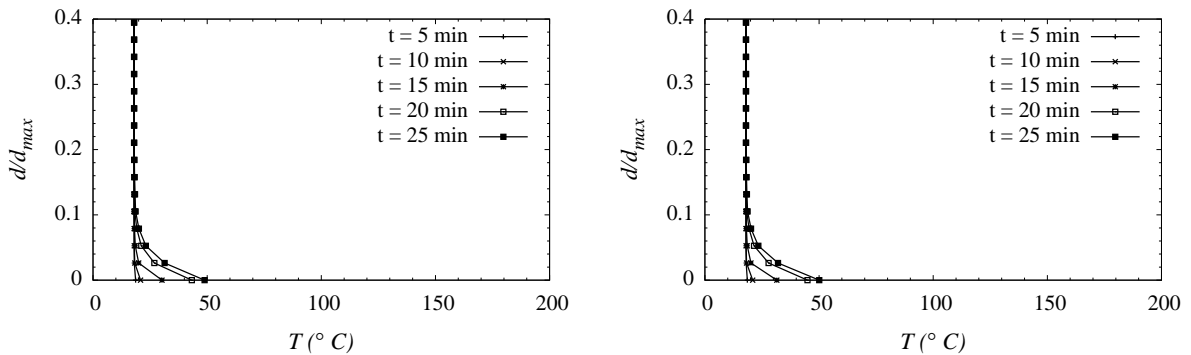


Figure E.22: Temperature profiles inside the tunnel lining along the center-line ( $z = 0$  m) at  $x = 100$  m for the rectangular (*left*) and arced (*right*) cross-section for different time instants



## E.9 Contour plots of velocity magnitude for a ventilation velocity of 3 m/s

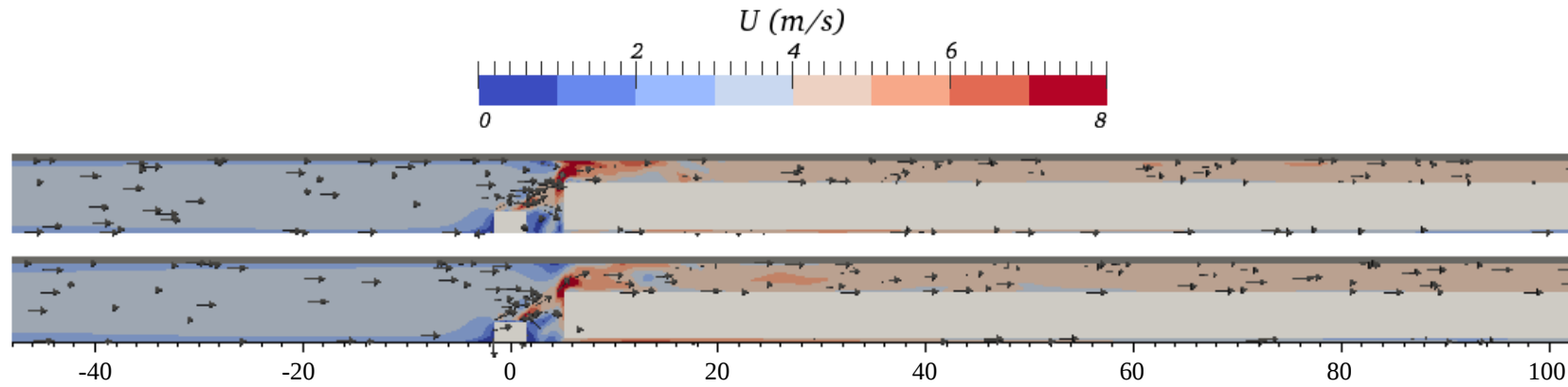


Figure E.23: Contour plots of velocity magnitude at  $z = -2.3$  m for the rectangular (*top*) and arced (*bottom*) cross-section for  $t = 25$  min (dimensions in m)

### E.9.1 Arced and rectangular cross-section ( $x = 50$ and $100$ m)

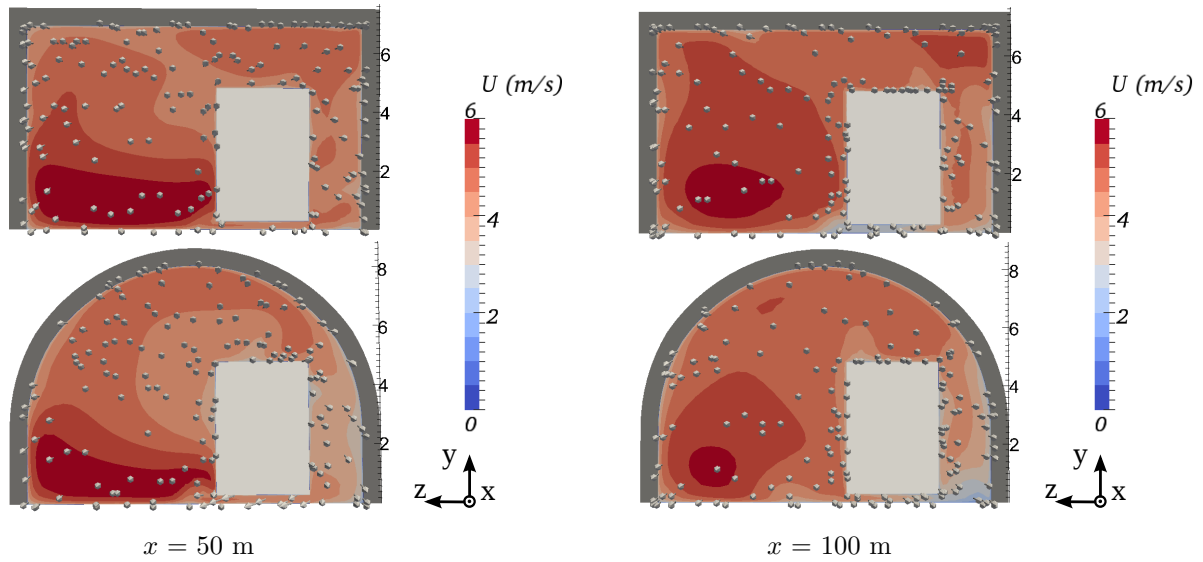


Figure E.24: Contour plots of velocity magnitude at  $x = 50$  and  $100$  m for  $t = 25$  min for the rectangular (*top*) and arced (*bottom*) cross-section (dimensions in m)